From Fault Dynamics to Seismic Hazard Assessment

Sylvain Michel

Darwin College

April 2018

This dissertation is submitted for the degree of Doctor of Philosophy.

Summary

Candidate: Sylvain MICHEL

Title: From Fault Dynamics to Seismic Hazard Assessment

My work focused on the development of improved methodologies for the evaluation of seismic hazard and its related uncertainties, based on the study of active faults systems and dynamic modelling of the seismic cycle. I worked in particular on the probabilistic estimate of a fault's maximum magnitude earthquake and of its return period. Those parameters are indeed crucial to estimate seismic hazard. Seismicity can be viewed as a stochastic process which is constrained by the principle of moment conservation: seismic ruptures must in principle rupture fault portions which had accumulated a deficit of slip, in view of their long term slip rate, during the interseismic period. In Chapter 1, I explain how we implemented those constraints in the evaluation of the probability distribution describing the magnitude and return period of the largest earthquake, propagating the geodetic uncertainties up to the hazard calculation. We applied this methodology to the Parkfield Segment of the San Andreas Fault, where the seismic cycle is particularly well documented. Our study implies potential maximum magnitude between 6.5 and 7.5, with a return period of 140 to 300 years. In Chapter 2, we applied the same methodology to the Cascadia subduction zone, known to have produced a $M\sim9$ earthquake in 1700 but where the seismic hazard remains poorly constrained. As part of this study we determined a model of interseismic coupling and of fault slip due to Slow Slip Events using an Independent Component Analysis-based inversion method. Finally, in Chapter 3, I use dynamic modelling to tackle the problem of partial ruptures. Large earthquakes tend to be confined to fault areas locked in the interseismic period but they often rupture them only partially. For example, during the 2015 M7.8 Gorkha earthquake, Nepal, a slip pulse propagating along-strike unzipped the bottom edge of the locked portion of the Main Himalayan Thrust. The lower edge of the rupture produced dominant high-frequency (>1 Hz) radiation of seismic waves. We showed that similar partial ruptures occur spontaneously in a simple dynamic model of earthquake sequences on a planar fault without mechanical, frictional and geometrical heterogeneities.

Preface

- This dissertation is the result of my own work and includes nothing which is the outcome of work done in collaboration except as declared in the Preface and specified in the text.
- It is not substantially the same as any that I have submitted, or, is being concurrently submitted for a degree or diploma or other qualification at the University of Cambridge or any other University or similar institution except as declared in the Preface and specified in the text. I further state that no substantial part of my dissertation has already been submitted, or, is being concurrently submitted for any such degree, diploma or other qualification at the University of Cambridge or any other University or similar institution except as declared in the Preface and specified in the text
- It does not exceed the prescribed word limit for the relevant Degree Committee.

Sylvain Michel

April 2018

Acknowledgements

I would first like to thank Jean-Philippe Avouac for these wonderful 3 years and a half, during which I have been absorbing his passion about geoscience every day. I cannot thank him enough for giving me this opportunity to be able to work in research and teaching me the "b.a.-ba" in Geology, Geophysics, Aeolian physics and all the innumerable knowledge he somehow stores within his brain. It has been exceptionally fun and exciting to be able to work with him. "Chapeau bas".

I want to praise Nadia Lapusta, Adriano Gualandi and Romain Jolivet who are my other main academic pillars and who forged the new researcher that I am. I thank also all my other co-authors and colleagues who helped and followed me in my work.

I am extremely grateful to Richard Walters and David Al-Attar for my Viva; Alex Copley and James Jackson, who have followed my work and let me be part of the Bullard Laboratory, for their generosity; Lisa and the ISP office who handled my extremely complicated case. I thank, of course, the University of Cambridge and Caltech which both took me in and were the framework of all our exciting research.

I bless my wife, Manuela, architect of my last 5 years, cornerstone of my unending joy, who enlightened my life throughout this adventure. She owns a huge part of this Ph.D. since she gave the initial push and guided me through it. I thank all my close family, Frédéric, Josiane, Tristan and Li, my foundation, who give me eternal support, and my French and extended Argentinian family who are a permanent sunlight.

And finally, a tremendous hooray to all my friends, Lance, Adriano, William, the Bananas, Mortaza, Raven and family, Elle, the Caltech lads, Linley and Bob, the beautiful people of L.A., sunny California, crazy Berlin, exquisite and ancestral Cambridge, David, Andy, Camilla, Johnny, Christopher, Grace, Bullard and co, Aurélien and Rachel, all the AGU fellows and my childhood friends, Aline, Marie-France, Cyril, Nico and Polo!

A "révérence" to you all.

Content

List of Tables

List of Figures

Le savoir scientifique n'est pas absolu, mais socialement, culturellement, technologiquement et historiquement marqué, donc provisoire.

Aimé Césaire

Introduction

Earthquakes are among the most destructive natural hazards on Earth but the underlying physics leading to such devastating event remains to be elucidated. Earthquakes correspond to the sudden release of elastic potential energy resulting in fault slip and radiated seismic waves. Between earthquakes, during the so-called interseismic period, continuous tectonic plate motion leads to the accumulation of energy within locked sections of faults, but some portions of active faults slip aseismically and may accumulate a fraction of the total potential energy in the long-term. Further aseismic deformation also occurs after major earthquakes, accommodating the new state of stress. The moment conservation principle requires that the deficit of moment resulting from fault locking in the interseismic period be balanced by the moment released by aseismic and seismic fault slip, and off-fault deformation.

Seismic hazard studies aim at assessing the probability that the ground motion, which can be quantified using the peak ground acceleration, peak ground velocity or some other quantity correlated with potential damages to buildings, will exceed a given threshold over a chosen period. Seismic hazard in a region thus depends primarily on the probability that an earthquake will occur in a given geographic area, within a given window of time, as well as on the probability of its magnitude. The estimation of the magnitude and recurrence time of the largest seismic event possible in a region is thus highly important, since the probability distribution of these quantities are needed to quantify expected ground motion in a set time period with a certain level of probability. It is a difficult task due to the short time period of observation (in general a few decades). This thesis focuses on improving methods to estimate the seismic potential evaluation of three regions with different tectonic settings: the strike-slip San Andreas Fault in California, the subduction zone in the Cascadia region, and the continental megathrust in the Himalayas. Throughout this work we address the seismic potential evaluation through divers means, using a probabilistic approach based on the afford mention moment conservation principle, but also using forward modelling methodologies to try to understand the origin of certain pattern of fault dynamics leading to large earthquakes, and refining fault's kinematics visualisation allowing us a better assessment of future potential threats. This thesis aims at improving our understanding of the mechanics and dynamics of active faults during all phases of the earthquake cycle and at

developing physics-based methods for the evaluation of seismic hazard, that take advantage of the full range of geodetic, geological and seismological data available.

One way to describe potential earthquakes in a seismic hazard study is to consider that they result from a stochastic process associated with a given probability distribution. The process must, however, obey some physical constraints such as the principle of seismic moment conservation. In Chapter 1, we develop a methodology implementing the constraint of moment conservation to evaluate the probability distribution describing the magnitude and return period of the largest earthquake in a given region, propagating the geodetic uncertainties up to the hazard calculation [*Michel et al.,* Bulletin of the Seismological Society of America, 2017b]. We apply the technique to the Parkfield segment of the San Andreas Fault (SAF), which was chosen as a test example because of the large amount of geological and geophysical information available [*e.g., Sieh*, 1978; *Murray and Segall,* 2005; *Bruhat et al.,* 2011; *Wang et al.,* 2014; *Jolivet et al.,* 2015].

Chapter 2 is focused on the Cascadia subduction zone (West Canada and US). In this densely-populated area, the pacific plate subducts underneath North America, and is presumed to have caused M9 earthquakes [e.g., *Atwater,* 1987; *Satake et al.,* 1996; *Goldfinger et al.,* 2012], comparable to those that occurred in Japan or Chile. Despite the profusion of available geodetic and seismological data, the associated seismic hazard is poorly constrained. The analysis of geodetic data and moment budget are difficult due to the presence of slow slip events (SSEs) [e.g., *Dragert et al.,* 2001; *Roger and Dragert,* 2003], ongoing post-seismic deformation after large earthquakes, and the influence of surface loads, linked to surface hydrology. We apply a variational Bayesian Independent Component Analysis (vbICA) on GPS time series of displacement to separate the different sources of signal [e.g., *Gualandi et al.,* 2016; 2017]. This technique is effective at identifying and filtering non-tectonic sources of strain such as surface loading, which can be compared using GRACE gravimetric data, and thermal origin deformation. It also separates different tectonic processes. This technique, combined with an inversion of the tectonically-related Independent Components (ICs), allows us to characterize the spatio-temporal evolution of slip related to SSEs along the megathrust from 2007 to 2017 (ICA-based Inversion Method, or ICAIM). We also determine the pattern of interseismic coupling along the Megathrust from inverting the secular geodetic signal due to interseismic strain. We discuss the

implications of our kinematic model for SSEs dynamics, and for seismic hazard based on the moment budget approach.

Chapter 3 [*Michel et al.,* Geophysical Research Letter, 2017a] illustrates how dynamic modelling of the seismic cycle [*e.g.*, *Lapusta and Liu,* 2009] can be used to test certain feature and behaviour of particular earthquakes and assess the relationships between interseismic loading and coseismic stress release. A number of recent studies have shown that large earthquakes tend to be confined to fault areas locked in the interseismic period [*e.g.*, *Konca et al.,* 2007; *Moreno et al.,* 2010], commonly imaged nowadays with geodetic methods. These events often rupture locked areas only partially and the reason for partial ruptures are poorly understood. The 2015 M7.8 Gorkha earthquake in Nepal is an example of a partial rupture in a region where much larger events could occur [*Bollinger et al.,* 2016, *Stevens and Avouac,* 2016]. In this chapter, we use dynamic modelling of the seismic cycle in order simulate the main features of the Gorkha earthquake, including the partial rupture of the Main Himalayan Thrust (MHT), the pulse-like behaviour, and the dominant radiation of high-frequency (>1 Hz) seismic waves at depth [*e.g.*, *Avouac et al.,* 2015; *Elliott et al.,* 2016]. The simulations incorporate inertial wave-mediated effects during seismic ruptures (i.e., they are fully dynamic) and account for all phases of the seismic cycle in a self-consistent way. We propose that stress heterogeneities, deduced from geodetic data, exert control on the rupture behaviour. The rupture during the Gorkha earthquake remained confined in the high stress rate accumulation zone located at the base of the locked area of the MHT during the interseismic period. The study of the influence of physical properties of faults on active fault dynamics thus sheds light on potential outcomes of seismic sequences.

Bibliography

Atwater, B. F. (1987), Evidence for great Holocene earthquakes along the outer coast of Washington State. *Science*, *236*(4804), 942-944.

Avouac, J.-P. (2015), From Geodetic Imaging of Seismic and Aseismic Fault Slip to Dynamic Modeling of the Seismic Cycle, *Annu. Rev. Earth Planet. Sci.*, *43*, 233-271, doi:10.1146/annurev-earth-060614-105302.

Bollinger, L., P. Tapponnier, S. Sapkota, and Y. Klinger (2016), Slip deficit in central Nepal: omen for a repeat of the 1344 AD earthquake?, *Earth, Planets and Space*, *68*(12).

Bruhat, L., S. Barbot, and J. P. Avouac (2011), Evidence for postseismic deformation of the lower crust following the 2004 Mw6.0 Parkfield earthquake, *J. Geophys. Res.*, *116*(B08401), 1–10, doi:10.1029/2010JB008073.

Dragert, H., Wang, K., & James, T. S. (2001), A silent slip event on the deeper Cascadia subduction interface. *Science*, *292*(5521), 1525-1528.

Elliott, J. R., R. Jolivet, P. J. González, J. Avouac, J. Hollingsworth, and M. P. Searle (2016), Himalayan megathrust geometry and relation to topography revealed by the Gorkha earthquake, *Nat. Geosci.*, *9*, 174–180, doi:10.1038/NGEO2623.

Goldfinger, C., Nelson, C. H., Morey, A. E., Johnson, J. E., Patton, J. R., Karabanov, E., ... & Enkin, R. J. (2012), Turbidite event history: Methods and implications for Holocene paleoseismicity of the Cascadia subduction zone. *US Geological Survey Professional Paper*, *1661*, 170.

Gualandi, A., J. Avouac, J. Galetzka, J. F. Genrich, G. Blewitt, and L. B. Adhikari (2016), Pre- and post-seismic deformation related to the 2015, Mw7.8 Gorkha earthquake, Nepal, *Tectonophysics*, doi:10.1016/j.tecto.2016.06.014.

Gualandi, A., Perfettini, H., Radiguet, M., Cotte, N., & Kostoglodov, V. (2017), GPS

deformation related to the Mw7. 3, 2014, Papanoa earthquake (Mexico) reveals the aseismic behavior of the Guerrero seismic gap. *Geophysical Research Letters*.

Jolivet, R., M. Simons, P. S. Agram, Z. Duputel, and Z.-K. Shen (2015), Aseismic slip and seismogenic coupling along the central San Andreas Fault, *Geophys. Res. Lett.*, *42*, 297–306, doi:10.1002/2014GL062222.

Konca, A. O., J. P. Avouac, A. Sladen, A. J. Meltzner, K. Sieh, P. Fang, Z. H. Li, J. Galetzka, J. Genrich, M. Chlieh, D. H. Natawidjaja, Y. Bock, E. J. Fielding, C. Ji, and D. V. Helmberger (2008), Partial rupture of a locked patch of the Sumatra megathrust during the 2007 earthquake sequence, *Nature*, *456*(7222), 631-635.

Lapusta, N., and Y. Liu (2009), Three-dimensional boundary integral modeling of spontaneous earthquake sequences and aseismic slip, *J. Geophys. Res.*, *114*(B09303), doi:10.1029/2008JB005934.

Michel, S., Avouac, J. P., Lapusta, N., & Jiang, J. (2017a), Pulse-like partial ruptures and high-frequency radiation at creeping-locked transition during megathrust earthquakes. *Geophysical Research Letters*, *44*(16), 8345-8351.

Michel, S., Avouac, J. P., Jolivet, R., & Wang, L. (2017b), Seismic and Aseismic Moment Budget and Implication for the Seismic Potential of the Parkfield Segment of the San Andreas Fault. *Bulletin of the Seismological Society of America*.

Moreno, M., Rosenau, M., & Oncken, O. (2010), 2010 Maule earthquake slip correlates with pre-seismic locking of Andean subduction zone. *Nature*, *467*(7312), 198.Murray, J. R., and P. Segall (2005). Spatiotemporal evolution of a transient slip event on the San Andreas fault near Parkfield, California, *J. Geophys. Res.*, *110*(B09407), doi:10.1029/2005JB003651.

Rogers, G., & Dragert, H. (2003), Episodic tremor and slip on the Cascadia subduction zone: The chatter of silent slip. *Science*, *300*(5627), 1942-1943.

Satake, K., Shimazaki, K., Tsuji, Y., & Ueda, K. (1996), Time and size of a giant earthquake in

Cascadia inferred from Japanese tsunami records of January 1700. *Nature*, *379*(6562), 246.

Sieh, K. E. (1978), Slip along the San Andreas fault associated with the great 1857 earthquake, *Bull. Seismol. Soc. Am.*, *68*(5), 1421–1448.

Stevens, V. L., and J.-P. Avouac (2016), Millenary Mw >9.0 earthquakes required by geodetic strain in the Himalaya, *Geophys. Res. Lett.*, *43*, 1118–1123, doi:10.1002/2015GL067336.

Wang, L., S. Hainzl, and G. Zöller (2014), Assessment of stress coupling among the inter-, co- and post-seismic phases related to the 2004 M6 parkfield earthquake, *Geophys. J. Int.*, *197*(3), 1858–1868, doi:10.1093/gji/ggu102.

Chapter 1

Seismic and Aseismic Moment Budget and Implication for the Seismic Potential of the Parkfield Segment of the San Andreas Fault

Published as “Michel, S., J.-P. Avouac, R. Jolivet, and L. Wang, Seismic and Aseismic Moment Budget and Implication for the Seismic Potential of the Parkfield Segment of the San Andreas Fault (2017b), *Bulletin of the Seismological Society of America*, 108 (1), 19–38. doi: https://doi.org/10.1785/0120160290”

Abstract

This study explores methods to assess the seismic potential of a fault based on geodetic measurements, geological information of fault slip rate and seismicity data. The methods are applied to the Parkfield section along the San Andreas Fault (SAF) at the transition zone between the SAF creeping segment in the North and the locked section of Cholame to the south, where $\boldsymbol{M_w}$~6 earthquakes occurred every 24.5 years on average since the $\boldsymbol{M_w}$7.7 Fort Tejon earthquake of 1857. We compare the moment released by the known earthquakes and associated postseismic deformation with the moment deficit accumulated during the interseismic period derived from geodetic measurement of interseismic strain. We find that the recurring M6 earthquakes are insufficient to balance the slip budget. We discuss and evaluate various possible scenarios which might account for the residual moment deficit and implications of the possible magnitude and return period of $\boldsymbol{M_w}$>6 earthquakes on that fault segment. The most likely explanation is that this fault segment hosts $\boldsymbol{M_w}$6.5 to $\boldsymbol{M_w}$7.5 earthquakes, with a return period of 140 to 300 years. Such events could happen as independent earthquakes in conjunction with ruptures of the Carrizo plain segment of the SAF. We show how the results from our analysis can be formally incorporated in probabilistic seismic hazard assessment assuming various magnitude-frequency distribution and renewal time models**.**

1. Introduction

Tectonic-relative plate motion is mostly taken up by slip localized on a limited number of large faults. This paradigm holds in particular in California [*Meade and Hager*, 2005] where the San Andreas Fault and its peripheral faults form the main fault system. Since earthquakes represent increments of fault slip and that deformation of the upper crust is considered to be mostly seismic, these faults are also assumed to host the largest crustal earthquakes. The relationship between seismicity, faults and geodetic strain has long been conceptualized by the elastic rebound theory of Reid [1910] which states that, on the long term average, elastic strain accumulating around a fault should be balanced by elastic strain released during earthquakes. It is clear, however, that within the seismogenic depth range, slip can be either seismic or aseismic and that the slip rate on a fault and the partitioning of seismic and aseismic slip are the primary factors determining the seismic hazard associated with a particular fault [e.g., *Avouac*, 2015]. The long-term slip rate on a fault can be determined from geological and morphotectonic studies. Once this information is known, the partitioning of seismic and aseismic slip can in principle be derived from seismicity but would require catalogues long enough to be representative of the long-term seismicity. Such catalogues are generally not available. Another approach is based on the assumption that the partitioning of seismic and aseismic slip is determined by spatial variations of fault frictional properties, assumed constant with time. In that case, geodetic measurements of interseismic strain can be used to reveal locked asperities, where friction is presumably rate-weakening, and estimate the accumulation rate of moment deficit building up in the interseismic period (between major earthquakes). This moment needs then to be balanced by the moment released by the large earthquakes and transient aseismic slip. Such slip budget offers ways to estimate the most probable magnitude and frequency of the larger earthquakes on a particular fault. This approach has been recently applied to the Himalayan arc, the Sumatra subduction zone and the longitudinal valley fault in Taiwan [*Ader et al.*, 2012; *Thomas et al.*, 2014; *Stevens and Avouac*, 2016].

Here, we test and refine this approach on the Parkfield segment of the San Andreas fault. This segment lies at the transition zone between the locked segment of the San Andreas Fault (SAF) to the south and the creeping zone in the north (Figure 1.1). It has experienced six M_w

~ 6 earthquakes since the M_w ~ 7.7 Fort Tejon event of 1857 [*Sieh*, 1978; *Bakun et al.*, 2005]. Owing to its quasi-periodic behavior and occurrence of the latest M_w6.0 earthquake in 2004, this section of the SAF has been intensively studied. These studies have yielded good constraints on co- and postseismic deformation related to the 2004 earthquake [*Langbein et al.*, 2005, 2006; *Johanson et al.*, 2006; *Murray and Langbein*, 2006; *Barbot et al.*, 2009; *Bruhat et al.*, 2011; *Wang et al.*, 2012, 2014], transient slow-slip events [*Murray and Segall*, 2005], and interseismic loading [*Murray et al.*, 2001; *Murray and Langbein*, 2006; *Johnson*, 2013; *Wang et al.*, 2014; *Jolivet et al.*, 2015; *Tong et al.*, 2015]. Several studies have noted that strain build-up in the interseismic period does not seem to be balanced by the strain released by M~6 events, given their rate since 1857 [*Segall and Harris*, 1987; *Murray and Segall*, 2002; *Murray and Langbein*, 2006; *Toké and Arrowsmith*, 2006]. This finding has implications for seismic hazard, as it implies that M~6 events should be more frequent, on the long-term average, than has been observed since 1857, or that occasional larger events should occur. The amount of data and the frequent M_w ~ 6 events makes the Parkfield segment of the SAF a particularly appropriate test case to assess the possibility of constraining seismic hazard based on a moment budget approach.

Hereafter, we first describe the methodology used in this study. We then apply it to the Parkfield segment of the SAF and test the sensitivity of our results to various assumptions about the contribution of aftershocks and postseismic deformation. We conclude that M_w > 6 earthquakes are required to close the budget and assess the impact of this result on seismic hazard.

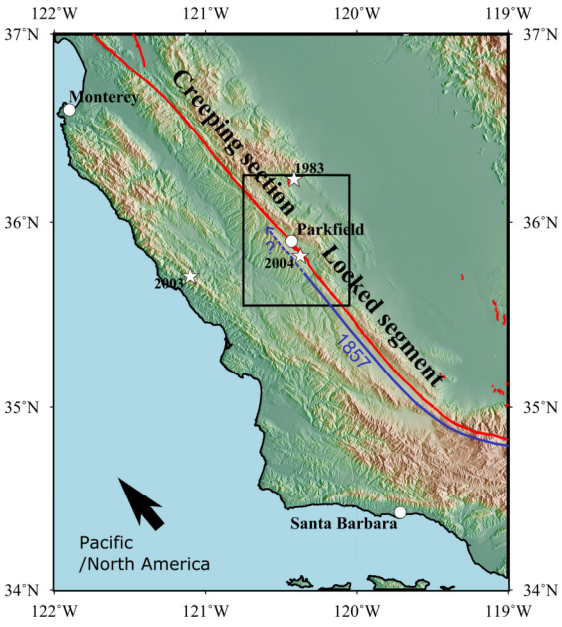

Figure 1.1. *Setting of the Parkfield segment of the San Andreas Fault. This segment lies at the transition between the M7.7 Fort Tejon earthquake rupture of 1857 (thin arrow along the SAF), to the South, and the creeping segment of the SAF to the North. The white stars indicate the latest epicenters of M6+ earthquakes in the region corresponding to the 2004 M6 Parkfield, 1983 M6.3 Coalinga and 2003 M6.6 San Simeon earthquakes. The black box correspond to Figure 1.5 location.*

2. Method

We base our approach on the assumption that the rate of moment deficit accumulating in the interseismic period is, on average over the long-term, equal to the rate of moment released by seismic and transient aseismic slip. Our objective is to derive a probabilistic estimate of the magnitude of the largest possible earthquake along a fault segment, together with an associated recurrence time for such an earthquake. To do so, we calculate the moment released by observed seismicity and afterslip, and divide by the duration of the catalogue to get the average moment release rate. We compare this estimate with the moment deficit rate derived from models of interseismic strain. If the moment deficit rate is larger than the observed moment release rate, the observed maximum magnitude earthquake might not be the most extreme event that can occur along the fault segment. We thus explore the space of magnitude and frequency of maximum magnitude earthquakes to find which events can balance the moment budget and be plausible considering the current statistical distribution of earthquakes. We account for aftershocks, background seismicity and postseismic slip for each maximum magnitude earthquake tested. This method allows us to assess seismic hazard considering uncertainties on the seismic and geodetic data and accounting for our understanding of the behavior of a fault segment. In the following, we detail the method. A flow chart describing the approach, step by step, is available in the supplementary material (Table 1.S.1). Table 1.1 lists the parameters used in this study.

The rate of moment deficit accumulation, $\dot{m}_0$ (in N.m.yr^{-1}), can be written

$$\dot{m}_0 = \int_{Fault} \mu \, D \, dA, \tag{1.1}$$

where μ and A are the shear modulus and the fault area, and D is the slip deficit rate. The slip deficit rate can be expressed as $D = V_{plate} * \chi$ where V_{plate} is the long-term plate rate and χ is the interseismic coupling. The interseismic coupling is defined as the ratio between the deficit of slip and the long-term slip of the fault and is given by

$$\chi = 1 - \frac{S}{V_{plate}}, \tag{1.2}$$

where S is the creep rate observed during the interseismic period. χ is 0 for a fault patch creeping at the long-term slip rate and 1 for a fully locked patch.

The amount of moment released seismically can be estimated from earthquake catalogues, for example an historical catalogue. The average total seismic moment released per year $\dot{m}_S$ is given by

$$\dot{m}_S = \frac{\sum_{j=1}^{N} m_{S,j}}{t_{hist}}, \tag{1.3}$$

where N is the total number of events in the catalogue, $m_{S,j}$ is the seismic moment of each earthquake j and t_{hist} is the time period covered by the catalogue. The observed seismicity might be seen as one particular realization of a stochastic process over a certain period of time. It might not be representative of the long-term average seismic moment rate if the period of time covered by the data is short compared to the return period of the largest possible earthquake.

The moment released by the known seismicity most often does not balance the moment deficit due to interseismic coupling. Many causes can lead to a deficit of seismicity ($\dot{m}_0 > \dot{m}_S$): (1) the largest possible earthquake is not present in the catalogue because of its too short time span; (2) the largest possible earthquake is present in the catalogue but the duration of the catalogue is longer than the average return period of such an event; (3) the undetected seismicity contributes significantly to the moment budget; (4) transient aseismic slip such as afterslip or slow slip events contribute significantly to the moment budget; (5) a fraction of interseismic strain is anelastic and aseismic and is therefore not to be released seismically; (6) interseismic strain is not stationary in time and the period covered by the geodetic data corresponds to a loading rate that is more than the average over the long term. (7) a large earthquake with its epicenter outside the study area may have extended into the area of interest and released a fraction of the moment deficit. In this case, the catalogue does not capture the event. In the context of this study, this could have happened during the M~7.7 1857 Fort Tejon mainshock or possibly as a foreshock. This earthquake ruptured the San Andreas Fault south of Parkfield (Figure 1.1) and might have ruptured the Parkfield segment as well [*Sieh*, 1978].

Table 1.1. *List of variables used in this study*

Variables	*Symbol*	*Comments*
Moment (N.m)	*m*	$\dot{m}_0$: rate of moment deficit accumulation
		$\dot{m}_S$: average total moment release rate of seismicity
		$\dot{m}_{Sa}$: moment release rate of aftershocks and background seismicity
		$\dot{m}_{Sm}$: moment release rate of the largest earthquake
Magnitude	*M*	M_{max} : magnitude of the largest event
		M_{hist}: magnitude of the largest observed event (in catalogue)
		M_{Test}: magnitude tested for the probability to have an earthquake with $\mathrm{M} > \mathrm{M_{Test}}$ during a certain time period ($\mathrm{P_{Hazard}}$)
Shear Modulus (Pa)	μ	
Slip Deficit Rate (N.m.yr^{-1})	*D*	
Fault Area (m^2)	*A*	
Long Term Plate Rate (mm.yr^{-1})	V_{plate}	
Interseismic Coupling	χ	
Slip Rate in the Interseismic Period (mm.yr^{-1})	*S*	
Return Period of Events (yrs)	τ	τ_{max}: return period of the largest event
		τ_{GR}: return period predicted by the observed GR law for $M > M_{hist}$
		τ_M: average recurrence time of independent events with $\mathrm{M} > \mathrm{M_{Test}}$ predicted by a given GR law
Total Number of Earthquakes Recorded per Year (from the GR law)	*a*	
Relative Distribution between Small and Large Earthquakes (from the GR law)	*b*	
Cumulative Number of Earthquakes per Year over Magnitude *M*	*N*	
Number of Events per Year in a Magnitude Range	*r*	
Percentage of aseismic afterslip moment release compared to the moment released seismically	α	
Time Period (yrs)	t	t_{hist}: time period covered by the earthquake catalogue
Number of events during the time period t	*n*	

Alternatively, $\dot{m}_S$, the rate of moment released seismically, can exceed $\dot{m}_0$, the rate of moment build up: (1) the largest possible event is in the catalogue but the period of time covered by the catalogue is shorter than the average return period of such an event; (2) such events have occurred more frequently over this period of time than over the long term average; (3) interseismic strain is not stationary in time and the period covered by the geodetic data corresponds to a loading rate that is less than the average over the long term. In any case, the comparison between $\dot{m}_S$ and $\dot{m}_0$ provides information on the magnitude and average return period of the largest earthquake needed to balance the slip budget on the long term.

The next step consists of calculating the probability of a seismicity model to balance the moment budget and be consistent with the known seismicity. Key parameters of the seismicity model are the magnitude and return period of the largest earthquake.

The probability that the largest event is of magnitude M_{max} and has on average a return period of τ_{max} can be written as the product of two probabilities,

$$P(M_{max}, \tau_{max}) = P_{Budget}(M_{max}, \tau_{max}) * P_{Hist}(M_{max}, \tau_{max}) \, . \qquad (1.4)$$

$P_{Budget}(M_{max}, \tau_{max})$ is the probability that an earthquake of magnitude M_{max} and its associated aftershocks and aseismic afterslip release a moment equal to the deficit of moment accumulated over the return period τ_{max} (i.e. the probability that an earthquake of magnitude M_{max} balances the budget). $P_{Hist}(M_{max}, \tau_{max})$ is the probability that an event of magnitude M_{max} and return period τ_{max} is the maximum possible earthquake based on the historical seismicity.

We calculate P_{Budget} based on the assumption that the maximum-magnitude earthquake is followed by aftershocks and that aseismic afterslip releases a moment proportional to the moment released seismically. For a given mainshock moment magnitude and recurrence time, we compare the moment released by the mainshock and postseismic relaxation (aftershocks and aseismic afterslip) to the estimated rate of moment deficit building up on the fault. Interseismic models of fault coupling derived using a Bayesian approach directly provide the Probability Density Function (PDF) of the rate of moment accumulation [*Wang et al.*, 2014; *Jolivet et al.*, 2015].

We assume that, on average over the long-term, seismicity follows the empirical Gutenberg-Richter (GR) law [*Gutenberg and Richter*, 1944]

$$log_{10}(N_M) = a - b\,M, \tag{1.5}$$

where a and b are constants relating respectively to the total number of earthquakes recorded per year and the relative distribution between small and large earthquakes, and N_M is the cumulative number of earthquakes per year over magnitude M. We assume that the law applies to a catalogue of independent events (with aftershocks removed through 'declustering') as well as to dependent events (a catalogue including aftershocks) and that the b-value is the same in both cases (for a same given area). These assumptions are for examples consistent with the earthquake statistics observed in Southern California [*Marsan and Lengline*, 2008].

The number of events per year with magnitudes in the range $[\,M - \frac{\partial M}{2}, M + \frac{\partial M}{2}]$, is then

$$r = N_{M-\frac{\partial M}{2}} - N_{M+\frac{\partial M}{2}} \tag{1.6}$$

The moment release rate of earthquakes with moment between 0 and m_a, over a period of time, should then converge (in the limit of infinite time) towards

$$\dot{m}_{Sa} = \int_0^{m_a} r\,dm. \tag{1.7}$$

We assume that earthquakes in the study area are bounded by a maximum event of moment m_{max} and magnitude M_{max}. The largest aftershock has often a magnitude of about 1 unit less than the magnitude of the mainshock [*Båth*, 1965] which might imply a bi-modal earthquake distribution. Assuming that the background seismicity does not reach magnitudes larger than the largest aftershock, the return period of the main event and that of the maximum aftershock is the same and the GR relationship runs through $M = M_{max} - 1$ and $\tau = \tau_{max}$.

However, the Båth law is not a physical law and is probably linked to a statistical finite size effect (the number of aftershocks above a certain magnitude is finite and this finite number determines the difference of magnitude between the mainshock and the largest aftershocks) [*Helmstetter and Sornette*, 2003]. It is possible that at the limit of infinite time, although each single cluster of earthquakes could follow the Båth law, the total GR distribution would apply up to the maximum value of the distribution $M = M_{max}$ and $\tau = \tau_{max}$.

In the following, we test both cases and assume that these hypothesis bracket the contribution to the total seismic moment release of earthquakes smaller than the maximum earthquake.

Additionally, we assume that the moment released by aseismic afterslip is a proportion α of the moment released seismically. Assuming that the moment release rate of seismic and aseismic transient slip events balances the rate of moment deficit accumulation on the long run, we get

$$\dot{m}_0 = (\dot{m}_{Sm} + \dot{m}_{Sa})\,(1+\alpha), \tag{1.8}$$

where $\dot{m}_{Sm}$ is the moment release rate of the largest earthquake (the subscript 'S' stands for seismic and 'm' for mainshock), and $\dot{m}_{Sa}$ the moment release rate of aftershocks and background seismicity (the subscript 'S' stands for seismic and the subscript 'a' stands for aftershock).

With the assumptions listed above, it is possible to calculate the probability P_{Budget} of closing the moment budget for a given magnitude and return period of the maximum earthquake. Without taking the Båth law into account, this probability is highest along a straight line in the Gutenberg-Richter plot corresponding to the return period of the largest event [*Molnar*, 1979; *Ader et al.*, 2012],

$$\tau_{max}(m_{max}) = \frac{1}{1-2\,b/3}\frac{(1+\alpha)\,m_{max}}{\dot{m}_0} \quad if \quad b < 3/2, \tag{1.9}$$

where m_{max} is the moment released by the largest mainshock. With the Båth law, the contribution of smaller events become nearly negligible,

$$\tau_{max}(m_{max}) = \frac{10^{-\frac{3\,B}{2}}}{1-2\,b/3}\frac{(1+\alpha)\,m_{max}}{\dot{m}_0}, \tag{1.10}$$

with B the difference in magnitude between the largest event and its largest aftershock. The probability density distribution P_{Budget} depends on the uncertainties on $\dot{m}_0$.

To illustrate the procedure, let us consider a magnitude of 7 with a return time of τ_{max}. The mainshock would release a moment of 3.5 10^{19} N.m. We add to this moment the contribution of aftershocks, background seismicity and aseismic afterslip. The resulting moment is divided by τ_{max} to estimate the average moment release rate for the events of magnitude 7 and

return period τ_{max}. We compare this moment release rate to the rate of accumulation of moment deficit in the interseismic period calculated from interseismic slip rate models.

Without any other constraint, the maximum possible magnitude on a fault that is accumulating moment deficit at a rate $\dot{m}_0$ is actually unbounded: a small and frequent largest earthquake would balance the moment budget as well as a larger infrequent one. Seismicity observations can be used to tighten the space of possible solutions and incorporated through the calculation of $P_{Hist}(M_{max}, \tau_{max})$. This probability represents the probability of the largest earthquake having a magnitude M_{max} and a return period τ_{max} given the known seismicity. To calculate this probability, we consider two approaches:

- Approach 1: We assume that the magnitude and frequency of the maximum-magnitude earthquake falls on the GR law derived from a declustered catalog of local seismicity. This hypothesis is questionable as it is not proven that the GR law applies up to the largest possible event at a local scale;
- Approach 2: The possible magnitude and frequency of the maximum-magnitude earthquake must be consistent with the observed largest event over the observation period (it has to be larger than or equal to the known largest event, and the return period of the larger event cannot be significantly smaller than the observation period)

In both cases, a model of inter-event time distribution is required. In the results presented here, we consider that independent events follow a Poisson process. This is probably a reasonable assumption for events that would rupture only a fraction of the studied fault segment, as two successive events would generally not occur at the same location, so that rebuilding stresses might not be required. For larger events, it might be more appropriate to assume a renewal-time model. In the supplement, we show the results obtained using a Brownian Passage Time model [*Matthews et al.*, 2002; *Field and Jordan*, 2015], which are only marginally different from the ones obtained with the Poisson model.

In the case of a Poisson model, the probability of n events occurring during the time period t is

$$P_{poisson}(n, t, \tau) = \frac{(t/\tau)^n}{n!} e^{-t/\tau}, \quad (1.11)$$

where τ is the average recurrence time of the Poisson process.

Following the first approach, the probability of (M_{max}, τ_{max}) being the magnitude and return period of the largest event depends on the magnitude of the largest observed earthquake M_{hist} and on the return period $\tau_{GR}(M_{max})$ predicted by the GR law derived from a declustered catalog:

$$if\ M_{max} < M_{hist},\ \ P_{Hist}(M_{max}, \tau_{max}) = 0, \tag{1.12}$$

$$if\ M_{max} > M_{hist},\ \ P_{Hist}(M_{max}, \tau_{max}) \propto P_{poisson}(n = 1, \tau_{max}, \tau_{GR}(M_{max})) = (\tau_{max}/\tau_{GR}(M_{max}))e^{-\tau_{max}/\tau_{GR}(M_{max})}. \tag{1.13}$$

We use the sign ∝ to indicate proportionality, as the PDF is normalized.

Following the second approach, the probability of (M_{max}, τ_{max}) being the magnitude and return period of the largest event depends on the magnitude of the largest observed earthquake M_{hist} and on time period covered by the catalog t_{hist}. It can be defined as the probability to have no earthquakes of magnitude over M_{hist} occurring during the time period of the catalog:

$$if\ M_{max} < M_{hist},\ \ P_{Hist}(M_{max}, \tau_{max}) = 0, \tag{1.14}$$

$$if\ M_{max} > M_{hist},\ \ P_{Hist}(M_{max}, \tau_{max}) \propto P_{poisson}(n = 0, \tau_{hist}, \tau_{max}) = e^{-\frac{t_{hist}}{\tau_{max}}}. \tag{1.15}$$

The probability drops rapidly to zero as τ_{max} becomes smaller than t_{hist}. It becomes uniform quickly as τ_{max} gets larger than t_{hist}.

Figure 1.2 shows a schematic representation of the probability $P_{Budget} * P_{Hist}$ in both cases. In the first case, the probability that an earthquake is the maximum possible earthquake in view of the observed seismicity and also closes the moment budget is highest at the intersection between the GR law (equation 1.4) and the line representing the return period of the largest earthquake required to close the moment budget (equation 1.9 or 1.10). In the second case, the probability that an earthquake is the maximum possible earthquake in view of the observed seismicity and also closes the moment budget is highest along the line representing the budget closure condition (equation 1.9 or 1.10). Any large magnitude

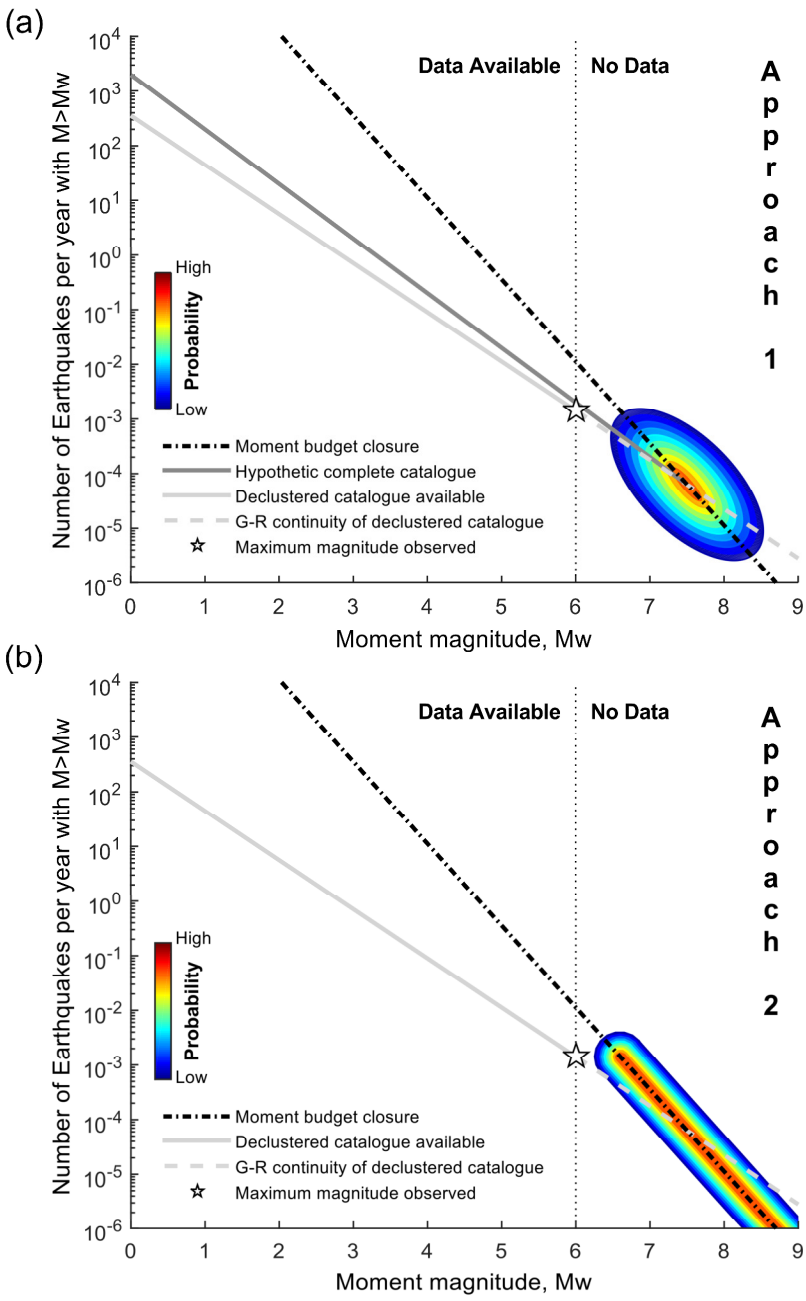

Figure 1.2. *Schematic representation of the two methods used in this study to estimate magnitude and frequency of the largest earthquake on the Parkfield segment of the San Andreas Fault. In both cases it is assumed that, over the long-term average, the moment released by earthquakes and aseismic afterslip balances the deficit of moment accumulating in the interseismic period due to partial fault locking. The black dash-dotted line represents the magnitude-frequency distribution of the largest earthquake according to that condition. The continuous grey line shows the magnitude-frequency distribution of observed earthquakes based on instrumental/and or historical seismicity and after declustering. They are assumed to follow the Gutenberg-Richter law. The star is the maximum earthquake in the catalog and the dashed grey line shows extrapolation to larger magnitudes. (a) Here we assume that, over the long-term average, the Gutenberg-Richter law applies up to the largest possible earthquake. The most probable maximum-magnitude earthquake should then lie at the intersection between the moment budget closure line and the Gutenberg-Richter distribution of the declustered catalogue. (b) Here we only assume that the maximum earthquake exceeds the largest observed earthquake and that the probability of not observing this maximum earthquake over the historical period can be calculated assuming a Poisson law. Any large magnitude is possible but the frequency (hence the probability of occurrence over a given period) drop because of the condition of closure of the moment budget.*

($M_{max} > M_{hist}$) and very infrequent maximum earthquake that closes the moment budget is considered acceptable as long as its return period is long compared to the observation period ($\tau_{max} > t_{hist}$).

In principle, we could also use phenomenological scaling laws, or physical constraints [*Scholz*, 1982] to limit the range of possible earthquake magnitude on a particular fault segment. For instance, we could impose the co-seismic stress drop to be between 0.1MPa and 100MPa, as generally observed [e.g., *Kanamori and Brodsky*, 2004]. This would constrain the maximum possible moment given the size of the locked area. We find such constraints to be too loose to be useful and are therefore not included as an a priori in our analysis. We use them a posteriori to validate our assessment qualitatively.

When it comes to seismic hazard, the two methods should not yield much different outcomes if the hazard is calculated over a period of time t similar in duration to the earthquake catalog t_{hist}. They could however differ significantly for $t \gg t_{hist}$. To assess the impact of choosing between approaches 1 and 2, we calculate the probability $P_{Hazard}(M > M_{Test}, t)$ of an independent event over a period t exceeding a magnitude M_{Test} for different values of t. The probability P_{Hazard} of an independent event with magnitude $> M_{Test}$ during a period of time t is

$$P_{Hazard}(M > M_{Test}, t, \tau_M) = 1 - P_{poisson}(n = 0, t, \tau_M) = 1 - e^{-\frac{t}{\tau_M}}, \quad (1.16)$$

where τ_M is the average recurrence time of independent earthquakes with magnitude larger than M_{Test}which can be calculated from the Gutenberg-Richter law ($\tau_M = 10^{-(a-b\,M_{Test})}$, with a and b being determined from a 'declustered' catalog). The probability P_{Hazard} calculated this way does not account for aftershocks.

To construct Figure 1.3 we first choose a value of t. We then grid the magnitude-frequency space and test systematically all magnitudes of the maximum possible earthquake and all the return periods within a search area. For each sample tested, we represent the probability $P_{Hazard}(M > M_{Test}, t)$ with a curve shaded according to the probability $P_{Budget} * P_{Hist}$. We can thus apprehend visually the most likely earthquake scenarios that might happen during the time period t (Figure 1.3). A mean probability of all the possibilities tested, which we weight with the product $P_{Budget} * P_{Hist}$, can be obtained from equation

$$\bar{P}_{Hazard}(M > M_{Test}, t) = \frac{\sum_{k=1}^{N} P_{Hazard,k} * P_{Budget,k} * P_{Hist,k}}{\sum_{k=1}^{N} P_{Budget,k} * P_{Hist,k}}, \quad (1.17)$$

where N is the number of samples tested, k is the sample index, $P_{Hazard,k}$ is the probability of an independent event with magnitude $>M_{Test}$ during the time period t for the sample k, and $P_{Budget,k} * P_{Hist,k}$ is the probability of sample k given the seismicity observations and the moment budget closure condition.

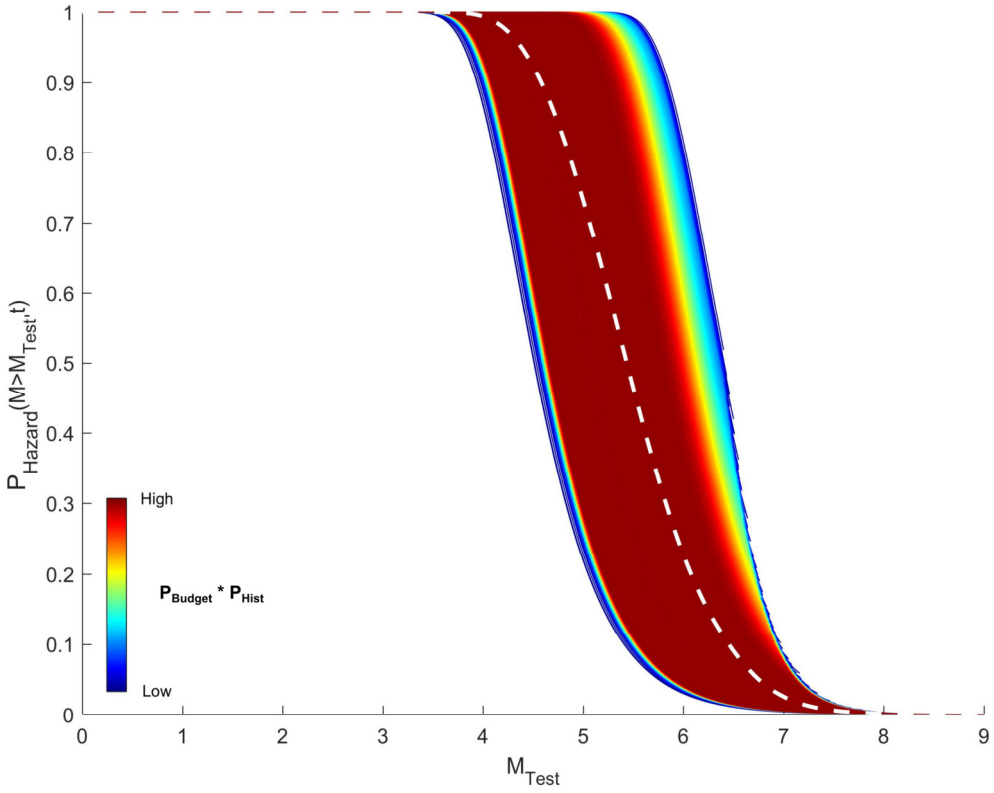

Figure 1.3. *The probability of an earthquake exceeding a certain magnitude in a period of time of* $\boldsymbol{t}$ *years can be calculated based on our analysis. To do so we calculate for each possible truncated frequency-magnitude distribution the probability of exceeding a given magnitude and multiply this probability by the probability of the model based on* $\boldsymbol{P_{Budget} * P_{Hist}}$*. The white dashed line represents* $\boldsymbol{\bar{P}_{Hazard}}$ *from considering all possible scenarios.*

To illustrate the procedure, let us first choose a sample of maximum magnitude, M_{max}, and its time recurrence, τ_{max}. We assume that this event belongs to a distribution of independent events that follows the GR law. Choosing $M_{Test} = 4$ (for example), we can calculate the probability of having an independent earthquake over magnitude 4 during a time period t, knowing that those events have a recurrence time given by the GR law (equation 1.16). Applying this to the full range of $M_{Test} \in [0, M_{max}]$, P_{Hazard} will be represented by a line in Figure 1.3. This P_{Hazard} is associated with a specific M_{max} and τ_{max}, and corresponds to a

specific $P_{Budget}(M_{max}, \tau_{max}) * P_{Hist}(M_{max}, \tau_{max})$. If we test each possible M_{max} and τ_{max}, and plot their P_{Hazard} in the same representation, the shade of each line indicating $P_{Budget} * P_{Hist}$, we then obtain Figure 1.3. We could then calculate the average P_{Hazard} of all those lines, but it would not account for the probability to close the moment budget and be plausible considering the observed seismicity. We then weight each P_{Hazard} obtained for a particular choice of M_{max} and τ_{max} by its related $P_{Budget} * P_{Hist}$, and use this to calculate the weighted average $\bar{P}_{Hazard}$ (equation 1.17) represented by the white dashed line in Figure 1.3.

We sample the probabilities using the Hasting-Metropolis Monte Carlo Markov Chain (MCMC) procedure [*Metropolis et al.*, 1953; *Hasting*, 1970]. We calculate for each sample k, with a given magnitude and frequency of the largest earthquake, the probability that it is realistic knowing the data $P_{Hist,k}$ and the probability that it closes the budget $P_{Budget,k}$. The final probability $P_{G,k}$ (i.e. the posteriori probability) of a given sample would thus be

$$P_{G,k} \propto U_M U_{Freq} P_{Budget,k} P_{Hist,k}, \tag{1.18}$$

where U_M and U_{Freq} are the uniform laws chosen for the MCMC sampling for the magnitude and frequency, respectively (i.e. the a priori probability).

3. Application to the Parkfield segment of the San Andreas Fault

3.1. MOMENT BUDGET

Interseismic strain around the Parkfield segment of the San Andreas fault has been investigated in a number of recent studies [*Johnson*, 2013; *Wang et al.*, 2014; *Jolivet et al.*, 2015; *Tong et al.*, 2015]. Here we rely on the studies of Wang *et al*. [2014] and Jolivet *et al*. [2015], as they provide a probabilistic description of slip rate from Bayesian inversions which can be directly used as an input in our study. We consider the same fault geometry and focus on the same fault area as Wang *et al*. [2014] (Figure 1.4 and 1.5). To assess the moment budget, we use interseismic models from Wang *et al*. [2014] and Jolivet *et al*. [2015] which were both derived from inversion of interseismic displacements measured at the surface assuming a fault embedded in an elastic medium. Wang *et al*. [2014] assumed a homogeneous elastic half-space and Jolivet *et al*. [2015] considered depth variations of elastic

moduli. We convert slip potency (the integral of slip over fault area) to moment according to the elastic structure assumed in these studies.

Wang *et al.* [2014] present three different Bayesian inversions of GPS data from 14 stations covering the period from 1999 to 2004 including the mainshock of 2004 and 5 days of postseismic relaxation. They use a 70km long, ~19 km deep fault subdivided into 180 patches,

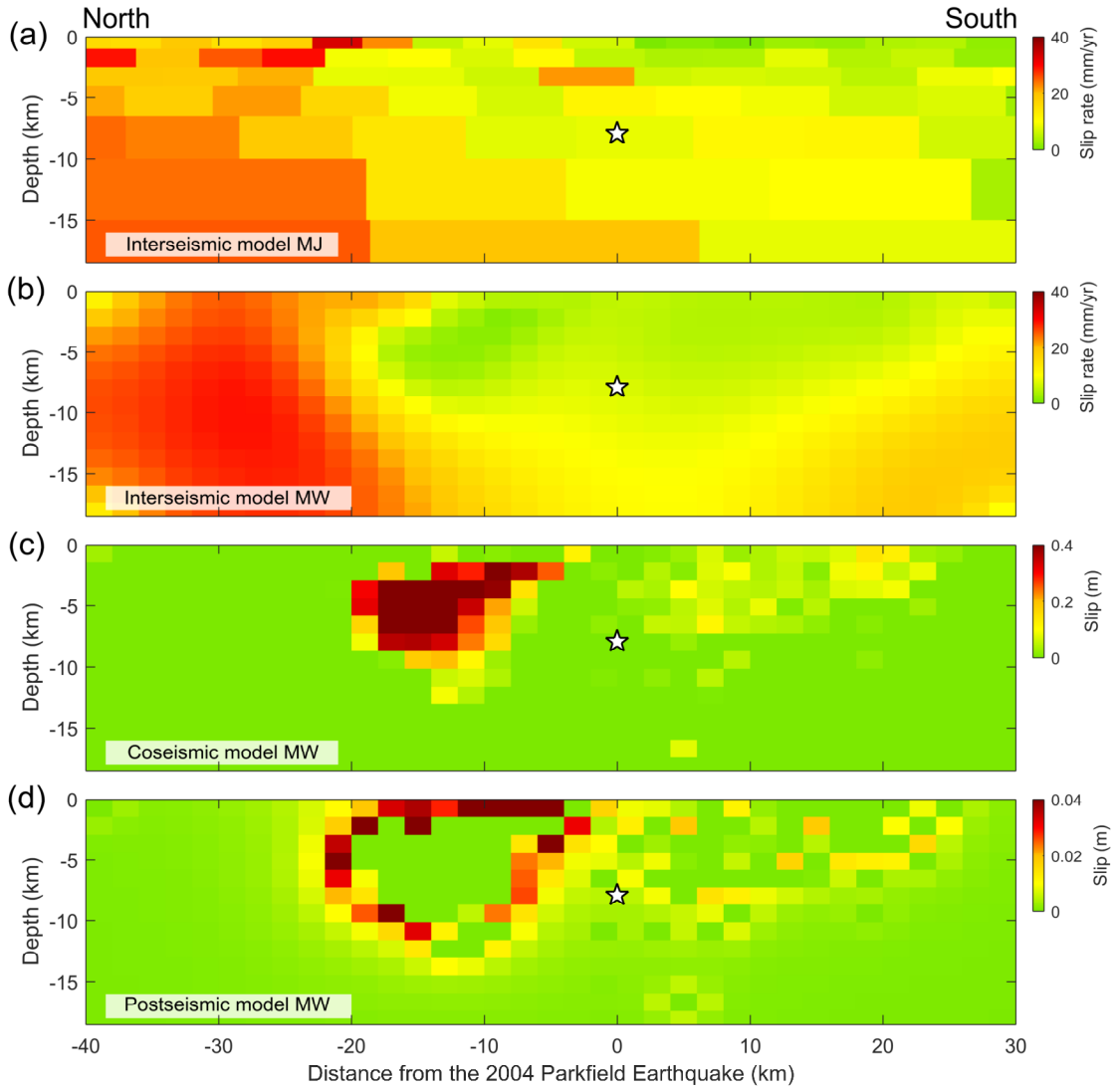

Figure 1.4. *Presentation of the interseismic models used in this study. (a) Interseismic model of Jolivet et al. (2015), referred to as model MJ in this study, which was derived from GPS and INSAR data between 2006 and 2010. (b) Interseismic model of Wang et al. (2014), referred to as model MW. This model was derived from geodetic data from 1999 to 2004. It was obtained from a joint inversion of interseismic, coseismic and postseismic slip with the constraints that co-seismic slip occurs in an interseismically locked area and that post-seismic slip (afterslip) is driven by co-seismic stress increase. The corresponding coseismic and afterslip models are shown in panels (c) and (d). The white star represents the hypocenter of the 2004 Parkfield earthquake.*

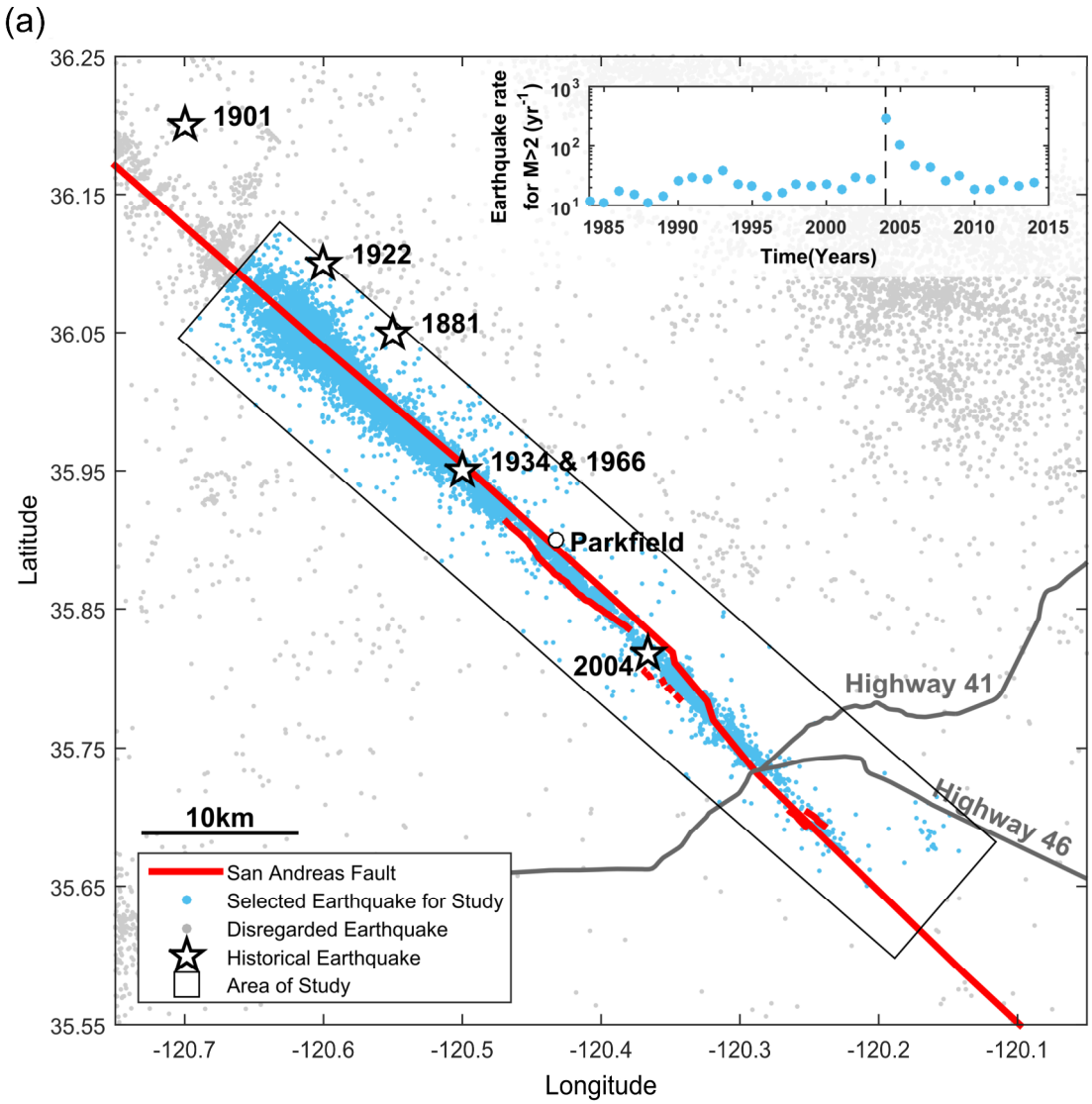

Figure 1.5. *(a) Map of the Parkfield segment of the San Andreas Fault. Dots show seismicity from the Northern California earthquake catalogue of the Northern California Earthquake Data Center [NCEDC, 2014] between 1984 and 2015. Our study is based on the earthquakes less than 5 km away from fault segment considered here (within the black rectangle). Epicenters of the six M~6 earthquakes since 1857 are from Toppozada et al. [2002] (black and white stars). The town of Parkfield is also indicated by a white dot. (b) Parkfield seismicity rate from 1984 to 2015 for earthquakes with magnitude over 2. The vertical black dashed line corresponds to the 2004 M6 earthquake.*

each 1.4 km long along strike and 1 km wide. A steady slip rate is assumed at depth greater than 19 km. We considered their favored model (referred to as MW hereafter), which was obtained from a joint inversion of the interseismic, co-seismic and 5-days postseismic data, designed to maximize the consistency between the three slip distributions. The slip distributions are therefore complementing each other (Figure 1.4): the co-seismic rupture is restricted to the area that was locked during the interseismic period; the inversions assume

that postseismic slip is driven by the co-seismic stress change and thus yields a ring of afterslip surrounding the co-seismic rupture. The steady slip rate on the deeper extension of the fault is estimated to 32.1 mm/yr in this model. The Bayesian framework provides uncertainties on all quantities determined from the inversion.

Jolivet *et al*. [2015] (MJ) also used a Bayesian approach and derived an interseismic model from GPS and InSAR data covering the period from 2006 to 2010. The modeled fault zone extends over 200 km from the Cholame plain to north of San Juan Baptista (SJB). The patch size varies depending on the resolution from 4 km at the surface to 25 km at 20 km depth. The long-term slip rate varies along strike. In the Parkfield area considered in this study, it varies from 31.1 mm/yr to 36.6 mm/yr. The model shows a gradual northward decrease of interseismic coupling from the locked zone in the southeast to the creeping zone in the northwest (Figure 1.4). This model shows a deficit of slip extending to depth greater than 19km, thus deeper than the seismogenic depth. Given the absence of seismicity at such depth and the fact that temporal variations of strain rates in this depth range are probably primarily due to viscoelastic relaxation as was observed following the 2004 earthquake [*Bruhat et al.*, 2011], we consider slip deficit accumulation only in the 0-19 km depth range of our fault model.

Both models yield deep slip rates in agreement with the geological long term slip rate on the SAF which is estimated to 33.9±2.9 mm/yr in the Carrizo plain south of the Parkfield segment [*Sieh and Jahns*, 1984]. These rates are also consistent with those (34.9-36.0±0.5 mm/yr) derived from elastic block modeling of regional tectonics [*Meade and Hager*, 2005; *Tong et al.*, 2014]. They are, however, larger than the local estimate of 26.2 +6.4/- 4.3 mm/yr of Toké et al. [*Toké et al.*, 2011]. Both models show high interseismic coupling in the area that ruptured in 2004. They differ significantly in part because they use different interseismic observations but also because of different methods and a priori assumptions. In addition to enforcing consistency between the three phases of the earthquake cycle, the inversion used to derive MW was regularized via spatial smoothing. By contrast MJ was obtained without any constraint on the smoothness of the slip rate distribution nor on the relationship between interseismic and co-seismic slip. Note that the long-term slip-rate on the continuation of the fault at the depth is constant in MW but varies along strike in MJ. For MJ, fault patches are assigned the long-term slip rate of the deeper creeping patches. Those located astride

different deep creeping patches are divided in sub-patches. The shear modulus used to convert slip to moment is 30GPa for MW and varies between 20.5GPa and 66.2GPa for MJ [*Jolivet et al.*, 2015].

The Bayesian approach used in Jolivet *et al*. [2015] and Wang *et al.* [2014] provides thousands of scenarios, which were tested against geodetic data. For both studies, we calculate the moment deficit rate of every scenario using equation 1.1 and 1.2 to derive the PDF of the moment deficit rate. The rate of accumulation of moment deficit for each model is indicated in Table 1.2 and the corresponding PDFs are shown in Figure 1.6.

Table 1.2. *Parkfield moment deficit rate*

Interseismic models	*Moment deficit rate (N.m/yr)*
MW [*Wang et al.*, 2014]	6.90 +/- 0.64 10^{17}
MJ uncut [*Jolivet et al.*, 2015]	1.40 +/- 0.28 10^{18}
MJ cut at 19km depth	8.82 +/- 1.10 10^{17}
MW cut at 15km depth	6.04 +/- 0.52 10^{17}

We calculated and represented in Figure 1.7 the moment deficit rate on a completely locked 70 x 20 km section loaded at 32.1 mm/yr (full black line) and a section with the coupling pattern from the MW model (black dashed line). Based on interseismic model MW the moment deficit builds up at a rate of 6.90 +/- 0.64 10^{17} N.m/yr. The PDF associated with this estimate is shown in Figure 1.6. Some of this deficit was released by aseismic afterslip following the 2004 event which released about 3.7 10^{18} N.m Bruhat *et al.* [2011]. We do not use the afterslip model of Wang *et al.* [2014], as their model covers only 5 days after the mainshock. The dotted line in Figure 1.7 shows the remaining deficit of moment which amounts to 5.39 10^{17} N.m/yr.

Based on interseismic model MJ, the moment deficit accumulates in the interseismic period at a rate as large as 8.82 +/- 1.10 10^{17} N.m/yr (Figure 1.6). The difference with the rate obtained with MW is partly due to the different pattern of coupling and to the difference of deep creep rates (31.1 and 36.5 mm/yr for MJ and 32.1 mm/yr for MW). The rate is reduced to 7.31 10^{17} N.m/yr if aseismic afterslip is substracted (Figure 1.8).

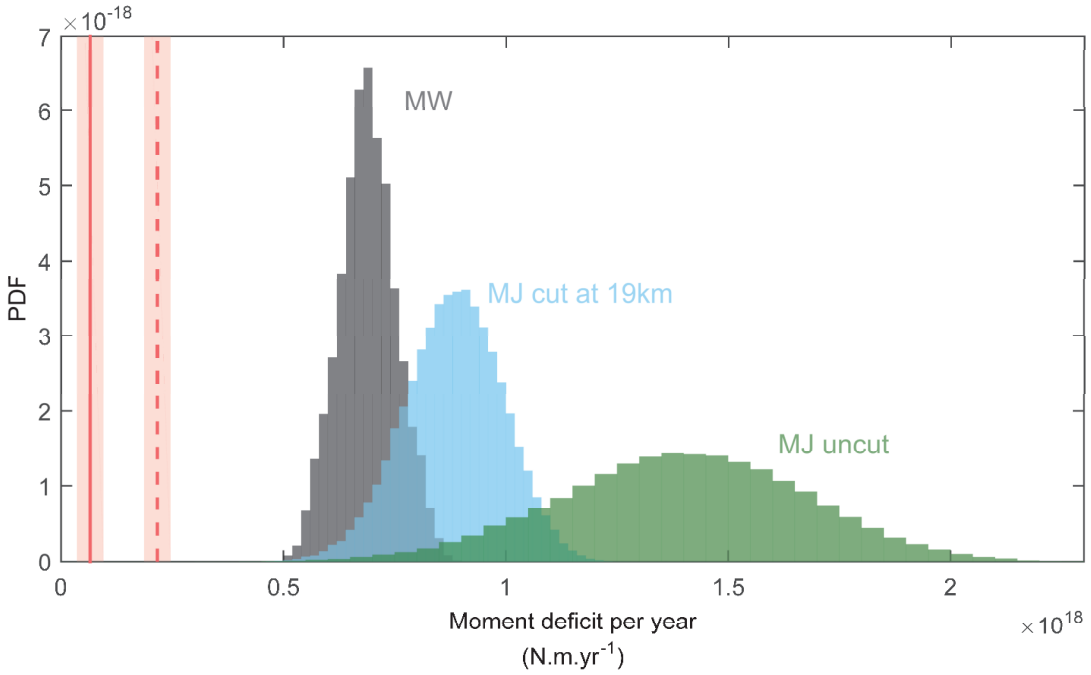

Figure 1.6. *Probability Distribution Function of the rate of moment deficit accumulation on the Parkfield segment of the San Andreas Fault calculated based on interseismic models MW [Wang et al. , 2014] and MJ [Jolivet et al., 2015]. The uncertainties are calculated based on the uncertainties of the interseismic slip models estimated in the original studies. Other sources of uncertainties (e.g. those related to the elastic properties of the subsurface) are ignored. The three histograms corresponds respectively, from left to right, to the model MW, MJ cut at 19km depth and MJ uncut, extending down to 40km. The vertical solid line is the seismic moment that would be released annually assuming that over the long term an event similar to the 2004 earthquake occurs every 24.5 years and is assigned a moment magnitude of M6.08, which represent some average value from various studies (see text for discussion). The vertical dashed line is the same but takes into account the postseismic moment released after a M6 mainshock similar to the 2004 event. The shaded patches associated with the vertical lines are the 1-sigma standard deviation from the seismic moment average of values taken from various studies.*

The moment released by seismicity is estimated from the Northern California earthquake catalog [*NCEDC*, 2014] from 1984 to 2015 (up to 5/2/2015). We consider earthquakes located within 5 km of the fault (Figure 1.5). Figure 1.7 shows the cumulative moment released by earthquakes of magnitude under M taken directly from the catalog (gray dashed line). This estimate might not be representative of the interseismic cycle. The inset in Figure 1.5 shows minor temporal fluctuations except for the strong increase of seismicity associated to the 2004 aftershocks. The moment released by seismicity over the 31 years covered by the catalog, representative of the 2004 event (87%), its aftershocks (7%) and the background seismicity (6%), accounts for only 5% of the deficit of moment that has accumulated over this time period according to the interseismic model MW, or 7% if the postseismic moment

released is taken into account (Figure 1.7). It represents an even lower fraction (4%) of the deficit of moment calculated based on the interseismic model MJ (5% if taking into account the aseismic moment released by afterslip; Figure 1.8). As mentioned above, the deficit could suggest that the return period of the maximum magnitude earthquake is over-estimated or that larger magnitude events are needed on this fault segment. We now consider the first possibility.

Six $Mw{\sim}6$ earthquakes occurred at Parkfield between 1857 and 2004, yielding an average return period of 24.5 years. The catalog covers 31 years and includes the 2004 event and its aftershocks. Some corrections might thus be needed to represent the long-term average seismicity. Let us assume that the 2004 Parkfield earthquake is characteristic of the sequence of Mw 6 earthquakes that have occurred since 1857. We assume that such an event and its associated aftershocks, return every 24.5 ± 9.2 year on average, where the uncertainty is the 1-sigma standard deviation of the time intervals. We consider the moment released by such an event to be equal to the mean moment estimated for 2004 from various publications [*Johanson et al.*, 2006; *Langbein et al.*, 2006; *Liu et al.*, 2006; *Murray and Langbein*, 2006; *Barbot et al.*, 2009; *Bruhat et al.*, 2011; *NCEDC*, 2014; *Wang et al.*, 2014]. We use the standard deviation of these estimates as an estimate of the uncertainty at the 67% confidence level. The average moment released is then 1.48 10^{18} ± 4.7 10^{17}N.m (Mw 6.08).

We estimate the moment released by aftershocks by comparing the seismicity rate over the 2004-2008 period with the 1984-2004 period. We also assume that each event triggered as much aseismic afterslip as the 2004 event. According to Bruhat *et al.*, 2011, afterslip following the 2004 event released about 1.57 10^{18} N.m assuming viscous flow under 19km depth, or about 3.7 10^{18} N.m if viscous relaxation is excluded, which is more than twice the coseismic moment release. Hereafter we assume that afterslip released up to 200% of coseismic moment, which gives us an upper-bound on the total moment released by this sequence of earthquake. The moment released by afterslip is subtracted from the deficit of moment accumulating in the interseismic period (Figure 1.7 and 1.8). The values corresponding to this moment budget estimate are reported in Table 1.2 and Table 1.3, and illustrated in Figure 1.6, 1.7 and 1.8. Clearly, the moment released by 2004-like events returning every 24.5 ± 9.2 year on average falls still way short of balancing the moment budget (12.1% of MW's model).

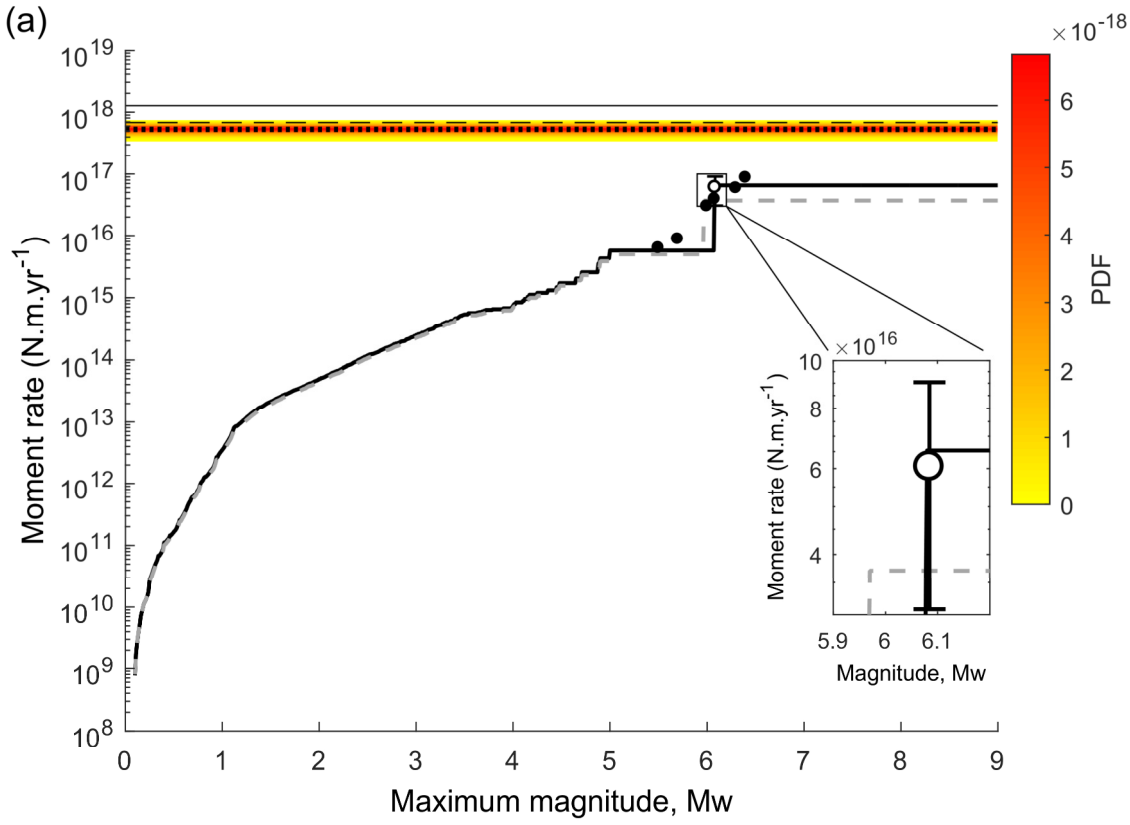

Figure 1.7. *(a) Representation of the budget of seismic and aseismic slip on the Parkfield segment of the SAF based on interseismic model MW [Wang et al., 2014]. The gray dashed curve is the cumulated moment released per year by earthquakes with magnitude less than the value in abscissa. This curve is based on seismicity within 5km of the Parkfield fault segment over 31 years, from 1984 to 2015. The catalogue includes the 2004 earthquake, which is assigned a moment magnitude 5.97, and aftershocks. The black solid curve is the cumulated moment that would be released annually assuming that over the long term an event similar to the 2004 earthquake occurs every 24.5 years and is assigned a moment magnitude of M6.08, which represent some average value from various studies (see text for discussion). The white dot is the moment released assuming a M6.08 every 24.5yr and neglecting the contribution of aftershocks and background seismicity to the seismic moment release rate. The black dots show the moment released by historical seismicity from 1857 to 2015 according on the catalogue of Toppozada et al. [2002]. The thin horizontal solid black line is the moment deficit accumulating per year if the modeled fault area was completely locked (for a loading rate of 32.1mm/yr). The thin horizontal dashed black line shows the moment deficit rate based on the interseismic model of MW. The thin horizontal dotted black line takes into account the postseismic moment released after a M6 mainshock similar to the 2004 event. The shading represent the uncertainty associated to this estimate. (b) Zoom of the black box which enables the appreciation of the large impact of the mainshock magnitude change and the weak impact of the background seismicity and aftershock's on the total amount of moment released by earthquakes.*

Table 1.3. *Parkfield seismic and aseismic moment release*

Catalog used	*Seismic Moment rate (N.m/yr)*
Initial Catalog (31 years) [*NCEDC*, 2014]	3.70 10^{16}
Modified catalog : *M*6.08+Aftershocks every 24.5 years	6.54 10^{16}
Toppozada's catalogue [*Toppozada et al.*, 2002]	8.67 10^{16}
Modified catalog : M6.08+Aftershocks every 17 years	9.32 10^{16}

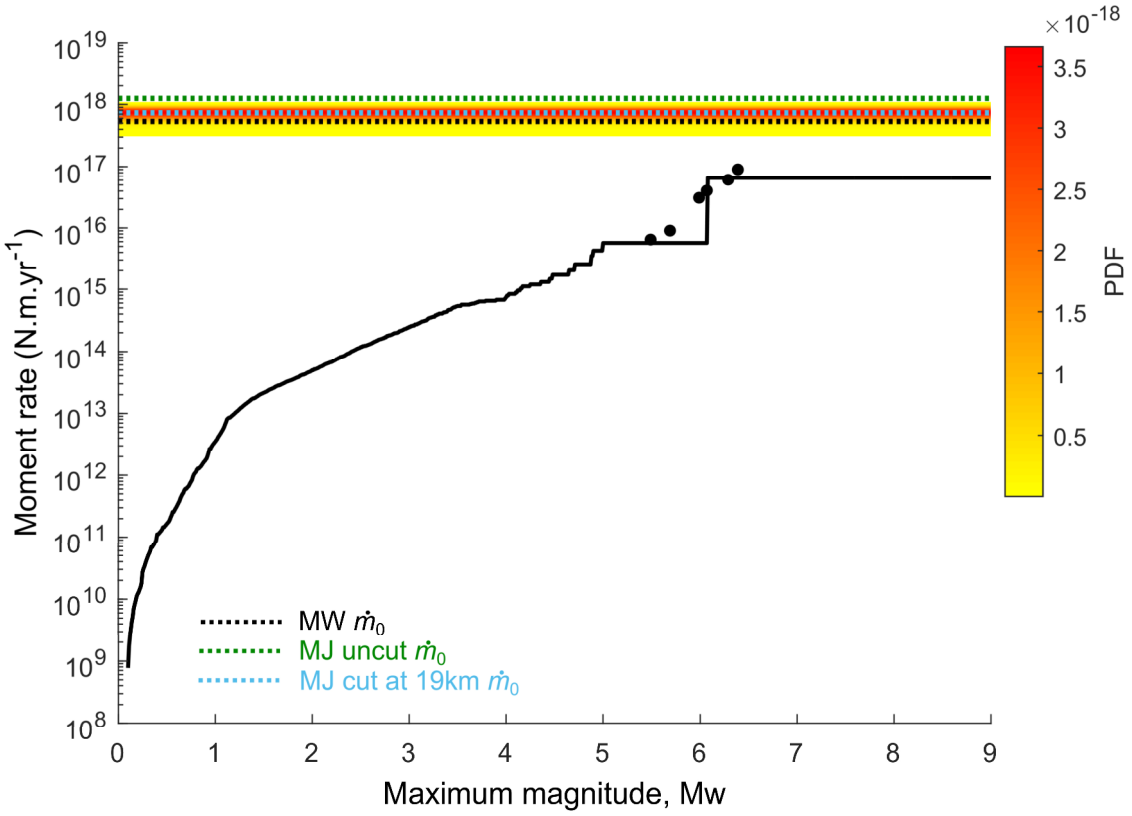

Figure 1.8. *Representation of the budget of seismic and aseismic slip on the Parkfield segment of the SAF based on interseismic model MJ [Jolivet et al., 2015] with postseismic moment release taken into account. The solid black curve is the cumulated moment that would be released annually assuming that over the long term an event similar to the 2004 earthquake occurs every 24.5 years and is assigned a moment magnitude of M6.08, which represent some average value from various studies (see text for discussion). The black dots show the moment released by historical seismicity from 1857 to 2015 according on the catalogue of Toppozada et al. [2002]. The dotted lines are the moment deficit accumulating per year based on the interseismic models (MW, MJ cut at 19km depth, MJ uncut, from bottom to top, respectively), and taking into account the postseismic moment released after a mainshock similar to the 2004 event.. The shading represent the uncertainty associated to the estimate of MJ cut at 19km depth.*

Returning $Mw{\sim}6$ earthquakes at Parkfield do not necessarily release the same moment as the 2004 event. The 1966 Parkfield earthquake is considered to be relatively similar to the 2004 one in terms of its moment release and rupture area [*Bakun et al.*, 2005]. According to the reported damages [*Toppozada et al.*, 2002], the events of 1901 and 1922 may have been stronger (Mw 6.4 and Mw 6.3 respectively). Moreover, several Mw>5 earthquakes that occurred between 1857 and 2015 are considered to be independent from the $Mw{\sim}6$ earthquake ($M5.5$ in 1877 and $M5.8$ in 1908), or direct aftershocks of the 1901 and 1922 earthquakes. Figures 1.7 and 1.8 show that if we now consider the historical catalog of Toppozada et al. [2002], the moment released by seismicity is higher but still too small to balance the moment budget (Table 1.3). Assuming that the interseismic period covered by geodetic data is representative of the long-term average, we derive that seismicity and afterslip released at most 16.1% (MW) of the deficit of moment accumulated since 1857. The epicenter of the 1901 $M6.4$ earthquake is actually located slightly north of our study area. The damage distribution indicates that the rupture propagated within the Parkfield area, but it is not sure that the rupture area was confined to the fault area consider in our study. By assuming that the moment of this earthquake was entirely released by slip on the fault segment considered in this study we probably tend to overestimate the seismic moment release.

Considering this time only for the moment deficit rate from the seismogenic zone (~15km depth) and reducing the recurrence time of the $M6$ to 17 years as estimated by [*Wang et al.*, 2015] does not close the moment budget either. The moment deficit rate is reduced to 3.86+/-0.52 10^{17} N.m/yr based on the interseismic model MW cut at 15km depth with afterslip subtracted, and the seismic moment released is increased to 9.32 10^{16} N.m/yr. Giving this extreme scenario, the percentage of seismic moment released compared to the moment deficit rate is still low (24%).

Some coseismic models of the 2004 $M6$ earthquake indicate slip up to 30km south of the hypocenter [*Wang et al.*, 2014, 2015] and a similar rupture extent to that proposed for the 1966 earthquake [*Murray and Langbein*, 2006]. However, most models indicate that the 2004 rupture did not go further than 10 km south of the hypocenter [*Johanson et al.*, 2006; *Liu et al.*, 2006; *Allmann and Shearer*, 2007; *Barbot et al.*, 2009; *Bruhat et al.*, 2011]. By limiting the extent of our area of study to 10 km south of the 2004 hypocenter and by cutting the

interseismic models at an even more shallower seismogenic zone (10km depth), we obtain a moment deficit rate of 2.93 10^{17} N.m/yr for MW and 2.99 10^{17} N.m/yr for MJ. The moment deficit rate PDF of the model MJ would then slightly overlap with the moment released by earthquakes and postseismic slip. The probability to close the moment budget is nevertheless 2%. On the other hand, the MW model would still not overlap.

This analysis shows that balancing the moment budget on the Parkfield segment of the San Andreas fault probably requires more frequent or larger earthquakes than what the instrumental and historical data suggest. All the seismic moment release rate discussed in this section are available in Table 1.3.

Note that Tong *et al.* [2015] integral method yields a moment deficit rate around 5.8 10^{17} N.m/yr, which is slightly smaller than the best fitting value of MW but within the uncertainty range. We consider that the range of rates of moment deficit explored by using the Bayesian inversions of MJ and MW models of interseismic coupling provides a reasonable estimate of the range of possible values given the uncertainties on the geodetic data and choice of the modeling technique.

3.2. MAXIMUM-MAGNITUDE EARTHQUAKE EVALUATION

We now explore the range of possible magnitudes and frequencies for the largest possible earthquake needed to balance the moment budget. We first compute the probability of closing the moment budget for a given magnitude and frequency for the largest possible earthquake. We next calculate the probability of the possible earthquake models based on either approach 1 (seismicity follows the Gutenberg-Richter law up to the largest possible earthquake) or 2 (larger earthquakes can fall off the Gutenberg-Richter distribution indicated by instrumental and historical data).

We use the MCMC method to sample these probabilities. Each sample is taken from a uniform PDF between 6.4 and 9 for magnitudes, and between 10^{-6} and 10^{4} yrs^{-1} for frequencies. We calculate for each sample k the value proportional to the probability $P_{G,k}$ as described in the method section. For each estimation, we run the sampler for 900000 steps, rejecting the first 500 steps to ensure accurate sampling of the PDF. The magnitude-frequency space is then binned into cells of size 0.01 for the moment magnitude axis and logarithmically binned into cells of size 0.01 concerning the frequency axis. The number of samples in each cell divided

by the total number of samples approximates the probability $P_{G,k}$ as defined by the MCMC method.

3.2.1. *Moment Budget closure,* $\boldsymbol{P_{Budget}}$

We calculate the probability $P_{Budget,k}$ of closing the moment budget based on the uncertainties on the parameters of interseismic models MJ or MW. We estimate the moment released by seismicity for a tested magnitude M_k and recurrence time τ_k of the largest earthquake and estimate the probability that it balances the moment budget using interseismic models MJ or MW. The probabilities on the interseismic models are taken from the distribution of their moment deficit using a bin of 10^{16} N.m.

The moment released by aftershocks and independent events with magnitude smaller than the largest earthquake is integrated by assuming that their magnitude-frequency distribution follows the GR law. We consider two cases. In the first case, the aftershocks and independent events follow the GR law up to the largest earthquake included. In the second case, we account for Båth law; the largest aftershock is 1 unit of magnitude unit lower than the mainshock, as it is observed in the 2004 event. We suppose also that the *b*-value is constant and equal to the one estimated from the modified 1984-2015 catalog. We use the maximum curvature method [*Wiemer and Wyss*, 2000] and Bender's formula [*Aki*, 1965; *Utsu*, 1966; *Bender*, 1983] to evaluate the magnitude of completeness and the b-value. The estimated magnitude of completeness is increased by 0.2 to compensate a methodological bias of the method [*Woessner and Wiemer*, 2005]. The *b*-value, estimated at 0.91±0.06, is then used to account for the magnitude-frequency distribution of both aftershocks and independent events. The *a*-value is easily calculated from equation (1.1.5).

Moment released by aseismic afterslip is accounted for by supposing that, for all earthquakes, it amounts to a fixed percentage of the seismic moment. This percentage might in fact depend on earthquake magnitude but the available data are insufficient to derive a reliable law [*Lin et al.*, 2013]. We considered a value of 25%, close to the mean value observed from various case studies [*Avouac*, 2015], and a more extreme value of 200%, similar to that estimated for the 2004 earthquake. The value of 200% is an overestimation of Bruhat *et al.*, [2011].

3.2.2. $\boldsymbol{P_{Hist}}$: *First Approach*

In the Method section, we proposed two different approaches regarding how the frequency-magnitude of the largest possible earthquake might be evaluated based on the known seismicity. The first case, the most restrictive, assumes that the distribution of a declustered catalog follows the GR law up to the largest event. Some declustered catalogs are available for California [*Dutilleul et al.*, 2015] but they contain less than 200 earthquakes within 5 km from the fault segment considered in our study. This small number does not permit any reliable *b*-value estimation [*Woessner and Wiemer*, 2005]. Therefore, we will rely on a non-declustered catalog.

Assuming a postseismic moment release equivalent to 200% of the mainshock seismic moment, not accounting for Båth's law and selecting MW as the interseismic model represents the most "optimistic" situation where the magnitude of the largest earthquake needed to close the moment budget is minimum. In this scenario, P_G (Equation 1.1.18) peaks around $\sim M7.6$, corresponding to a seismic moment of 2.8 10^{20} N.m, with a recurrence time period of ~3300 years (Figure 1.9). The release of such a large moment on a 70km long segment seems however improbable, however, especially in view of the limited locked zone in the interseismic period. The average slip in such an event, supposing that the whole fault ruptures (20x70 km) and taking a 30GPa shear modulus, would be of ~7m. If we assume a rupture restricted to the locked portion of this fault segment, which represents only 1/3 of the fault area, the average slip would need to be as great as 21m. This seems highly improbable.

We note in Figure 1.9 that the magnitude-frequency distribution of instrumental earthquakes does not align well with the historical seismicity. The earthquake rate is lower than expected if we assume the GR law extends up to larger magnitudes. The misalignment could be due to various causes. One is that the historical catalog essentially consists of independent events while the instrumental catalog contains aftershocks. The two catalogs could belong to the same Gutenberg-Richter distribution if the *b*-value of the declustered catalogs was lower than when the aftershocks are included as some studies suggest [*Frohlich and Davis*, 1993]. Extrapolating the Gutenberg-Richter law to the largest possible magnitude might be incorrect as a number of studies have argued that larger magnitude events are more frequent than would be expected from extrapolating the b-value estimated from lower magnitude

seismicity [*Schwartz and Coppersmith*, 1984]. Another possibility is that the seismicity rate between 1984 and 2015 would have been particularly low compared to a longer term average [*Page and Felzer*, 2015]. In both case, the method used here to estimate P_{Hist} would overestimate the magnitude of the largest magnitude earthquake.

With the first approach, using the marginal cumulative probabilities, we can assess the probability that the largest event does not exceed a certain magnitude and the frequency of the largest event is inferior to a certain value (Figure 1.10.a and c). The probability of closing the moment budget on the Parkfield segment of the San Andreas Fault with the magnitude

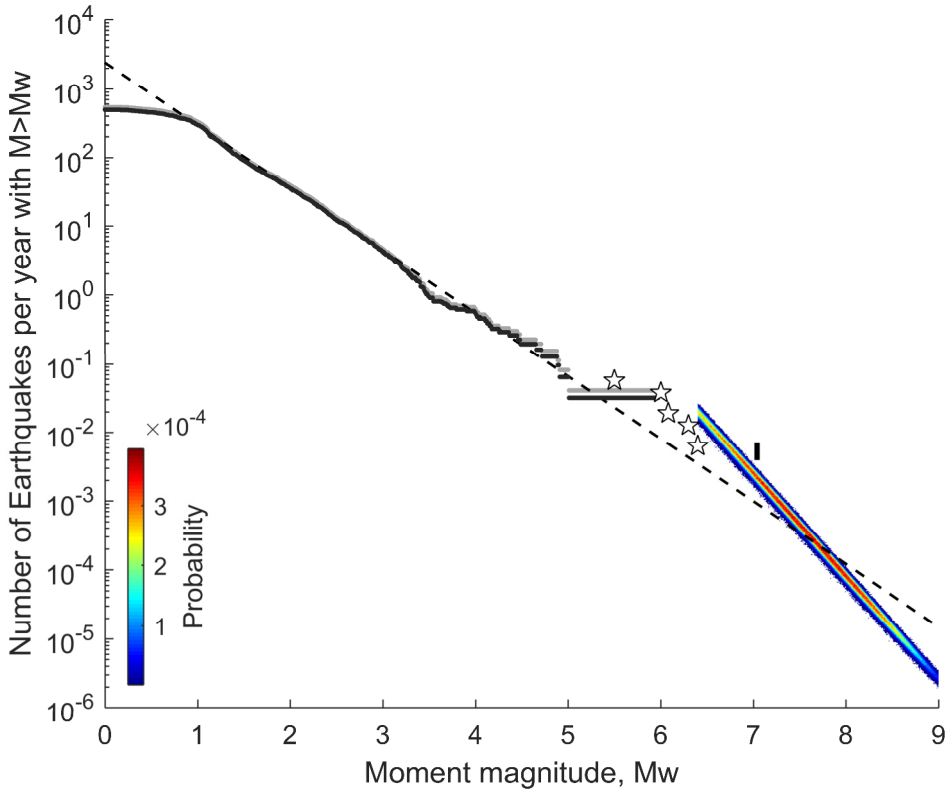

Figure 1.9. *Maximum-magnitude earthquake probability assuming the case where large earthquakes should follow the GR law of a declustered catalog. We use here the model MW, do not account for Bath's law, and suppose that the ratio between postseismic and coseismic moment release is equal to 200%. The number of events from the declustered ANSS catalog being too low in the area selected, we apply the method on a undeclustered ANSS catalog. The results are thus biased and must be interpreted accordingly. The black curve represents the magnitude-frequency distribution of the Parkfield area using the ANSS catalog between 1984 and 2015. The gray curve is the modified magnitude-frequency distribution where the M6 and its aftershocks are fixed to occur every 24.5 years. The GR law (black dashed line) is taken from this distribution. The stars represent the historical data [Toppozada et al., 2002] and the black line represents a M7 earthquake with a recurrence time between 140 and 250.*

of the maximum earthquake not exceeding 6.4 is only 0.3%. Therefore, provided that the GR law is valid up to magnitude M6.4, which seems a reasonable assumption, the analysis requires larger earthquakes. Figure 1.10 indicates that there is a 95% chance that the maximum event does not exceed a $M8.63$. There is also a 95% chance that the return period of the largest magnitude event does not exceed ~112000 years. It seems very improbable that the Parkfield segment could host an earthquake of such a magnitude as it would require 253m of slip in a 19x70km area. The probability of balancing the moment budget with a maximum earthquake not exceeding 7.4 is about 50%, indicating that even with such a large maximum earthquake, balancing the moment budget remains unlikely if the GR law applies. Note that if the largest earthquakes involve ruptures that extend beyond the Parkfield segment, our analysis only provides constraints on the moment released within the Parkfield segment. In that case, the assumption that this earthquake belongs to a GR distribution defined by earthquakes on the Parkfield segment is certainly incorrect and the second approach is then more relevant.

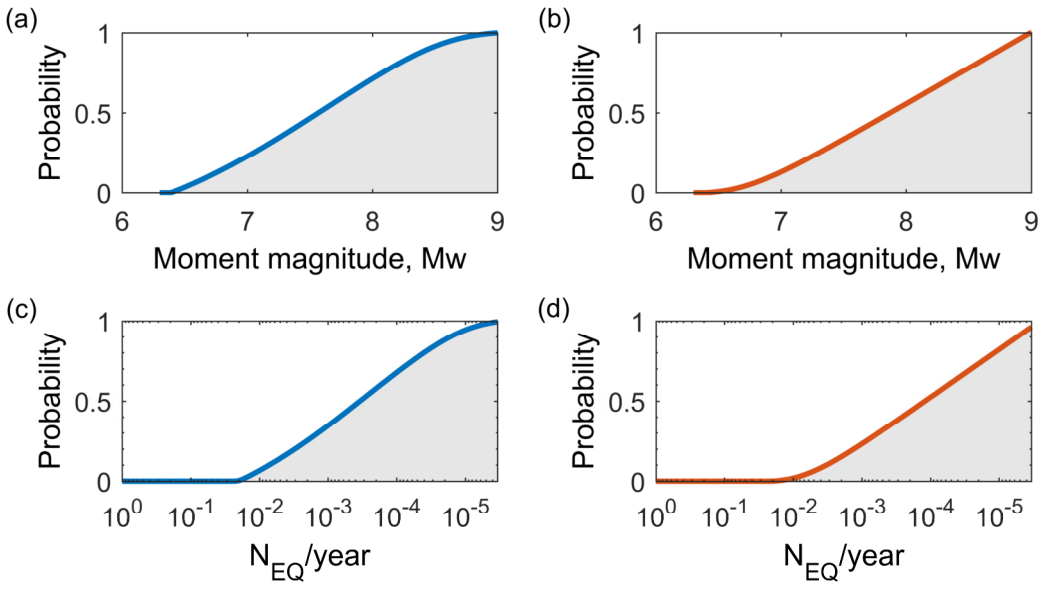

Figure 1.10. *Marginal cumulative probabilities for a maximum magnitude earthquake to close the moment budget and be plausible considering the data and the two approaches explained in the Method section. (a) and (c) are the marginal cumulative probabilities for the magnitude and frequency, respectively, for our first approach. It shows the probability of the largest earthquake to not exceed a certain magnitude (a) and the probability of the frequency of the largest event to not exceed a certain value (c). (b) and (d) are the equivalent of (a) and (c) for our second approach.*

3.2.3. $\boldsymbol{P_{Hist}}$: *Second approach*

Our second approach only assumes that the largest possible earthquake needs to be less frequent than the largest known earthquake. The probability of its return period is estimated based on the historical catalog (only the duration of the period covered matters) assuming a Poisson process. If we consider the interseismic model MW, discard the Båth law and assume that postseismic deformation releases 200% of the coseismic moment we get a more reasonable result than with approach 1 (Figure 1.11). A $M6.7$ every 140 years is then sufficient to balance the moment budget and is acceptable in view of the known seismicity. This point aligns well with the frequency-magnitude distribution of historical events but is off the distribution of instrumental events, essentially because of the break in slope around M~4. This is our favored scenario. Note, however, that the method does not exclude $M > 6.7$ events.

Figure 1.12 shows that the PDF of the magnitude-frequency of the largest event varies depending on the choice of the interseismic model (MJ or MW), on whether or not Båth's law is accounted for, and on the assumption that either 25% or 200% of the mainshocks seismic moment is released by postseismic effects. The Båth law has a significant impact. If it is taken into account, aftershocks and independent events amount to only ~8% of the moment released by the largest earthquake compared to ~156% if the Båth law is discarded. Consequently, when the Båth law is not accounted for, the aftershocks and independent events sequence decrease drastically the maximum-magnitude needed for budget closure. Similarly, postseismic deformation amplifies the moment released by the largest earthquake, its aftershocks and the associated independent events. The higher the ratio between the postseismic and coseismic effect is, the lower the magnitude or the frequency of the largest event needed to balance the slip budget.

The estimate of the b-value could also impact the moment budget balance and the implication of the magnitude-frequency of the largest earthquake. By only taking the background seismicity time period (1983-2004 and 2008-2015), the largest event drops down to a $M4.9$ and the b-value is equal to ~0.90 which is quite close to the b-value estimate used above. To further investigate the b-value influence, we use our favored scenario: model MW, Båth law discarded and postseismic deformation equivalent to 200% of the coseismic moment release. This scenario should be the most sensitive to changes in b-value considering

that there is no gap between the largest and next largest magnitude earthquakes and considering as well the high post-coseismic ratio. Applying the background b-value to our favored model, a M6.71 is then needed every 140 years to close the budget instead of a $M6.70$. The changes added by the Parkfield 2004 event and its aftershocks are therefore minimal. Additionally, if we raise our initial b-value by its standard deviation (σ~0.06), i.e. 0.97, the largest magnitude needed would drop down to 6.67 if it had to happen every 140 years. Changes in the b-value inside a reasonable range have thus a very limited impact on the maximum-magnitude event which turns to negligible if we assume Båth's law.

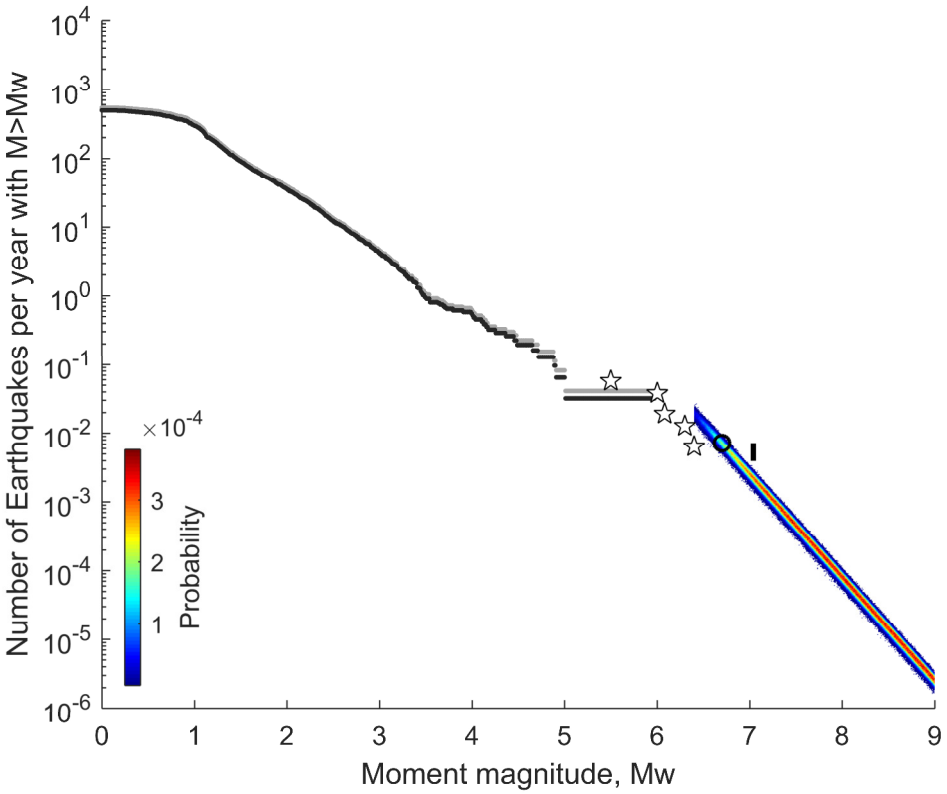

Figure 1.11. *Maximum-magnitude earthquake probability assuming the case where large earthquakes should have a recurrence time lower than the largest earthquake currently observed. We use here the model MW, do not account for Bath's law, and suppose that the ratio between postseismic and coseismic moment release is equal to 200%. The black curve represents the magnitude-frequency distribution of the Parkfield area using the ANSS catalog between 1984 and 2015. The gray curve is the modified magnitude-frequency distribution where the M6 and its aftershocks are fixed to occur every 24.5 years. The stars represent the historical data [Toppozada et al., 2002] and the black line represents a M7 earthquake with a recurrence time between 140 and 250. The black circle defines the location of a M6.7 event occurring every 140 years, our favored scenario.*

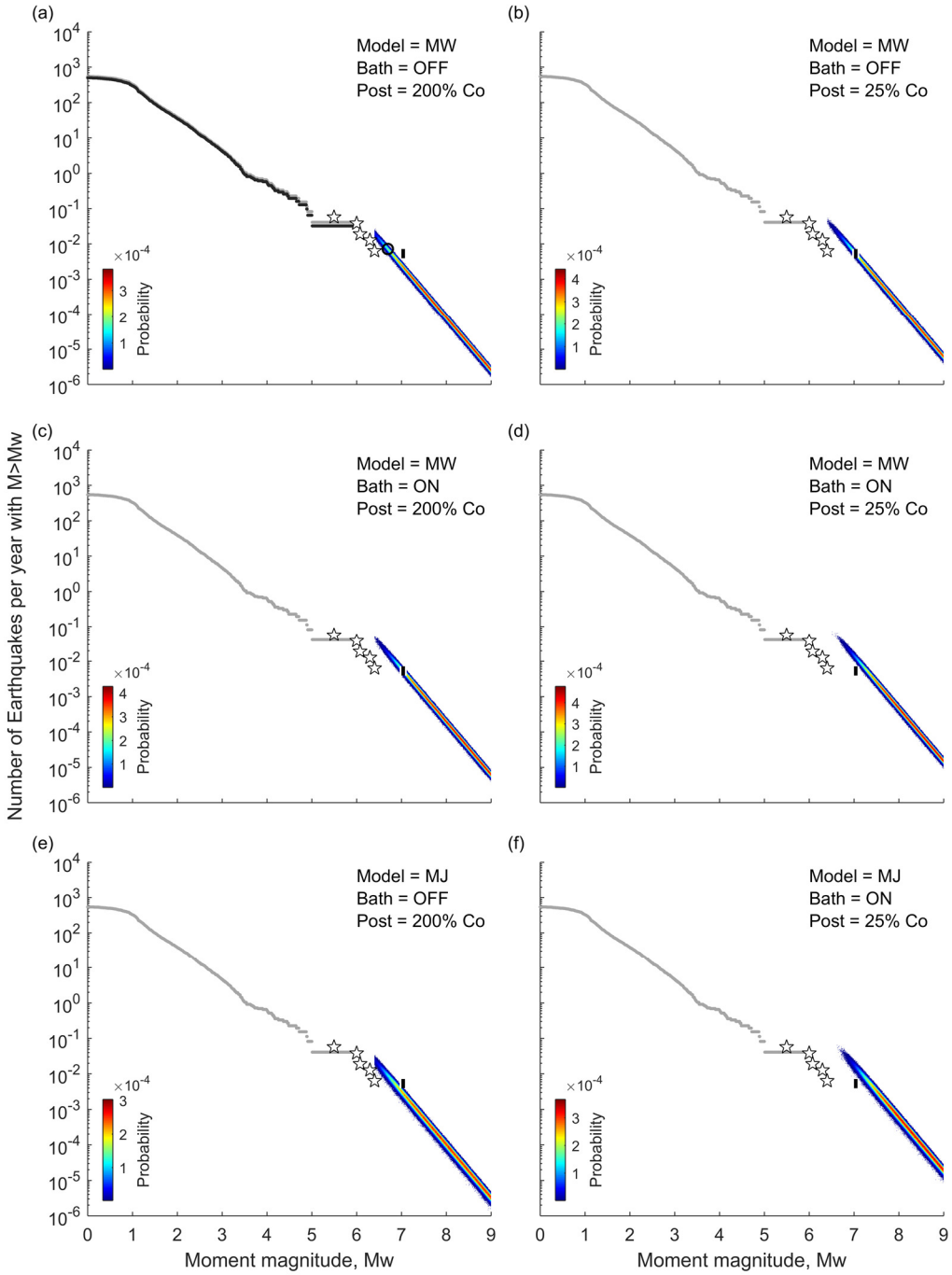

Figure 1.12. *Probability distribution to have a maximum-magnitude event that might exist and close the moment budget. The black curve represents the original magnitude-frequency distribution of the Parkfield area using the ANSS catalog between 1984 and 2015. The gray curve depicts the modified magnitude-frequency distribution of earthquakes in the Parkfield region with a $M6.08$ and its aftershocks every 24.5 years. The stars represent the historical data [Toppozada et al., 2002] and the black line represents a $M7$ earthquake with a recurrence time between 140 and 250 years. The probabilities computed depend on the model chosen, either MW or MJ, on the ratio between the postseismic and the coseismic moment release, and on whether the Båth law is applied or not.*

The two extreme cases illustrated by Figure 1.12.a and f enables to appreciate the range of magnitude and frequency for an earthquake to close the moment budget. For a 140-year recurrence time, the largest earthquake required would range between $M6.7$ for the first case and $M7.3$ for the second. This underlines the sensitivity to the hypothesis regarding the contribution to the moment budget of aftershocks and postseismic deformation. As an example, if we suppose that there is a magnitude 7 occurring every 140 years and we assume Båth's law, the postseismic moment released would be between 162±34 % (MW) and 236±59 % (MJ).

Following the second approach, the marginal cumulative probabilities reflect primarily the assumptions that the a priori probabilities are uniform, between 6.3 and 9 for the magnitude of the largest earthquake, and 10^{4} and 10^{-6} for its frequency (Figure 1.10.b and d). It shows that the historical catalogue does not put any constraint on the magnitude of the maximum event for return periods much longer than the catalogue. The magnitude for which 95% of the maximum non-cumulative probability is reached can instead give us an indication of the magnitude and frequency needed to close the moment budget (Figure 1.S2). A $M7.34$ is sufficient to close the moment budget at a 95% confidence level, as well as a time recurrence of 2000 years. Higher magnitudes and recurrence times than those estimates are equally plausible but would not be necessary.

Scaling laws linking stress drop, $\Delta\boldsymbol{\sigma}$, area of rupture, A, and moment released during an earthquake, m, can give us an indication of the maximum magnitude through the equation $\Delta\boldsymbol{\sigma} \approx \boldsymbol{C\,m\,A^{-3/2}}$, where C is a geometric constant close to unity [Scholz, 1982]. Earthquake stress drops generally vary between 0.1MPa and 100MPa [Kanamori and Brodsky, 2004]. Consequently, the rupture of the full fault (70 x 19km) would be equivalent to a maximum magnitude of between M6.39 and M8.38. For events that rupture half of the segment length and for which the down dip extent is 13km (35 x 13km), the maximum magnitude would vary between M5.92 and M7.92. For comparison, Parkfield 2004 stress drop is ~0.61MPa [Wang et al., 2014]. However, such range of stress drop and the corresponding magnitude is too large to provide any useful constraints on our problem, hence we decided not to include this criterion in our analysis.

3.3. IMPLICATIONS FOR SEISMIC HAZARD

For each tested value of the magnitude and frequency of the largest event, one can determine a seismic hazard quantity, such as for example, the probability P_{Hazard} that an independent earthquake (not an aftershock) would exceed a given magnitude M_{Test} over a given period of time t. Each curve can then be weighted according to the probability of the scenario. The weighted mean $\bar{P}_{Hazard}$ then represents the overall hazard resulting from all possible scenarios. As explained in the section of the first approach, the number of independent events taken from the declustered catalog is too low to estimate the local b-value. So, we use the b-value derived from a non-declustered catalog.

Figures 1.13.a and 1.13.b show the probability of having an earthquake larger than a given magnitude over a period of 30 years and 200 years based on the probability distribution of the magnitude-frequency of the largest earthquake derived with the second approach. The two panels correspond to different a priori assumptions regarding the maximum possible magnitude of the largest earthquake. If we assume that the largest earthquake cannot exceed 7.5, the probability of a M>6 event over 30 years is 43% or 6% for a M>7 (Figure 1.13.a). If we assume that the largest earthquake can be as large as magnitude 9, a certainly outrageous value, the probability is reduced to 23% for a M> 6 and 3% for a M>7 (Figure 1.13.b). The earthquakes with magnitudes between 7.5 and 9 with a high P_G contribute to the seismic moment release so that smaller magnitude earthquakes don't need to be as frequent as in the previous case, leading to a lower $\bar{P}_{Hazard}$. Similarly, Figures 1.13.c and 13.d show the hazard curves resulting from the probabilities of the magnitude-frequency of the largest earthquake derived with the second approach described above for a period of time of 200 years. If we assume that the largest earthquake cannot exceed 7.5, the probability of a M>6 event over 200 years is 96%, and 30% for a M>7 (Figure 1.13.c). If we assume that the largest earthquake can be as large as magnitude 9, the probability is reduced to 68% for M>6 and to 15% for M>7. These tests illustrate the significant sensitivity of the method to the a priori assumption on the maximum value of the largest possible magnitude.

The first approach, assuming a GR Richter distribution up to the largest event, yields very similar results (Figure 1.S4) showing that these curves are not very sensitive to the choice of

method, essentially because the periods chosen (of 30 and 200 years) are small compared with the return period of the maximum earthquake.

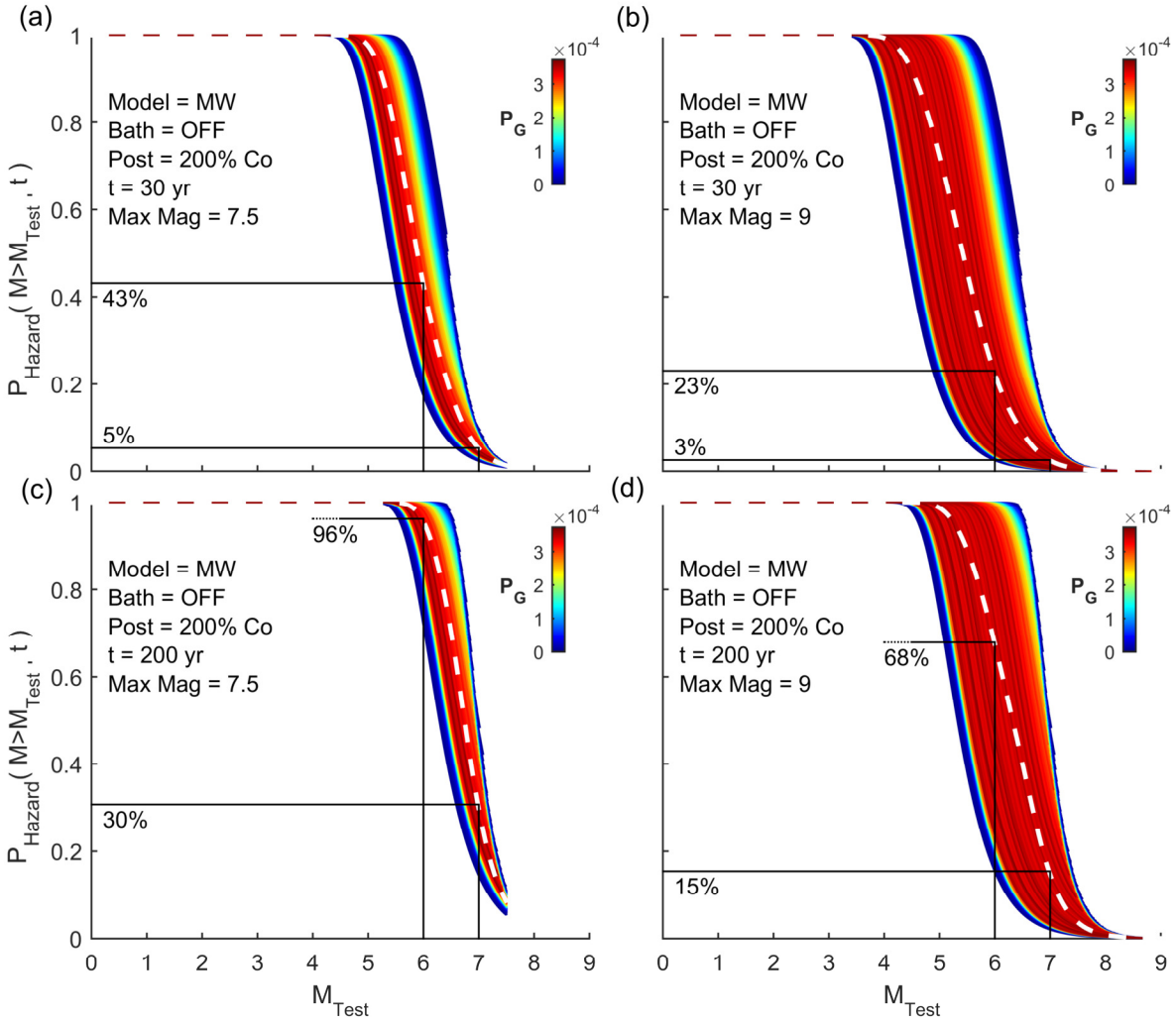

Figure 1.13. *Probability to have earthquakes over a certain magnitude in a period of time of* $\boldsymbol{t}$ *years considering the probability distribution of a maximum-magnitude earthquake to exist and close the moment budget. We test our favored scenario using model MW, with the Bath law not accounted for and with a postseismic moment release equivalent to 200% of the coseismic one. The white dashed line corresponds to* $\overline{\boldsymbol{P}}_{\boldsymbol{Hazard}}$*. (a) and (b) are the results for* $\boldsymbol{t}$*=30 years, and (c) and (d) are for* $\boldsymbol{t}$*=200years. (a) and (c) suppose a maximum-magnitude possible of M7.5, and (b) and (d) suppose that the maximum-magnitude possible is a M9.*

4. Discussion

Our assessment of the moment budget on the Parkfield segment of the SAF suggests that the sequence of M~6 events returning every ~24 years as observed since 1857 accounts for only

about 12.1% of the deficit of moment that is accumulating in the interseismic period. This conclusion would imply that this fault segment must hold larger, less frequent, earthquakes. Before discussing this possibility, we examine various factors that could be responsible for the moment deficit. The hypothesis of a larger earthquake is indeed not the only scenario that can explain residual moment deficit. Our analysis relies on a number of assumptions that might be questioned.

First, we assume that interseismic coupling is stationary in time and use models of interseismic coupling derived from decades of geodetic data (GPS and InSAR). The time period covered by these data might seem in fact short if the moment deficit is primarily balanced by events with a return period on the order of centuries. Furthermore, significant changes in interseismic coupling have been reported on subduction megathrusts [*Meltzner et al.*, 2015; *Tsang et al.*, 2015; *Yokota and Koketsu*, 2015]. The stationary hypothesis is supported locally by the consistency between the model MJ proposed by Jolivet *et al.,* (2015) based on InSAR and GPS data from 2006 to 2010, and the model MW proposed by *Wang et al*., (2014) based on GPS data ranges from 1999 to 2004. However, according to Barbot *et al.* [2013], the southern end of the Parkfield segment underwent some changes before and after the 2004 $M6$ event. The boundary between the Parkfield and Cholame segments appears to creep faster following the 2004 earthquake than previously, which would indicate a variation in time of the coupling pattern. Moreover, except for an aseismic transient slip coincident with three $M{\sim}4.5$ earthquakes in the mid-1990s [*Gwyther et al.*, 1996; *Langbein et al.*, 1999; *Nadeau and McEvilly*, 1999; *Gao et al.*, 2000; *Roeloffs*, 2001; *Murray and Segall*, 2005], no strong changes in the interseismic slip rate seems to have been detected between 1966 and 2004 [*Murray and Langbein*, 2006; *Barbot et al.*, 2013]. This suggests no modification of the locked section pattern or presence of other creep events during this time. However, if an event equivalent to the one in the mid-1990s (~$M5.6$) occurred once every 24.5 years (the period of the $M6$ interseismic cycle), the moment released would be insufficient to close the moment budget of any of the models used in this study. It would cover 2.4% of the smallest residual moment deficit, calculated from the model of Wang *et al.*, (2014). Temporal variations of coupling and slow events seem thus much too small to be able to account for the deficit of moment reported in our study.

Second, we assumed that all of the geodetic deformation is elastic strain. The overall consistency of geodetic strain rates with geologic slip rates supports this assumption for the San Andreas Fault. However, there are a number of segments where significant discrepancies have been reported. Such discrepancies are expected from stress redistribution among faults during the seismic cycle [*Ben-Zion et al.*, 1993; *Loveless and Meade*, 2011; *Tong et al.*, 2014] or could be due to distributed anelastic strain during the interseismic period [*Oskin et al.*, 2008]. In that regard, it is interesting to note that the deep creep rates that we used to estimate interseismic loading (31.1 and 36.5 mm/yr for MJ and 32.1 mm/yr for MW) are larger than the local estimate of 26.2 +6.4/-4.3 mm/yr of Toké et al. [*Toké et al.*, 2011]. This discrepancy could reflect either distributed anelastic strain or temporal variations in interseismic loading.

Our analysis thus suggests that the Parkfield segment of the SAF needs to release more seismic moment on the long-term average than was released by the M~6 events that have occurred repeatedly since after the Fort Tejon earthquake of 1857. This imbalance points to occasional larger events. This fault segment could probably host significantly larger events. We note that the zone of high coupling derived from modeling interseismic geodetic data seems larger than the area that ruptured in 2004 (Figure 1.4a). If we assume an average stress drop similar to the 0.61 MPa observed during the 2004 earthquake [*Wang et al., 2014*], which was at the lower end of commonly observed values, and a complete rupture of the locked area of Figure 1.4b (equal to 632 km^2 for $\chi > 0.7$), we could expect a *M*~6.3 event. Assuming an average stress drop of 1.5 MPa, larger than in 2004, this fault segment could produce a *M*6.6 earthquake. In fact, the locked area of Figure 1.4a, appears to be made of two locked patches separated by a zone of lower interseismic coupling. The partially creeping zone could act as a barrier to the propagation of seismic rupture. This pattern, analog to that investigated by Kaneko *et al*., 2010, is favorable to generate a bimodal seismic behavior with moderate earthquakes rupturing one or the other asperity and larger infrequent earthquakes rupturing the whole patch. Another possibility is that the Parkfield segment would occasionally rupture together with large events on the Carrizo plain segment of the SAF. In that case, the interaction between the two fault segments could lead to a larger moment release on the Parkfield segment than in the case of rupture confined to it (a longer rupture length requires larger slip if the stress drop is similar).

There are actually hints that the $M7.7$ 1857 Fort Tejon earthquake may have ruptured the Parkfield segment. Paleoseismic studies [*Sieh*, 1978; *Lienkaemper*, 2001] indicate 2 to 6 m of slip at sites near highway 46 due to this earthquake. The northernmost observation attributed to the 1857 earthquake is a 4.5 m offset, 1.7 km north of highway 46 [*Lienkaemper*, 2001], whereas a 3.5 m offset has also been measured 1.3 km south of it [*Sieh*, 1978]. Such large surface slip measurements show that the Parkfield segment can occasionally slip much more than during the 2004 earthquake (i.e. typically ~20cm).

Assuming a 3.8m slip (as averaged over the measurements along the Cholame section [*Sieh*, 1978; *Zielke et al.*, 2012]) with a 10 km along dip width rupture that reaches 22 km North-west of the highway 46, the moment released within the limits of the model of Wang et al (2014) is of 4.38 10^{19} N.m, equivalent to a $M7.03$ earthquake. The moment includes the aftershocks and postseismic effects since no distinction between them and the mainshock can be estimated from paleoseismic data. Assuming aftershocks contribute between 8% and 156% (depending on whether we assume Bath's law or not) and that the postseismic impact is about 200% of the coseismic released, then the seismic rupture alone would account between a $M6.72$ and $M6.47$.

In the literature, the recurrence time of 1857-like earthquakes, if there are any characteristic earthquakes [*Zielke et al.*, 2012], is suggested to be roughly between 140 and 255 years [*Sieh*, 1978; *Zielke et al.*, 2010]. In this case, the return of co-seismic ruptures similar to that of 1857 would contribute between 2.88 10^{17} N.m/yr and 1.58 10^{17} N.m/yr to the moment release rate. This would reduce the moment deficit rate, i.e. between 42% and 23% for MW (between 61% and 33% of the moment deficit residual rate), and 21% and 11% for MJ (between 24% and 13% of the moment deficit residual rate).

Finally, it has been proposed that enhanced fault weakening could occasionally allow large ruptures to propagate in creeping areas [*Noda and Lapusta*, 2013]. In such case, the Parkfield segment could also occasionally release much more seismic moment than during a *M*~6 event confined to the locked area of the Parkfield segment.

5. Conclusion

In principle, the rate of accumulation of moment deficit on a fault, determined from modeling of interseismic strain measurements, can be used to constrain the frequency and magnitude of the largest possible earthquake by requiring the moment budget to balance over the seismic cycle. Testing this approach on the Parkfield segment shows that a M~6 earthquake returning about every 24 years, as has been observed over the last 150 years, falls short of balancing the rate of moment deficit accumulation. The conclusion seems robust in view of the uncertainties on the data and model assumptions.

The most likely explanation is that this fault segment hosts larger earthquakes, in the range *M*6.5 to *M*7.5, with a return period of 140 to 300 years. Such episodes of seismic moment release could happen as independent earthquakes rupturing the locked asperities revealed by interseismic coupling models or in conjunction with rupture of the Carrizo plain segment of the SAF, as potentially happened in 1857. The methodology presented in this study allows the incorporation of formal geodetic constraints on the rate of moment deficit accumulation into probabilistic seismic hazard assessments.

Data and Resources

The ANSS catalog was searched using http://www.quake.geo.berkeley.edu/anss/catalog-search.html (last accessed February 2015)

Acknowledgment

We would like to thank Adriano Gualandi for insightful discussions and for providing the recurrence time equation taking account Bath's law (Equation 1.10). We thank two anonymous reviewers for their detailed and constructive criticisms which helped improve our study substantially. We thank Alex Copley, James Jackson and Andy Howell for discussions. Some of the figures were created using the Generic Mapping Tool (GMT) software [*Wessel and Smith,* 1998].

Bibliography

Ader, T., J.-P. Avouac, J. Liu-Zeng, H. Lyon-Caen, L. Bollinger, J. Galetzka, J. Genrich, M. Thomas, K. Chanard, S. Sapkota et al. (2012), Convergence rate across the Nepal Himalaya and interseismic coupling on the Main Himalayan Thrust: Implications for seismic hazard, *J. Geophys. Res.*, *117*(B04403), 1–16, doi:10.1029/2011JB009071.

Aki, K. (1965), Maximum Likelihood Estimate of b in the Formula logN=a-bM and its Confidence Limits, 東京大学地震研究所彙報, *43*(2), 237–239.

Allmann, B. P., and P. M. Shearer (2007), A High-Frequency Secondary Event, *Science*, *318*, 1279–1283, doi:10.1126/science.1146537.

Avouac, J.-P. (2015), From Geodetic Imaging of Seismic and Aseismic Fault Slip to Dynamic Modeling of the Seismic Cycle, *Annu. Rev. Earth Planet. Sci.*, *43*, 233-271, doi:10.1146/annurev-earth-060614-105302.

Bakun, W. H., B. Aagaard, B. Dost, W. L. Ellsworth, J. L. Hardebeck, R. A. Harris, C. Ji, M. J. S. Johnston, J. Langbein, J. J. Lienkaemper, et al. (2005), Implications for prediction and hazard assessment from the 2004 Parkfield earthquake, *Nature*, *437*(7061), 969–974, doi:10.1038/nature04067.

Barbot, S., Y. Fialko, and Y. Bock (2009), Postseismic deformation due to the Mw 6.0 2004 Parkfield earthquake: Stress-driven creep on a fault with spatially variable rate-and-state friction parameters, *J. Geophys. Res.*, *114*(B07405), 1–26, doi:10.1029/2008JB005748.

Barbot, S., P. Agram, and M. De Michele (2013), Change of apparent segmentation of the San Andreas fault around Parkfield from space geodetic observations across multiple periods, *J. Geophys. Res. Solid Earth*, *118*, 6311–6327, doi:10.1002/2013JB010442.

Båth, M. (1965), Lateral inhomogeneities of the upper mantle, *Tectonophysics*, *2*(6), 483–514, doi:10.1016/0040-1951(65)90003-X.

Bender, B. (1983), Maximum likelihood estimation of b values for magnitude grouped data, *Bull. Seismol. Soc. Am.*, *73*(3), 831–851.

Bruhat, L., S. Barbot, and J. P. Avouac (2011), Evidence for postseismic deformation of the

lower crust following the 2004 Mw6.0 Parkfield earthquake, *J. Geophys. Res.*, *116*(B08401), 1–10, doi:10.1029/2010JB008073.

Dutilleul, P., C. W. Johnson, R. Bürgmann, Y. Wan, and Z. Shen (2015), Multifrequential periodogram analysis of earthquake occurence: An alternative approach to the Schuster spectrum, with two examples in central California, *J. Geophys. Res. Solid Earth*, *120*, 8494–8515, doi:10.1002/2015JB012467.

Field, E. H., and T. H. Jordan (2015), Time-Dependent Renewal-Model Probabilities When Date of Last Earthquake is Unknown, *Bull. Seismol. Soc. Am.*, *105*(1), 459–463, doi:10.1785/0120140096.

Frohlich, C., and S. D. Davis (1993), Teleseismic b values; Or, much ado about 1.0, *J. Geophys. Res.*, *98*(B1), 631, doi:10.1029/92JB01891.

Gao, S. S., P. G. Silver, and A. T. Linde (2000), Analysis of deformation data at Parkfield, California: Detection of a long-term strain transient, *J. Geophys. Res.*, *105*(B2), 2955-2967, doi:10.1029/1999JB900383.

Gutenberg, B., and C. F. Richter (1944), Frequence of earthquakes in California, *Bull. Seismol. Soc. Am.*, *34*, 185–188.

Gwyther, R. L., M. T. Gladwin, M. Mee, and R. H. G. Hart (1996), Anomalous shear strain at Parkfield during 1993-1994, *Geophys. Res. Lett.*, *23*(18), 2425–2428.

Hasting, W. K. (1970), Monte Carlo sampling methods using Markov chains and their applications, *Biometrica*, *57*, 97.

Helmstetter, A., and D. Sornette (2003), Bath's law derived from the Gutenberg-Richter law and from aftershock properties, *Geophys. Res. Lett.*, *30*(20), 4, doi:2069\r10.1029/2003gl018186.

Johanson, I. A., E. J. Fielding, F. Rolandone, and R. Bürgmann (2006), Coseismic and postseismic slip of the 2004 Parkfield earthquake from space-geodetic data, *Bull. Seismol. Soc. Am.*, *96*(4 B), 269–282, doi:10.1785/0120050818.

Johnson, K. M. (2013), Is stress accumulating on the creeping section of the San Andreas fault?, *Geophys. Res. Lett.*, *40*(23), 6101–6105, doi:10.1002/2013GL058184.

Jolivet, R., M. Simons, P. S. Agram, Z. Duputel, and Z.-K. Shen (2015), Aseismic slip and seismogenic coupling along the central San Andreas Fault, *Geophys. Res. Lett.*, *42*, 297–306, doi:10.1002/2014GL062222.

Kanamori, H., and E. E. Brodsky (2004), The physics of earthquakes, *Reports Prog. Phys.*, *67*, 1429–1496, doi:10.1088/0034-4885/67/8/R03.

Kaneko, Y., J.-P. Avouac, and N. Lapusta (2010), Towards inferring earthquake patterns from geodetic observations of interseismic coupling, *Nat. Geosci.*, *3*(5), 363–369, doi:10.1038/ngeo843.

Langbein, J., R. L. Gwyther, R. H. G. Hart, and M. T. Gladwyn (1999), Slip-rate increase at Parkfield in 1993 detected by high-precision EDM and borehole tensor strainmeters, *Geophys. J. Int.*, *26*(16), 2529–2532.

Langbein, J., R. Borcherdt, D. Dreger, J. Fletcher, J. L. Hardebeck, M. Hellweg, C. Ji, M. Johnston, J. R. Murray, and R. Nadeau (2005), Preliminary Report on the 28 September 2004, M 6.0 Parkfield, California Earthquake, *Seismol. Res. Lett.*, *76*(1), 10–26, doi:10.1785/gssrl.76.1.10.

Langbein, J., J. R. Murray, and H. A. Snyder (2006), Coseismic and initial postseismic deformation from the 2004 Parkfield, California, earthquake, observed by global positioning system, electronic distance meter, creepmeters, and borehole strainmeters, *Bull. Seismol. Soc. Am.*, *96*(4 B), 304–320, doi:10.1785/0120050823.

Lienkaemper, J. J. (2001), 1857 slip on the San Andreas fault Southeast of Cholame, California, *Bull. Seismol. Soc. Am.*, *91*(6), 1659–1672, doi:10.1785/0120000043.

Lin, Y. N. N., A. Sladen, F. Ortega-Culaciati, M. Simons, J.-P. Avouac, E. J. Fielding, B. A. Brooks, M. Bevis, J. Genrich, A. Rietbrock et al. (2013), Coseismic and postseismic slip associated with the 2010 Maule Earthquake, Chile: Characterizing the Arauco Peninsula barrier effect, *J. Geophys. Res. Solid Earth*, *118*, doi:10.1002/jgrb.50207.

Liu, P., S. Custodio, and R. J. Archuleta (2006), Kinematic Inversion of the 2004 M 6.0 Parkfield Earthquake Including an Approximation to Site Effects, *Bull. Seismol. Soc. Am.*, *96*(4B), S143–S158, doi:10.1785/0120050826.

Marsan, D., and O. Lengline (2008), Extending Earthquakes' Reach Through Cascading, *Science*, *319*(5866), 1076–1079, doi:10.1126/science.1148783.

Matthews, M. V, W. L. Ellsworth, and P. A. Reasenberg (2002), A Brownian Model for Recurrent Earthquakes, *Bull. Seismol. Soc. Am.*, *92*(6), 2233–2250.

Meade, B. J., and B. H. Hager (2005), Block models of crustal motion in southern California constrained by GPS measurements, *J. Geophys. Res.*, *110*(B03403), doi:10.1029/2004JB003209.

Meltzner, A. J., K. Sieh, H.-W. Chiang, C.-C. Wu, L. L. H. Tsang, C.-C. Shen, E. M. Hill, B. W. Suwargadi, D. H. Natawidjaja, B. Philibosian et al. (2015), Time-varying interseismic strain rates and similar seismic ruptures on the Nias-Simeulue patch of the Sunda megathrust, *Quat. Sci. Rev.*, *122*, 258–281, doi:10.1016/j.quascirev.2015.06.003.

Metropolis, N., A. W. Rosenbluth, M. N. Rosenbluth, A. H. Teller, and E. Teller (1953), Equation of State Calculations by Fast Computing Machines, *J. Chem. Phys.*, *21*(6), 1087–1092, doi:doi:10.1063/1.1699114.

Molnar, P. (1979), Earthquake Recurrence Intervals and Plate Tectonics, *Bull. Seismol. Soc. Am.*, *69*(1), 115–133.

Murray, J., and J. Langbein (2006), Slip on the San Andreas fault at Parkfield, California, over two earthquake cycles, and the implications for seismic hazard, *Bull. Seismol. Soc. Am.*, *96*(4 B), 283–303, doi:10.1785/0120050820.

Murray, J., and P. Segall (2002), Testing time-predictable earthquake recurrence by direct measurement of strain accumulation and release, *Nature*, *419*, 287–291, doi:10.1038/nature00984.

Murray, J. R., and P. Segall (2005), Spatiotemporal evolution of a transient slip event on the San Andreas fault near Parkfield, California, *J. Geophys. Res.*, *110*(B09407), doi:10.1029/2005JB003651.

Murray, J. R., P. Segall, P. Cervelli, W. Prescott, and J. Svarc (2001), Inversion of GPS data for spatially variable slip-rate on the San Andreas Fault near Parkfield, CA, *Geophys. Res. Lett.*, *28*(2), 359–362, doi:10.1029/2000GL011933.

Nadeau, R. M., and T. V. McEvilly (1999), Fault Slip Rates at Depth from Recurrence Intervals of Repeating Microearthquakes, *Science*, *285*(5428), 718–721, doi:10.1126/science.285.5428.718.

NCEDC (2014), *Northern California Earthquake Data Center*, Northern California Earthquake Data Center. UC Berkeley Seismological Laboratory. Dataset. doi:10.7932/NCEDC.

Noda, H., and N. Lapusta (2013), Stable creeping fault segments can become destructive as a result of dynamic weakening., *Nature*, *493*(7433), 518–521, doi:10.1038/nature11703.

Oskin, M., L. Perg, E. Shelef, M. Strane, E. Gurney, B. Singer, and X. Zhang (2008), Elevated shear zone loading rate during an earthquake cluster in eastern California, *Geology*, *36*(6), 507–510, doi:10.1130/G24814A.1.

Page, M., and K. Felzer (2015), Southern San Andreas Fault Seismicity is Consistent with the Gutenberg-Richter Magnitude-Frequency Distribution, *Bull. Seismol. Soc. Am.*, *105*(4), 1–11, doi:10.1785/0120140340.

Reid, H. F. (1910), *The California Earthquake of April 18, 1906, Report of the State Earthquake Investigation Commission, The Mechanism of the Earthquake*, Washington, DC.

Roeloffs, E. A. (2001), Creep rate changes at Parkfield, California 1966–1999: Seasonal, precipitation induced, and tectonic, *J. Geophys. Res.*, *106*(B8), 16,525-16,547, doi:10.1029/2001JB000352.

Scholz, C. H. (1982), Scaling laws for large earthquakes: consequences for physical models, *Bull. Seism. Soc. Am*, *72*(1).

Schwartz, D. P., and K. J. Coppersmith (1984), Fault behavior and characteristic earthquakes: Examples from the Wasatch and San Andreas Fault Zones, *J. Geophys. Res.*, *89*(B7), 5681-5698, doi:10.1029/JB089iB07p05681.

Segall, P., and R. Harris (1987), Earthquake Deformation Cycle on the San Andreas Fault Near Parkfield, California, *J. Geophys. Res.*, *92*(B10), 10511–10525, doi:10.1029/JB092iB10p10511.

Sieh, K. E. (1978), Slip along the San Andreas fault associated with the great 1857 earthquake, *Bull. Seismol. Soc. Am.*, *68*(5), 1421–1448.

Sieh, K. E., and R. H. Jahns (1984), Holocene activity of the San Andreas fault at Wallace Creek, California Holocene activity of the San Andreas fault at Wallace Creek, California, *Geol. Soc. Am. Bull.*, (8), 883–896, doi:10.1130/0016-7606(1984)95<883.

Stevens, V. L., and J.-P. Avouac (2016), Millenary Mw >9.0 earthquakes required by geodetic strain in the Himalaya, *Geophys. Res. Lett.*, *43*, 1118–1123, doi:10.1002/2015GL067336.

Thomas, M. Y., J. P. Avouac, J. Champenois, J. C. Lee, and L. C. Kuo (2014), Spatiotemporal evolution of seismic and aseismic slip on the Longitudinal Valley Fault, Taiwan, *J. Geophys. Res. Solid Earth*, *119*, doi:10.1002/2013JB010603.

Toké, N. a., and J. R. Arrowsmith (2006), Reassessment of a slip budget along the Parkfield segment of the San Andreas fault, *Bull. Seismol. Soc. Am.*, *96*(4 B), 339–348, doi:10.1785/0120050829.

Toké, N. a., J. R. Arrowsmith, M. J. Rymer, A. Landgraf, D. E. Haddad, M. Busch, J. Coyan, and A. Hannah (2011), Late Holocene slip rate of the San Andreas fault and its accommodation by creep and moderate-magnitude earthquakes at Parkfield, California, *Geology*, *39*(3), 243–246, doi:10.1130/G31498.1.

Tong, X., B. Smith-Konter, and D. T. Sandwell (2014), Is there a discrepancy between geological and geodetic slip rates along the San Andreas Fault System?, *J. Geophys. Res. Solid Earth*, *119*, 2518–2538, doi:10.1002/2013JB010765.Received.

Tong, X., D. T. Sandwell, and B. Smith-Konter (2015), An integral method to estimate the moment accumulation rate on the Creeping Section of the San Andreas Fault, *Geophys. J. Int.*, *203*(1), 48–62, doi:10.1093/gji/ggv269.

Toppozada, T. R., D. M. Branum, M. S. Reichle, and C. L. Hallstrom (2002), San Andreas Fault Zone , California : M ≥ 5.5 Earthquake History, *Bull. Seismol. Soc. Am.*, *92*(7), 2555–2601.

Tsang, L. L. H., A. J. Meltzner, E. M. Hill, J. T. Freymueller, and K. Sieh (2015), A paleogeodetic

record of variable interseismic rates and megathrust coupling at Simeulue Island , Sumatra, *Geophys. Res. Lett.*, *42*, 10585–10594, doi:10.1002/2015GL066366.1.

Utsu, T. (1966), A Statistical Significance Test of the Difference in b-value between Two Earthquake Groups, *J. Phys. Earth*, *14*(2), 37–40, doi:10.4294/jpe1952.14.37.

Wang, L., S. Hainzl, G. Zöller, and M. Holschneider (2012), Stress- and aftershock-constrained joint inversions for coseismic and postseismic slip applied to the 2004 M6.0 Parkfield earthquake, *J. Geophys. Res.*, *117*(B07406), doi:10.1029/2011JB009017.

Wang, L., S. Hainzl, and G. Zöller (2014), Assessment of stress coupling among the inter-, co- and post-seismic phases related to the 2004 M6 parkfield earthquake, *Geophys. J. Int.*, *197*(3), 1858–1868, doi:10.1093/gji/ggu102.

Wang, L., S. Hainzl, and P. M. Mai (2015), Quantifying slip balance in the earthquake cycle: Coseismic slip model constrained by interseismic coupling, *J. Geophys. Res. Solid Earth*, *120*, doi:10.1002/2015JB011987.

Wiemer, S., and M. Wyss (2000), Minimum magnitude of completeness in earthquake catalogs: Examples from Alaska, the Western United States, and Japan, *Bull. Seismol. Soc. Am.*, *90*(4), 859–869, doi:10.1785/0119990114.

Woessner, J., and S. Wiemer (2005), Assessing the quality of earthquake catalogues: Estimating the magnitude of completeness and its uncertainty, *Bull. Seismol. Soc. Am.*, *95*(2), 684–698, doi:10.1785/0120040007.

Yokota, Y., and K. Koketsu (2015), A very long-term transient event preceding the 2011 Tohoku earthquake, *Nat. Commun.*, *6*, 5934, doi:10.1038/ncomms6934.

Zielke, O., J. R. Arrowsmith, L. G. Ludwig, and S. O. Akçiz (2010), Slip in the 1857 and Earlier Large Earthquakes Along the Carrizo Plain, San Andreas Fault, *Science*, *327*, 1119–1122, doi:10.1126/science.1182781

Zielke, O., J. R. Arrowsmith, L. G. Ludwig, and S. O. Akciz (2012), High-resolution topography-derived offsets along the 1857 Fort Tejon earthquake rupture trace, San Andreas fault, *Bull. Seismol. Soc. Am.*, *102*(3), 1135–1154, doi:10.1785/0120110230.

SUPPLEMENT

S.1. Description of the supplement

We present in the supplement the flowchart of the methodology and we show the results of our methodology obtained using a Brownian Passage Time model [*Matthews et al.*, 2002; *Field and Jordan*, 2015], which are only marginally different from the ones obtained with the Poisson model.

S.2. Methodology flowchart

Table 1.S1. *Flow chart of methodology*

Steps	*Parameters used*
Calculation of P_{Budget}	
1. Choose variables (M_{max}, τ_{max})	M_{max}, τ_{max}
2. Assume Bath law: ΔM between the mainshock and the larger aftershock	B (=0 or 1)
3. Assume contributions from aftershocks and background seismicity	b
4. Assume aseismic contribution	α
5. Calculate $P_{Budget}(M_{max}, \tau_{max})$	$\dot{m}_0$
Calculation of P_{Hist}	
1. Choose variables (M_{max}, τ_{max})	M_{max}, τ_{max}
2.a Assume Poisson model	τ
2.b Assume renewal model	τ, α_{BPT}
3.a Approach1: Assume the largest earthquake follows the GR law determined by known seismicity	a, b
3.b Approach2: The largest earthquake does not need to follow the GR law determined by known seismicity. Only the duration (t_{hist}) of the catalogue matters.	t_{hist}
4. Calculate P_{Real}	Equation 1.13 and 1.15
Calculate of P_G	Equation 1.18

S.3. Moment budget from the Brownian Passage Time model

In the methodology section of the main text, we base all our probability calculations on Poisson's model. However, other options are possible and we show here an example using a specific renewal model, the Brownian Passage Time (BPT) model [*Matthews et al.*, 2002; *Field and Jordan*, 2015].

The probability density function (PDF) of a renewal model, $f(t)$, describes the probability to have the first earthquake at time t since the last event. The PDF of the BPT model is

$$f(t;\tau,\alpha_{BPT}) = \left(\frac{\tau}{2\pi{\alpha_{BPT}}^2 t^3}\right)^{1/2} exp\left\{-\frac{(t-\tau)^2}{2\tau{\alpha_{BPT}}^2 t}\right\}, \quad (1.S1)$$

where τ is the earthquake mean recurrence time and α_{BPT} is defined by the ratio between the mean and the standard deviation of the recurrence time, σ.

Let *F*(t) represent the cumulative distribution function (CDF) of $f(t)$ and T the time since the last earthquake. The probability of having no earthquakes in a time interval ΔT knowing that no earthquakes happened until T can be rewritten as the probability to have no earthquake until $T+\Delta T$, knowing there has been no earthquakes up to T:

$$\begin{aligned} P(T+\Delta T<t \mid T<t) &= \frac{P(T+\Delta T<t)P(T<t \mid T+\Delta T<t)}{P(T<t)} \\ &= \frac{P(T+\Delta T<t)}{P(T<t)} \\ &= \frac{1-P(T+\Delta T\geq t)}{1-P(T\geq t)} \\ &= \frac{1-F(T+\Delta T)}{1-F(T)}. \end{aligned} \quad (1.S2)$$

Note that compared to the Poisson model, which just needed τ and ΔT to be set, the BPT model needs additionally two more variable: α_{BPT} and T. In our calculation, we fix the α_{BPT} of all events equal to the α_{BPT} of Parkfield's *M*6 (α_{BPT}=0.37). The PDF of the time of the last event for renewal models is given by: $p(T) = \frac{1-F(T)}{\tau}$ [*Field and Jordan*, 2015]. The probability P_{Hist} of our first approach for renewal models is then:

$$P_{Hist}(T \le t \le T + \Delta T \mid T < t, T_{unknown}) = \int_0^{\infty} p(T)\, P(T + \Delta T < t \mid T < t)\; dT$$

$$= \int_0^{\infty} \frac{1 - F(T)}{\tau} \frac{1 - F(T + \Delta T)}{1 - F(T)}\, dT$$

$$= \frac{\int_0^{\infty} (1 - F(T + \Delta T))\, dT}{\tau}. \qquad (1.S3)$$

It defines the probability to have no earthquakes in the time period T and $T + \Delta T$, knowing that there has been no earthquake until T but not knowing T. This probability takes into account all possible T given its initial BPT assumptions, avoiding us to sample it.

We now explore the range of possible magnitude and frequency for the largest possible earthquake needed to close the budget.

We use again the MCMC method to sample these probabilities. Each sample is taken from a uniform PDF between 6.4 and 9 for magnitudes, and between 10^{-6} and 10^{4} yrs^{-1} for frequencies. We calculate for each sample k the value proportional to the probability $P_{G,k}$ as described in the method section. For each estimate, we run the sampler for 900000 steps, rejecting the first 500 steps to ensure accurate sampling of the PDF. The space of magnitude-frequency-time of the last event is then binned into cells of size 0.01 for the moment magnitude axis and logarithmically binned into cells of size 0.01 concerning the frequency axis. The number of samples in each cell divided by the total number of samples approximates the probability $P_{G,k}$ as defined by the MCMC method. The results are shown in Figure 1.S1.

The probabilities computed using the BPT model for low magnitude and high frequency events are smaller than Poisson model. As already mentioned in the main text in the 2nd approach section, the marginal cumulative probabilities do not give us any useful information. This is due to the fact that the maximum magnitude and lowest frequency are unbounded a priori. The magnitude for when 95% of the maximum non-cumulative probability is reached can instead give us an indication on the magnitude and frequency needed to close the moment budget (Figure 1.S2). We obtain almost the exact same values as for the Poisson model: a M7.42 with a recurrence time of 2000 years is sufficient to close the moment budget at a 95% confidence level. However, the normalized probabilities are lower for the BPT model between *M*6.4 and *M*7 than Poisson's model. Note that the 95% value does not actually represent a probability due to the normalization of the non-cumulative probabilities. Higher

magnitudes and recurrence times than those estimations are as plausible but would not be necessary.

The hazard probability estimation, P_{Hazard}, for renewal models is given by Field and Jordan, 2015:

$$P_{Hazard}(T \leq t \leq T + \Delta T | \, T < t, T_{unknown}) = \int_0^{\infty} p(T) P(\,(T \leq t \leq T + \Delta T | \, T < t)\, dT$$

$$= \frac{\Delta T - \int_0^{\Delta T} F(T) dT}{\tau}, \qquad (1.S4)$$

where $p(T)$ is the probability distribution for the time since the last event, *T*. It defines the probability to have an earthquake in the time period *T* and $T + \Delta T$, knowing that there has been no earthquake until *T* but not knowing *T*.

Figure 1.S3 shows the hazard estimation for BPT model derived from the probabilities of the magnitude-frequency of the largest earthquake using our second approach described above for a period of time of 30 years. $\bar{P}_{Hazard}$ for the Poisson model is also indicated in the figure.

The $\bar{P}_{Hazard}$ of the BPT model is equivalent to the Poisson's model for $M_{Test} \lesssim 4$; they are both almost equal to 1. They then differentiate, the BPT model having higher probabilities for $4 \lesssim M_{Test} \lesssim 6$. The BPT model $\bar{P}_{Hazard}$ joins back to Poisson's model $\bar{P}_{Hazard}$ for larger M_{Test}. This highlights the fact that $\bar{P}_{Hazard}$ for the BPT model is significantly higher for events over M_{Test} that have frequencies around ΔT.

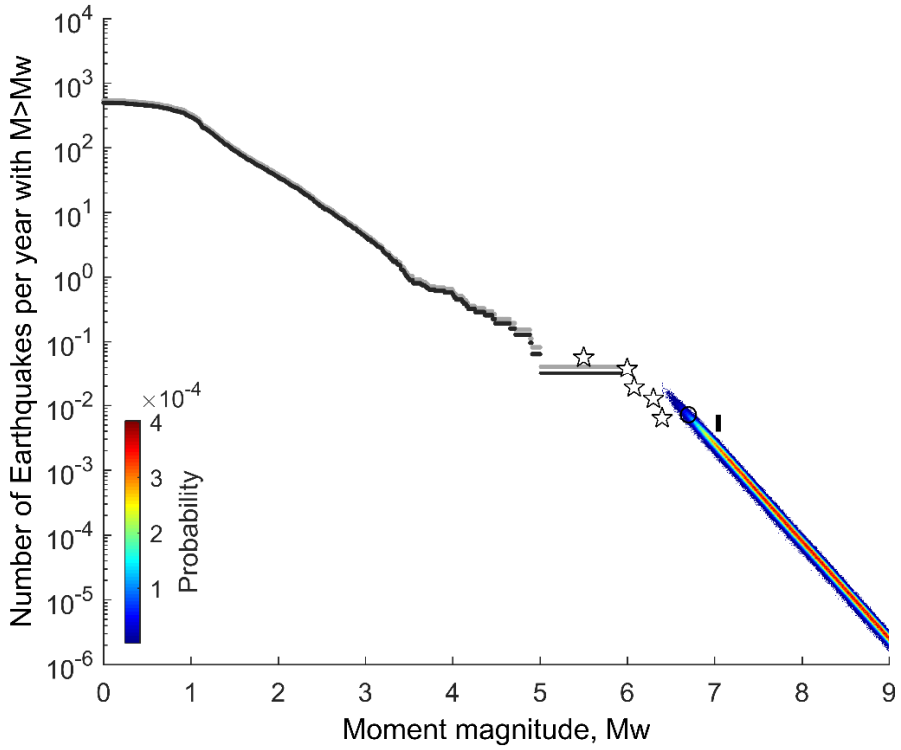

Figure 1.S1. *Maximum-magnitude earthquake probability assuming the case where large earthquakes should have a recurrence time lower than the largest earthquake currently observed, using the BPT model. We use here the model MW, do not account for Bath's law, and suppose that the ratio between postseismic and coseismic moment release is equal to 200%. The black curve represents the magnitude-frequency distribution of Parkfield's area using the ANSS catalog between 1984 and 2015. The gray curve is the modified magnitude-frequency distribution where the M6 and its aftershocks are fixed to occur every 24.5 years. The stars indicate the historical data [Toppozada et al., 2002] and the black line represents a M7 earthquake with a recurrence time between 140 and 250. The black circle defines the location of a M6.7 event occurring every 140 years, our favored scenario.*

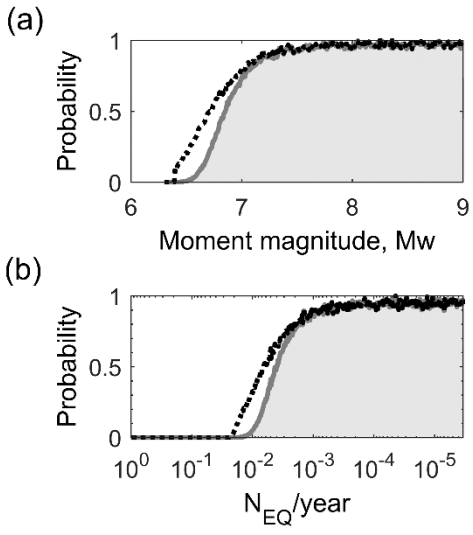

Figure 1.S2. *(a) and (b) are the marginal non-cumulative probability normalized by their maximum value for the magnitude and frequency, respectively, for our second approach. They give an indication about the magnitude and frequency of the largest event needed to close the moment budget, using the BPT (gray line) and Poisson model (black dotted line).*

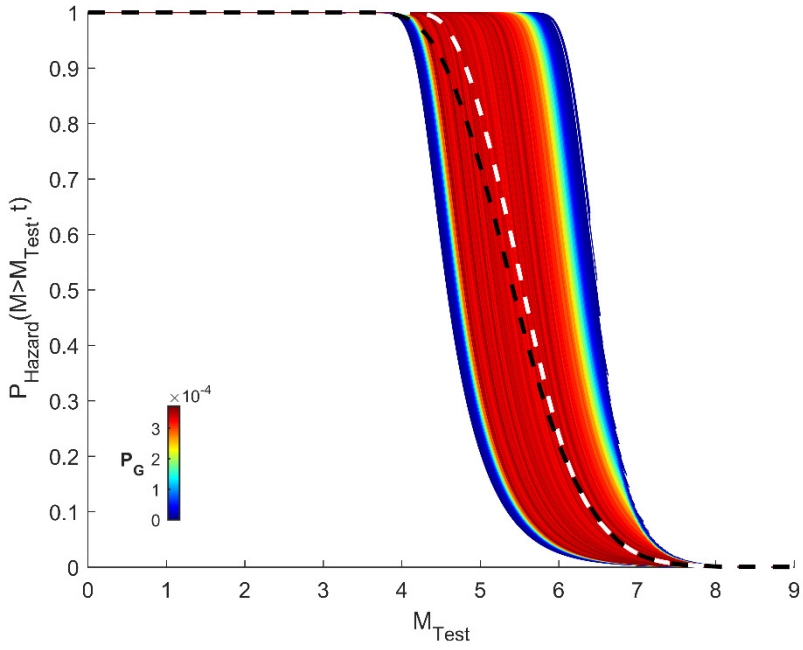

Figure 1.S3. *Probability to have earthquakes over of a certain magnitude in a period of time of t=30 years considering the probability distribution of a maximum-magnitude earthquake to exist and close the moment budget for the BPT model. We test our favored scenario using model MW, with Bath's law not accounted for and with a postseismic moment release equivalent to 200% of the coseismic one. The white dashed line corresponds to $\bar{P}_{Hazard}$ for the BPT model and the black dashed line corresponds to $\bar{P}_{Hazard}$ for the Poisson model.*

S.4. Seismic Hazard implications from the 1st and 2nd Approach

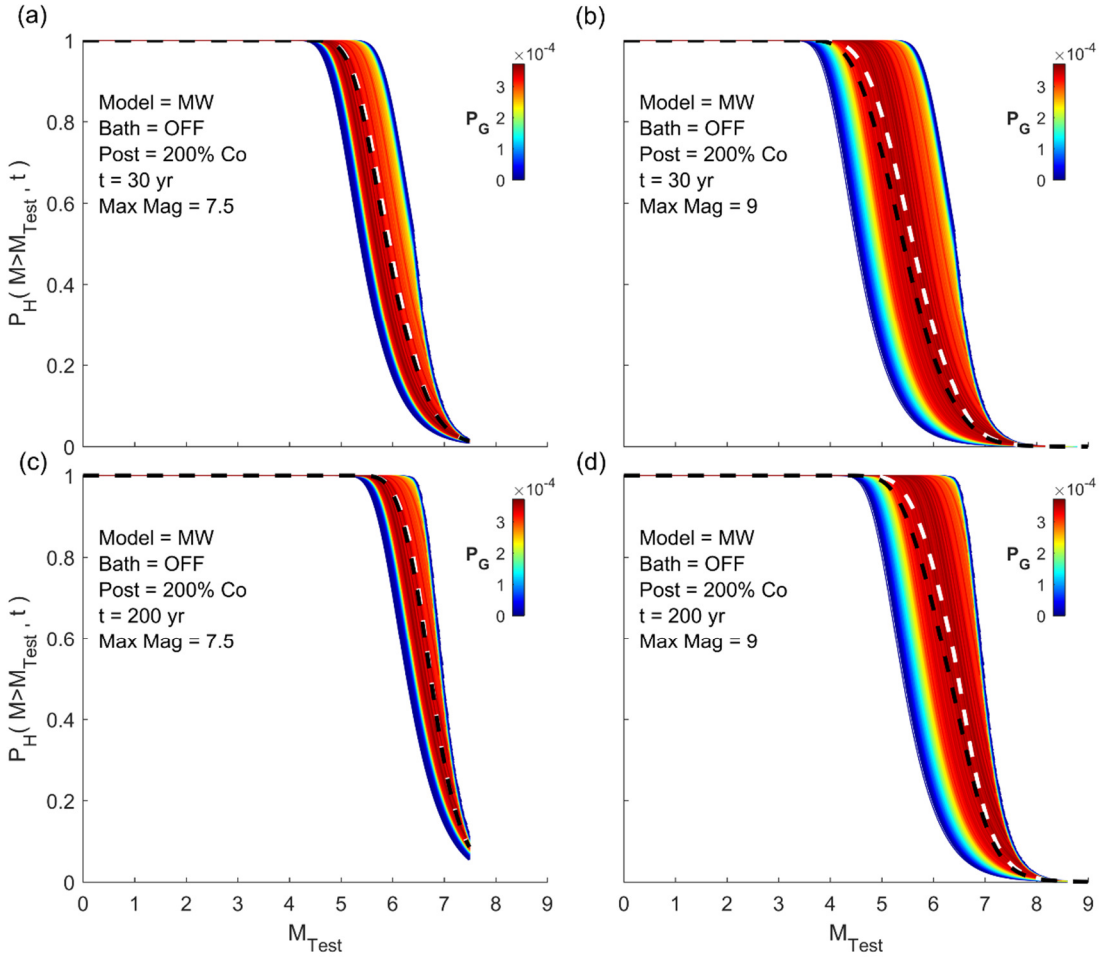

Figure 1.S4. *Probability to have earthquakes over a certain magnitude in a period of time of t years considering the probability distribution of a maximum-magnitude earthquake to exist and close the moment budget for approach 1. We test our favored scenario using model MW, with Bath's law not accounted for and with a postseismic moment release equivalent to 200% of the coseismic one. The white dashed line corresponds to* $\bar{P}_{Hazard}$ *for approach1, and the black dashed line is for approach2. (a) and (b) are the results for t=30 years, and (c) and (d) are for t=200years. (a) and (c) suppose a maximum-magnitude possible of M7.5, and (b) and (d) suppose that the maximum-magnitude possible is a M9.*

Bibliography

Field, E. H., and T. H. Jordan (2015), Time-Dependent Renewal-Model Probabilities When Date of Last Earthquake is Unknown, *Bull. Seismol. Soc. Am.*, *105*(1), 459–463, doi:10.1785/0120140096.

Matthews, M. V, W. L. Ellsworth, and P. A. Reasenberg (2002), A Brownian Model for Recurrent Earthquakes, *Bull. Seismol. Soc. Am.*, *92*(6), 2233–2250.

Toppozada, T. R., D. M. Branum, M. S. Reichle, and C. L. Hallstrom (2002), San Andreas Fault Zone , California : M ≥ 5.5 Earthquake History, *Bull. Seismol. Soc. Am.*, *92*(7), 2555–2601.

Chapter 2

Interseismic Coupling and Slow Slip Events on the Cascadia Megathrust, Implication for Seismic Hazard and SSE Dynamics

Abstract

In this study we model geodetic strain accumulation along the Cascadia subduction zone between 2007.0 and 2017.632 using position time series from 352 continuous GPS stations. First, we use the secular linear motion to determine interseismic locking along the megathrust. We determine two end member models, assuming that the megathrust is either *a priori* locked or creeping, which differ essentially along the trench where the inversion is poorly constrained by the data. In either case, significant locking of the megathrust updip of the coastline is needed. The downdip limit of the locked portion lies ~20 to 80 km updip from the coast assuming a locked *a priori*, but very close to the coast for a creeping *a priori*. From the resulting pattern of interseismic coupling, a seismic potential analysis based on a moment budget approach indicates that a maximum magnitude earthquake of the order of M_w9.0, with a return period of 263 yrs, is needed to balance the moment budget. This lends additional support to the interpretation that the tsunami recorded on the coast of Japan in the XVIII century was caused by a M~9 originated from Cascadia. Second, we use a variational Bayesian Independent Component Analysis (vbICA) decomposition to model geodetic strain time variations, approach which is effective to separate the geodetic strain signal due to non-tectonic and tectonic sources. The Slow Slip Events (SSEs) kinematics is retrieved by linearly inverting for slip on the megathrust the Independent Components related to these transient phenomena. The procedure allows the detection and modelling of 64 SSEs which spatially and temporally match with the tremors activity. SSEs and tremors occur well inland from the coastline and follows closely the estimated location of the mantle wedge corner. The transition zone, between the locked portion of the megathrust and the zone of tremors, is creeping rather steadily at the long-term slip rate and probably buffers the effect of SSEs on the megathrust seismogenic portion. The moment-duration distribution of SSEs indicates a $M_0 \propto T^3$ scaling, and the moment-area distribution a $M_0 \propto A^{3/2}$ scaling. Both scaling laws are similar to regular earthquakes.

1. Introduction

The Juan de Fuca (JdF) plate subducts beneath the North American plate along the Cascadia megathrust off the coast of southwestern Canada and northwestern United States (Figure 2.1). This subduction system is a typical warm case example, due to the subducting plates young age (<10 Ma) and moderate convergence rates (27-45 mm/yr) [e.g., *Hyndman et al.,* 1997; *DeMets and Dixon*, 1999].

The Cascadia megathrust hosted a $M\sim9$ earthquake in 1700, producing a tsunami that was reported in Japan [*Satake et al.,* 2003]. Additional $M\sim9$ in the last 10 000 years have been documented from turbidite sequences [*Goldfinger et al.,* 2017], tsunami deposits and coastal geological evidence [*Atwater,* 1987; *Clague and Bobrowsky,* 1994; *Atwater and Hemphill-Haley,* 1997; *Kelsey et al.,* 2005; *Wang et al.,* 2013; *Kemp et al.,* 2018]. However, since 1700, the megathrust has remained relatively silent. At present, the background seismicity is very quiet except at its Northern and Southern ends [*Wang and Trehu,* 2016]. The interseismic loading retrieved from surface geodetic measurements allowed to estimate the degree of locking of the megathrust and create maps of interseismic coupling (defined as the ratio of slip deficit rate along the megathrust, determined from the geodetic interseismic data, and the long-term slip rate). Interseismic coupling maps are useful for seismic hazard assessment as locked portions of the megathrust are indeed expected to potentially slip in large interplate earthquakes as has been observed in several seismically active regions [e.g., *Chlieh et al.,* 2008; *Moreno et al.,* 2010; *Loveless and Meade*, 2011]. Previous inversions of geodetic strain rate measured onshore indicate that the megathrust is locked to some degree in the interseismic period [*Hyndman et al.,* 1997; *Wang et al.,* 2003]. The locked portion of the plate interface presumably unlocks during the $M\sim9$ events. Our knowledge of the spatial distribution of locking of the plate interface in the interseismic period is however limited in particular due to the absence of constraints from sea-bottom geodesy. The seismic hazard associated with the Cascadia Megathrust is therefore poorly constrained despite the profusion of available data, geodetic in particular, and is a well suited target to apply the methods described in Michel *et al.* [2017] (Chapter 1). To do so we need the pattern of interseismic coupling on the megathrust and associated uncertainties as an input. This requires determining the secular geodetic strain signal associated with locking of the plate interface.

We use the secular velocity field from 352 continuous GPS (cGPS) stations corrected for post-glacial rebound using the model of *Peltier et al.* [2015], to determine an interseismic coupling map for the 2007-2017 period. We also determine temporal variations of slip along the megathrust over that time period to clarify the relative position of the portions of the megathrust that are locked in the interseismic period and those that are producing transient slip events. The geodetic position time series from Cascadia show strong temporal variations which indicate episodic aseismic slip events, commonly called Slow Slip Events (SSEs) [*Dragert et al.,* 2001; *Miller et al.,* 2002]. These slip events are mostly aseismic but are correlated in time and space with tremors, [*Rogers and Dragert,* 2003; *Wech and Bartlow,* 2014] which presumably occur on the plate interface [*Wech and Creager,* 2007]. It is therefore likely that SSEs are related to episodic slip along the megathrust. SSEs are however not the only source of variation of the geodetic time-series from their secular trend. These variations can be related to various causes. The larger earthquakes in the area may have caused some offsets and transient post-seismic deformation. The geodetic time series also show variations that are seasonal and likely due to surface load variations as has been observed in various other settings [*Blewitt et al.,* 2001; *Bettinelli et al.,* 2008; *Fu et al.,* 2012]. Temporal variations in geodetic series can also be spurious due to the ITRF realisation generally used to express position in a global reference frame [*Dong et al.,* 2002].

In this study we analyse the geodetic position time series from Cascadia with the objective of separating the terms due to the various temporally varying factors and to interseismic coupling. To that effect, we apply to the detrended position time series a variational Bayesian Independent Component Analysis (vbICA) [*Choudrey and Roberts*, 2003], a signal processing technique which has proven to be effective in extracting different sources of deformation (afterslip, SSEs, and seasonal signals) in geodetic time series [*Gualandi et al.,* 2016; 2017a; 2017b; 2017c]. We next perform an inversion of the Independent Components (ICs) related to SSEs, following the general approach of the Principal Component Analysis-based Inversion Method [*Kositsky and Avouac*, 2010]. With this vbICA-based Inversion Method, (vbICAIM), we produce a kinematic model of the spatio-temporal variation of slip on the Megathrust from 2007 to 2017. We also determine the pattern of interseismic coupling along the megathrust from inverting the secular geodetic signal due to interseismic strain.

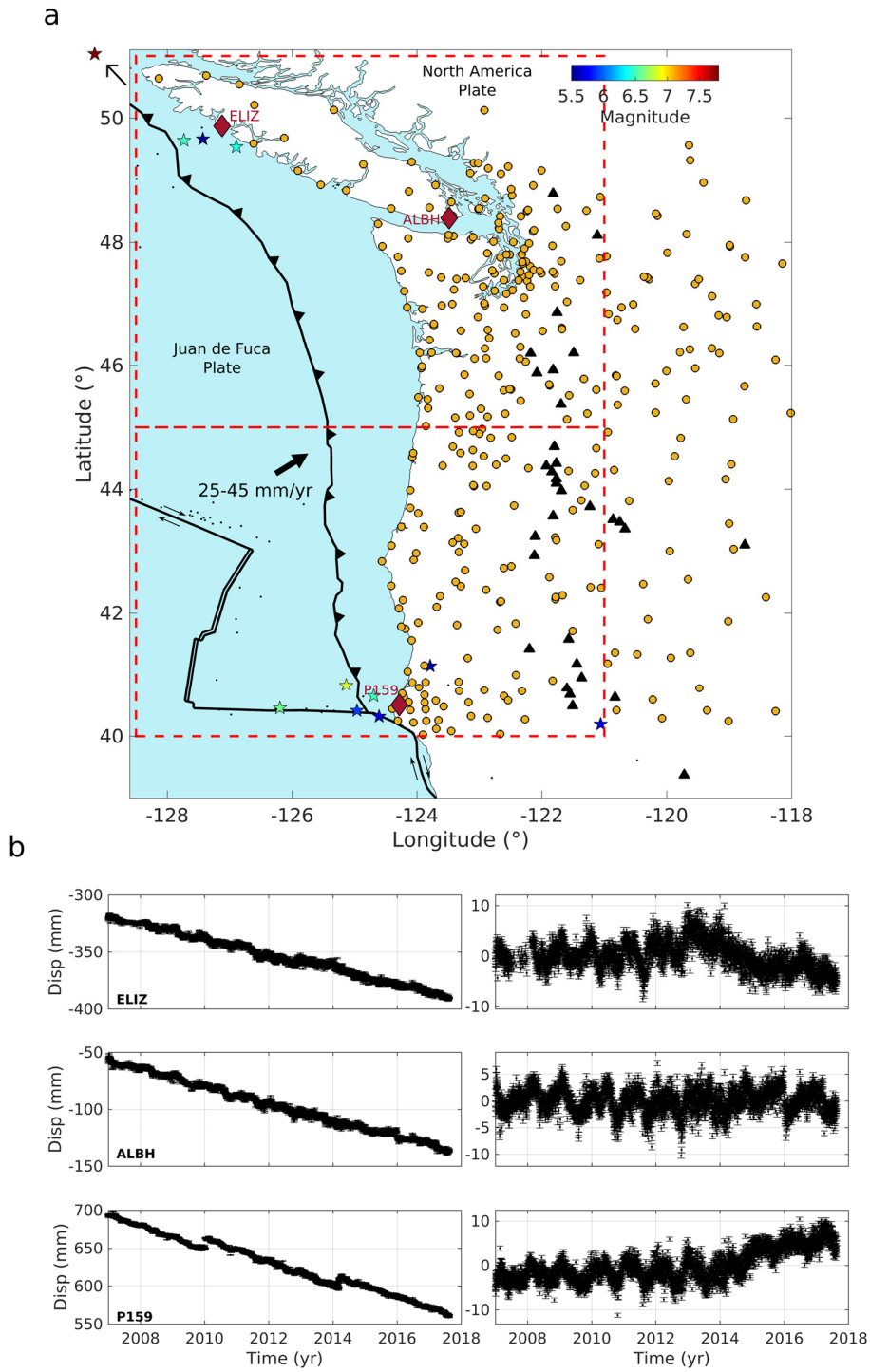

Figure 2.1. *(a) Distribution of GPS stations (yellow dots) along the Cascadia subduction zone. The black lines are the plate boundaries, and the black triangles indicate active volcanoes locations (USGS). The black dots indicate M5.5+ seismicity from 1984 to 2017 (ANSS catalogue). The stars indicate the 11 earthquakes that affected the GPS stations, the colour indicating their magnitude. The red diamonds indicate, from North to South, the location of the stations ELIZ, ALBH and P159. The two dashed red rectangles delimits the North and South sections as indicated in section 3.1.2. (b) Left panels indicate the raw time series of the East component for the stations ELIZ, ALBH and P159. The right panels show the detrended, time series of those 3 stations corrected for offsets and regional tectonics using the block-model of [Schmaltze et al., 2014].*

The remaining of the manuscript is organized as follows. We first introduce the data considered in this study in Section 2. We then describe how we extract the signals related to the different sources of interest. In Section 4 we present the results of the inversions to retrieve interseismic coupling and the SSEs kinematics, respectively. In Section 5 we discuss the implications of our kinematic model for SSEs dynamics. In Section 6 we look at the implications of our kinematic model for seismic hazard based on the moment budget approach of Michel *et al.* [2017] (Chapter 1). Final remarks and further discussions conclude the manuscript.

2. Data

2.1. GPS POSITION TIME SERIES

We use daily sampled position time series in the IGS08 reference frame from the Pacific Geodetic Array (PANGA) and the Plate Boundary Observatory (PBO) maintained by UNAVCO and processed by the Nevada Geodetic Laboratory (http://geodesy.unr.edu, last access August 2017). Most of the available continuous GPS (cGPS) stations were deployed in 2007, and we consider the time range spanning 2007.0 to 2017.632. We use only time series with at most 40% of missing data, and we exclude all the stations in the proximity (<15 km) of volcanoes to avoid contamination by volcanic signals. We also discard station BLYN because of spurious large displacements of unknown origin that were clearly not observed at nearby stations. The final selection includes N_{GPS} = 352 cGPS stations (Figure 2.1.a). We then refer all the stations to the North America reference frame using the regional block model of Schmaltze *et al.* [2014]. The position time series are then organized in a MxT matrix X_{obs}, where $M = 3xN_{GPS}$ is the total number of time series (East, North, and Vertical direction per each station), and T = 3883 is the total number of observed epochs.

2.2. TREMOR AND SEISMICITY DATA

Two tremor catalogues are used in this study, one from Ide [2012] between 2007 and 2009.595, and one from the Pacific Northwest Seismic Network (PNSN) catalogue from 2009.595 to 2017.632 (https://pnsn.org/tremor). We use the ANSS catalogue of instrumental seismicity, taking M>0 events from 1984 to 2018.222. We select all the events within 5 km

from the fault geometry given by McCrory *et al.* [2012]. We end up with 2188 earthquakes (Figure 2.S1), with magnitudes ranging from 0.19 to 6.5. The maximum curvature method [*Wiemer and Wyss*, 2000] and Bender's formula [*Aki*, 1965; *Utsu*, 1966; *Bender*, 1983] are used to estimate the magnitude of completeness and the *b*-value, respectively. The estimated magnitude of completeness is increased by 0.2 to compensate a methodological bias of the method [*Woessner and Wiemer*, 2005], resulting to a value of 2.09. The *b*-value is estimated at 0.87±0.03.

For our moment budget analysis we additionally use the paleo-earthquake catalogue from Goldfinger *et al.* [2012], which is based on turbiditic sequences observed in drillcore and seismic profiles collected off the coast of Cascadia. With these observations, Goldfinger *et al.* [2012] were able to estimate the time and magnitude of the $\sim M$+9 earthquakes over the last 10 000 years. We understand that the estimated magnitudes need to be considered with caution as they are based only on the estimated rupture length derived from correlating the paleoturbidites at different locations.

3. Methodology

Our goal is to retrieve: i) the secular strain rate due to the average pattern of locking of Cascadia's megathrust, and ii) the SSEs history on the megathrust in the considered time span.

To attain our first goal, we use the long-term linear trend estimated from a 'trajectory' model (Equation 2.S1) in which each position time series is modelled using a combination of predetermined functions. We use a linear combination of a linear trend, annual and semi-annual terms, co-seismic step functions and exponential post-seismic functions. This approach provides a reasonable estimate of the linear trend with limited bias introduced by the non-linear terms. We do not model at this step the SSEs, but they do have a limited influence on the secular motion estimate since their typical returning period is much smaller than the overall observed time span, as it will be verified a posteriori. The secular geodetic velocities estimated from this approach are used to determine interseismic locking ratio on the Cascadia megathrust (Section 4.1). We use the long-term linear trend and the offsets that are simultaneously estimated by the trajectory model (Equation 2.S1 and Supplementary Material S1) to correct the position time series. These time series are then the input for the variational Bayesian Independent Component Analysis (vbICA) algorithm. A brief description

of the vbICA algorithm is offered in the next Section 3.1.1. We then describe its application to the extraction of post-seismic relaxation (Section 3.1.2), seasonal deformation (Section 3.1.3), and SSEs displacement (Section 3.1.4).

3.1. SSE SURFACE DEFORMATION EXTRACTION

3.1.1. *vbICA algorithm*

The vbICA algorithm allows the centered position time series (X) to be reconstructed by a linear combination of a limited number (R) of Independent Components (ICs). The centring step is performed by removing from a time series its mean value. Each IC is fully characterized by a spatial distribution (U_r), a temporal function (V_r), and a relative weight (S_r). None of these quantities is a priori determined, allowing the data to reveal their inner structure. These quantities are organized in matrices such that the following approximation holds [*Gualandi et al.,* 2016]:

$$X_{M\times T} \approx U_{M\times R} S_{R\times R} V^T_{R\times T} + N_{M\times T} \tag{2.1}$$

where U and V have unit norm columns, S is a diagonal matrix, and N characterizes the noise, assumed to be Gaussian. Recall $M = 3xN_{GPS}$ is the total number of time series (East, North, and Vertical direction per each station), and $T = 3883$ is the total number of observed epochs. This notation is similar to that of Principal Component Analysis (PCA), but here the constraint of orthogonality between the columns of U is relaxed, as well as between the columns of V. The vbICA algorithm assumes that i) a finite number of sources generates the observed data, ii) these sources are mixed linearly, and iii) the probability density function (pdf) related to the temporal evolution of a source is statistically independent from the pdfs of the other sources. The vbICA technique then allows us to determine the best reference frame onto which project the data in order to optimally separate the contribution of each singular source. Moreover, any ICA algorithm is not aiming at the diagonalization of the variance-covariance matrix of the data, as in a PCA, and thus the diagonal values in S do not represent a percentage of the dataset variance explained. Both U and V are non-dimensional, while S and N are in the same unit as X (mm). In contrast to standard ICA algorithms [e.g., FastICA, Hyvarinen and Oja, 1997], vbICA allows for more flexibility in the description of the temporal sources V since it can model multimodal time function distributions. More details can be found in Gualandi *et al.* [2016] and references therein.

3.1.2. *Post-seismic relaxation*

The largest deformation signal in the corrected position time series is due to post-seismic relaxation following the earthquakes listed in Table 2.1.

Table 2.1. *Earthquakes affecting GPS time series from the North and South section [USGS].*

Section	Magnitude	Year	Month	Day	Latitude	Longitude	Depth
North	6.4	2011	9	9	49.535	126.893	22
	7.8	2012	10	28	52.788	132.101	14
	5.5	2013	8	4	49.661	127.429	10
	6.5	2014	4	24	49.639	127.732	10
South	6.5	2010	1	10	40.652	124.693	28.7
	5.9	2010	2	4	40.412	124.961	23
	5.6	2012	2	13	41.143	123.79	27.4
	5.7	2013	5	24	40.192	121.06	8
	6.8	2014	3	10	40.829	125.134	16.4
	5.7	2015	1	28	40.318	124.607	16.9
	6.6	2016	12	8	40.454	126.194	8.5

Due to the complexity of the tectonically active region in the proximity of northern Vancouver island in the North, and in the proximity of the triple junction in the South (Table 2.1), it is challenging to obtain a clean source separation using the data from the entire network of stations. A first attempt to apply the vbICA to the whole dataset did not bring a clean separation between post-seismic events occurring at the northern and southern edges of the subducting plate. We therefore decided to first divide the study area into two sectors, split by the latitude 45° and limited to the east by the longitude -121°, as shown in Figure 2.1.a.

We run a first vbICA on each section in order to extract the post-seismic deformation, and we retrieve 8 and 6 ICs for the northern and southern section, respectively (Figures 2.2 and 2.3). The amount of variance explained by the decomposition is over 68.27%, considered here as a threshold for the selection of the number of components to be retained. For the southern section, we interpret IC1 and IC2 as related to post-seismic deformation in the region. The temporal functions show clear non-linear patterns starting at the time of occurrence of the large earthquakes (Figure 2.3). Moreover, their spatial functions (U) show a signal localized in the south-western section, in the proximity of the earthquake epicentres. The same argument is valid for the analysis of the northern section, where IC1 and IC2 are interpreted as post-seismic sources (Figure 2.2). We admit that we cannot isolate the contribution of every single

post-seismic deformation episode, and certainly there is cross-talk between the post-seismic ICs. Nonetheless, due to the spatially localized responses, we are confident that the information thus extracted is referring to the post-seismic deformation.

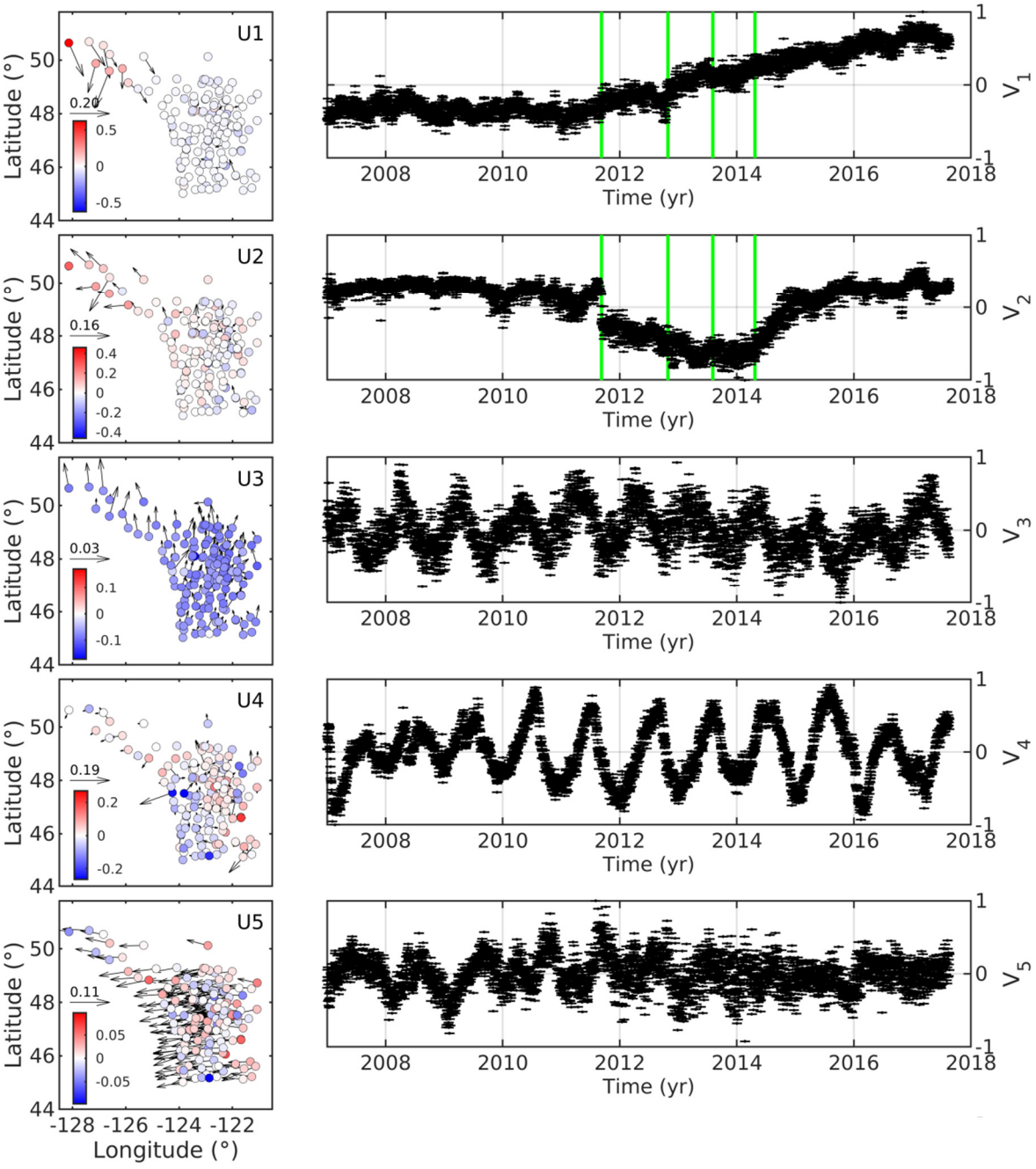

Figure 2.2. *Spatial and temporal functions of the independent components obtained from applying a vbICA decomposition to the data from the Northern area (see location in Figure 2.1) for 8 components. The left panels show the spatial functions (matrix U). The arrows and the colored dots indicate horizontal and vertical motion, respectively. The right show the temporal functions (matrix V). The green lines indicate the timing of the earthquakes of the northern section as indicated in Table 2.1. We consider components 1 and 2 to be related to postseismic displacements following earthquakes in the North (Figure 2.1 and Table 2.1).*

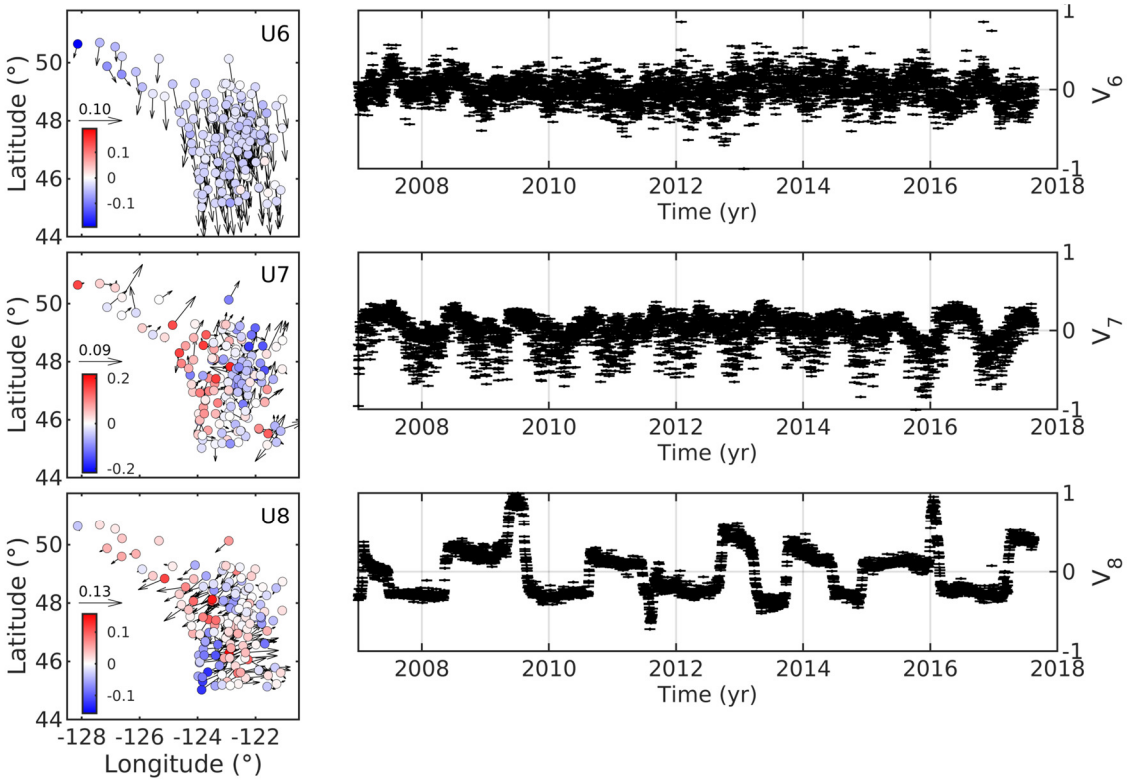

Figure 2.2. *(continued)*

In the South, six M5.5+ events (Table 2.1) have visibly induced detectable geodetic signals (stars in Figure 2.1.a and green dashed lines in Figure 2.2) and all are strike-slip events (USGS). In the North, similarly, three strike slip M5.5+ earthquakes have occurred and affected GPS stations (Table 2.1, Figure 2.1.a and 2.3). There is one $M7.8$ with a reverse mechanism that occurred in 2012 (Table 2.1, star out of frame in Figure 2.1.a and Figure 2.3), which might have induced post-seismic deformation on the megathrust or on a crustal fault of the North American plate [*Hayes,* 2017]. The mainshock occurred 363 km from the closest GPS station (HOLB). Its rupture extended ~100-150 km along strike. This event seems to have affected the northernmost stations. In either case we make a distinction between afterslip and SSEs and thus correct our dataset X for the displacement associated with all the retrieved post-seismic ICs. The stations corrected for post-seismic deformation are listed in Table 2.S1. They are the stations which are visually the most affected.

3.1.3. *Seasonal deformation*

After the removal of post-seismic deformation, the largest source of deformation is due to seasonal effects. Several mechanisms can be at the origin of seasonal deformation, but the

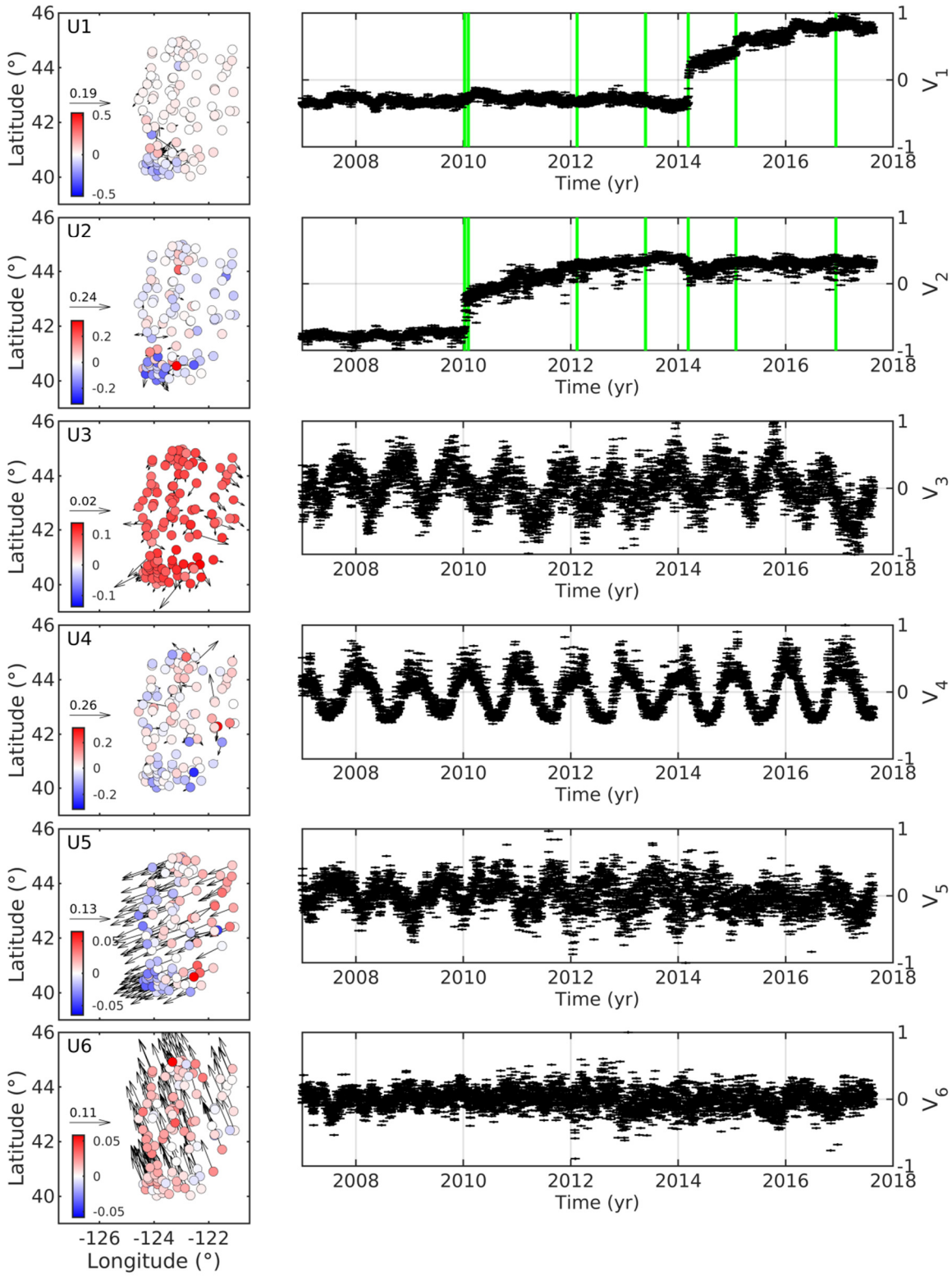

Figure 2.3. *Spatial and temporal functions of the independent components obtained from applying a vbICA decomposition to the data from the Southern area (see location in Figure 2.1) for 6 components. The left panels show the spatial functions (matrix U). The arrows and the coloured dots indicate horizontal and vertical motion, respectively. The right panels indicate the components temporal evolution (matrix V). The green lines indicate the timing of the earthquakes of the southern section as indicated in Table 2.1. We consider components 1 and 2 to be related to postseismic displacements following earthquakes in the South (Figure 2.1 and Table 2.1).*

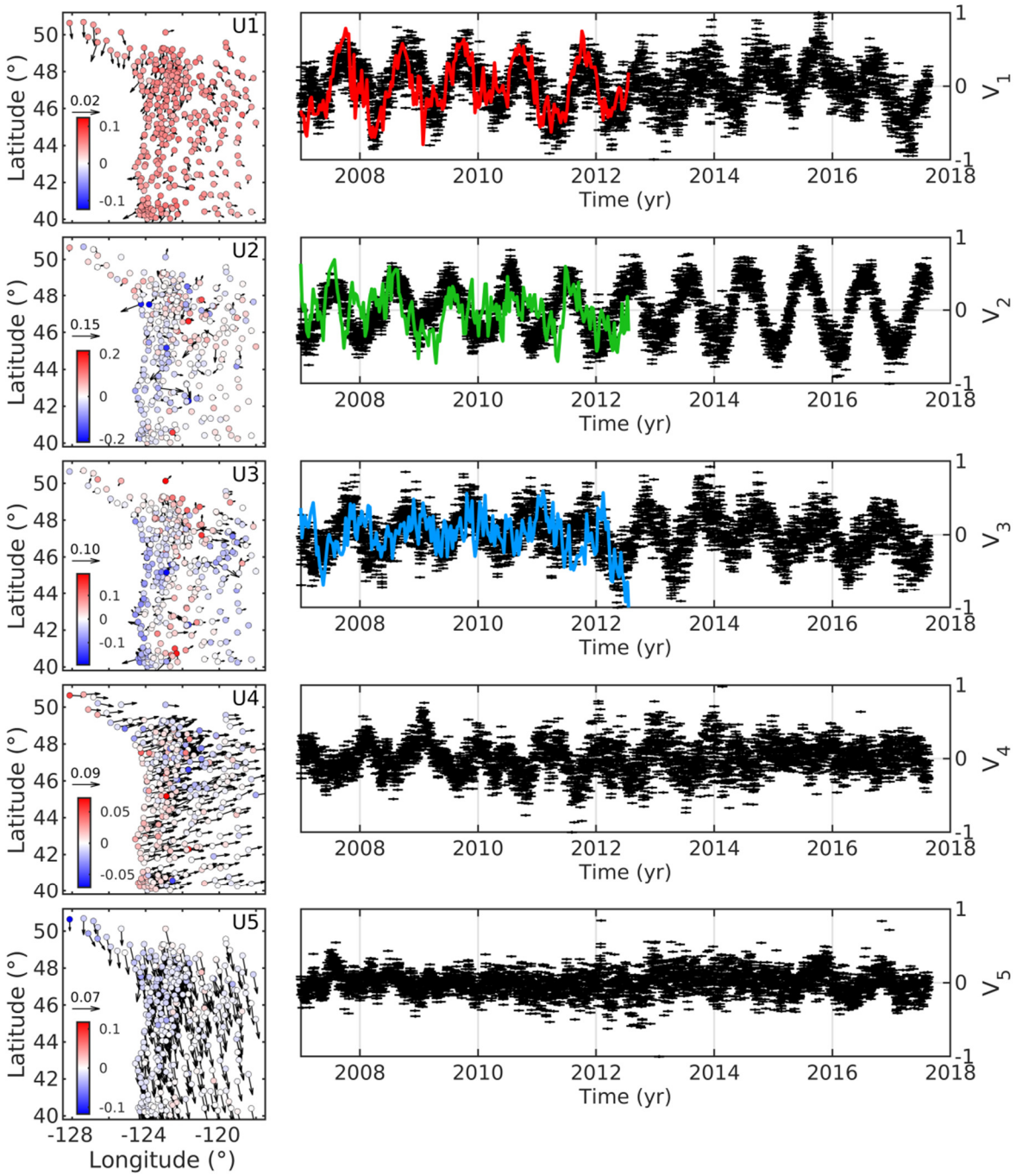

Figure 2.4. *Spatial pattern and temporal evolution of each component of an 11-component decomposition (section 3.1.3.). The left panels show the spatial pattern (matrix U). The arrows and the coloured dots indicate horizontal and vertical motions, respectively. The right panels show the components temporal functions (matrix V). . The red, blue and green lines in the temporal evolution of components 1, 2 and 3 correspond to the temporal evolution of the components 1, 3 and 2, obtained from the decomposition of the theoretical geodetic time-series due to surface load variations derived from GRACE. For clarity they are plotted (right panels) separately and together with the temporal function of their associated components derived from the GPS time series (black dots). We consider components 1 to 3 to be seasonal deformation, 4 and 5 to be common mode, 6 to be a local effect, 7 to be seasonal scattered noise and 8 to 11 to be related to SSEs.*

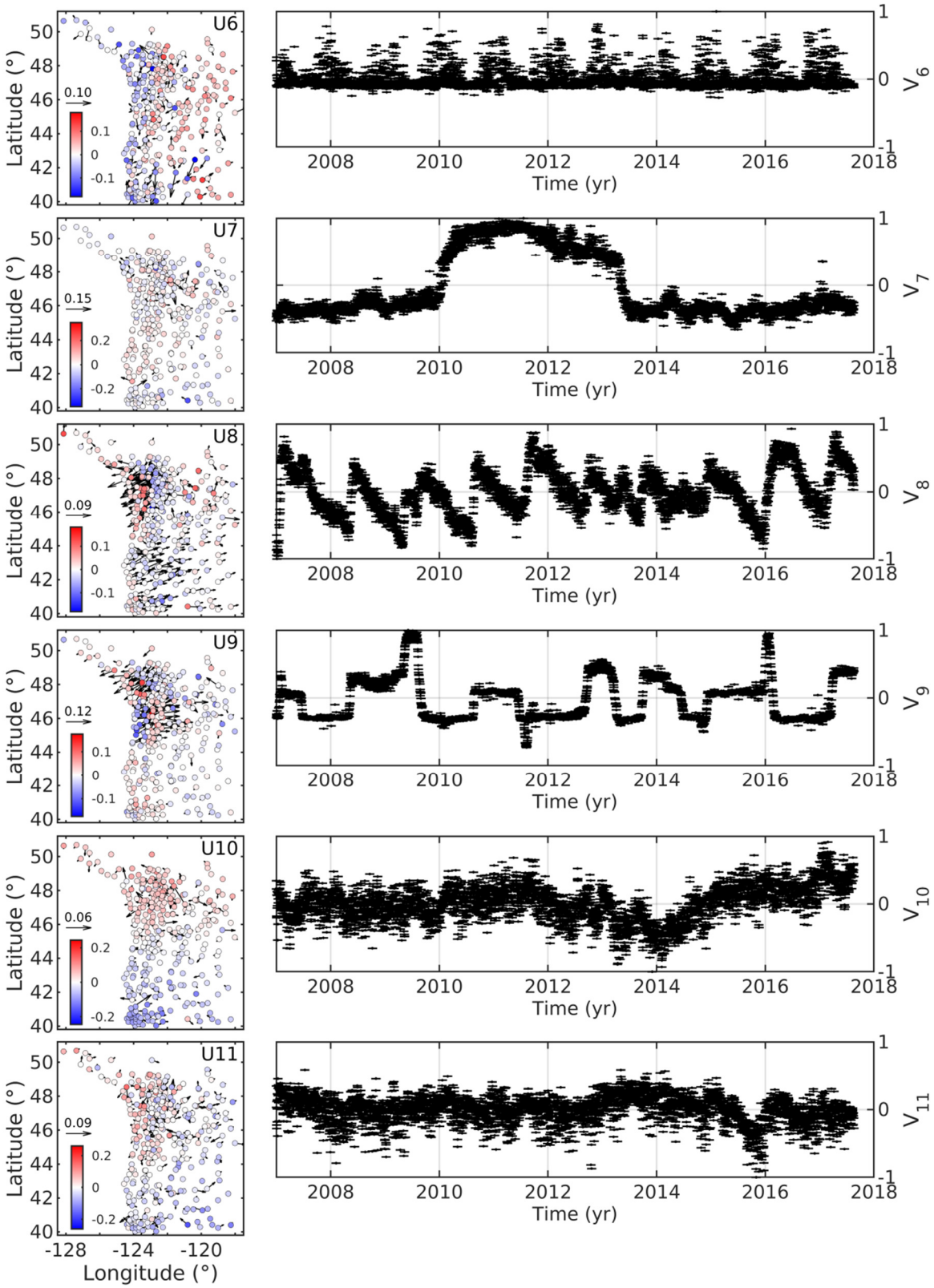

Figure 2.4. *(continued)*

strongest is related to the load induced by surface mass variations [e.g., *Blewitt et al.,* 2001; *Dong et al.,* 2002; *Bettinelli et al.,* 2008]. Thanks to satellite gravity records from the Gravity Recovery and Climate Experiment (GRACE) [*Tapley et al.,* 2004], it is possible to estimate the

load in Equivalent Water Thickness (EWT). From this dataset, and assuming a certain composition of the Earth, it is possible to model the predicted seasonal deformation due to this source [e.g., Chanard *et al.,* 2014, 2018]. We perform a vbICA on both the GPS position time series and the deformation predicted from the GRACE data at the same locations (Figure 2.4). From the GPS decomposition, the 68.27% of the amount of variance explained threshold is reached taking 11 components. We identify components 1, 2 and 3 as seasonal sources of deformation. A decomposition with 3 ICs on the GRACE-derived time series explains 100% of the variance. A comparison of the temporal evolution of the GPS-derived and GRACE-derived ICs shows a good correlation (>60%) between the first GPS-derived and GRACE-derived components (Figure 2.4) (Table 2.S2). We conclude that the first GPS-derived component is most likely associated with hydrological loading. The other two seasonal GPS-derived components have poor correlations with any GRACE-derived component and thus cannot be interpreted as related to surface hydrology. Their origin is unknown and might be due to other seasonal non-tectonic effects here not taken into account (e.g. thermal strain [*Xu et al.,* 2017]). Given the uniform spatial pattern of ICs 4 and 5 (Figure 2.4), we make the hypothesis that they are related to a network Common Mode Error (CME). IC6 (Figure 2.4) can be described as a seasonal scatter, potentially due to the effect of snow and consequent multipath, and is considered as noise. The spatial pattern of IC7 (Figure 2.4) is very localized and we assume that it is a local effect. The deformation related to the ICs from 1 to 7 is thus removed from the time series, which have at this point been corrected from inter-block motion, long-term linear tectonic motion, co-seismic and instrumental offsets, post-seismic relaxation, seasonal signals, network errors and local effect deformations. Those are strong signals, compared to the signals related to SSEs, and would corrupt the extracted SSEs signals (Section 3.1.4) if not removed before hand.

3.1.4. *SSEs displacement*

Finally, we apply a vbICA on the residual displacement time series. The SSEs signal is buried in the noise, and the percentage of variance explained grows very slowly as the number of components increases. The number of components is chosen based on the Negative Free Energy (NFE) of the decomposition, which balances the fit to the data and the complexity of the model [*Choudrey and Roberts,* 2003; *Gualandi et al.,* 2016]. The NFE indicates how close the approximating probability density function (pdf) of the hidden variables of the model is

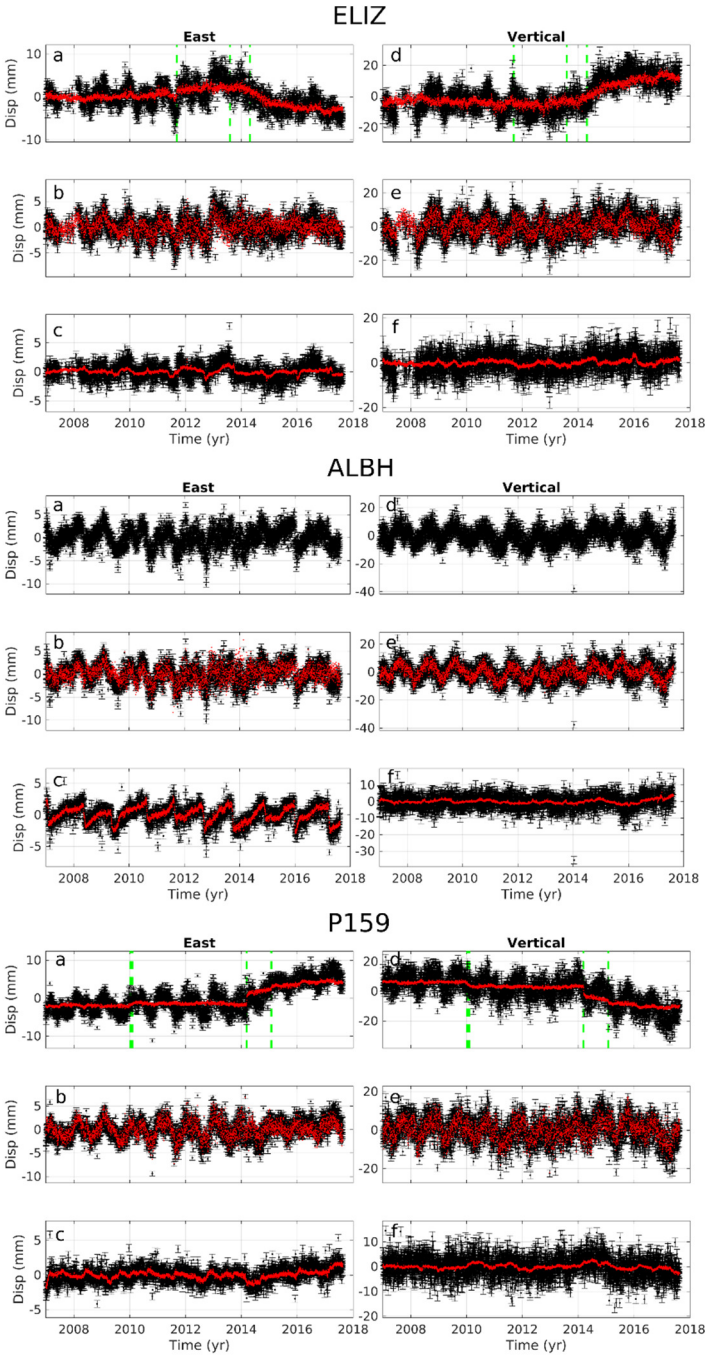

Figure 2.5. *Comparison between the corrected GPS time series used as input for the vbICA decomposition and the modeled signal for station ELIZ, ALBH and P159, at each correction step (sections 3.1.2., 3.1.3. and 3.1.4.). The left and right panels indicate the East and vertical directions of the GPS time series, respectively. For each station, (a) and (d) shows the detrended GPS time-series (black dots and associated errorbars) and the displacement modelled from the ICs related to postseismic deformation (red line). (b) and (e) shows the detrended GPS time-series corrected from postseismic displacement (black dots and associated errorbars) and the displacement modelled from the ICs related to noise, and seasonal and local effects deformations (red line). (c) and (f) shows the detrended GPS time-series corrected from noise and postseismic, seasonal and local effects deformation (black dots and associated errorbars) and the displacement modelled from the ICs related to SSEs (red line). ALBH has no postseismic ICA model since we did not correct any postseismic deformation at this station.*

to the true posterior pdf. When the NFE reaches its maximum value, the Kullback-Leibler divergence between the aforementioned pdfs is minimum. When passing from 32 to 33 ICs the NFE decreases, and we thus select 32 components for our final decomposition (Figure 2.S2). Among these 32 ICs, we ascribe 15 of them to the kinematics of SSEs (components 1 to 15 in Figure 2.S3). The remaining 17 sources are considered as either noise (components 16 to 25) or local effects (components 26 to 32) (Figure 2.S3).

The comparison between the GPS position time series and the vbICA reconstruction at each extraction step (i.e. section 3.1.2., 3.1.3. and 3.1.4.) is shown in Figure 2.5 for the 3 stations indicated in Figure 2.1.

4. Kinematic Inversions

4.1. COUPLING MAP INVERSION

We perform a static inversion of the velocity field estimated from the trajectory model. We correct the long-term linear trends from post-glacial rebound displacements using estimations from Peltier *et al.* [2015] (Figure 2.7.e). We use a downsampled version of the fault geometry determined by McCrory *et al.* [2012]. The total number of subfaults is $P = 3339$, and they have triangular shape, with a characteristic length of ~15 km. The Green's functions are calculated using Okada [1992] dislocation model. We use the same regularisation scheme of Radiguet *et al.* [2011], which allows to give an interseismic back-slip *a priori* model as input. Two *a priori* interseismic back-slip models are tested, one with a fully locked fault (coupling equal to 1), and the other with a fully creeping fault (coupling equal to 0). We expect the poorly resolved areas, specifically near the trench where no data is available, to stay near the *a priori* model. Those two *a priori* models define thus the 2 extreme cases where the fault trench is either fully locked or creeping. A rake direction constraint is imposed using the plate rate direction from Schmalzle *et al.* [2014] block model. We adopt as smoothing parameter the *a priori* uncertainty on the model parameters σ_0, while fixing the correlation distance λ to

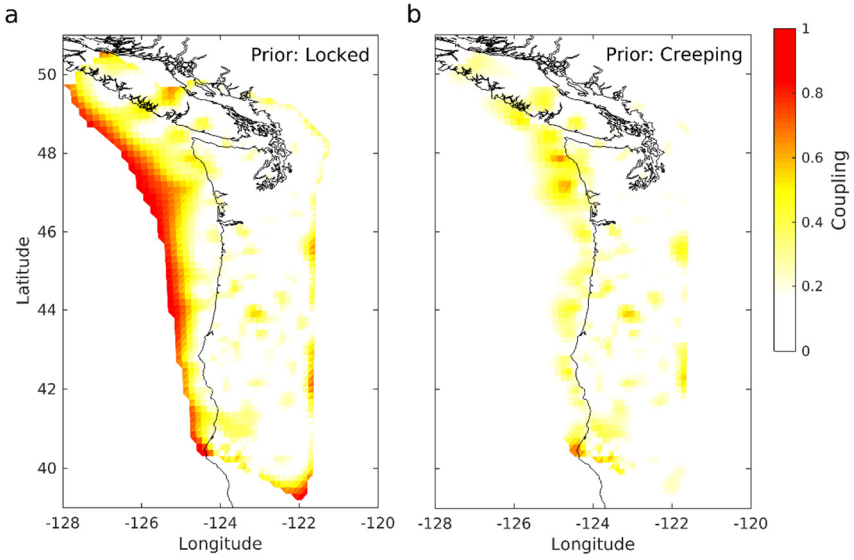

Figure 2.6. Interseismic *coupling maps obtained with different a priori hypothesis on fault coupling. Interseismic coupling is defined as the ratio of the slip rate deficit derived from the modeling of interseismic geodetic strain over the long-term slip rate on the megathrust predicted by the block-model. (a) The megathrust is assumed fully locked a priori. (b) The megathrust is a priori assumed to be creeping at the long-term slip rate. The black line corresponds to the coastline.*

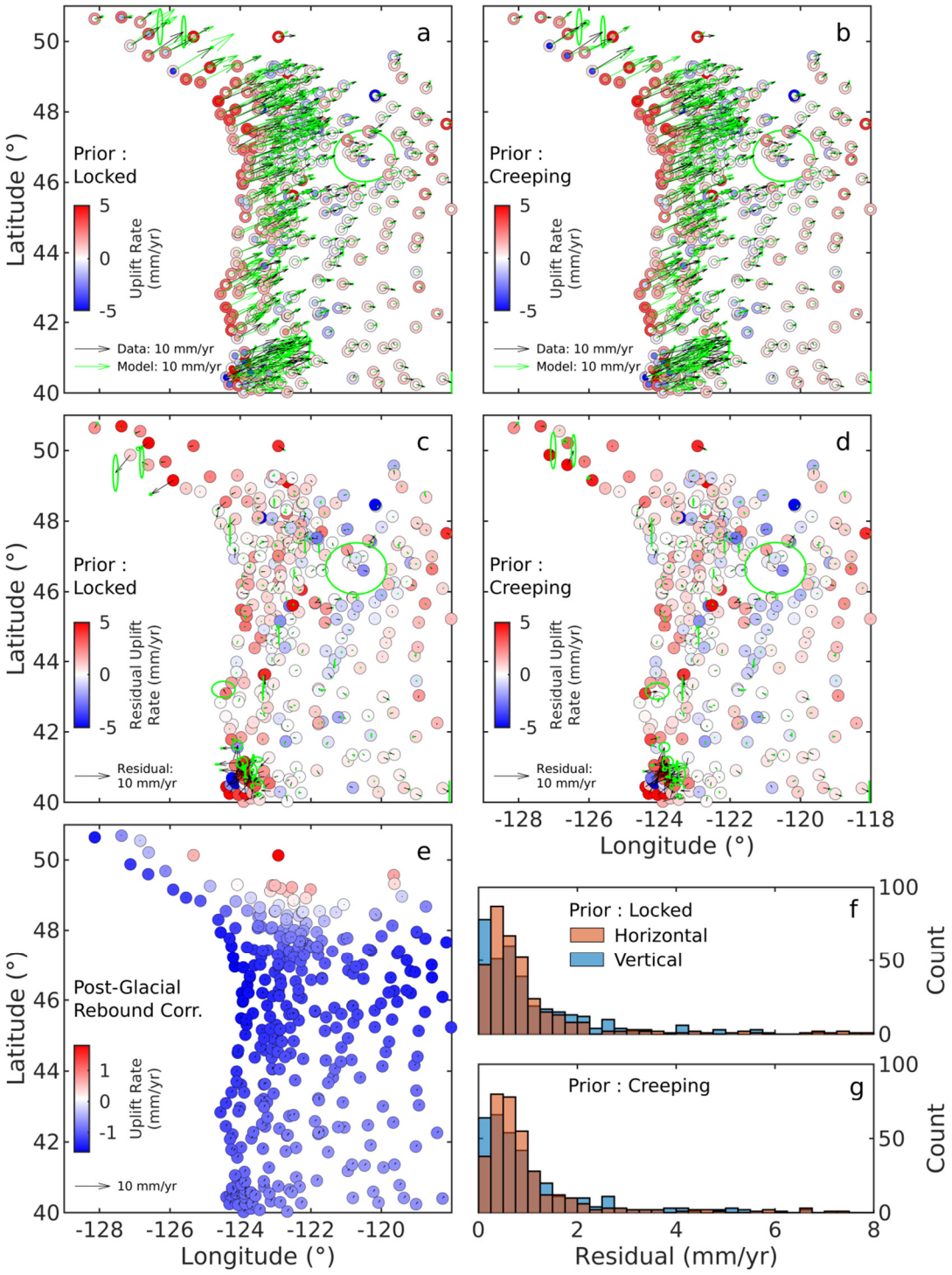

Figure 2.7. *(a) and (b) show the comparison between the observed and modeled secular rates for the models assuming a priori that the megathrust is locked and creeping, respectively. (c) and (d) show the corresponding residuals assuming locking or creep a priori, respectively. (e) shows the post-glacial rebound correction based on Peltier et al [2015]. The arrows and the colored dots indicate horizontal and vertical motion, respectively. The inner and outer dots in (a) and (b) represent the data and model vertical secular rates, respectively. The green ellipses indicate 1-sigma uncertainties. (f) and (g) show histograms of the residuals assuming locking or creep a priori, respectively.*

the average patch size. Taking the locked *a priori* model, varying σ_0 produces the L-curve shown in Figure 2.S4. We select $\sigma_0=10^{-0.1}$ for our preferred inversion that yields the best trade-off between misfit and smoothness of the slip distribution. We use the same parametrisation for the creeping *a priori* model. We calculate the interseismic coupling map dividing each sub-fault's back slip rate, given by the inversion, by its associated block model plate rate. The coupling maps for the two cases are given in Figure 2.6. The fit to the data and the residuals are shown in Figure 2.7. The resolution and restitution maps are shown in Figure 2.S5. Test on the inversion sensitivity are shown in Figure 2.S6.

The two interseismic coupling maps (Figure 2.6) show a partially locked shallow portion of the fault. The position of the locked zones, however, differs from one model to the other. Interestingly, the *a priori* fully creeping fault has locked areas that are closer to the coast than the *a priori* fully locked fault.

4.2. SSES INVERSION

Once the surface deformations associated with the SSEs are isolated, we perform a static inversion of the spatial distribution related to the 15 extracted temporal functions. This approach follows the one adopted in Gualandi *et al.* [2017a, 2017b, 2017c]. The principle is the same as the one described in Kositsky and Avouac [2010], but a vbICA is replacing the PCA decomposition of the data. We invert the selected ICs on the same geometry used for the interseismic velocities, and we adopt the same regularisation scheme. A null a priori model is imposed, which implies that we expect a null a posteriori solution where the data do not require for slip on the fault. No constraints on the rake direction are imposed. Varying σ_0 produces the L-curve shown in Figure 2.S7. We select $\sigma_0=10^{-1.5}$ for our preferred inversion that yields the best trade-off between misfit and smoothness of the slip distribution. We invert the 15 ICs using the same parametrisation for each IC and recombine them linearly.

We thus obtain the spatio-temporal evolution of slip deficit related to SSEs ($\delta_{deficit}(p,t)$) with respect to the long-term slip deficit given by the locking ratio (see Section 4.1). In order to get a coherent slip deficit rate ($\dot{\delta}_{deficit}(p,t)$) time evolution ($t$ = 1, ..., T) on each sub-fault (p = 1, …, P), we take the time derivative of the low-pass filtered slip deficit. In particular, we apply an equiripple low-pass filter with passband frequency of 1/21 days^{-1}, stopband of 1/35 days^{-1}, passband ripple of 1dB with 60dB of stopband attenuation. If the slip deficit increases

on a given patch (i.e., positive slip deficit rate) then that patch is accumulating strain, i.e. it is loading. When the slip deficit decreases (i.e., negative slip deficit rate), then the patch undergoes slip. SSEs thus correspond to time periods of negative slip deficit rate. A movie of the SSEs kinematics is available in the supplement (Movie 2.S1). Tests on the inversion sensitivity are shown in Movie 2.S2, 2.S3 and 2.S4.

5. SSEs analysis

5.1. SSE SPATIAL AND TEMPORAL DETERMINATION

To isolate each SSE in space and time, we proceed as follow. We consider only periods where slip deficit rate is negative, thus associated with the SSEs unloading. To enable the detection of SSEs over the noise level of our kinematic model, we make the hypothesis that at a given epoch *t* a given sub-fault *p* is experiencing an SSE if $\dot{\delta}_{deficit}(p,t) < V_{thresh} = -40$ mm/yr. For the specific epoch under exam we identify all the sub-faults with slip rates below this threshold by applying a contour at V_{thresh}. The number of contours defines the number of SSEs occurring at time *t.* We do the same at time *t*+1 and verify which contours at time *t*+1 overlap with the contours at time *t*. If there is an overlap, we assume that they are the same SSE. For every SSE we thus automatically select a starting and ending time (t_k^{in} and t_k^{fin}, with *k* = 1, …, N_{SSEs}). Special cases can arise where a SSE splits itself or two SSEs merge together. In both scenarios, the SSEs at time *t* and *t*+1 are considered to be the same. With this procedure, we identify 119 potential SSEs between 2007 and 2017. From those 119, some involve only 1 or 2 sub-faults and are very short in time. We consider them as noise. We also remove any candidate under 60 km depth. Our final selection of SSEs gathers $N_{SSEs} = 64$ events shown in Figure 2.8.

With this procedure we are able to estimate the temporal and spatial evolution of each SSE. To get their moment rate function we proceed as follow. Since SSEs can migrate, we estimate the full area involved in the *k*-th event as the union of all the sub-faults participating to it, denoted by the set $\{s_k\} = \{p \mid \dot{\delta}_{k\,deficit}(p,t) < V_{thresh} \text{ for } t_k^{in} \leq t \leq t_k^{fin}\}$. However, the V_{thresh} parameter might truncate spatially and temporally our estimated SSEs. To relax slightly this constraint, we extend the spatial influence of each SSE to their neighbouring sub-

faults and extend their time delimitation by one day before and after. Note that during and within the area of influence of each SSE, the slip deficit rate of sub-faults can be negative or positive depending on the SSE's history of propagation. For one event, within its area of influence and time period, we calculate the moment rate function at time t, $\dot{M}_0(t)$, using the following equation:

$$\dot{M}_{0,k}(t) = -\sum_{s_k=1}^{S_k} \mu A_{s_k} \dot{\delta}_{k\ deficit}(s_k, t), \text{ for } t_k^{in} \leq t \leq t_k^{fin} \text{and with } k\text{=1, ..., } N_{SSEs} \qquad (2.2)$$

where μ is the shear modulus (here fixed to 30 GPa), S_k is the total number of sub-faults belonging to the k-th SSE's area of interest, A_{s_k} is the area of sub-fault s_k. The negative sign in front of the sum is added in order to have positive moment rates during SSEs, reference that we will keep for the rest of this study.

Applying this moment rate calculation methodology on the filtered $\delta_{deficit}$ described in section 4.2 (passband frequency of 1/21 days^{-1}, stopband of 1/35 days^{-1}) results, however, in very smoothed moment rate functions. To retrieve more detailed moment rate functions we perform instead a zero-phase digital filtering on the rough $\delta_{deficit}$ using a 8-days window, but focus only on the area and time period of each SSE as estimated before from the very smoothed data. The moment rate of each SSE acquired from the rougher version of $\delta_{deficit}$ is shown in Figure 2.8. Those moment rates do not take into account interseismic loading during SSEs. To estimate the uncertainty on the SSEs moment rate function we assume that it is represented by their short term variability before filtering. The uncertainties represented in Figure 2.8 are calculated based on the standard deviation of the mean on the rough version of $\delta_{deficit}$ using a 16-days moving window centered in the epoch of interest.

To evaluate SSEs propagation speed from our kinematic model, we estimate SSE propagation front locations as followed. A representative line of the average along-strike location of SSEs is first chosen (red line in Figure 2.9.a, Table 2.S3). The intersection between this line and the contour of the cumulative slip area of SSEs at each time step ($\dot{\delta}_{deficit} < V_{thresh}$) defines the position of the SSE propagation fronts. The distance, along the SSEs location representative line, between the propagation fronts and the onset location of each SSE is then calculated at each time step. The onset location of SSEs is assumed to be the projected barycentre of their first slip area contour on the SSE location representative line. Figure 2.9 shows the position of 14 SSEs front as a function of time.

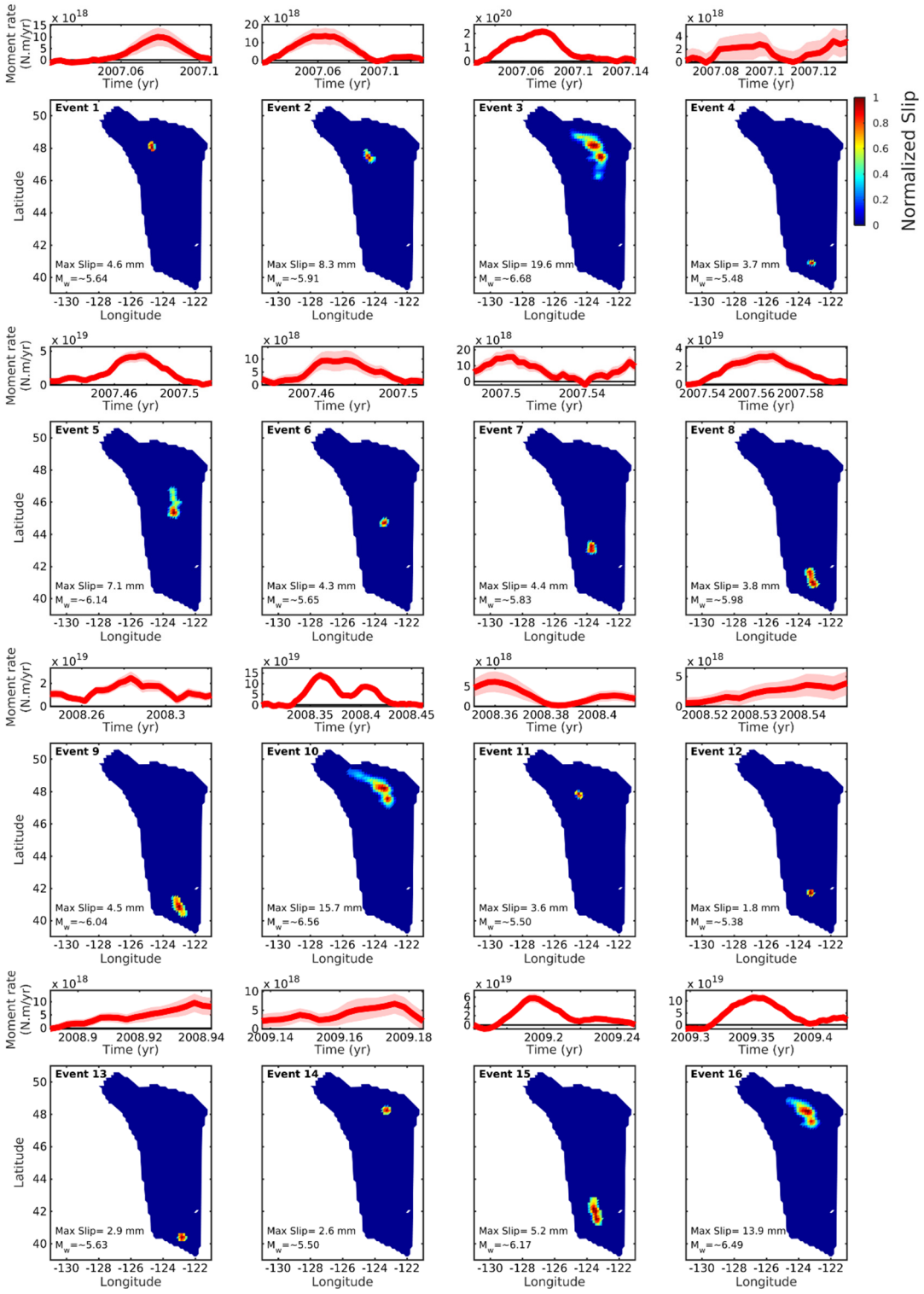

Figure 2.8. *Catalogue of 64 detected SSEs which occurred between 2007 and 2017. The bottom panels indicate the normalised slip distribution of each SSEs based on the initial low-pass filtering of $\delta_{deficit}$ with a cutoff at 21 days^{-1}. The top panels with the red curve indicate their moment rate functions based on the $\delta_{deficit}$ 8-days window smoothing. The pink shading represent the moment rate function uncertainty based on the standard deviation of the mean on the rough version of $\delta_{deficit}$ using a 16-days moving window centered in the epoch of interest.*

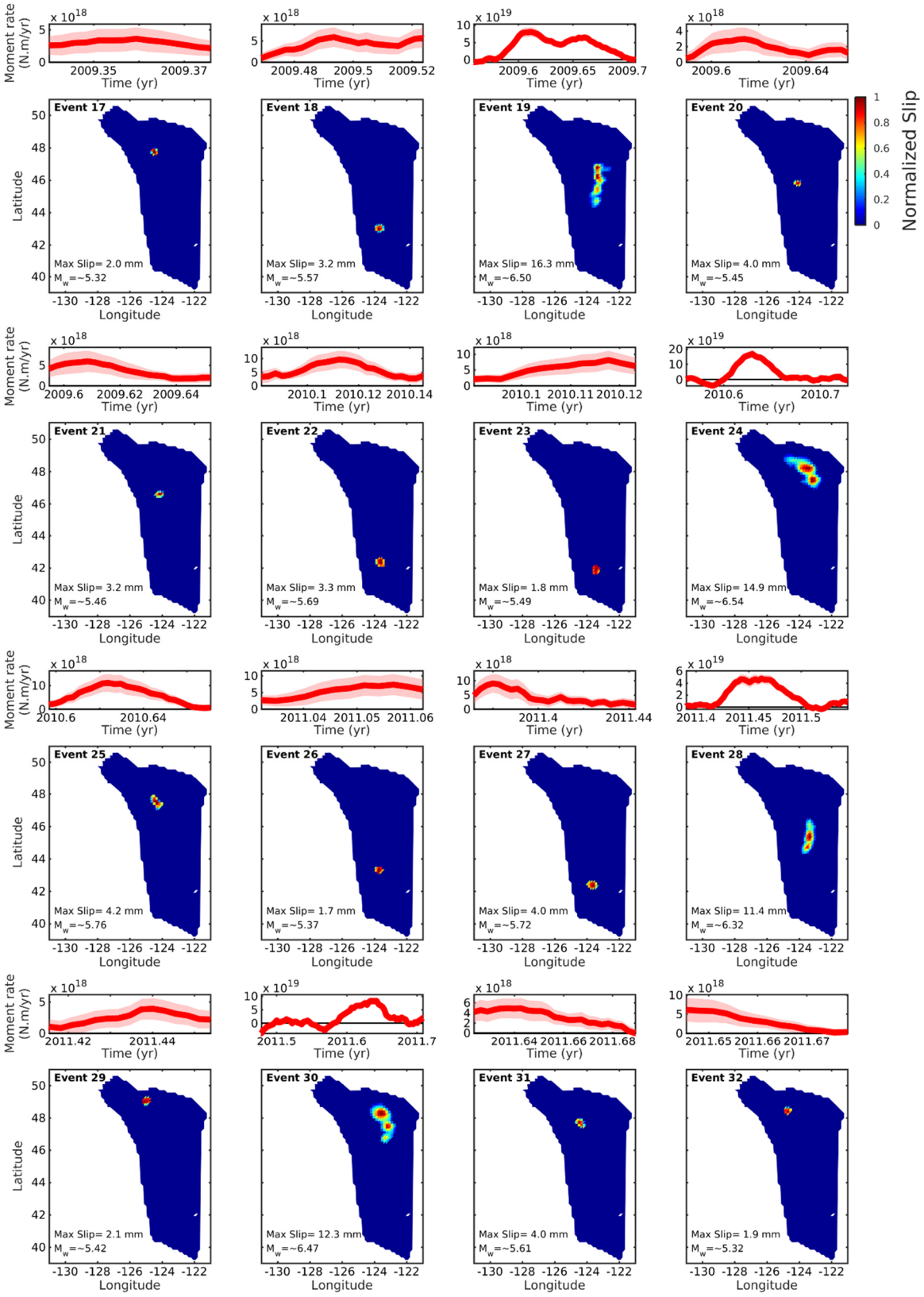

Figure 2.8. *(continued)*

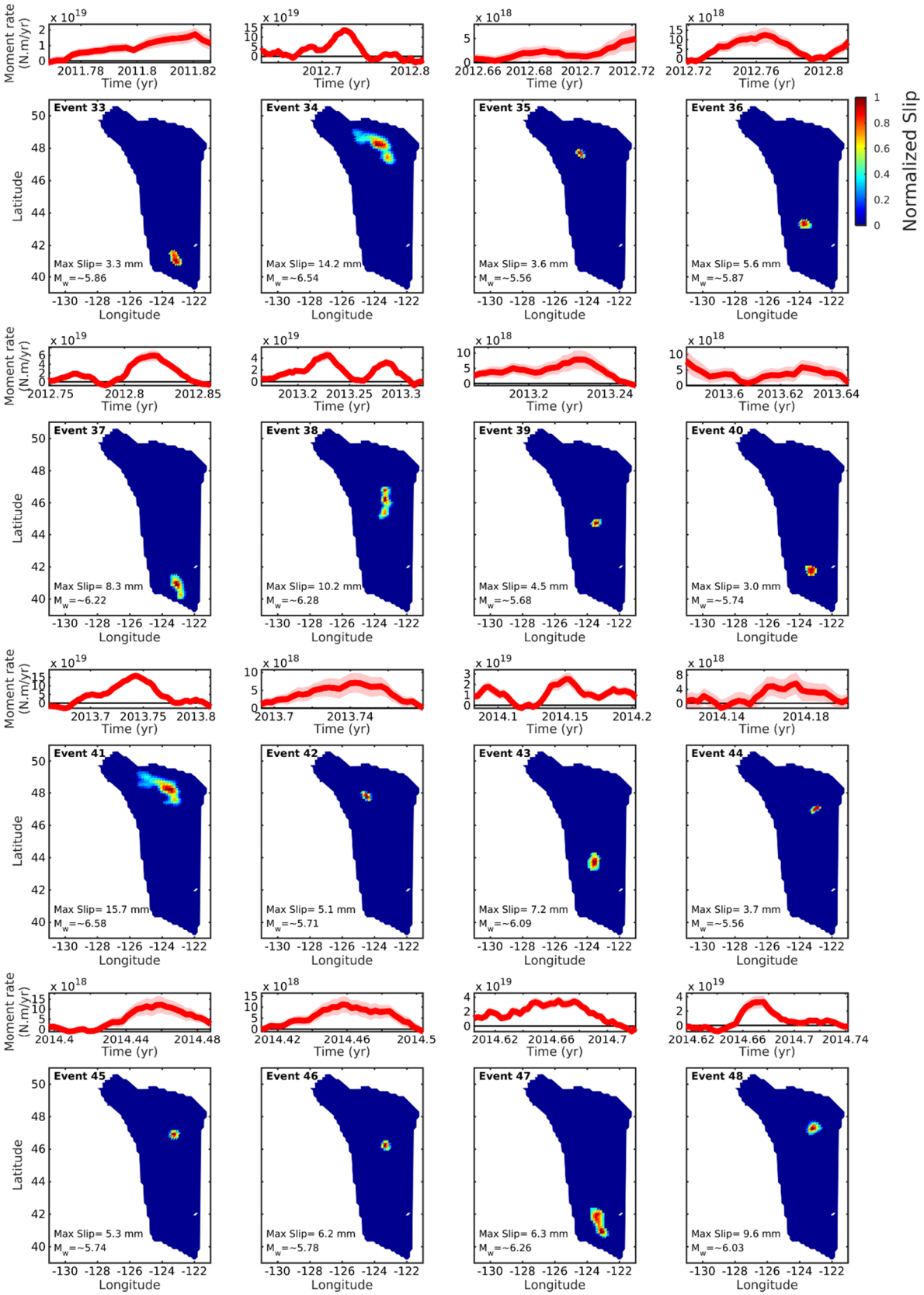

Figure 2.8. *(continued)*

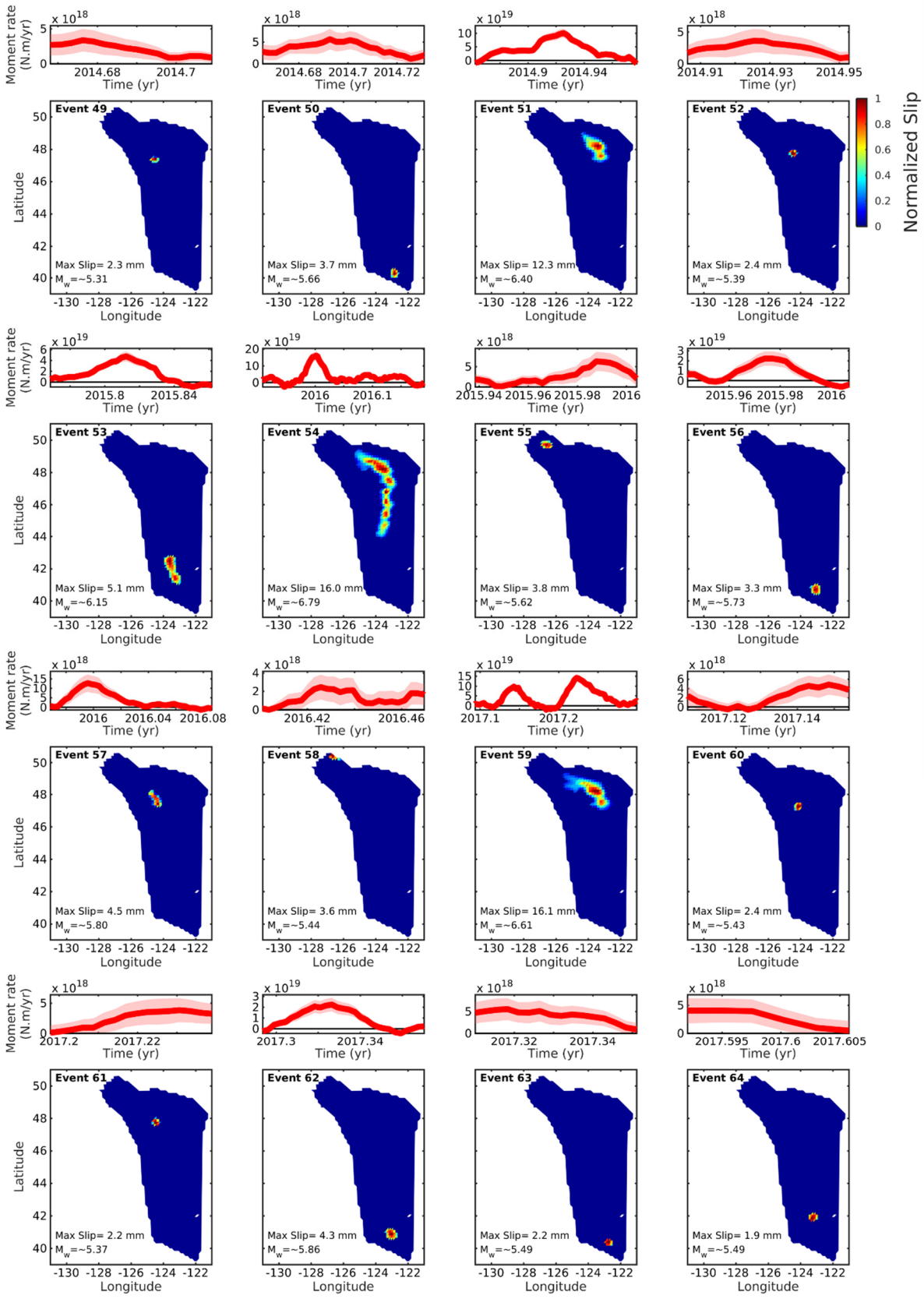

Figure 2.8. *(continued)*

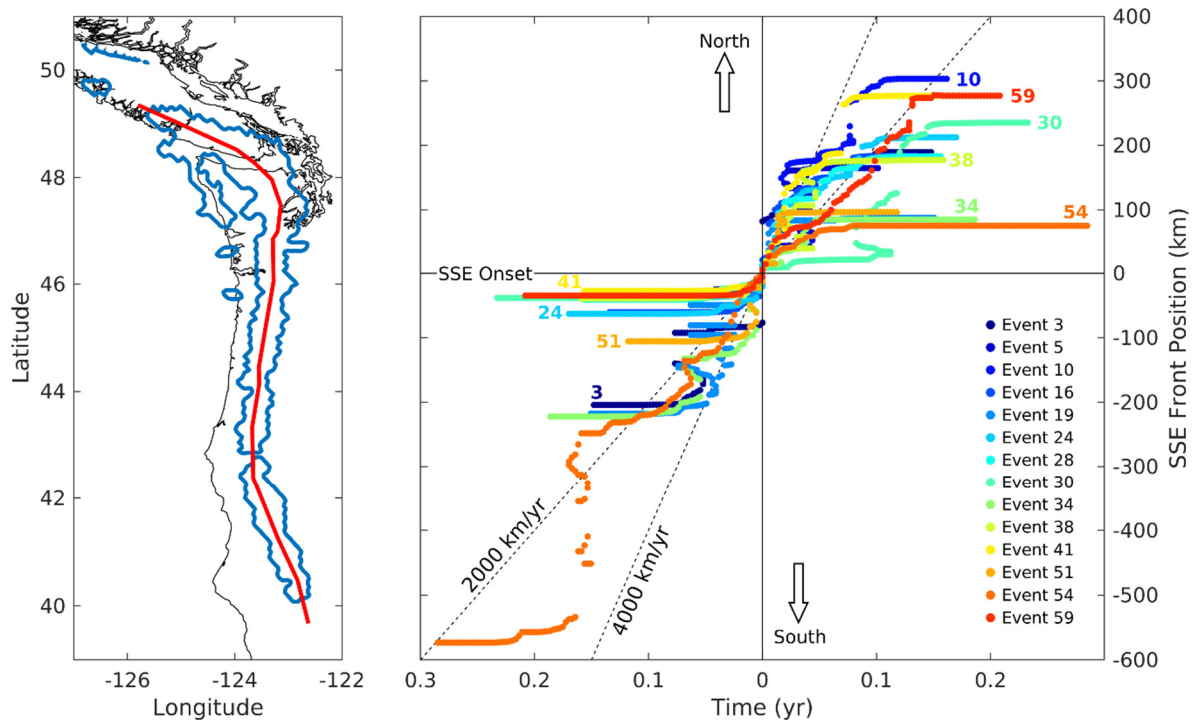

Figure 2.9. *SSE front position evolution of 14 events. (a) Map showing the representative line of the average along-strike location of SSEs (red line). The intersection between this line and the SSEs cumulative slip contour at each time step indicates location of the SSEs fronts. The blue line indicates the cumulative slip area contour of all SSEs. The black lines indicate the coast. (b) SSEs front positions as a function of time in reference to the SSEs onset locations. Positive position is to the North, negative to the South. Time axes are symmetric (positive on both sides), recording the time after the SSE onset. The two green dashed lines are reference propagation rates of 2000 (~5.5 km/day) and 4000 km/yr (~11 km/day).*

5.2. SSES KINEMATICS AND SCALING PROPERTIES

Our SSE catalogue (Figure 2.8) contains events with moment magnitude from 5.3 to 6.8 and duration between 14 to 106 days. Their propagation speed is of the order of ~2000-4000 km/yr (respectively ~5.5-11 km/day) (Figure 2.9).

First we observe that, from M_w 5.3 to 6.4, they obey the same magnitude-frequency relationship as regular earthquakes, the Gutenberg-Richter law. The SSEs have a *b*-value of ~0.8 (Figure 2.10.a). The events larger than M_w 6.4 suggest a larger *b*-value, as would be expected at the transition from unbounded ruptures to bounded ruptures [Romanowicz and Ruff, 2002]. However this explanation does not hold in our case: this transition must occur at a much lower magnitude (~*Mw* 5.8) given the aspect ratio of the ruptures (Figure 2.10.b). With only 11 events with M_w>6.4, this observation should however be considered with

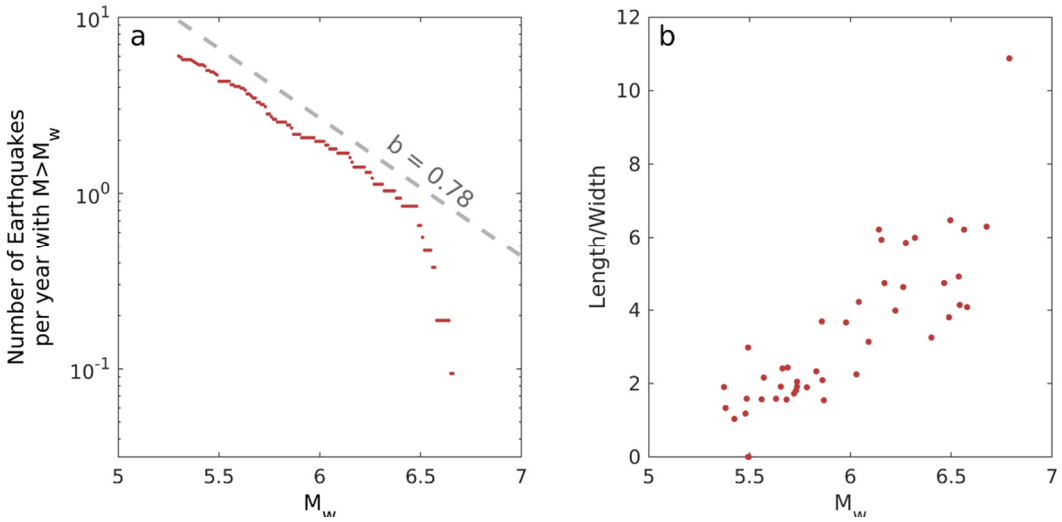

Figure 2.10. *Frequency-Magnitude distribution and aspect ratio of SSEs in Cascadia. (a) Logarithm of the number of SSEs with moment magnitude larger than the value in abscissa. As regular earthquakes SSEs are observed to follow a linear trend, i.e. the Gutenberg-Richter relationship. The b-value is estimated to ~0.8 using the maximum likelihood method [Aki, 1965]. The apparent larger b-value at Mw>6.5 is defined by only 11 events. (b) Aspect ratio of rupture areas. See supplements S3 for details about area and aspect ratio measurements.*

caution. A previous study had also argued for SSEs obeying the Gutenberg-Richter law [Wech *et al.*, 2010] but used moment inferred from duration assuming linear proportionality. It seems that the conclusion holds in spite of this incorrect assumption.

Taking the moment magnitudes, durations and rupture areas from the catalog at face value, we get remarkably well defined scaling laws: $M_0 \propto T^c$, with c=3.27 ± 0.48 and $M_0 \propto A^d$, with d= 1.42 ± 0.06 (95% confidence interval) (Figure 2.S8). We explored the possibility that the method used to extract the SSEs and characterize their duration could be a source of bias and we therefore carried out manual measurements (see Supplements S2 for details). The moment-duration data fall in the slow-slip domain identified by Ide *et al.* [2007] (red shading in Figure 2.11.b), however they clearly don't follow the linear scaling proposed in that study, but align along the $M_0 \propto T^3$ scaling of earthquakes. So we conclude that SSEs occurring under restricted conditions, as is the case in the deep SSEs from Cascadia analyzed here, follow a cubic moment-duration scaling like regular earthquakes. This finding is all the more unexpected since the SSEs in our catalog have large aspect ratios (Figure 2.10.b) and would therefore be expected to follow a linear scaling [Gomberg *et al.,* 2016]. Most of them indeed ruptured the entire width of the zone of episodic slow slip and tremors defined from the

cumulated slip (Figure 2.S9). It is noteworthy that, while the cubic scaling of regular earthquake is generally justified based on the circular crack model [Scholz, 1990], the same scaling is observed in our dataset where most ruptures are very elongated with aspect ratios of 2 to 12 (Figure 2.10.b).

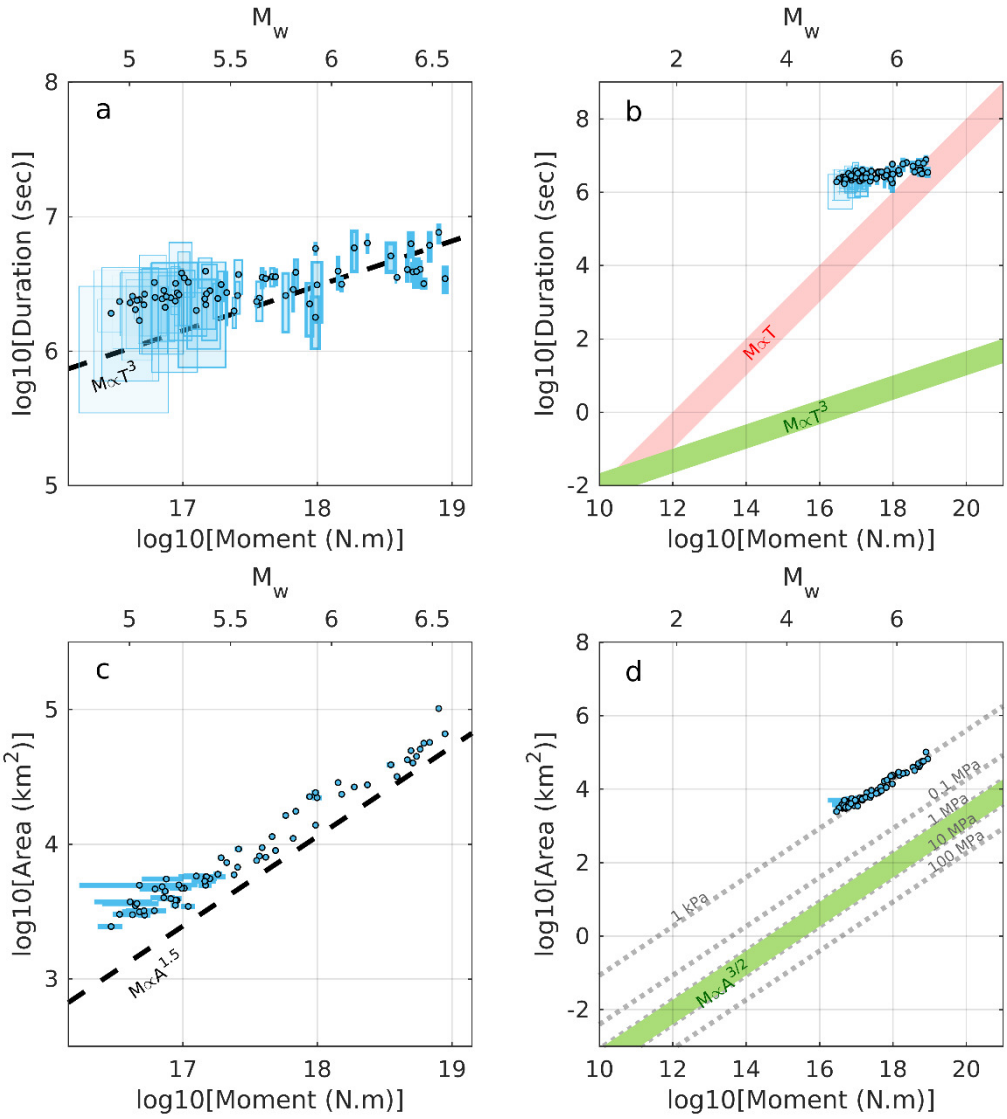

Figure 2.11. *Moment-Duration and Moment-Area scaling laws. (a) Relationship between the moment released by SSEs and their duration. The black dashed line indicates the scaling law for regular earthquakes. (b) Comparison with the scaling laws for slow (red shading) and regular earthquakes (green shading) proposed by Ide et al. [2007]. (c) Relationship between the moment released by SSEs and their rupture area. The black dashed line indicates the scaling law for regular earthquakes. (b) Comparison with the scaling laws regular earthquakes (green shading). Stress drop iso-lines are estimated based on the circular crack model [Kanamori & Anderson, 1975] :* $M_o = C^{-1}\Delta\tau A^{3/2}$*, with* M_o *being the seismic moment,* $\Delta\tau$ *the stress drop, A the rupture area and C=2.44. See supplement S2 for details about the measurements.*

Our manual measurement also define a tightly constrained moment-rupture area scaling following the same $M_0 \propto A^{3/2}$ scaling law as regular earthquakes (Figure 2.11.c and d). The pre-factor is however three orders of magnitude smaller, implying a stress drop in the range of 864±202 Pa, based on the circular crack model generally used to quantify seismic ruptures [Kanamori & Anderson, 1975], *vs* 1-10MPa for regular earthquakes. Our stress drop estimate is about 10 times lower than the value proposed by Schmidt & Gao [2010] based on the slip model of 16 Mw 6.2-6-7 events between 1998 and 2008. Given that the slip-distributions look similar for SSEs of similar magnitudes in both studies, we suspect that this difference is due to the way rupture area were measured and the possibility that our slip models might be smoother due to stronger regularization.

The spatio-temporal evolution of the tremors (section 2) and SSEs are systematically correlated (Movie 2.S1) as shown for example for event 34 in Figure 2.12, as had already been shown in some previous studies [*Wech and Bartlow,* 2014]. The SSEs located slightly offshore, along the coast between 47° and 49° of latitude (e.g. events 1, 2), are most likely inversion artefacts since a limited number of stations is present in the offshore portion of the megathrust.

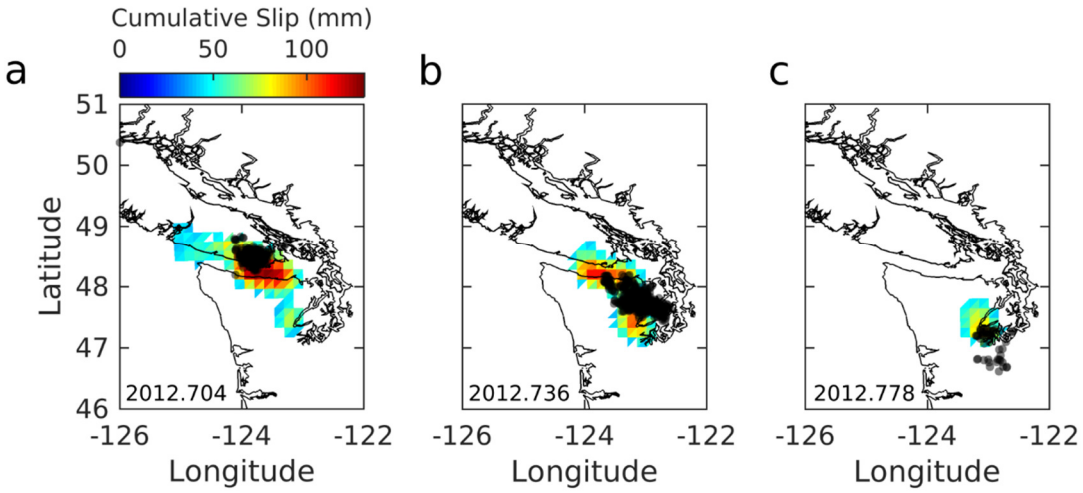

Figure 2.12. *Three snapshot of the slip cumulated over 1 day during the propagation of SSE 34. The black dots correspond to tremors for the same days. The black lines indicate the coast. The bottom left number corresponds to the date. The tremors closely track the propagation of the SSE.*

From our catalogue (Figure 2.8 and 2.13.c), we observe that SSEs often rupture the northern (i.e. event 10, 16, 24, 34, 41, 51, and 59), centre (i.e. events 5, 19, 28 and 38) or southern (i.e. events 8, 9, 15, 33, 37, 47 and 53) segments of Cascadia independently, but sometime multiple segments are ruptured during a single event (i.e. event 54). Segments are thus not completely independent from one another [*Schmidt and Gao,* 2010; *Wech and Bartlow,* 2014]. We also observe that SSEs can rupture segments from either North to South or South to North, showing that the direction of propagation is variable [*Schmidt and Gao,* 2010]. Some events propagate also bilaterally [*Schmidt and Gao,* 2010; *Dragert and Wang,* 2011; *Wech and Bartlow,* 2014] as is observed for the event 24 in our inversion (Movie 2.S1).

Our catalog confirms a strong segmentation as reported in previous studies for Cascadia [Gao *et al.*, 2012] and southwest Japan [Obara, 2010]. We indeed note systematics in the location, extent and timing of the SSEs (Figure 2.13). The zone of SSEs can be divided into a discrete number of segments. Each segment is defined as a sub-area of the megathrust that slips systematically as a whole. From the SSEs' rupture extent (Figure 2.13), cumulative slip distribution, and number of time a sub-fault has slipped (Figure 2.S9), we defined 13 segments (Figure 2.13, Table 2.S4 and S5). We admit that the proposed segmentation is somewhat subjective and will likely evolve as the catalog of SEEs is refined and expanded. Segments 1 and 2 are extremely coupled. They, most of the time, rupture together except for a rupture restricted to segment 2 in 2014.612. Segment 7 ruptured in combination with segments 6 and 8 in 2014, but never by itself. To first order, the zone of SSEs and tremors might be considered to consist of a limited number of segments that slip either independently or jointly. The segmentation defined by SSEs in Cascadia is qualitatively very similar to the segmentation defined by regular earthquake [Kanamori & McNally, 1982; Konca *et al*., 2008].

The combined moment rate of all the SSEs from our catalogue between 2007 and 2017 is shown in Figure 2.13.a. Two endmembers are shown, one assuming that interseismic loading is negligible during SSEs and the other assuming the fault is loaded at the long term plate rate during this period. They represent the two possible extremes of moment rate released by the SSEs from our catalogue. Bias in segment determination is introduced from the selection of V_{thresh}. For example, certain SSEs might not be detected or a same SSE could have been cut into pieces (e.g. events 28 and 30 in 2011). Increasing V_{thresh} to -35 mm/yr, we retrieve instead 81 SSEs, several events are merged (events 1,2 and 3 in 2007 or 28 and 30 in 2011),

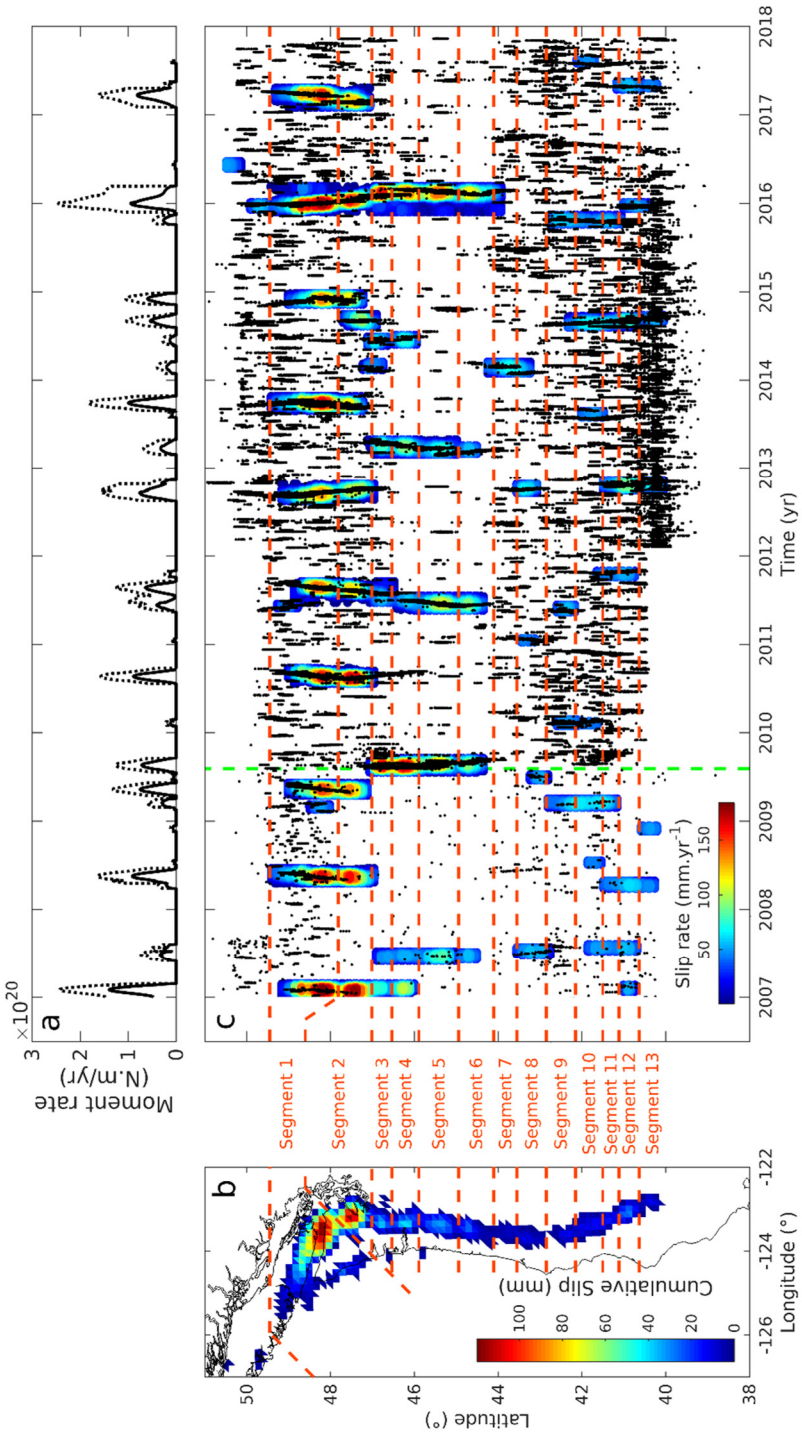

Figure 2.13. *(a) Combined moment rate functions of all the detected SSEs from our catalogue. The continuous and dashed black lines correspond to the moment rate taking and without taking into account interseismic loading during SSEs, respectively. To place an upper bound on the moment release during SSEs the dashed lines are calculated by comparison with the moment deficit that would have occurred during each SSE had the fault remained fully locked. Those moment rate functions are based on the low-pass filtered* $\delta_{deficit}$ *with the passband at 21 days*$^{-1}$ *(b) SSEs cumulative slip. (c) Occurrence of SSEs (colour shading) as a function of time. The black dots indicate tremors. The catalogue from Ide [2012] is used until 2009.595 (green dashed line), the catalogue from PNSN is used thereafter. The dashed pink lines in (b) and (c) correspond to the selection of segments.*

smaller events appear, but the global dynamics remains unchanged (Figure 2.S10). Additionally, increasing V_{thresh} also increases the risk of introducing noise.

5.3. DISCUSSION

The combination of the uncertainty on GPS measurements, the low-pass filtering, the value of V_{thresh} and the interpreted fault geometry, specifically in the North, hinders our possibility to retrieve small SSEs that remains within the noise level. In the most Northern part of the fault, our kinematic model is difficult to interpret due to the proximity of the fault's border which is prone to noise from the inversion. The southern part of Cascadia seems more prone to having small SSEs, which are more difficult to detect. This can be due to the slower convergence rate of the region (27 mm/yr) compared to the northern segments (45 mm/yr). The spatial distribution of GPS stations plays also a role in that matter.

Two opposite effects may affect the duration estimation of the SSEs. The temporal slip deficit filtering tend to augment SSEs duration. On the other hand, the selection of small enough (i.e., large enough in absolute value, in order to limit the effects of noise) V_{thresh} cuts the onset (t_k^{in}) and end (t_k^{fin}) of SSEs. Moreover, it additionally impacts SSEs' spatial extent, disregarding areas that do not slide fast enough. The merging or separation of events due to V_{thresh} will also impact the duration and areas of SSEs. The value of the estimated peak slip during a SSE (Figure 2.8) depends on the regularisation of the inversion. The fact that the inversions are ill-posed and require regularization thus probably explains why different inversions can yield significantly different peak slip values. For example, the SSEs peak slip reported in our study (~1.5 cm) are smaller than the peak slip indicated in Dragert and Wang [2011] (~3-5 cm) for the May 2008 event. Those biases will affect directly the moment-duration and moment-area scaling of SSEs. Nevertheless, they are likely not strong enough to affect the $M \propto T^3$ scaling observed in our results.

Whether the dynamics of SSEs can be explained with a smaller number of segments or not is hindered by the noise level of our kinematic model. This is the case in the south where SSEs barely overpass the noise level and where the similarity in dynamics between the selected asperities is difficult to estimate. The spatial distribution and temporal evolution of tremors might serve as an indicator of the SSEs that we are missing (Figure 2.13.c).

There is also a possibility that the number of selected ICs used for the SSE model (Section 3.1.4) bias the kinematic description. In our case, 15 components were selected to describe the kinematics and one could expect the number of segments within our model to be constrained by this number. However, the selection is initially based on a pool of 32 components with 17 components seemingly noise. Increasing or decreasing the total number of components produced by the vbICA changes slightly the number of components related to SSEs but does not change qualitatively the dynamics observe in our model. On the contrary, by increasing the total number of components, the vbICA extract further components estimated as local effects or noise. We tested up to 44 components.

The uncertainty on the position of the SSEs propagation front also depends on the factors mentioned above (i.e. GPS measurements, low-pass filtering, value of V_{thresh}, interpreted fault geometry and number of ICs). Additionally, the choice of the representative line of the average along-strike location of SSEs also plays a role, even though minor. Note that the initial phase of the SSEs front positions might represent more a shadow of the slip deficit rate of SSEs decreasing under V_{thresh} rather than the actual SSEs front propagation. The values of SSE front propagation rate estimated from our kinematic model are anyways similar to the ones estimated from tremor propagation since SSEs and tremors are most often correlated.

6. Seismic potential of Cascadia

6.1. MOMENT BUDGET SETTING

To assess Cascadia's moment budget, we follow the same methodology as in Chapter 1. We explore the magnitude, M_{max}, and occurrence frequency, $1/\tau_{max}$, space of the largest earthquake, and look for the scenarios with the highest probability to balance the moment budget. We estimate the moment deficit rate of the fault, $\dot{m}_0$ (Equation 1.1 from Chapter 1), from our two coupling maps (Figure 2.6), which represent two extremes coupling cases at the trench (fully locked or unlocked trench). We assume that below 30 km depth the fault is fully creeping and estimate $\dot{m}_0$ over this depth. In doing so, we avoid introducing errors related to border effects in the coupling estimation. We compare the resulting $\dot{m}_0$ with seismicity models constructed as followed. Each seismicity model is composed of independent events

with magnitude up to a maximum-magnitude, M_{max}, earthquake with a recurrence time τ_{max}. Each independent earthquake is followed by aftershocks. The combined aftershocks and independent events magnitude-frequency distribution follows a Gutenberg-Richter (GR) distribution with a b-value set equal to the one estimated from our ANSS catalogue ($b = 0.87 \pm 0.03$). Aftershocks are assumed to obey or not the Bath law, which is a phenomenological law stating that the largest aftershocks does not exceed $M - 1$, M being the magnitude of the mainshock. Afterslip is assumed to follow each earthquake and to release aseismically a moment proportional to the moment released seismically (see Chapter 1 for details and justifications).

The probability that the largest event is of magnitude M_{max} and has on average a return period of τ_{max} can be written as the product of two probabilities,

$$P(M_{max}, \tau_{max}) = P_{Budget}(M_{max}, \tau_{max}) * P_{Hist}(M_{max}, \tau_{max}) \, . \qquad (2.5)$$

$P_{Budget}(M_{max}, \tau_{max})$ is the probability that an earthquake of magnitude M_{max} and its associated aftershocks and aseismic afterslip release a moment equal to the deficit of moment accumulated over the return period τ_{max} (i.e. the probability that an earthquake of magnitude M_{max} balances the budget). $P_{Hist}(M_{max}, \tau_{max})$ is the probability that an event of magnitude M_{max} and return period τ_{max} is the maximum possible earthquake based on the known 'historical' seismicity (known from historical accounts or instrumental observations).

The pdf of P_{Budget} is based on two extreme cases, representing the hardest and the easiest scenarios to close the moment budget. The first one, the hardest, is based on the fully locked trench case and assumes M_{max} is followed by seismic events with a b-value equal to 0.87-0.06, the next biggest event is one magnitude less than M_{max} (Bath law), and all the seismic events produce no afterslip. The second, the easiest, is based on the fully creeping trench case and assumes M_{max} is followed by seismic events with a b-value equal to 0.87+0.06, Bath law doesn't apply, and all the moment released by afterslip is equal to 25% of the seismic moment. We assume that P_{Budget} pdf follows a Gaussian with 95% uncertainty limit (2 sigma) corresponding to the two extreme cases. If M_{max} occurred every year the peak probability would be equal to 7.49±0.32 where the uncertainty is the standard deviation.

P_{Hist} is based on Chapter's 1 approach 2 of the methodology section. It assumes that the possible magnitude and frequency of the maximum-magnitude earthquake must be

consistent with the observed largest event over the observation period (it has to be larger than or equal to the known largest event, M_{hist}, and the return period of the larger event cannot be significantly smaller than the observation period, t_{hist}). Following equations 1.14 and 1.15 of Chapter 1, we estimate P_{Hist} setting the largest historical event to the one observed in the ANSS Catalogue, $M_{hist} = 6.5$ and $t_{hist} \sim 34$ years. The calculation is ignorant of the fact that the Cascadia Megathrust is presumed to have generated $M \sim 9$ earthquakes in the past.

We use the Hasting-Metropolis Monte Carlo Markov Chain (MCMC) method to sample these probabilities. We calculate for each sample k, with a given magnitude and frequency of the largest earthquake, the probability that it is realistic knowing the data $P_{Hist,k}$ and the probability that it closes the budget $P_{Budget,k}$. The final probability $P_{G,k}$ (i.e. the posteriori probability) of a given sample would thus be

$$P_{G,k} \propto U_M U_{Freq} P_{Budget,k} P_{Hist,k}, \tag{2.6}$$

where U_M and U_{Freq} are the uniform laws chosen for the MCMC sampling for the magnitude and frequency, respectively (i.e. the a priori probability). This equation is the same as Equation 1.18 in Chapter 1.

Each sample is taken from a uniform PDF between 6.5 and 11 for magnitudes, and between 10^{-6} and 10^{1} yrs^{-1} for frequencies. We calculate for each sample k the value proportional to the probability $P_{G,k}$. We run the sampler for 8500000 steps, rejecting the first 500 steps to ensure accurate sampling of the PDF. The magnitude-frequency space is then binned into cells of size 0.01 for the moment magnitude axis and logarithmically binned into cells of size 0.01 concerning the frequency axis. The number of samples in each cell divided by the total number of samples approximates the probability $P_{G,k}$ as defined by the MCMC method.

6.2. MOMENT BUDGET RESULTS

The results are shown in Figure 2.14. The colour shading indicate the probability distribution of the possible magnitude and frequency of the maximum earthquakes taking into account the geodetic constraints on the moment budget and the seismicity reported in the ANSS catalogue. The plot shows that clearly M_{max} > 8 as also seen in the marginal cumulative probabilities (Figure 2.15.b and c). The magnitude for which 95% of the maximum non-cumulative probability is reached gives us an indication of the magnitude and frequency

needed to close the moment budget (Figure 2.15.a). A maximum of M9.5 is sufficient to close the moment budget at a 95% confidence level. The recurrence time of such an event, is estimated to 389+/-10 years. Higher magnitudes and with longer recurrence times than those estimates are equally plausible but would not be necessary. Note that the marginal probabilities reflect the assumptions that the *a priori* probabilities are uniform, between 6.5 and 11 for the magnitude of the largest earthquake, and 10^4 and 10^{-1} for its frequency. It shows that the historical catalogue does not put any constrain on the magnitude of the maximum event for return period's much longer than the catalogue.

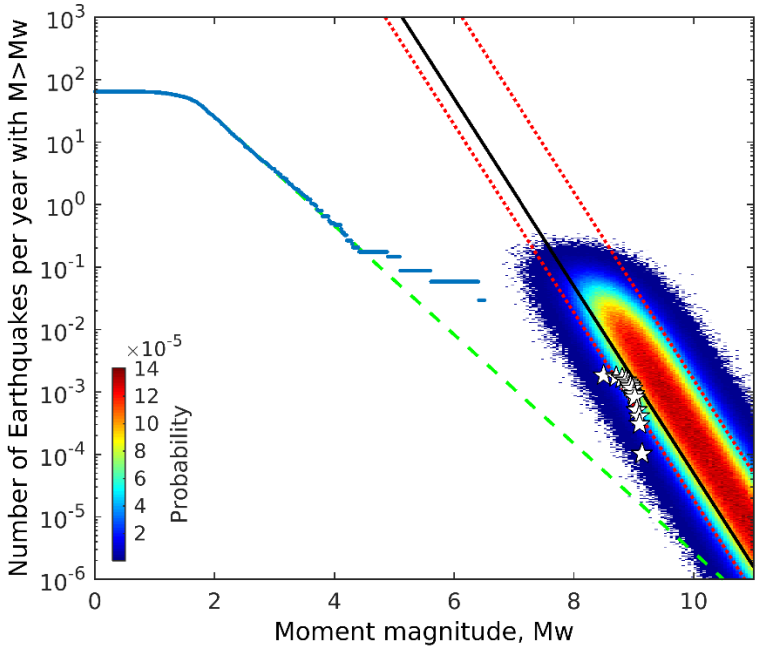

Figure 2.14. *Maximum-magnitude earthquake probability assuming the case where large earthquakes should have a recurrence time lower than the largest earthquake currently observed. The blue line represents the magnitude-frequency distribution of Cascadia's region using the ANSS catalogue between 1984 and 2018. The green dashed line is the GR law extrapolation from the current catalogue. The stars incarnate the paleo-earthquake data [Goldfinger et al., 2012]. The red dashed lines represent the 95% uncertainty of P_{Budget}, corresponding to the two extreme scenarios: i) creeping trench, b=0.87+0.06, no Bath's law, ratio between postseismic and coseismic moment release equal to 25% (bottom red dashed line); ii) locked trench, b=0.87-0.06, apply Bath's law, and no postseismic moment release (top red dashed line). The full black line represent the scenarios with a locked trench, b=0.87-0.06, no Bath's law, and no postseismic moment release.*

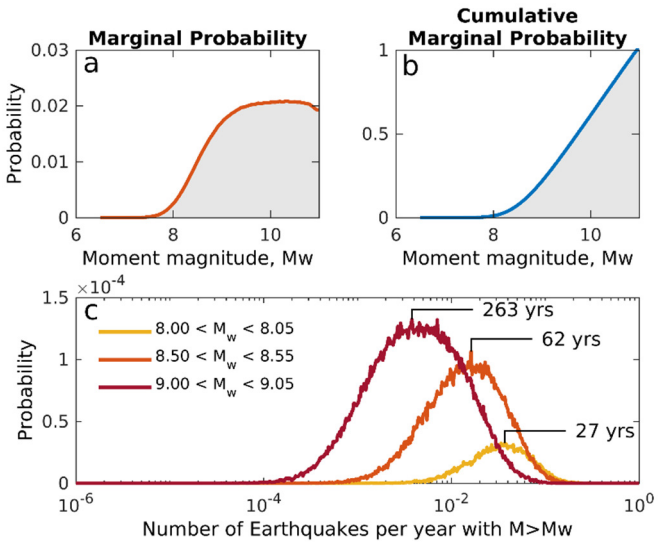

Figure 2.15. *Marginal non-cumulative (a) and cumulative (b) probabilities for a maximum magnitude earthquake to close the moment budget and be plausible considering the data. We also show the probabilities of the return period assuming* $M_{max} = 8.0, 8.5$ *and* 9.0 *(c).*

6.3. SEISMIC POTENTIAL CURVES

Here we demonstrate how the result of our study can be used for a probabilistic seismic hazard analysis. One might for example be interested in calculating the probability of a M>8 earthquake happening within a time period of 30 years. For each tested value of the magnitude and frequency of the largest event, one can determine a seismic hazard quantity, such as for example, the probability P_{Hazard} that an independent earthquake (not an aftershock) would exceed a given magnitude M_{Test} over a given period of time t (Equation 1.16 in Chapter 1). Each curve can then be weighted according to the probability of the scenario. The weighted mean $\bar{P}_{Hazard}$ (Equation 1.17 in Chapter 1) then represents the overall hazard resulting from all possible scenarios. Note that we use the *b*-value derived from a non-declustered catalogue to represent the magnitude-frequency distribution of independent events (given a M_{max}) and might therefore be overestimating the hazard level.

Figures 2.16 shows the probability of having an earthquake larger than a given magnitude over a period of 30 years based on the probability distribution of the magnitude-frequency of the largest earthquake shown in Figure 2.14. We assumed that the largest earthquake cannot exceed magnitude 10. The probability of a M>9 event over 30 years is 13%, 53% for a M>8 and 90% for a M>7. Note that this analysis is only based on the geodetic and instrumental seismicity. It does not account for the fact that we know that M9 earthquakes happened in the past and that none happened over the last 300yr. If this information is now included in the calculation, the possibility of closing the moment budget with M_{max}<9.0 is excluded, and

the hazard curves are then modified substantially (Figure 2.17). The probability of a M>9 event over 30 years is 8%, 37% for a M>8 and 83% for a M>7.

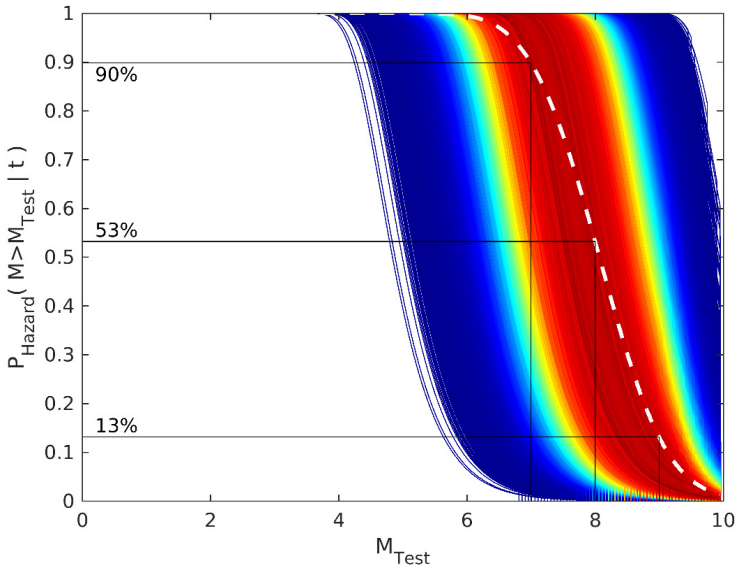

Figure 2.16. *Probability to have earthquakes over a certain magnitude, M_{Test}, in a period of time of $\boldsymbol{t}$=30 years considering all the possible seismicity models and their probability of occurrence based on their consistency with the maximum event in the ANSS catalogue (M6.5) amd its duration (34 years), and the probability that they balance the interseismic deficit of moment.. The white dashed line corresponds to the mean $\overline{\boldsymbol{P}}_{\boldsymbol{Hazard}}$. We suppose a maximum-magnitude possible of M10.*

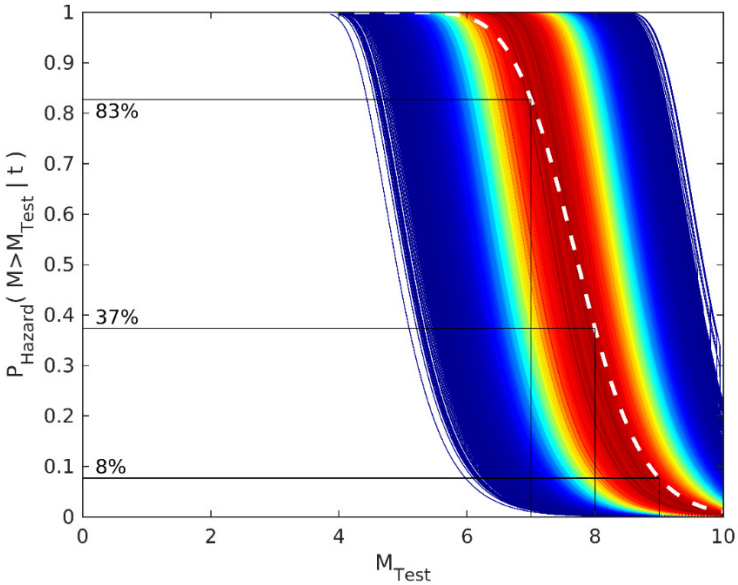

Figure 2.17. *Probability to have earthquakes over a certain magnitude, M_{Test}, in a period of time of $\boldsymbol{t}$=30 years considering all the possible seismicity models and their probability of occurrence based on their consistency with the historical event of 1700 (assigned a magnitude M9.0) and the fact that no similarly large or larger earthquake occurred since then, and the probability that they balance the interseismic deficit of moment. The white dashed line corresponds to the mean $\overline{\boldsymbol{P}}_{\boldsymbol{Hazard}}$. We suppose a maximum-magnitude possible of M10.*

6.4. DISCUSSION

The $M\sim9$ paleoearthquake catalogue from Goldfinger *et al.* [2012], represented by the stars in Figure 2.14, falls within the bottom portions of frequency-magnitude domain that would allow closing the moment budget. Despite the large uncertainties on the interseismic coupling model and the limited information on long term seismicity included in the ANSS catalogue, our analysis requires a maximum magnitude event and frequency compatible with the paleoturbidite records. The portion where a consistency is found corresponds to seismicity models that do not assume the Bath law. Note that the locked trench case with no Bath law (no Bath law, b-value equal to 0.87 and postseismic moment released equal to 25% of the seismic moment) results in scenarios (full black line in Figure 2.14) which are both concordant with the catalogue of Goldfinger *et al.* [2012]. The GR law from the current catalogue (dashed green line) predicts M_{max} at unreasonable values ($M_{max} > 10$). It does not reconcile with the catalogue of Goldfinger *et al.* [2012]. This might be due to the poor representation of large events within the current catalogue (M_w>=4.3), which, if integrated, would shift the whole seismicity catalogue curve (in dark blue) to higher values. Another way to reconcile the instrumental, paleoearthquake catalogue, and the closure of moment budget balance would be to assume that independent earthquakes follow a Gutenberg-Richter distribution with a b-value of ~0.5 significantly smaller than the value we assumed.

These hazard curves should be considered as tentative and are included here only as a proof of concept. For example the hazard level would drop substantially if we were to assume a lower *b*-value for the independent events. Also the analysis assume that independent events follow a Poisson process. Another renewal model like the Brownian passage time model [*Field and Jordan*, 2015] might be more appropriate.

Concerning M_{max}, the largest event with the highest probability is estimated at $M9.14$, $M9.49$ and $M10.16$ if the recurrence time is between 300, 1000 and 10 000 years. The extent of the probability distribution of the largest event and its recurrence time is however largely dependent on the Bath law application (Chapter 1). The paleo-earthquake catalogue [*Goldfinger et al.,* 2012] (Figure 2.14) seems to indicate that $M\sim9$ events, combined with their associated seismicity, are sufficient to close the moment budget for seismicity models that do not take into account Bath law (bottom full red line and full black line). Taking those two

extreme scenarios without applying Bath law, the largest event with the highest probability is estimated at $M8.64$, $M8.99$ and $M9.66$ if the recurrence time is between 300, 1000 and 10 000 years, respectively. Additionally, our coupling maps represent a snapshot in time of the faults loading rate. It is worth noting that the long term loading rate, as indicated by decades of levelling data, do not reconcile with the loading rate estimated by GPS [*Bruhat and Seagall,* 2016]. It has been argued that the creeping-locked transition location has been migrating towards the trench [*Bruhat and Seagall,* 2017]. This would increase the probability for bigger events.

7. Conclusion

We determined the secular model of interseismic coupling on the megathrust (the time-average pattern of locking ratio) and the kinematics of SSEs from 2007 to 2017 in a consistent and coherent way. The vbICA has shown to be very effective at separating the SSEs from the various other sources of temporal variations in the position time series such as those due to surface hydrology, post-seismic signals, local effects or common mode motion.

With our vbICA-based Inversion Method we were able to describe the kinematics of fault slip on the Cascadia megathrust between 2007 and 2017 using 352 cGPS position time series. Our kinematic description separates the linear term over that period and the deviations from the secular motion. Inversion of the linear term reveals the pattern of interseismic coupling on the megathrust. The interseismic model can be used to estimate the seismic potential of the megathrust. We find that given the seismicity observed over the last 34 years, the rate of moment deficit accumulation calls for earthquakes much larger than the largest interplate event recorded over that period, which reached M_w6.5. A maximum magnitude of the order of M_w9.0, with a return period of 263 yrs, is needed to balance the moment budget. This lends additional support to the interpretation that the tsunami recorded on the coast of Japan in the XVIII century was caused by a $M\sim$9 originated from Cascadia [*Satake et al.,* 1996]. We also find the return period of the maximum event, if $M_w\sim$9.0, to be consistent with the paleoturbite record [*Goldfinger et al.,* 2012].

Our kinematic model provides the most comprehensive view of the SSEs along Cascadia. We were able to produce a catalogue of 64 events over the 2007-2017 time period. As documented in previous studies of particular SSEs [e.g., *Wech and Bartlow,* 2014] we find a remarkable correlation in space and time between the SSEs and the tremors. As inferred in previous studies, the system seems segmented [*Brudzinski et al.,* 2010; *Obara,* 2010]. To first order the zone of SSEs and tremors consist of 13 segments that slip either jointly or independently. The along-strike segmentation, dynamics and scaling properties of SSEs on the Cascadia subduction zone are found to be remarkably similar to those of regular earthquakes.

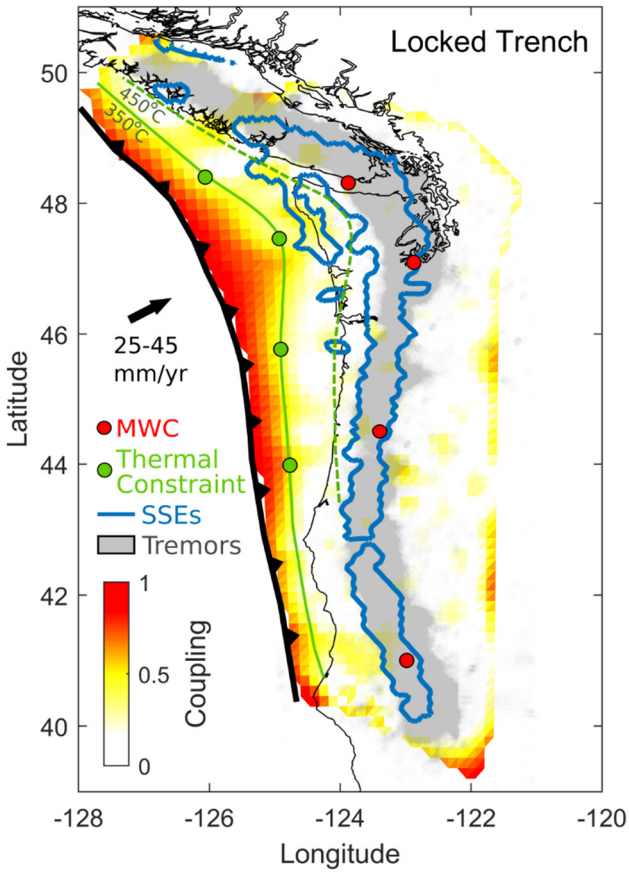

Figure 2.18. *Interseismic coupling (white to red shading) and tremor (gray dots) distribution. The thin black curve indicates the coast. The blue contour indicates the area influenced by SSEs as measured in this study. The red dots indicate the position of the intersection between the forearc Moho and the megathrust, so the tip of the mantle wedge corner (MWC), determined from geophysical profiles along which* dV_s/V_s *and* V_s *was determined (*POLARIS *at the southern tip of the Vancouver Island [Nicholson et al., 2005],* CASC93 *in central Oregon [Nabelek et al., 1996; Rondenay et al., 2001],* CAFE *at Puget Sound [McGary et al., 2011; Abers et al., 2009], and* FAME, BDSN *and* USArray/TA *in the south of Cascadia). The solid and dashed green lines indicate the location of the 350°C and 450°C isotherms on the megathrust [Hyndman et al., 2015]. The green dots represent the location of thermal constraints used to estimate the isotherms.*

Our analysis demonstrates a clear along-dip segmentation of the mode of slip along the megathrust (Figure 2.18). Some locked zone is clearly needed between the trench and the coastline to account for the secular compression and the secular pattern of subsidence and uplift (Figure 2.7). The resolution near the trench is poor and we cannot determine if the locked zone extends all the way to the trench or not. The models obtained assuming either *a priori* creep or locking of the megathrust fit the data equally well. They yield somewhat different position of the downdip limit of the locked zone (Figure 2.6). It lies about ~20-80 km updip of the coastline at a depth of about ~5-15 km when the megathrust is assumed locked *a priori* (Figure 2.6a). It lies much closer to the coastline, corresponding to a depth of about ~10-30 km, if the megathrust is assumed to be creeping *a priori* (Figure 2.6b). These observations are consistent with most previous studies of interseismic coupling [e.g., *Wang et al.*, 2001*; McCaffrey et al.*, 2000, 2007; *Bruhat and Segall*, 2016]. The portion of the megathrust that ruptures during large interplate earthquakes must lie mostly updip of such transition between locked and creeping sections. The lack of seismicity over the transition zone hints for a fully locked shallow portion of the fault [*Wang and Trehu,* 2016]. We would also expect earthquakes to nucleate along the zone of stress accumulation, at the transition between the locked and creeping region, as is observed for example in the context of other megathrusts [e.g., *Cattin and Avouac*, 2000; *Bollinger et al.,* 2004]. The lack of seismicity in this zone where stress is accumulating the fastest is intriguing. It suggests that the interseismic stress build up has not yet compensated the last stress drop event to trigger earthquakes there. It could also suggest that large interplate earthquakes penetrate deeper than the lower edge of the locked fault zone. Jiang and Lapusta [2016] demonstrated via numerical simulations of the seismic cycle under a rate-and-state friction framework that this mechanism would indeed produce a protracted period of seismic quiescence.

The zone of SSEs and tremors is relatively well resolved and, when compared with the interseismic coupling model (Figure 2.18), clearly reflects a downdip segmentation of the mode of slip on the megathrust. This zone lies inland from the coastline and is clearly disconnected from the locked zone as already pointed out in some past studies [e.g., *Gao and Wang*, 2017]. In this transition zone, which spans between ~100 km and ~150 km away from the trench, fault creep is remarkably stationary resulting in a slip rate close to the long-term slip rate along the megathrust. This zone thus seems to act as a buffer isolating the

seismogenic zone of the megathrust from the zone of SSEs. This buffering zone probably reduces the risk that a SSE triggers a large megathrust rupture [*Segall and Bradley,* 2012].

The downdip segmentation of the mode of slip along megathrust has long been noticed and considered to reflect the influence of both temperature and lithology [*Hyndman et al.*, 1997; *Scholz*, 1998, *Oleskevitch et al*., 1999]. These two factors could also explain the existence of two separate zones of unstable frictional sliding, as it has been proposed to relate to downdip variations of temperature and lithology along the megathrust [*Gao and Wang,* 2017]. The one closer to the trench would correspond to the zone of rate-weakening frictional sliding for continental rocks as the temperature above which frictional sliding becomes rate-strengthening, which is estimated to 350°C for quartzo-feldspathic rocks [*Blanpied et al*., 1995], is reached at depths shallower than the intersection with the forearc Moho [*Hyndman et al.,* 1997; *Scholz*, 1998; *Oleskevitch et al*., 1999] (Figure 2.18). The second region is instead located around the mantle wedge corner, where high-pore fluid pressure might result to low permeability of the serpentinized mantle [*Wada et al.,* 2008]. This hypothesis is consistent with the correlation between the zone of SSES and tremors with the forearc Moho (red dots in Figure 2.18) as proposed by Gao and Wang [2017].

Acknowledgement

We thank Kelin Wang for his constructive review of this work. This study was partially supported by NSF award EAR-1821853 to JPA. We thank also Zachary E. Ross for his help. We thank Kristel Chanard for discussions and providing the times series predicted based on the surface mass variations derived from GRACE.

Bibliography

Abers, G. A., MacKenzie, L. S., Rondenay, S., Zhang, Z., Wech, A. G., & Creager, K. C. (2009), Imaging the source region of Cascadia tremor and intermediate-depth earthquakes. *Geology*, *37*(12), 1119-1122.

Aki, K. (1965), Maximum Likelihood Estimate of b in the Formula logN=a-bM and its Confidence Limits, 東京大学地震研究所彙報, *43*(2), 237–239.

Atwater, B. F. (1987). Evidence for great Holocene earthquakes along the outer coast of Washington State. *Science*, *236*(4804), 942-944.

Atwater, B. F., & Hemphill-Haley, E. (1997), *Recurrence intervals for great earthquakes of the past 3,500 years at northeastern Willapa Bay, Washington* (No. 1576). USGPO.

Bender, B. (1983), Maximum likelihood estimation of b values for magnitude grouped data, *Bull. Seismol. Soc. Am.*, *73*(3), 831–851.

Bettinelli, P., Avouac, J. P., Flouzat, M., Bollinger, L., Ramillien, G., Rajaure, S., & Sapkota, S. (2008), Seasonal variations of seismicity and geodetic strain in the Himalaya induced by surface hydrology. *Earth and Planetary Science Letters*, *266*(3-4), 332-344.

Blanpied, M. L., D. A. Lockner, and J. D. Byerlee (1995), Frictional Slip of Granite at Hydrothermal Conditions, *Journal of Geophysical Research-Solid Earth*, *100*(B7), 13045-13064.

Blewitt, G., Lavallée, D., Clarke, P., & Nurutdinov, K. (2001), A new global mode of Earth deformation: Seasonal cycle detected. *Science*, *294*(5550), 2342-2345.

Bollinger, L., Avouac, J. P., Cattin, R., and Pandey, M. R. (2004), Stress buildup in the Himalaya, *Journal of Geophysical Research-Solid Earth*, *109*(B11).

Brudzinski, M. R., Hinojosa-Prieto, H. R., Schlanser, K. M., Cabral-Cano, E., Arciniega-Ceballos, A., Diaz-Molina, O., & DeMets, C. (2010), Nonvolcanic tremor along the Oaxaca segment of the Middle America subduction zone. *Journal of Geophysical Research: Solid Earth*, *115*(B8).

Bruhat, L., & Segall, P. (2016), Coupling on the northern Cascadia subduction zone from

geodetic measurements and physics-based models. *Journal of Geophysical Research: Solid Earth*, *121*(11), 8297-8314.

Bruhat, L., & Segall, P. (2017), Deformation rates in northern Cascadia consistent with slow updip propagation of deep interseismic creep. *Geophysical Journal International*, *211*(1), 427-449.

Cattin, R., & Avouac, J. P. (2000), Modeling mountain building and the seismic cycle in the Himalaya of Nepal. *Journal of Geophysical Research: Solid Earth*, *105*(B6), 13389-13407.

Chanard, K., Avouac, J. P., Ramillien, G., & Genrich, J. (2014), Modeling deformation induced by seasonal variations of continental water in the Himalaya region: Sensitivity to Earth elastic structure. *Journal of Geophysical Research: Solid Earth*, *119*(6), 5097-5113.

Chanard, K., Fleitout, L., Calais, E., Rebischung, P., & Avouac, J. P. (2018), Toward a global horizontal and vertical elastic load deformation model derived from GRACE and GNSS station position time series. *Journal of Geophysical Research: Solid Earth*.

Chlieh, M., Avouac, J. P., Sieh, K., Natawidjaja, D. H., & Galetzka, J. (2008), Heterogeneous coupling of the Sumatran megathrust constrained by geodetic and paleogeodetic measurements. *Journal of Geophysical Research: Solid Earth*, *113*(B5).

Choudrey, R., & Roberts, S. (2003), Variational Bayesian mixture of independent component analysers for finding self-similar areas in images. *ICA, NARA, JAPAN*.

Clague, J. J., & Bobrowsky, P. T. (1994), Evidence for a large earthquake and tsunami 100-400 years ago on western Vancouver Island, British Columbia. *Quaternary Research*, *41*(2), 176-184.

DeMets, C., & Dixon, T. H. (1999), New kinematic models for Pacific-North America motion from 3 Ma to present, I: Evidence for steady motion and biases in the NUVEL-1A model. *Geophysical Research Letters*, *26*(13), 1921-1924.

Dong, D., Fang, P., Bock, Y., Cheng, M. K., & Miyazaki, S. I. (2002), Anatomy of apparent seasonal variations from GPS-derived site position time series. *Journal of Geophysical Research: Solid Earth*, *107*(B4).

Dragert, H., Wang, K., & James, T. S. (2001), A silent slip event on the deeper Cascadia

subduction interface. *Science*, *292*(5521), 1525-1528.

Dragert, H., & Wang, K. (2011), Temporal evolution of an episodic tremor and slip event along the northern Cascadia margin. *Journal of Geophysical Research: Solid Earth*, *116*(B12).

Field, E. H., & Jordan, T. H. (2015), Time-dependent renewal-model probabilities when date of last earthquake is unknown. *Bulletin of the Seismological Society of America*, *105*(1), 459-463.

Fu, Y., Freymueller, J. T., & Jensen, T. (2012), Seasonal hydrological loading in southern Alaska observed by GPS and GRACE. *Geophysical Research Letters*, *39*(15).

Gao, H., Schmidt, D. A., & Weldon, R. J. (2012). Scaling relationships of source parameters for slow slip events. *Bulletin of the Seismological Society of America*, *102*(1), 352-360.

Gao, X., & Wang, K. (2017), Rheological separation of the megathrust seismogenic zone and episodic tremor and slip. *Nature*, *543*(7645), 416.

Goldfinger, C., Nelson, C. H., Morey, A. E., Johnson, J. E., Patton, J. R., Karabanov, E., ... & Enkin, R. J. (2012). Turbidite event history: Methods and implications for Holocene paleoseismicity of the Cascadia subduction zone. *US Geological Survey Professional Paper*, *1661*, 170.

Goldfinger, C., Galer, S., Beeson, J., Hamilton, T., Black, B., Romsos, C., ... & Morey, A. (2017). The importance of site selection, sediment supply, and hydrodynamics: A case study of submarine paleoseismology on the Northern Cascadia margin, Washington USA. *Marine Geology*, *384*, 4-46.

Gomberg, J., Wech, A., Creager, K., Obara, K., & Agnew, D. (2016), Reconsidering earthquake scaling. *Geophysical Research Letters*, *43*(12), 6243-6251.

Gualandi, A., Serpelloni, E., & Belardinelli, M. E. (2016), Blind source separation problem in GPS time series. *Journal of Geodesy*, *90*(4), 323-341.

Gualandi, A., Nichele, C., Serpelloni, E., Chiaraluce, L., Anderlini, L., Latorre, D., ... & Avouac, J. P. (2017a), Aseismic deformation associated with an earthquake swarm in the northern Apennines (Italy). *Geophysical Research Letters*.

Gualandi, A., Perfettini, H., Radiguet, M., Cotte, N., & Kostoglodov, V. (2017b), GPS deformation related to the Mw7. 3, 2014, Papanoa earthquake (Mexico) reveals the aseismic behavior of the Guerrero seismic gap. *Geophysical Research Letters*.

Gualandi, A., Avouac, J. P., Galetzka, J., Genrich, J. F., Blewitt, G., Adhikari, L. B., ... & Liu-Zeng, J. (2017c), Pre-and post-seismic deformation related to the 2015, Mw7. 8 Gorkha earthquake, Nepal. *Tectonophysics*, *714*, 90-106.

Hayes, G. P., Meyers, E. K., Dewey, J. W., Briggs, R. W., Earle, P. S., Benz, H. M., ... & Furlong, K. P. (2017), *Tectonic summaries of magnitude 7 and greater earthquakes from 2000 to 2015* (No. 2016-1192). US Geological Survey.

Hyndman, R. D., Yamano, M., & Oleskevich, D. A. (1997), The seismogenic zone of subduction thrust faults. *Island Arc*, *6*(3), 244-260.

Hyndman, R. D., McCrory, P. A., Wech, A., Kao, H., & Ague, J. (2015), Cascadia subducting plate fluids channelled to fore-arc mantle corner: ETS and silica deposition. *Journal of Geophysical Research: Solid Earth*, *120*(6), 4344-4358.

Hyvärinen, A., & Oja, E. (1997), A fast fixed-point algorithm for independent component analysis. *Neural computation*, *9*(7), 1483-1492.

Ide, S., Beroza, G. C., Shelly, D. R., & Uchide, T. (2007), A scaling law for slow earthquakes. *Nature*, *447*(7140), 76.

Ide, S. (2012), Variety and spatial heterogeneity of tectonic tremor worldwide. *Journal of Geophysical Research: Solid Earth*, *117*(B3).

Jiang, J., and Lapusta, N. (2016), Deeper penetration of large earthquakes on seismically quiescent faults, *Science*, *352*(6291), 1293-1297.

Kanamori, H., & Anderson, D. L. (1975), Theoretical basis of some empirical relations in seismology. *Bulletin of the seismological society of America*, *65*(5), 1073-1095.

Kanamori, H., & McNally, K. C. (1982), Variable rupture mode of the subduction zone along the Ecuador-Colombia coast. *Bulletin of the Seismological Society of America*, *72*(4), 1241-1253.

Kelsey, H. M., Nelson, A. R., Hemphill-Haley, E., & Witter, R. C. (2005), Tsunami history of an

Oregon coastal lake reveals a 4600 yr record of great earthquakes on the Cascadia subduction zone. *Geological Society of America Bulletin*, *117*(7-8), 1009-1032.

Kemp, A. C., Cahill, N., Engelhart, S. E., Hawkes, A. D., & Wang, K. (2018), Revising Estimates of Spatially Variable Subsidence during the AD 1700 Cascadia Earthquake Using a Bayesian Foraminiferal Transfer Function. *Bulletin of the Seismological Society of America*, *108*(2), 654-673.

Konca, A. O., Avouac, J. P., Sladen, A., Meltzner, A. J., Sieh, K., Fang, P., ... & Natawidjaja, D. H. (2008), Partial rupture of a locked patch of the Sumatra megathrust during the 2007 earthquake sequence. *Nature*, *456*(7222), 631.

Kositsky, A. P., & Avouac, J. P. (2010), Inverting geodetic time series with a principal component analysis-based inversion method. *Journal of Geophysical Research: Solid Earth*, *115*(B3).

Loveless, J. P., & Meade, B. J. (2011). Spatial correlation of interseismic coupling and coseismic rupture extent of the 2011 Mw= 9.0 Tohoku-oki earthquake. *Geophysical Research Letters*, *38*(17).

McCaffrey, R., Qamar, A. I., King, R. W., Wells, R., Khazaradze, G., Williams, C. A., ... & Zwick, P. C. (2007), Fault locking, block rotation and crustal deformation in the Pacific Northwest. *Geophysical Journal International*, *169*(3), 1315-1340.

McCrory, P. A., Blair, J. L., Waldhauser, F., & Oppenheimer, D. H. (2012). Juan de Fuca slab geometry and its relation to Wadati-Benioff zone seismicity. *Journal of Geophysical Research: Solid Earth*, *117*(B9).

McGary, R. S., Rondenay, S., Evans, R. L., Abers, G. A., & Wannamaker, P. E. (2011, December), A joint geophysical investigation of the Cascadia subduction system in central Washington using dense arrays of passive seismic and magnetotelluric station data. In *AGU Fall Meeting Abstracts*.

Michel, S., Avouac, J. P., Jolivet, R., & Wang, L. (2017b), Seismic and Aseismic Moment Budget and Implication for the Seismic Potential of the Parkfield Segment of the San Andreas Fault. *Bulletin of the Seismological Society of America*.

Miller, M. M., Melbourne, T., Johnson, D. J., & Sumner, W. Q. (2002), Periodic slow earthquakes from the Cascadia subduction zone. *Science*, *295*(5564), 2423-2423.

Moreno, M., Rosenau, M., & Oncken, O. (2010), 2010 Maule earthquake slip correlates with pre-seismic locking of Andean subduction zone. *Nature*, *467*(7312), 198.

Nabelek, J., Trehu, A., Li, X. Q., & Fabritius, A. (1996), Lithospheric structure of the Cascadia Arc beneath Oregon. *Trans. Amer. Geophys. Un*.

Nicholson, T., Bostock, M., & Cassidy, J. F. (2005), New constraints on subduction zone structure in northern Cascadia. *Geophysical Journal International*, *161*(3), 849-859.

Obara, K. (2010). Phenomenology of deep slow earthquake family in southwest Japan: Spatiotemporal characteristics and segmentation. *Journal of Geophysical Research: Solid Earth*, *115*(B8).

Okada, Y. (1992), Internal deformation due to shear and tensile faults in a half-space. *Bulletin of the Seismological Society of America*, *82*(2), 1018-1040.

Oleskevich, D. A., Hyndman, R. D., and Wang, K. (1999), The updip and downdip limits to great subduction earthquakes: Thermal and structural models of Cascadia, south Alaska, SW Japan, and Chile, *Journal of Geophysical Research-Solid Earth*, *104*(B7), 14965-14991.

Peltier, W. R., Argus, D. F., & Drummond, R. (2015), Space geodesy constrains ice age terminal deglaciation: The global ICE-6G_C (VM5a) model. *Journal of Geophysical Research: Solid Earth*, *120*(1), 450-487.

Radiguet, M., Cotton, F., Vergnolle, M., Campillo, M., Valette, B., Kostoglodov, V., & Cotte, N. (2011), Spatial and temporal evolution of a long term slow slip event: the 2006 Guerrero Slow Slip Event. *Geophysical Journal International*, *184*(2), 816-828.

Rogers, G., & Dragert, H. (2003), Episodic tremor and slip on the Cascadia subduction zone: The chatter of silent slip. *Science*, *300*(5627), 1942-1943.

Romanowicz, B., & Ruff, L. J. (2002), On moment-length scaling of large strike slip earthquakes and the strength of faults. *Geophysical Research Letters*, *29*(12), 45-1.

Rondenay, S., Bostock, M. G., and Shragge, J. (2001), Multiparameter two-dimensional

inversion of scattered teleseismic body waves 3. Application to the Cascadia 1993 data set. *Journal of Geophysical Research: Solid Earth,* 106, 30795-30807.

Satake, K., Shimazaki, K., Tsuji, Y., & Ueda, K. (1996), Time and size of a giant earthquake in Cascadia inferred from Japanese tsunami records of January 1700. *Nature*, *379*(6562), 246.

Satake, K., Wang, K., & Atwater, B. F. (2003), Fault slip and seismic moment of the 1700 Cascadia earthquake inferred from Japanese tsunami descriptions. *Journal of Geophysical Research: Solid Earth*, *108*(B11).

Schmalzle, G. M., McCaffrey, R., & Creager, K. C. (2014), Central Cascadia subduction zone creep. *Geochemistry, Geophysics, Geosystems*, *15*(4), 1515-1532.

Schmidt, D. A., & Gao, H. (2010), Source parameters and time-dependent slip distributions of slow slip events on the Cascadia subduction zone from 1998 to 2008. *Journal of Geophysical Research: Solid Earth*, *115*(B4).

Scholz, C. H. (1998), Earthquakes and friction laws. *Nature*, *391*(6662), 37.

Scholz, C. H. (2002), *The mechanics of earthquakes and faulting*. Cambridge university press.

Segall, P., & Bradley, A. M. (2012), Slow-slip evolves into megathrust earthquakes in 2D numerical simulations. *Geophysical Research Letters*, *39*(18).

Tapley, B. D., Bettadpur, S., Ries, J. C., Thompson, P. F., & Watkins, M. M. (2004), GRACE measurements of mass variability in the Earth system. *Science*, *305*(5683), 503-505.

Utsu, T. (1966), A Statistical Significance Test of the Difference in b-value between Two Earthquake Groups, *J. Phys. Earth*, *14*(2), 37–40, doi:10.4294/jpe1952.14.37.

Wada, I., Wang, K., He, J., & Hyndman, R. D. (2008), Weakening of the subduction interface and its effects on surface heat flow, slab dehydration, and mantle wedge serpentinization. *Journal of Geophysical Research: Solid Earth*, *113*(B4).

Wang, K., He, J., Dragert, H., & James, T. S. (2001), Three-dimensional viscoelastic interseismic deformation model for the Cascadia subduction zone. *Earth, Planets and Space*, *53*(4), 295-306.

Wang, K., Wells, R., Mazzotti, S., Hyndman, R. D., & Sagiya, T. (2003), A revised dislocation model of interseismic deformation of the Cascadia subduction zone. *Journal of Geophysical Research: Solid Earth*, *108*(B1).

Wang, P. L., Engelhart, S. E., Wang, K., Hawkes, A. D., Horton, B. P., Nelson, A. R., & Witter, R. C. (2013), Heterogeneous rupture in the great Cascadia earthquake of 1700 inferred from coastal subsidence estimates. *Journal of Geophysical Research: Solid Earth*, *118*(5), 2460-2473.

Wang, K., & Tréhu, A. M. (2016), Invited review paper: Some outstanding issues in the study of great megathrust earthquakes—The Cascadia example. *Journal of Geodynamics*, *98*, 1-18.

Wech, A. G., & Bartlow, N. M. (2014), Slip rate and tremor genesis in Cascadia. *Geophysical Research Letters*, *41*(2), 392-398.

Wech, A. G., Creager, K. C., Houston, H., & Vidale, J. E. (2010), An earthquake-like magnitude-frequency distribution of slow slip in northern Cascadia. *Geophysical Research Letters*, *37*(22).

Wech, A. G., & Creager, K. C. (2007), Cascadia tremor polarization evidence for plate interface slip. *Geophysical Research Letters*, *34*(22).

Wiemer, S., and M. Wyss (2000), Minimum magnitude of completeness in earthquake catalogs: Examples from Alaska, the Western United States, and Japan, *Bull. Seismol. Soc. Am.*, *90*(4), 859–869, doi:10.1785/0119990114.

Woessner, J., and S. Wiemer (2005), Assessing the quality of earthquake catalogues: Estimating the magnitude of completeness and its uncertainty, *Bull. Seismol. Soc. Am.*, *95*(2), 684–698, doi:10.1785/0120040007.

Xu, X., Dong, D., Fang, M., Zhou, Y., Wei, N., & Zhou, F. (2017), Contributions of thermoelastic deformation to seasonal variations in GPS station position. *GPS Solutions*, *21*(3), 1265-1274.

SUPPLEMENT

S.1. Trajectory Model

For every position time series $x_j(t)$, with j = 1, …, M, we perform a least square minimization to find the optimal parameters of the following model:

$$x_j(t) = x_{0j} + v_{0j}t + A_{1j}^{sin}sin(f_1 t + \phi_{1j}) + A_{2j}^{sin}sin(f_2 t + \phi_{2j}) + \sum_{k}^{N_{instr}} A_{jk}^{instr} H(t - t_k) + \sum_{k}^{N_{eq}} H(t - t_k)\left[A_{jk}^{co} + A_{jk}^{post}\left(1 - exp((t - t_k)/\tau_{jk})\right)\right]. \quad \text{(Eq. 2.S1)}$$

The model includes a linear trend with intercept x_{0j} and slope v_{0j}, two seasonal signals with fixed half-year ($1/f_1$) and one year ($1/f_2$) periods defined by the amplitudes A_{*j}^{sin} and phases ϕ_{*j}, instrumental offsets, co-seismic offsets and post-seismic displacement. The list of instrumental offsets is taken from the NGL database, and the offsets are described by the parameters A^{instr}_{jk}. The list of earthquakes potentially affecting a certain station is a reduced version of that present in the NGL database. In our study, a potential step record appears when the epicentral distance is less than 10^(M/3), where M is the earthquake magnitude, instead of 10^(M/2 - 0.8) originally used by NGL. The number of effective events is thus 11 (Table S1), and the co-seismic steps are described by the parameters A^{co}_{jk}. Finally, the post-seismic deformation is approximated with an exponential decay function for which the amplitude A^{post}_{jk} and the relaxation time τ_{jk} are estimated. We fix the post-seismic amplitude for the M_w 5.9 2010/02/04 event to 0 because it was preceded by a M_w 6.5, and the estimation of multiple exponential decays seems to compromise the slope of the linear trend. For the same reason, we impose an upper bound of 3 yr on the relaxation time τ_{jk} for all the listed events.

S.2. Measurements of SSE duration

In section 4.2, we applied an equiripple low-pass filter to the slip deficit, $\delta_{deficit}$, with passband frequency of 1/21 days^{-1}, stopband of 1/35 days^{-1}, passband ripple of 1dB with 60dB of stopband attenuation. Calling $\dot{\delta}_{deficit}$ the slip rate deficit on the megathrust with respect to the long-term creep, SSEs are detected when $\dot{\delta}_{deficit}(p,t) < V_{thresh}$, where V_{thresh} corresponds to a slip deficit rate threshold set to -40 mm/yr. The applied filter removes any

SSE with a duration under 3 weeks and bias the estimation of the start and end of moderate SSEs, thus their duration.

To attenuate the duration estimation bias of the 64 SSEs detected by the method described above, we proceed as follow. Starting from the first automatic detection [t'_{start}, t'_{end}], we consider an enlarged time span [t_{start}, t_{end}] = [t'_{start} – 35 days, t_{end} + 35 days]. Instead of applying a low-pass filter, which truncates all events with frequency higher than the specified passband frequency, we perform a zero-phase digital filtering on the rough $\delta_{deficit}$ using a 8-days window. We then convert $\delta_{deficit}$ into moment deficit, $M_{0deficit}$, taking a shear modulus $\mu = 30GPa$ and calculate the moment deficit rate, $\dot{M}_{0deficit}$ by taking the derivative in time. Note that, even by focusing directly on a specified SSE area, it is not possible to detect the onset and end of a SSE if looking at its global moment rate function. Indeed, the onset of a SSE can be masked by neighbouring sub-faults with positive $\dot{M}_{0deficit}$ (associated with loading). It is thus important to look at sub-faults individually to detect the onset and end of a SSE.

The complex $\dot{M}_{0deficit}$ signal makes it very difficult to establish an automated detection of the SSEs' time-boundaries, and we thus apply two manual methods to estimate the onset and end of SEEs. 1) The first method consists again in taking a slip deficit rate threshold,V_{thresh}, set to -40 mm/yr, and determine the timing of the first and last sub-fault with $\dot{\delta}_{deficit} < V_{thresh}$. This method is generally straight forward but provides an underestimation of the SSE's duration. 2) Thus we introduce also a second method which is an estimation of the timing of the first and last subfault when $\dot{\delta}_{deficit} < 0$. However, due to the noise in the slip time series, there is no simple way to determine this timing. We choose to consistently take the onsets and end of SSEs that determine their maximum duration possible regarding the data available. The two described methods provide a bracket on SSEs' duration (Figure 2.S11 and Table 2.S6).

S.3. Measurements of SSE rupture area and aspect ratio

The rupture areas of SSEs are defined as the sum of the sub-faults areas which experienced $\dot{\delta}_{deficit} < V_{thresh}$, extended to their neighboring sub-faults, based on the 21-days filtered $\dot{\delta}_{deficit}$. To evaluate the SSEs aspect ratio, the curved geometry of some SSEs needs to be taken into account (typically those over latitude 47°). We thus estimate the SSEs length and width relative to a representative line of the average along-strike location of SSEs

(Figure 2.9). For each SSE, the intersections between the representative line and its contour are then assumed to be its most Northern and Southern location. The distance between those points along the representative line is then assumed to be the SSE length. The SSEs width estimation is based on the nodes of their contour line. The average distance between those nodes and the SSEs representative line is assumed to correspond to half the SSEs width.

The SSEs area and contour estimations are sensitive to the inversion regularisation, the $\delta_{deficit}$ filtering and the chosen value for V_{thresh}. The SSEs aspect ratio are additionally dependent on the SSEs location relative to the representative line. Indeed, certain SSEs are quite small and their contour are thus not centred over the SSEs representative line or do not even cut it.

Table 2.S1. *Selection of stations for which we correct for postseismic deformation.*

Section	Stations
North	HOLB, BCPH, BCOV, ELIZ, WOST, NTKA, GLDR, TFNO, QUAD, UCLU, BAMF, PTAL
South	All stations within this section

Table 2.S2. *Correlation between GRACE-derived and GPS derived seasonal components.*

vbICA Components	GPS 1	GPS 2	GPS 3	GPS 4
GRACE 1	0.6736	0.1299	0.4053	0.4732
GRACE 2	0.2217	0.2514	0.0438	0.4161
GRACE 3	0.1815	0.1964	0.2732	0.4965

Table 2.S3. *Node coordinates of the representative line of the average along-strike location of SSEs.*

Node #	Longitude	Latitude
1	-125.805	49.3502
2	-125.13	49.0498
3	-124.464	48.7454
4	-123.968	48.52
5	-123.639	48.2797
6	-123.311	47.9643
7	-123.144	47.4876
8	-123.2	47.0
9	-123.291	46.8491
10	-123.277	46.0523
11	-123.416	45.2541
12	-123.551	44.4556
13	-123.545	44.1369
14	-123.676	43.3381
15	-123.656	42.3816
16	-123.205	41.2694
17	-122.83	40.4742
18	-122.628	39.6769

Table 2.S4. *Location of SSEs.*

Event	Segments	Comments
1	1	Coast
2	1	Coast
3	1, 2 ,3, 4	
4	12	
5	3, 4, 5	
6	6	
7	8	
8	10, 11, 12	Half 10
9	11, 12, 13	
10	1, 2	
11	1	Coast
12	10	
13	13	
14	1	Small: Not usual
15	9, 10, 11	
16	1, 2	
17	1	Coast
18	8	
19	3, 4, 5, 6	
20	5	Coast
21	3	Coast
22	9	
23	10	
24	1, 2	
25	1	Coast
26	8	
27	9	
28	4, 5, 6	
29	1	Small alone
30	1, 2, 3	
31	1	Coast
32	1	Small alone
33	11, 12	
34	1, 2	
35	1	Coast
36	8	
37	11, 12, 13	
38	3, 4, 5	
39	6	
40	10	
41	1, 2	
42	1	Coast

43	7, 8	Top of 8
44	2,3	Small between the 2 Segments
45	3	
46	4	
47	10, 11, 12, 13	
48	2	
49	1	Coast
50	13	
51	1, 2	
52	1	
53	9, 10, 11	
54	1, 2, 3, 4, 5, 6	
55	0	Top North Asperity
56	11, 12	
57	1	Coast
58	0	Top North Asperity
59	1, 2	
60	1	Coast
61	1	Coast
62	12	
63	13	
64	10	

Table 2.S5. *Boundaries of segments.*

Segment	Upper Limit (Latitude)
1	Latitude=Longitude+179.4
2	Latitude=Longitude+175.4
3	47.01
4	46.53
5	45.89
6	44.94
7	44.1
8	43.55
9	42.85
10	42.15
11	41.11
12	41.5
13	40.63

Table 2.S6. *SSEs duration manual estimation. The start and end pic for the minimum duration estimation are determined by the timing of the first and last sub-fault with* $\dot{\delta}_{deficit} < V_{thresh}$. *The start and end pic for the maximum duration estimation are determined by the timing of the first and last sub-fault when* $\dot{\delta}_{deficit} < 0$.

SSE #	Start (Max Duration)	Start (Min Duration)	End (Min Duration)	End (Max Duration)
1	2007.049	2007.035	2007.098	2007.158
2	2007.038	2007.027	2007.091	2007.131
3	2007.029	2007.027	2007.117	2007.158
4	2007.081	2007.076	2007.136	2007.15
5	2007.448	2007.394	2007.5	2007.539
6	2007.457	2007.388	2007.495	2007.528
7	2007.484	2007.462	2007.577	2007.593
8	2007.541	2007.487	2007.585	2007.607
9	2008.237	2008.223	2008.33	2008.374
10	2008.33	2008.316	2008.442	2008.461
11	2008.344	2008.33	2008.412	2008.464
12	2008.538	2008.491	2008.557	2008.617
13	2008.921	2008.886	2008.962	2008.972
14	2009.146	2009.121	2009.184	2009.217
15	2009.179	2009.17	2009.212	2009.25
16	2009.322	2009.31	2009.428	2009.45
17	2009.335	2009.318	2009.376	2009.439
18	2009.485	2009.433	2009.578	2009.589
19	2009.587	2009.552	2009.693	2009.702
20	2009.598	2009.559	2009.625	2009.685
21	2009.587	2009.565	2009.63	2009.68
22	2010.0958	2010.0679	2010.1287	2010.1752
23	2010.09858	2010.06846	2010.1287	2010.1971
24	2010.5969	2010.5804	2010.6927	2010.7324
25	2010.6051	2010.5613	2010.6544	2010.6845
26	2011.01	2010.9966	2011.069	2011.087
27	2011.372	2011.344	2011.396	2011.489
28	2011.425	2011.38	2011.598	2011.61
29	2011.432	2011.344	2011.451	2011.476
30	2011.555	2011.533	2011.678	2011.733
31	2011.607	2011.563	2011.656	2011.736
32	2011.626	2011.604	2011.662	2011.736
33	2011.741	2011.733	2011.837	2011.864
34	2012.619	2012.609	2012.779	2012.847
35	2012.708	2012.598	2012.746	2012.801
36	2012.735	2012.719	2012.831	2012.842
37	2012.753	2012.743	2012.842	2012.853
38	2013.181	2013.132	2013.305	2013.379
39	2013.19	2013.144	2013.236	2013.253
40	2013.562	2013.537	2013.636	2013.661
41	2013.682	2013.674	2013.776	2013.781
42	2013.71	2013.677	2013.765	2013.778
43	2014.033	2014.016	2014.2	2014.216
44	2014.159	2014.119	2014.192	2014.241
45	2014.438	2014.419	2014.485	2014.498
46	2014.43	2014.408	2014.49	2014.512
47	2014.616	2014.567	2014.708	2014.724

48	2014.649	2014.627	2014.712	2014.746
49	2014.66	2014.613	2014.693	2014.728
50	2014.679	2014.625	2014.709	2014.756
51	2014.871	2014.857	2014.975	2014.977
52	2014.909	2014.862	2014.942	2014.969
53	2015.791	2015.75	2015.832	2015.851
54	2015.963	2015.895	2016.168	2016.174
55	2015.979	2015.897	2016.001	2016.041
56	2015.925	2015.919	2015.993	2015.999
57	2015.975	2015.963	2016.059	2016.114
58	2016.42	2016.404	2016.464	2016.481
59	2017.124	2017.039	2017.274	2017.277
60	2017.077	2017.072	2017.157	2017.198
61	2017.209	2017.113	2017.25	2017.277
62	2017.305	2017.294	2017.403	2017.422
63	2017.306	2017.294	2017.343	2017.436
64	2017.578	2017.51	2017.589	2017.606

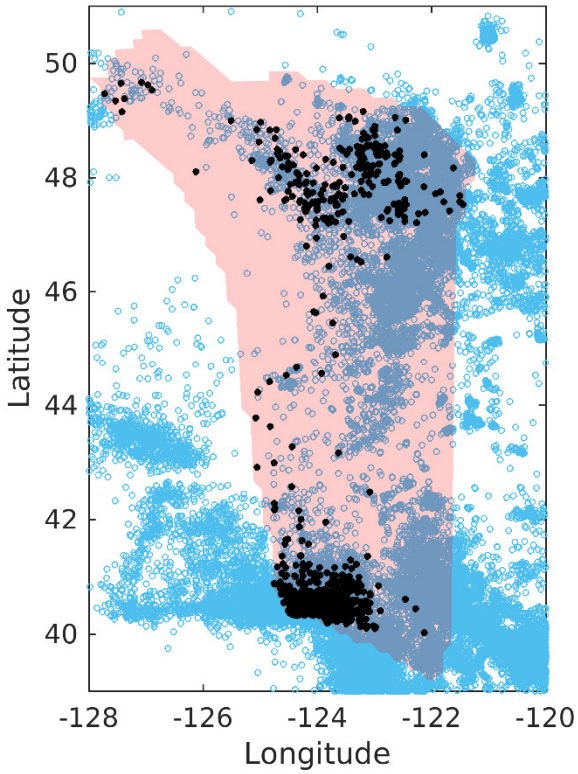

Figure 2.S1. *Seismicity map. The pink shading represents the fault location [McCrory et al., 2012]. The blue dots correspond to the ANSS earthquake catalogue from 1984 to 2018.22. The black dots correspond to earthquake within 5 km of the fault geometry.*

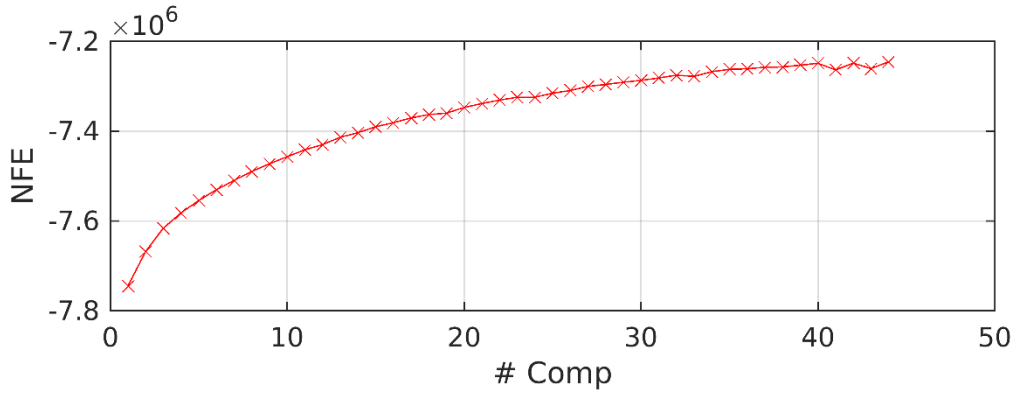

Figure 2.S2. *NFE evolution as a function of the total number of vbICA components. The curve decreases for the first time passing from 32 to 33 components. We thus selected 32 components as our final number of components.*

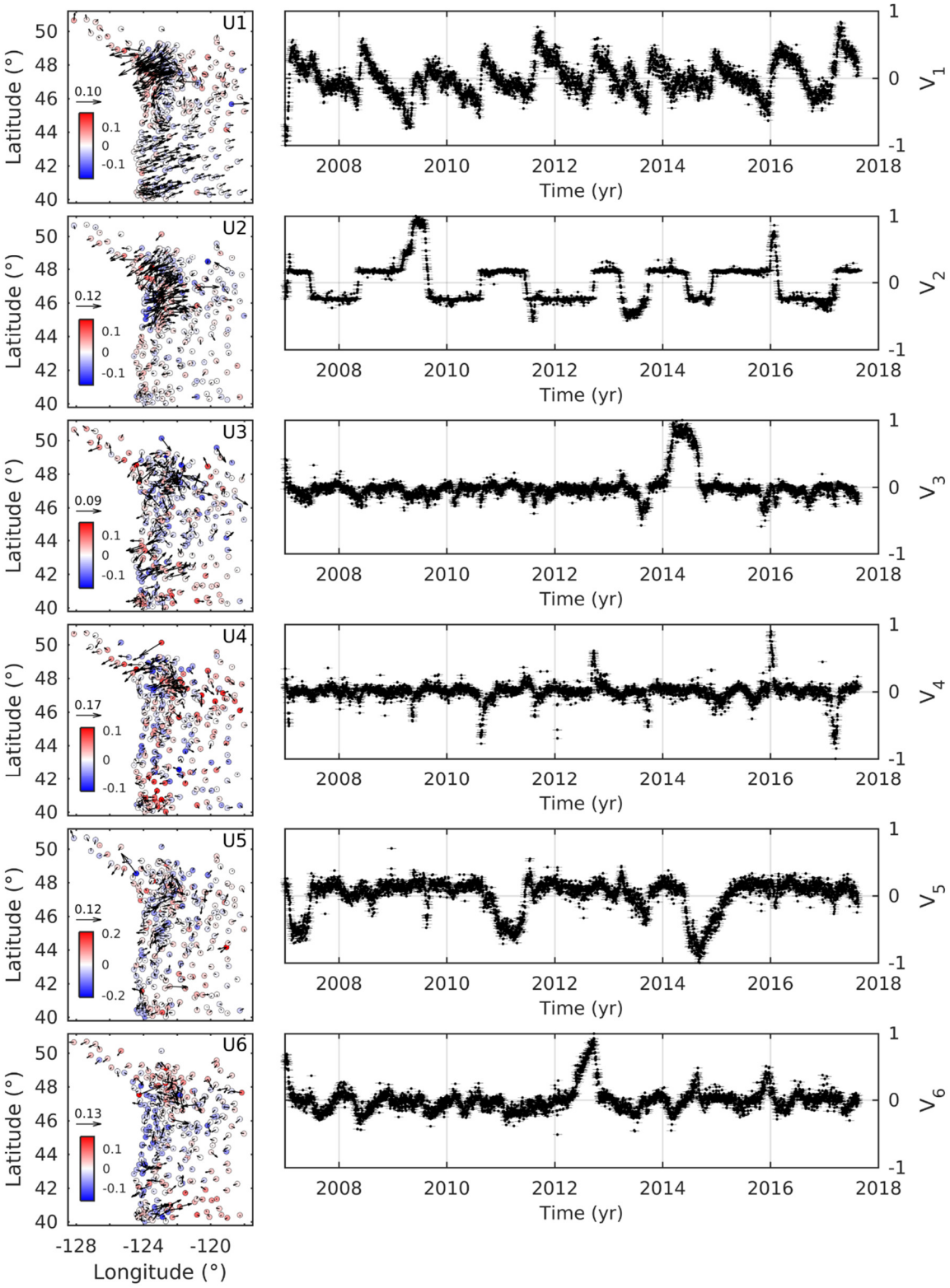

Figure 2.S3. *Spatial pattern and temporal evolution of each 32 components of Cascadia (section 3.1.4). Left column panels indicate the components spatial pattern (matrix U). The arrows and the coloured dots indicate horizontal and vertical motion, respectively. Right column panels indicate the components temporal evolution (matrix V). We consider component 1 to 15 to be related to SSE, 16 and 25 to be noise and 26 to 32 to be a local effects.*

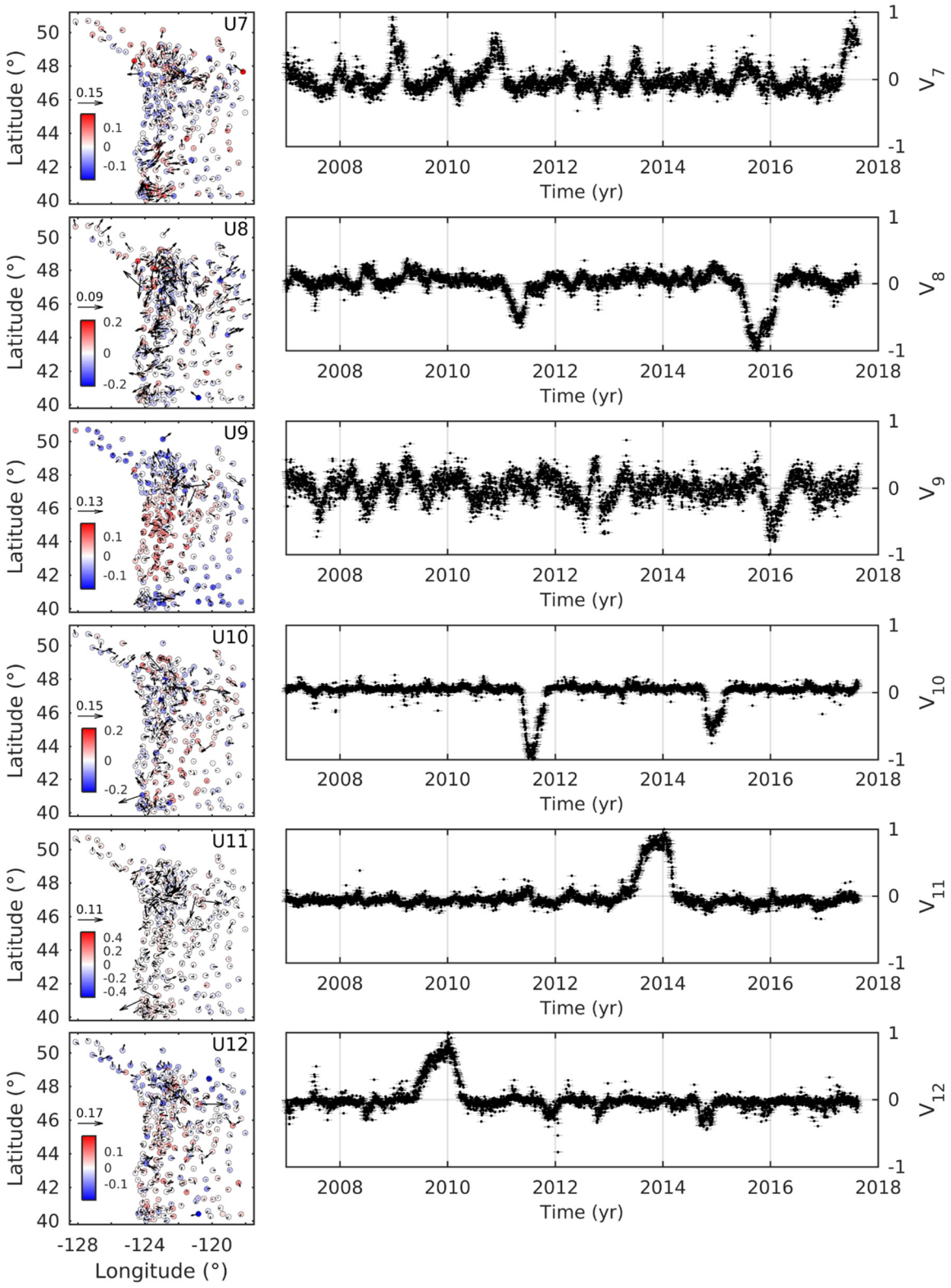

Figure 2.S3. *(Continued)*

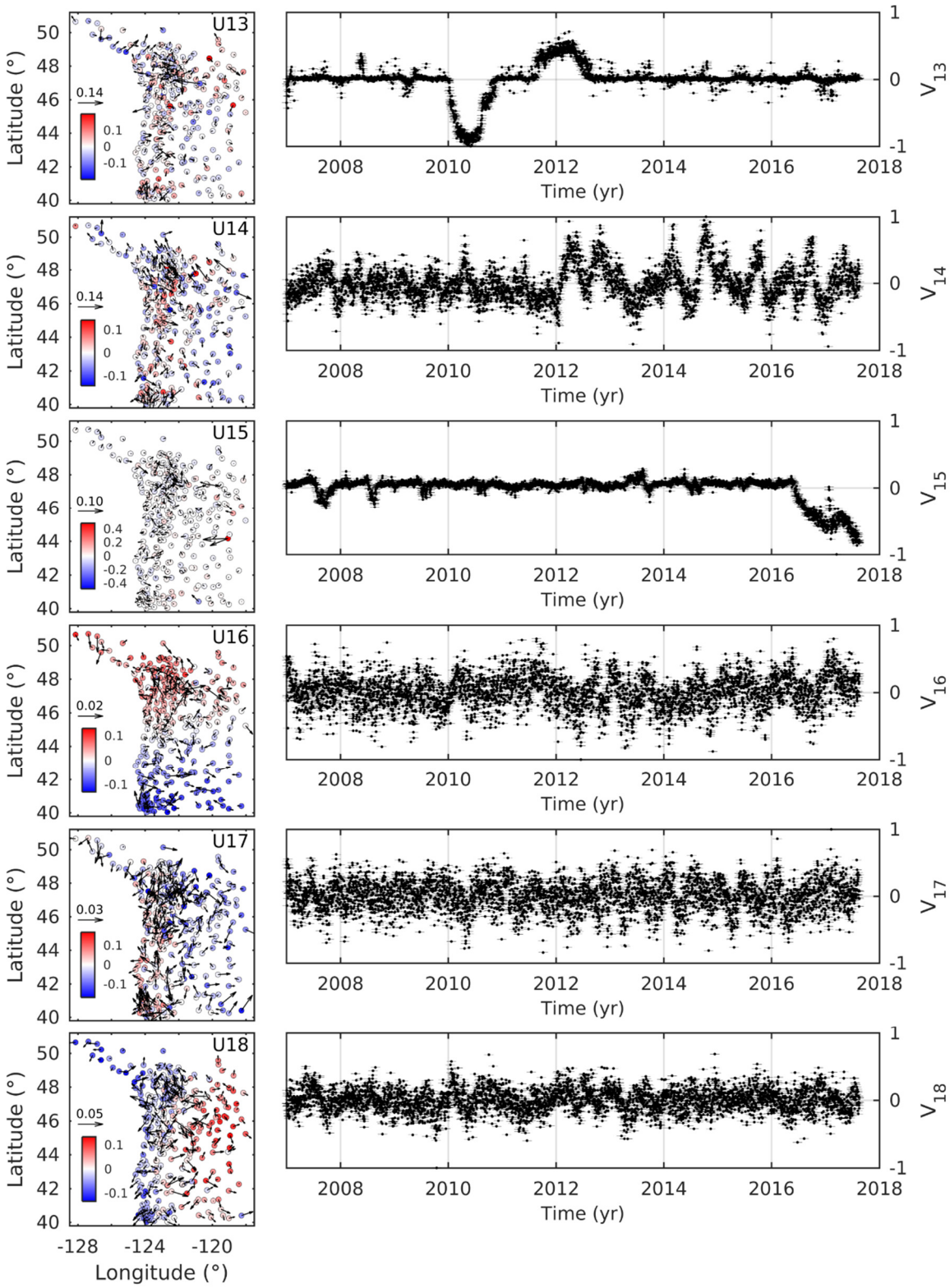

Figure 2.S3. *(Continued)*

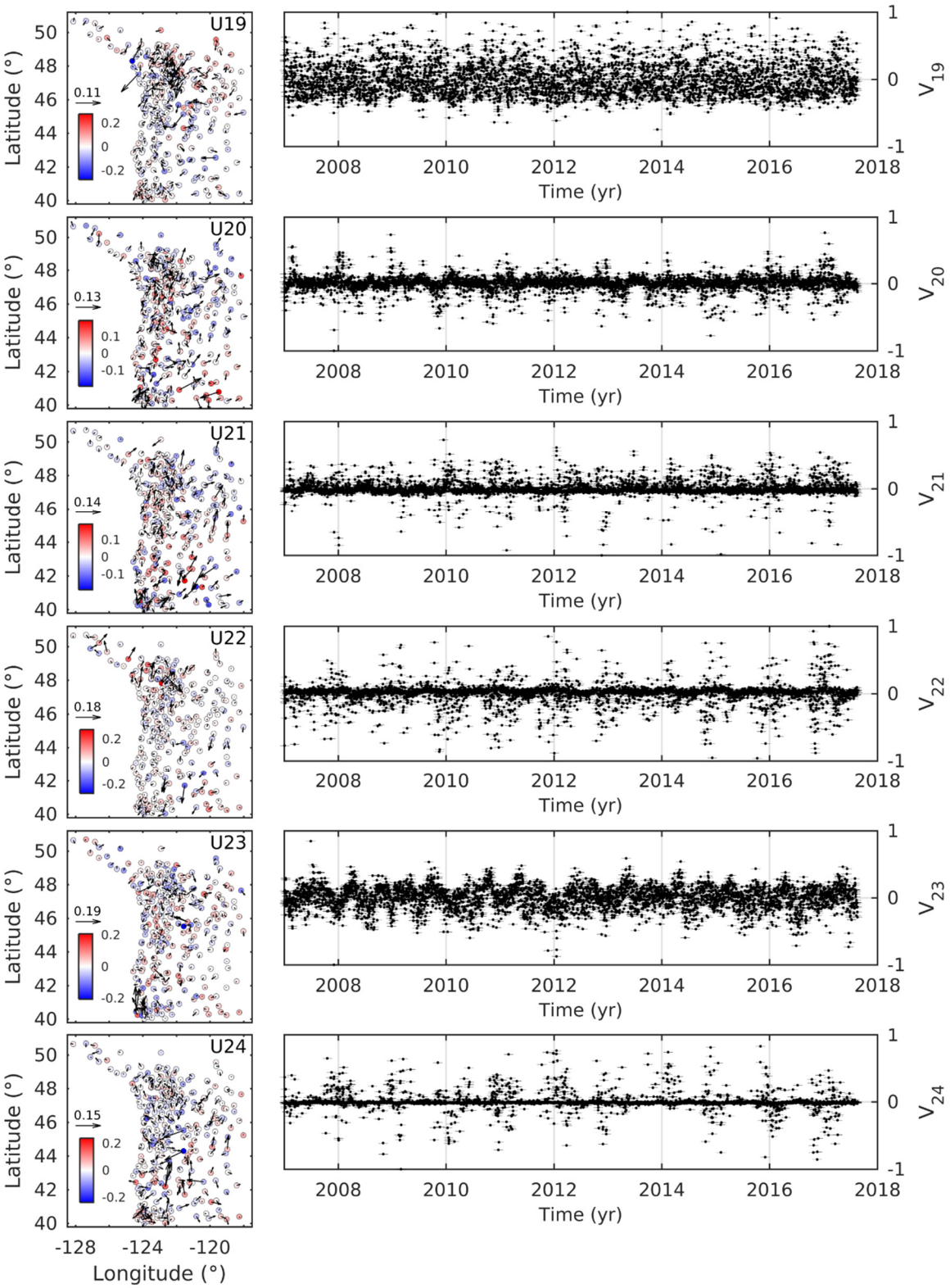

Figure 2.S3. *(Continued)*

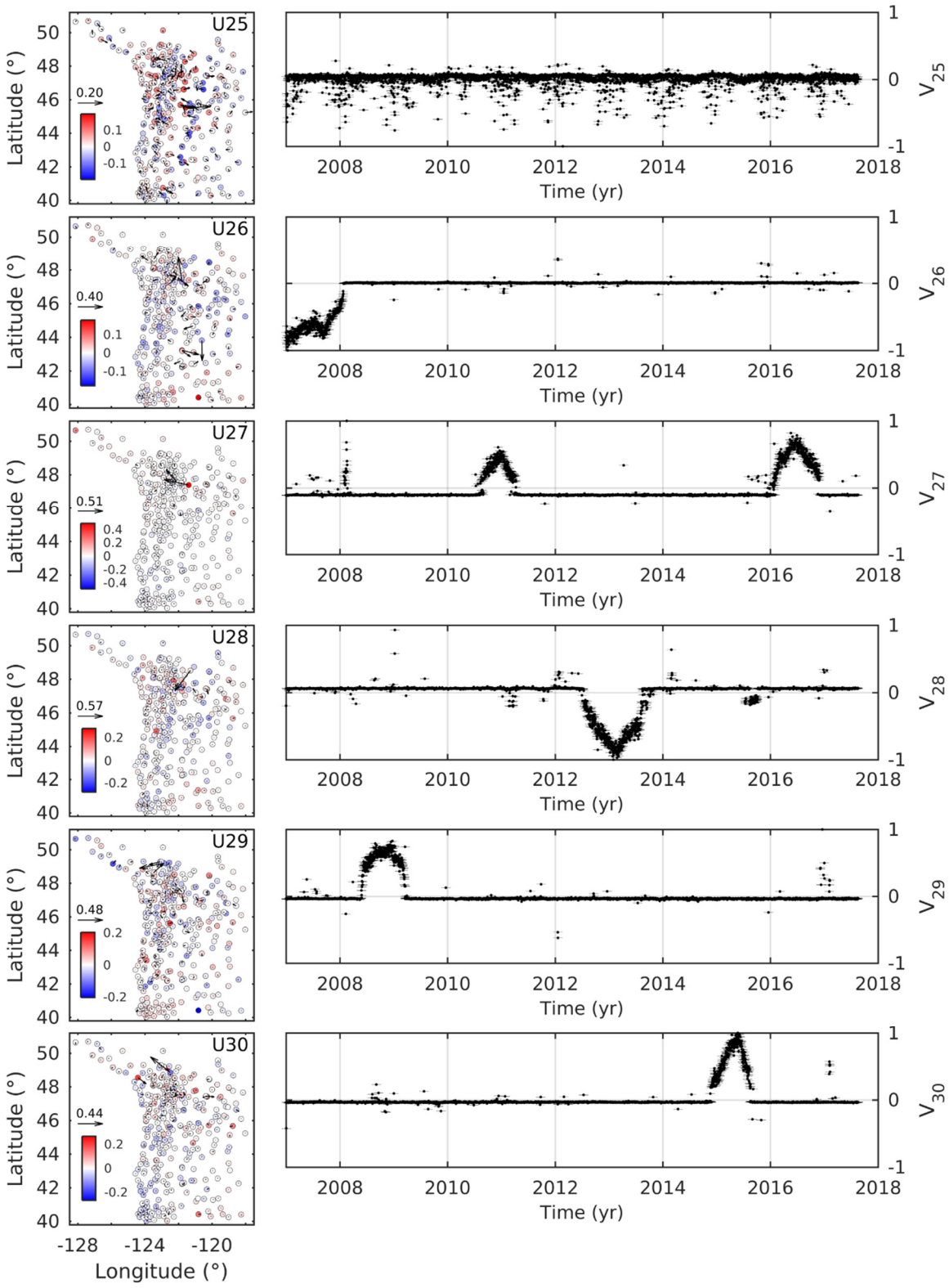

Figure 2.S3. *(Continued)*

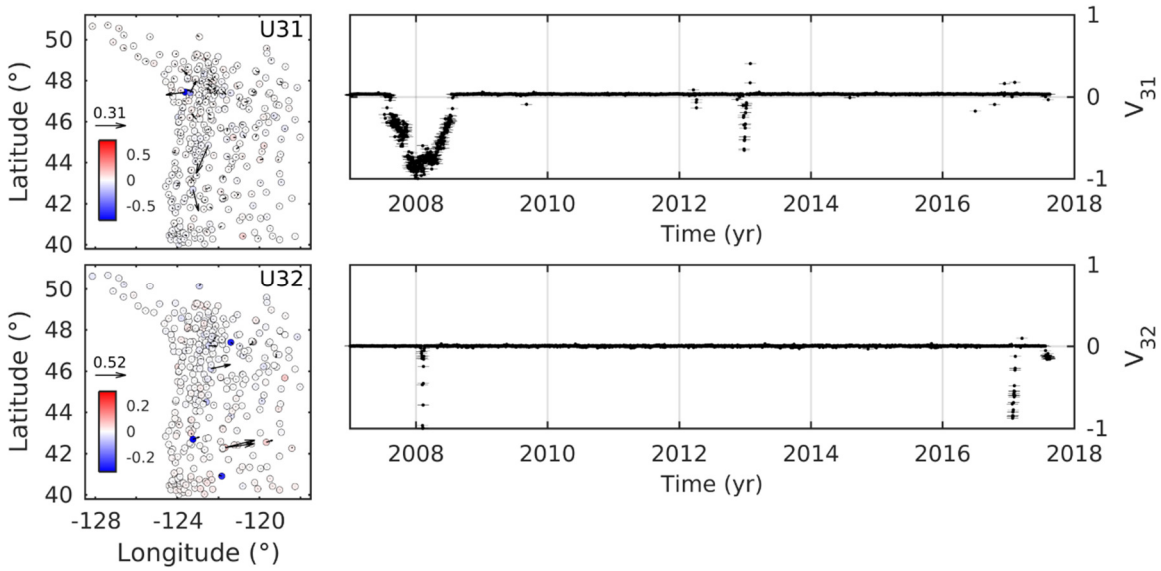

Figure 2.S3. *(Continued)*

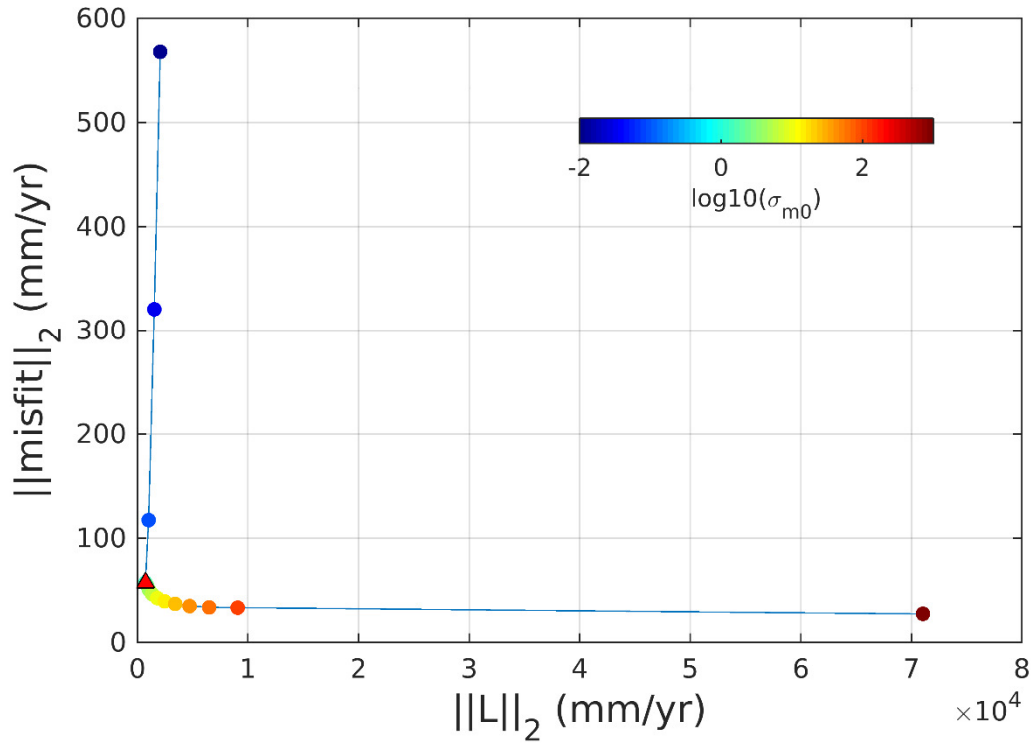

Figure 2.S4. *L-curve plot for the coupling map. On the x-axis the L_2 norm of the model obtained from the inversion of the linear system $U = GL$, where G is the matrix containing the Green's functions; on the y-axis the L_2 norm of the misfit between the spatial distribution of the inverted IC and the predicted value from the model. The colour scale indicates the values of σ_0, ranging from 10^{-2} to 10^3. The red triangle indicates the selected value for the inversion, corresponding to $\sigma_0 = 10^{-0.1}$. All the calculations have been performed with a fix smoothed parameter, $\lambda = 15.154\ km$. Fixed rake constraints have been imposed using the block model plate rate directions from Schmaltze et al. [2014]. No positivity constraints have been imposed.*

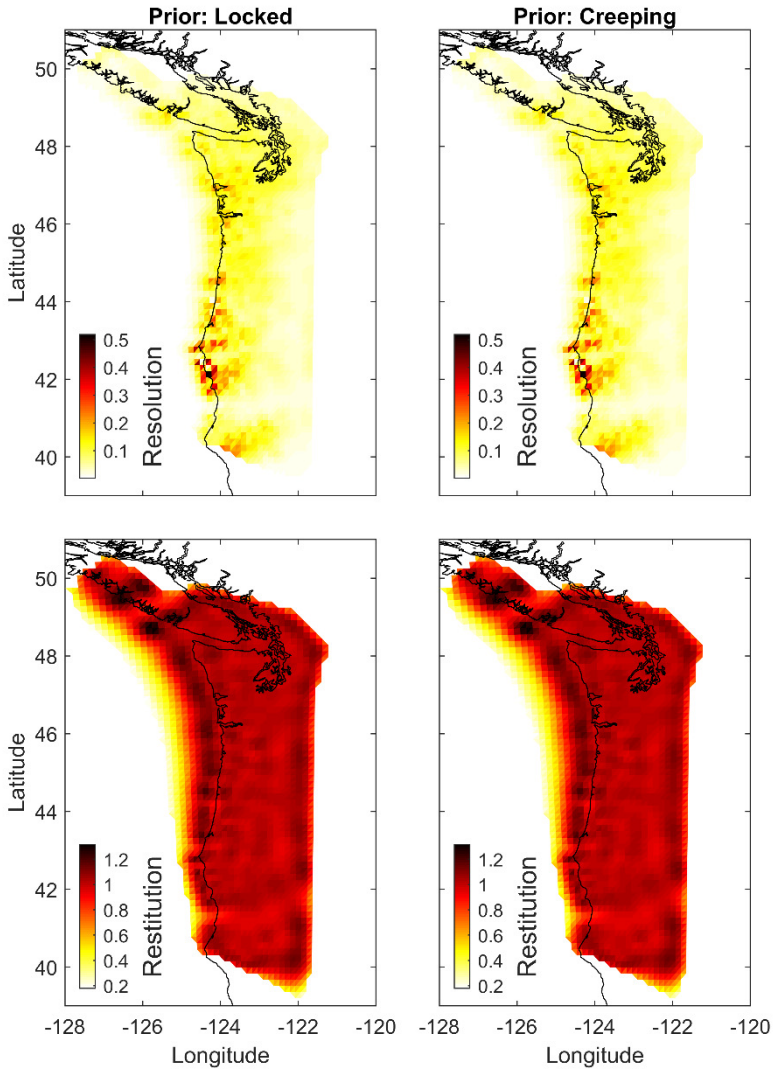

Figure 2.S5. *Resolution and restitution maps of the coupling inversions for both the locked (a,c) and creeping (b,d) a priori cases.*

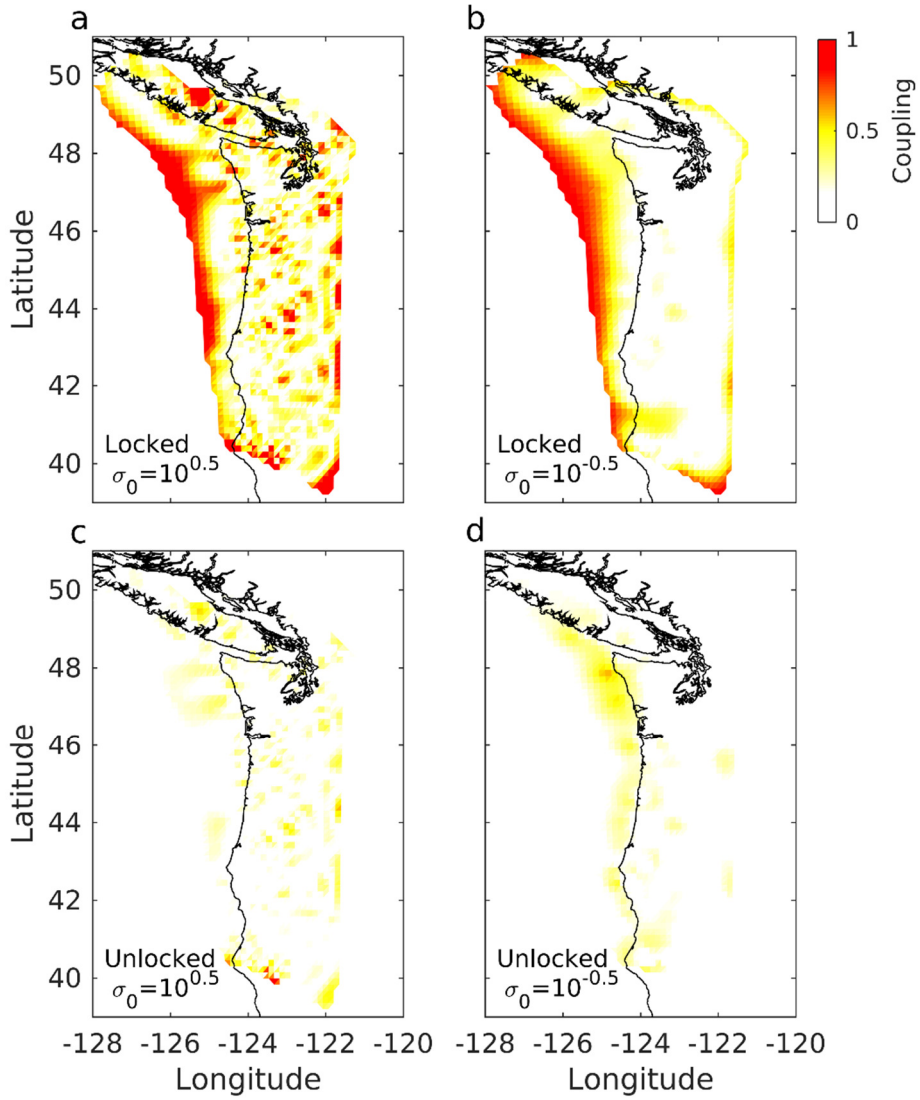

Figure 2.S6. *Coupling inversion sensitivity to σ_0. (a) and (b) show the results for inversions using a locked fault a priori and taking $\sigma_0=10^{0.5}$ and $\sigma_0=10^{-0.5}$, respectively. (c) and (d) show the results for inversions using a creeping fault a priori and taking $\sigma_0=10^{0.5}$ and $\sigma_0=10^{-0.5}$, respectively.*

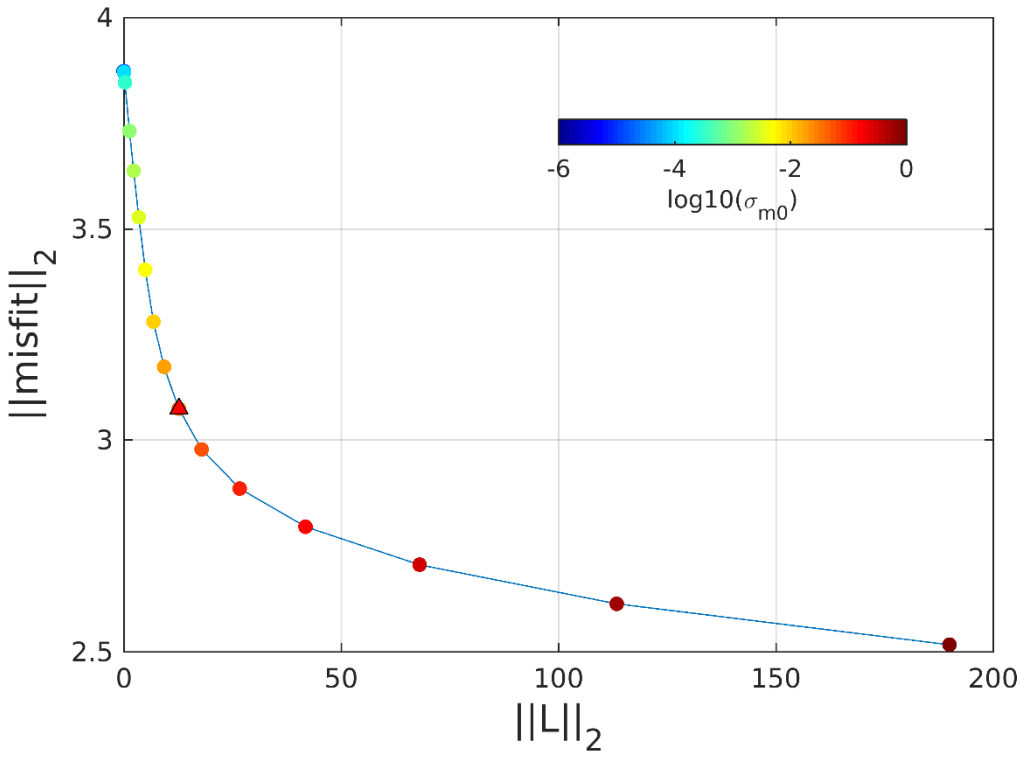

Figure 2.S7. *L-curve plot for the SSEs kinematics. On the x-axis the L_2 norm of the model obtained from the inversion of the linear system $U_{IC} = GL$, where G is the matrix containing the Green's functions; on the y-axis the L_2 norm of the misfit between the spatial distribution of the inverted IC and the predicted value from the model. Both quantities are non-dimensional. The colour scale indicates the values of σ_0, ranging from 10^{-6} to 1. The red triangle indicates the selected value for the inversion, corresponding to $\sigma_0 = 10^{-1.5}$. All the calculations have been performed with a fix smoothed parameter, $\lambda = 15.154\ km$. No positivity or fixed rake constraints have been imposed.*

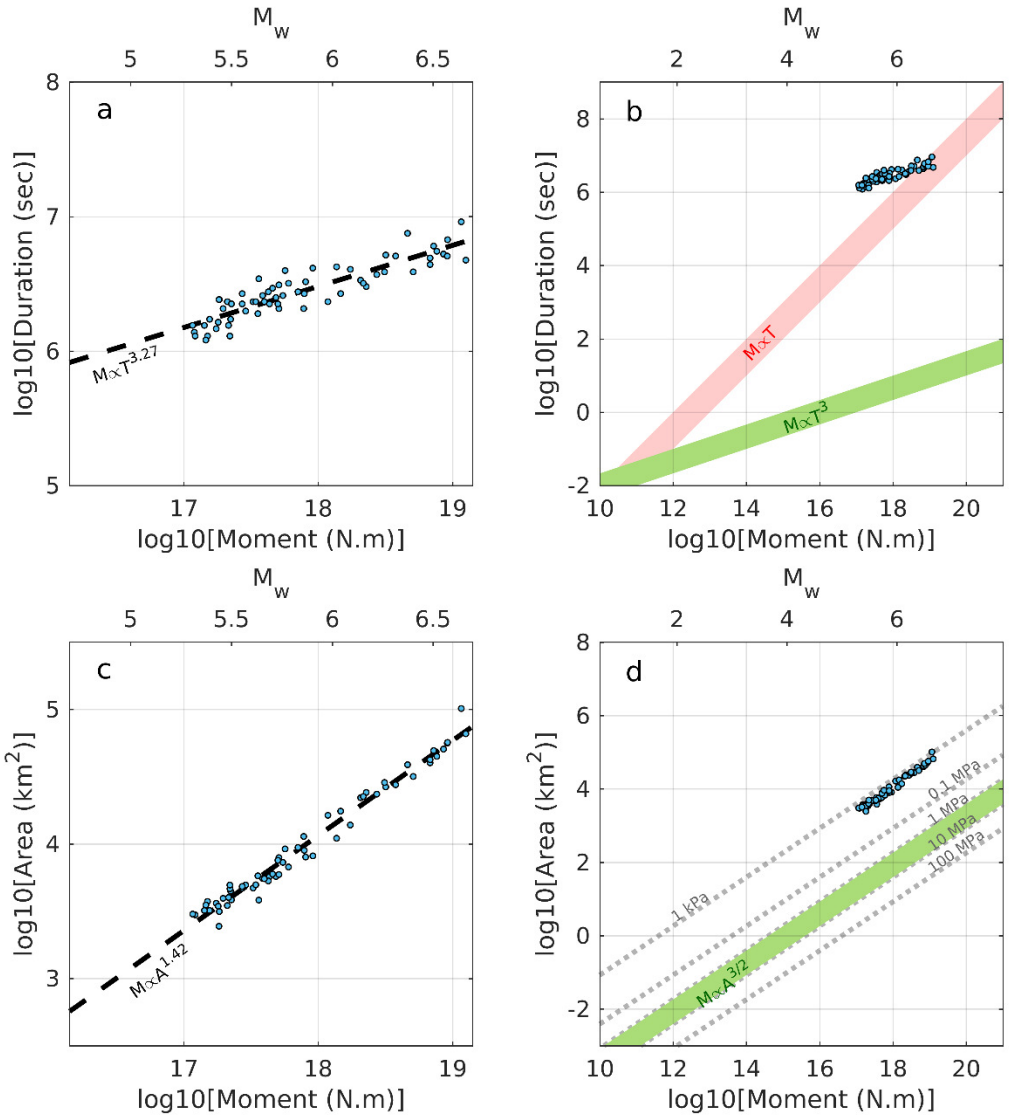

Figure 2.S8. *Moment-Duration and Moment-Area scaling laws for automatic measurements. (a) Relationship between the moment released by SSEs and their duration. The black dashed line shows the best linear fit. (b) Comparison with the scaling laws for slow (red shading) and regular earthquakes (green shading) proposed by Ide et al. [2007]. (c) Relationship between the moment released by SSEs and their rupture area. The black dashed line shows the best linear fit. (b) Comparison with the scaling laws regular earthquakes (green shading). Stress drop iso- lines estimated base on the circular crack model.*

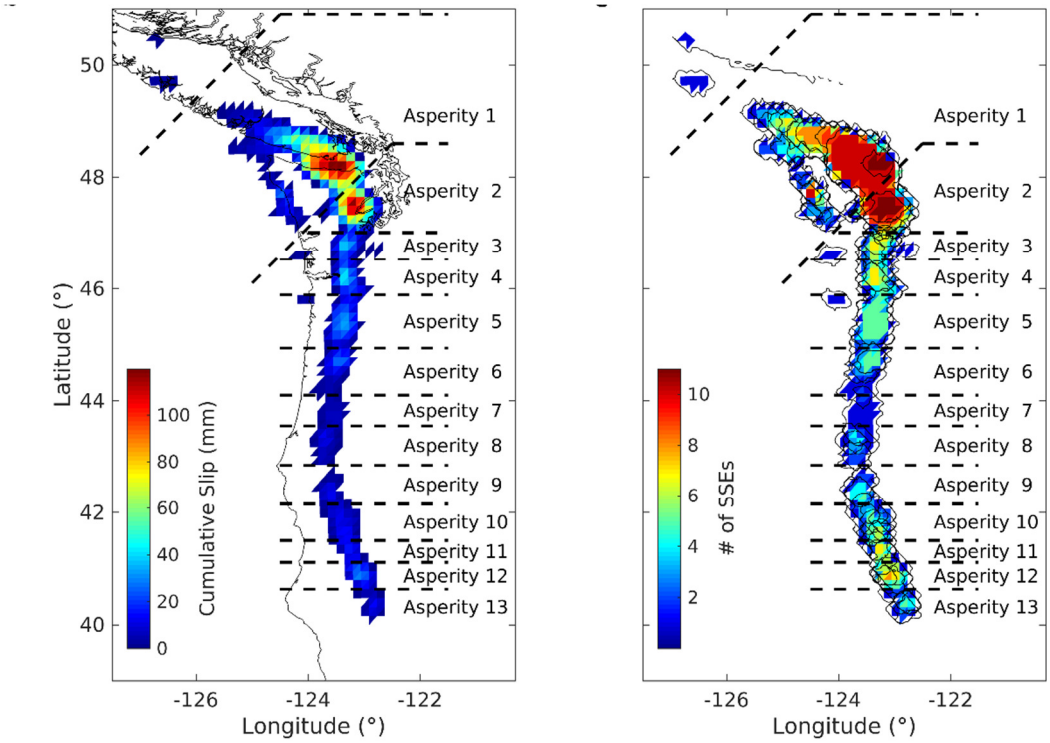

Figure 2.S9. *(a) SSEs cumulative slip. (b) Map indicating the number of time a sub-fault has experienced a SSE. The black contours delimit the extent of each SSE. The dashed black lines in (a) and (b) correspond to the selection of segments.*

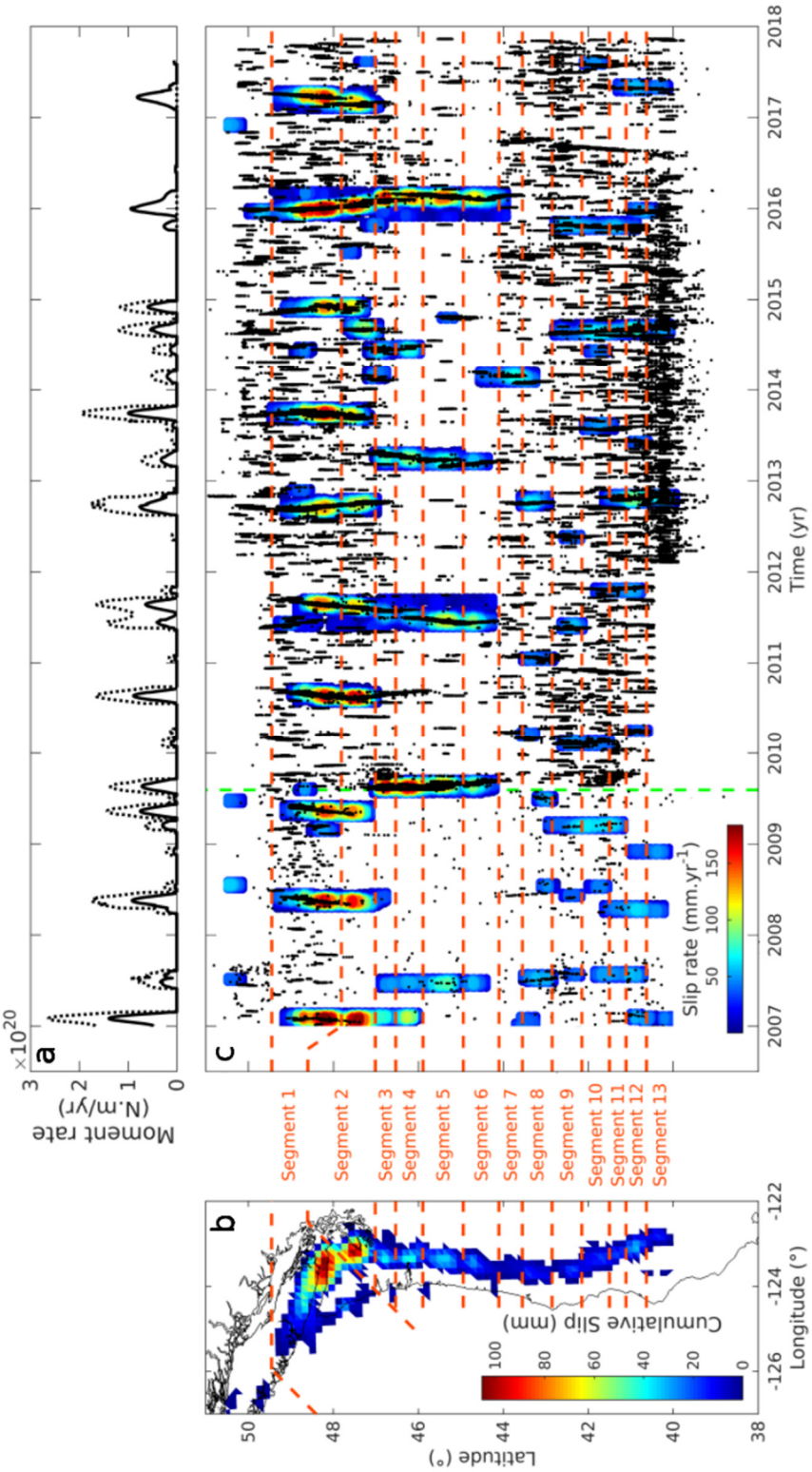

Figure 2.S10. *(a) Combined moment rate functions of all the 81 detected SSEs using $V_{tresh} = 35$ mm/yr. The full and dashed black line correspond to the moment rate taking and without taking into account interseismic loading during SSEs, respectively. A conservative interseismic loading is taken in this case, assuming a fully locked fault loading during SSEs. (b) SSEs cumulative slip. (c) Occurrence of SSEs (colour shading) as a function of time. The black dots indicate tremors. The catalogue from Ide et al. (2012) is used until 2009.595, the catalogue from PNSN is used thereafter. The dashed pink lines in (b) and (c) correspond to the initial selection of segments.*

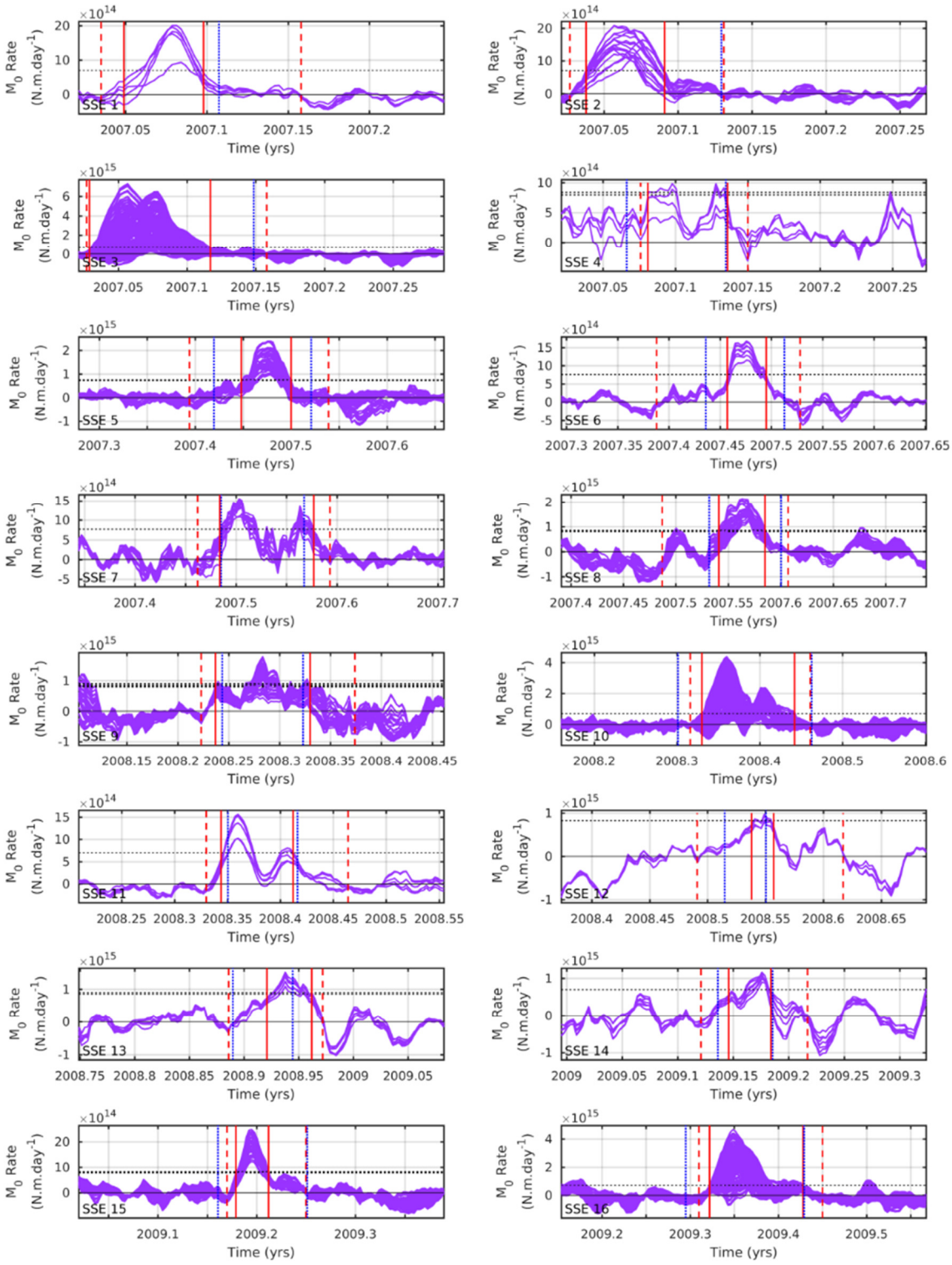

Figure 2.S11. *SSEs duration estimations. The purple lines indicate the SSEs sub-faults moment rates. The solid red lines indicate the manual SSEs start and end pic for the minimum duration estimation. They are determined by the timing of the first and last sub-fault with* $\dot{\delta}_{deficit} < V_{thresh}$*, represented by the black dashed line. The dashed red lines indicate the manual SSEs start and end pic for the maximum duration estimation. They are determined by the timing of the first and last subfault when* $\dot{\delta}_{deficit} < 0$*. The dotted blue lines indicate the automatic SSEs start and end pic.*

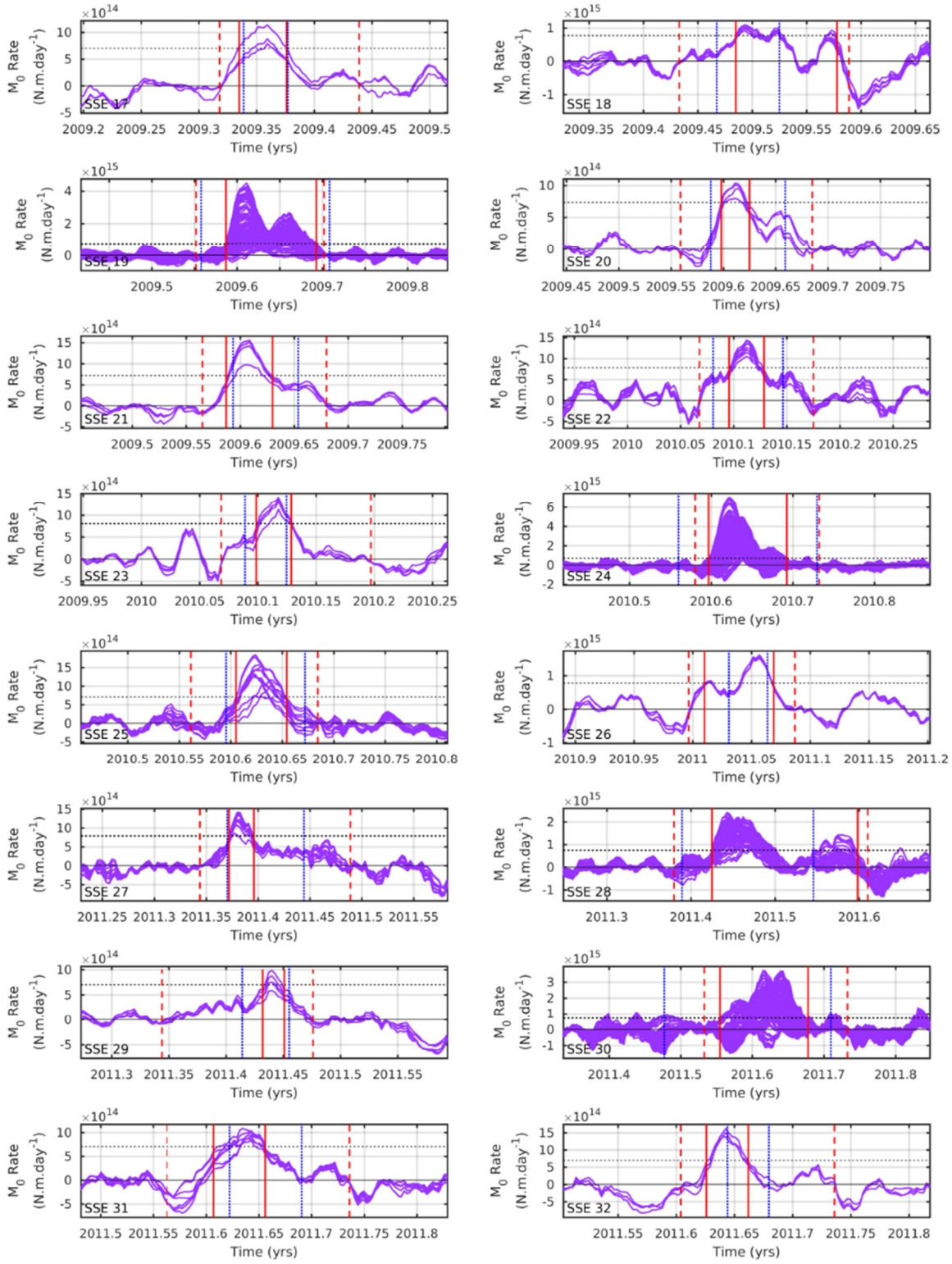

Figure 2.S11. *(Continued).*

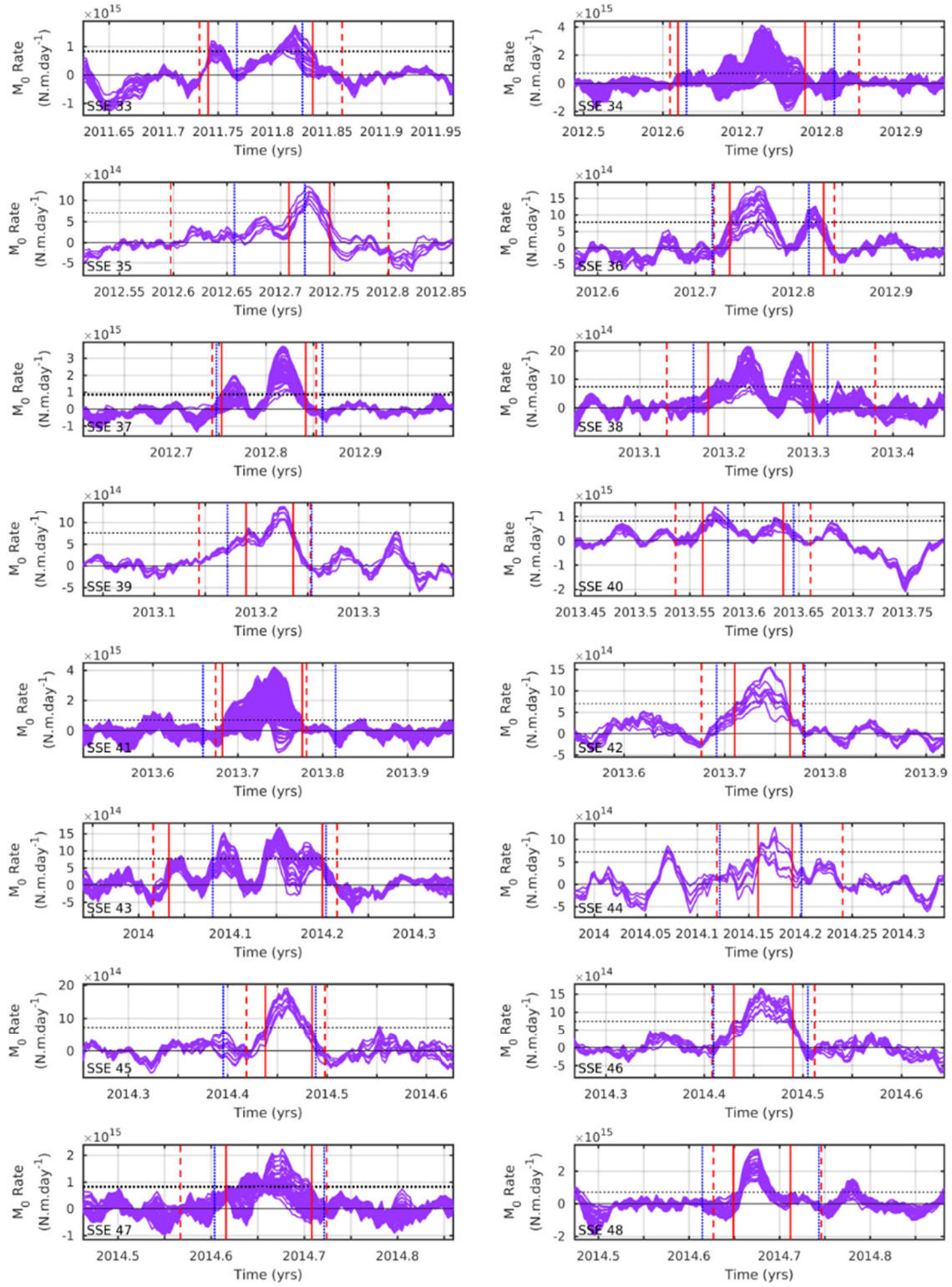

Figure 2.S11. *(Continued).*

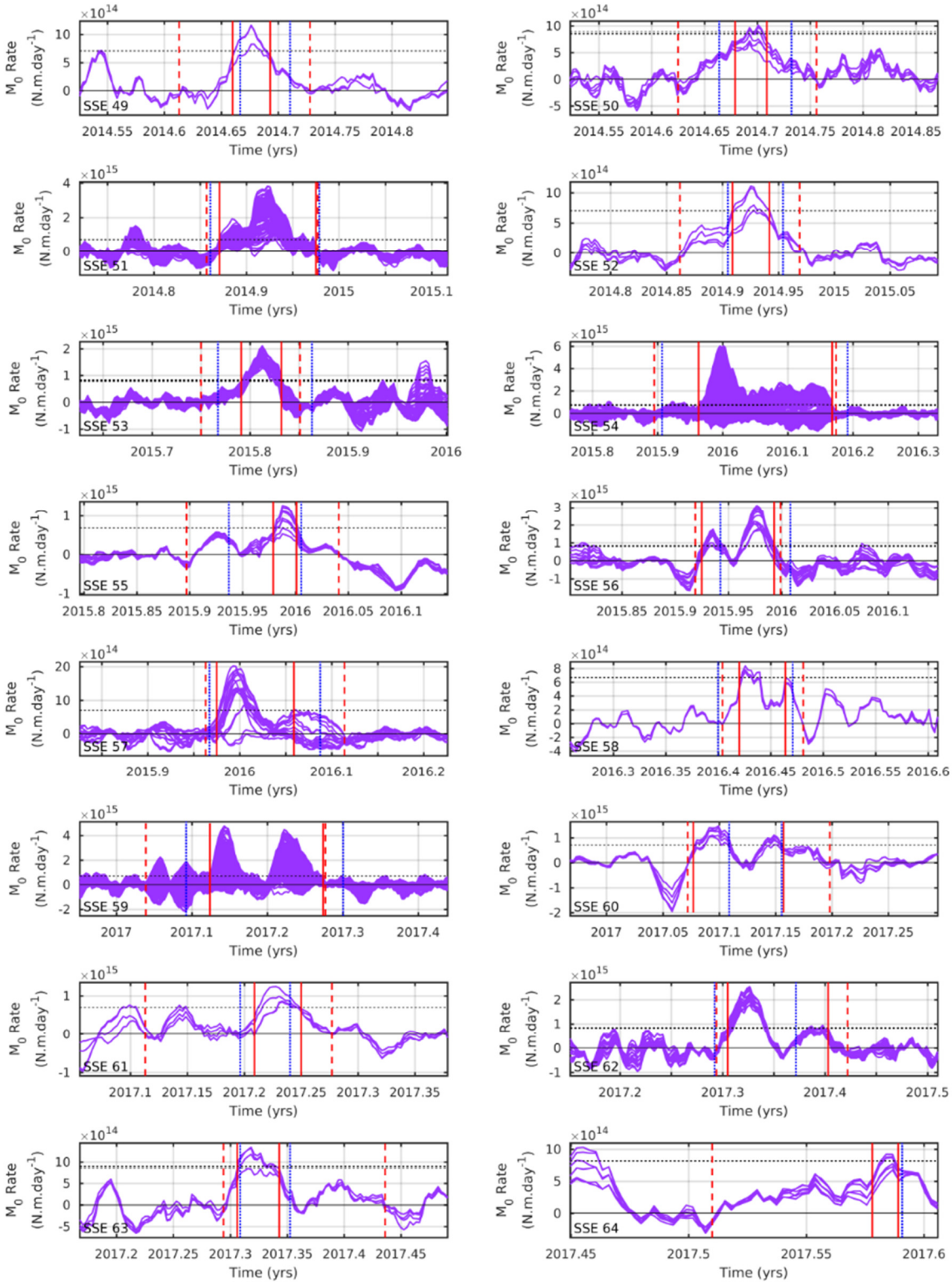

Figure 2.S11. *(Continued).*

Movie 2.S1. *The middle-left panel shows the moment rate deficit spatio-temporal evolution in respect to the long term interseismic loading. SSEs correspond to negative slip deficit rate (in blue). Tremors are indicated as black dots. The two triangles, in the north and center of Cascadia, correspond to the location for which we show the slip deficit in the top and bottom panel, respectively. The middle-right panel shows the coupling map (white to red shading) and the tremors location (black dots). The black thin lines indicate the coast. The black thick line indicates the trench location. Movie available on (*ftp://ftp.gps.caltech.edu/pub/smichel/).

Movie 2.S2 to 2.S4. *Inversion regularization sensitivity test for the SSEs kinematic model. The movies show the moment rate deficit spatio-temporal evolution of event 54 in respect to the long term interseismic loading using* $\sigma_0=10^{-1}$ *(Movie S2),* $\sigma_0=10^{-1.5}$ *(Movie S3) and* $\sigma_0=10^{-2}$ *(Movie S4) for the inversion regularization. SSEs correspond to negative slip deficit rate (in blue).* $\sigma_0=10^{-1.5}$ *is the selected value used also in Movie S1. Movies available on (*ftp://ftp.gps.caltech.edu/pub/smichel/).

Bibliography

Ide, S., Beroza, G. C., Shelly, D. R., & Uchide, T. (2007), A scaling law for slow earthquakes. *Nature*, *447*(7140), 76.

Ide, S. (2012), Variety and spatial heterogeneity of tectonic tremor worldwide. *Journal of Geophysical Research: Solid Earth*, *117*(B3).

McCrory, P. A., Blair, J. L., Waldhauser, F., & Oppenheimer, D. H. (2012). Juan de Fuca slab geometry and its relation to Wadati-Benioff zone seismicity. *Journal of Geophysical Research: Solid Earth*, *117*(B9).

Schmalzle, G. M., McCaffrey, R., & Creager, K. C. (2014), Central Cascadia subduction zone creep. *Geochemistry, Geophysics, Geosystems*, *15*(4), 1515-1532.

Chapter 3

Pulse-Like Partial Ruptures and High-Frequency Radiation at Creeping-Locked Transition during Megathrust Earthquakes

Published as "Michel, S., Avouac, J. P., Lapusta, N., & Jiang, J. (2017a), Pulse-like partial ruptures and high-frequency radiation at creeping-locked transition during megathrust earthquakes. *Geophysical Research Letters*, *44*(16), 8345-8351."

Abstract

Megathrust earthquakes tend to be confined to fault areas locked in the interseismic period and often rupture them only partially. For example, during the 2015 M7.8 Gorkha earthquake, Nepal, a slip pulse propagating along strike unzipped the bottom edge of the locked portion of the Main Himalayan Thrust (MHT). The lower edge of the rupture produced dominant high-frequency (>1 Hz) radiation of seismic waves. We show that similar partial ruptures occur spontaneously in a simple dynamic model of earthquake sequences. The fault is governed by standard laboratory-based rate-and-state friction with the ageing law and contains one homogenous velocity-weakening (VW) region embedded in a velocity-strengthening (VS) area. Our simulations incorporate inertial wave-mediated effects during seismic ruptures (they are thus fully dynamic) and account for all phases of the seismic cycle in a self-consistent way. Earthquakes nucleate at the edge of the VW area and partial ruptures tend to stay confined within this zone of higher prestress, producing pulse-like ruptures that propagate along strike. The amplitude of the high-frequency sources is enhanced in the zone of higher, heterogeneous stress at the edge of the VW area.

1. Introduction

Megathrust earthquake ruptures are generally confined to areas of the plate interface that were previously locked [*Konca et al.*, 2008; *Moreno et al.*, 2010; *Loveless and Meade*, 2011; *Protti et al.*, 2013], and they often rupture them only partially. The factors controlling the extent of such partial ruptures are unclear. The M7.8 Gorkha earthquake in Nepal of April 25th, 2015 is a well-documented example of such a rupture (Figure 3.1) [*Avouac et al.*, 2015; *Galetzka et al.*, 2015; *Meng et al.*, 2016]. It ruptured the Main Himalayan Thrust (MHT), the megathrust along which India is thrust under the Himalaya. The seismological and near-field high-rate geodetic records clearly show that it unzipped the lower edge of the locked portion of the fault, nucleating at 15 km depth and propagating eastward at ~2.8 km/s, in a pulse-like manner. High-frequency (HF) waves radiated from the lower edge of the rupture, tracking the pulse propagation (Figure 3.1a). Similar ruptures have been observed on subduction megathrusts, e.g. the Mw 7.7 Tocopilla earthquake offshore northern Chile in 2007 [*Béjar-Pizarro et al.*, 2010] and Mw 7.7 Nazca earthquake offshore southern Peru in 1996 [*Pritchard et al.*, 2007].

The factors that determine the extent of seismic ruptures remain poorly understood. They could reflect the geometry or heterogeneous frictional properties of the plate interface. For example, it has been proposed that the up-dip edge of the Gorkha rupture was arrested by a ramp along the MHT [*Hubbard et al.,* 2016]. This scenario was demonstrated to be a reasonable possibility based on quasi-dynamic simulations [*Qiu et al.*, 2016]. It is unlikely, however, that such a structural control would explain similar partial ruptures in the context of subduction megathrusts as ramp-and-flat systems are less likely to develop along the plate interface.

In this study, we investigate whether such partial ruptures and some of the specific characteristics of the Gorkha earthquake can be qualitatively reproduced without the need for any structural control. We resort to numerical simulations of earthquake sequences using the method of *Lapusta and Liu* [2009].

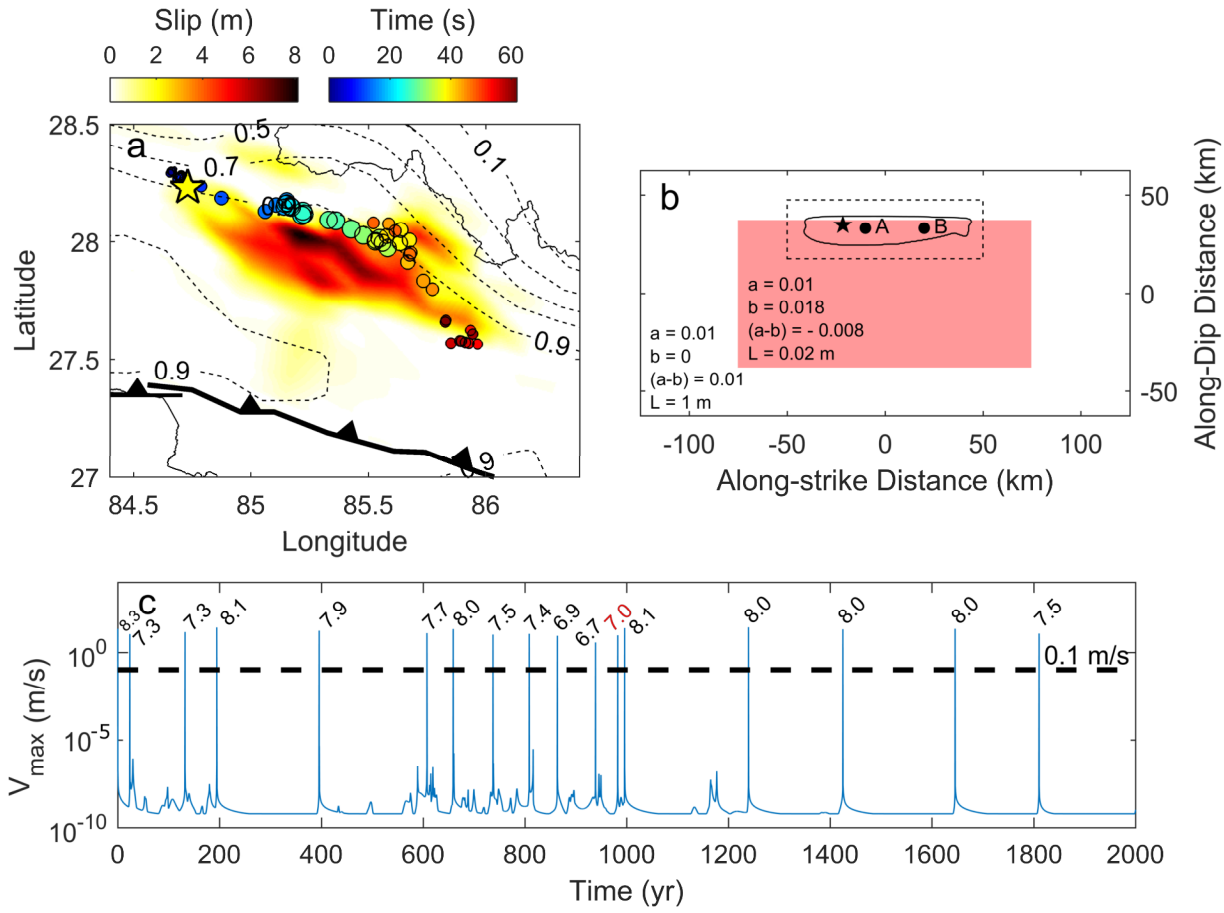

Figure 3.1. *Setting of the Mw7.8 Gorkha earthquake and dynamic simulations presented in this study. (a) Distribution of co-seismic slip, location and timing of the sources of high-frequency radiations (0.5-2 Hz), and pattern of interseismic coupling on the Main Himalayan Thrust fault (iso-contour of locking from 10% to 90%) [Avouac et al., 2015; Galetzka et al., 2015; Stevens and Avouac, 2015; Elliott et al., 2016]. (b) Our fault model, with the velocity-strengthening (VS) and velocity-weakening (VW) areas indicated by the white and pink areas, respectively. The fault is loaded by dip-slip motion (slip is parallel to the shorter dimension of the model). The solid black line and black star represent the rupture area and epicenter of event 12, respectively. The black dashed rectangle outlines the area shown in Figure 3.2. The black dots show the location of point A and B where slip and stress histories are shown in Figure 3.3. (c) Maximum slip rate as a function of time during the 2000-year-long simulation. The dashed horizontal line shows the 0.1 m/s threshold above which slip is considered to be seismic. Magnitudes are indicated, with event 12 in red.*

2. Model set up

We assume that slip along the megathrust is governed by a rate-and-state friction law, as this framework has been shown to produce realistic models of earthquake sequences, aseismic slip, and individual ruptures [*Barbot et al.*, 2012; *Cubas et al.*, 2015; *Thomas et al.*, 2017]. We assume that the state variable evolves according to the 'aging law' [*Dieterich*, 1972, 1979; *Ruina*, 1983]. The frictional resistance is then expressed as:

$$\tau = \sigma\left[f_* + a\,ln\left(\frac{V}{V_*}\right) + b\,ln\left(\frac{V_*\theta}{L}\right)\right], \tag{3.1a}$$

$$\frac{d\theta}{dt} = 1 - \frac{V\theta}{L}, \tag{3.1b}$$

where τ is the shear strength which is equal to the shear stress, σ is the effective normal stress, V is the slip rate, and f_* is the friction coefficient at the reference slip rate V_*. The parameter a quantifies the direct effect of a slip-rate change. The parameter b describes the effect of the state variable. The characteristic slip distance, L, governs the evolution of the state variable. Friction is said to be velocity-weakening (VW) if $a - b < 0$, and velocity-strengthening (VS) if $a - b > 0$. A VW behavior of the fault is required for seismic ruptures to nucleate. In dynamic simulations, VW patches produce a stick-slip motion if they are larger than the critical size for earthquake nucleation, i.e. the nucleation size, h^* [*Ampuero and Rubin*, 2008; *Chen and Lapusta*, 2009]:

$$h^* = \frac{\pi}{2}\frac{\mu^* bL}{(b-a)^2\sigma}, \tag{3.2}$$

where $\mu^* = \mu$ for mode III, and $\mu^* = \mu/(1-\nu)$ for mode II, with μ and ν being the shear modulus and Poisson ratio, respectively. Accordingly, smaller L values allow for smaller h^* and hence simulations of smaller earthquakes, thereby producing a broader range of earthquake magnitudes and adding further complexity to earthquake sequences. However, this comes at a computational cost.

We design a simple generic experiment meant to reproduce a single fault. We therefore consider only one homogeneous VW patch embedded in a VS area (Figure 3.1b). The model is not aimed to reproduce any particular detail of the MHT. For simplicity, we assume a constant effective normal stress.

The physical parameters used in this study are listed in Table 3.1. The parameters were chosen to keep the computational cost of the simulations reasonable. The modeled fault is 250 km

long along strike and 125 km wide along dip, and the VW region is 150 km long and 75 km wide. With the assumed parameters (Table 3.1), the nucleation size is ~5 km. The fault is loaded at a rate of 21 mm/yr perpendicular to the strike direction. Note that the loading is applied all around the frictional region (there is no free surface) so that all edges of the VW region will consequently concentrate stress during the interseismic period (not just the bottom edge). The effective normal stress is set at 50 MPa. The simulation starts with an earthquake artificially triggered by elevated shear stresses within a 20 km by 20 km area located at the edge of the VW region. The first several earthquakes reset the model from the initial imposed conditions on the fault.

Table 3.1. *List of physical parameters used in the model.*

	Symbol	Value
	Elastodynamic Properties	
Shear modulus	μ	30 GPa
Poisson's ratio	ν	0.25
Shear wave speed	c_s	3 km/s
	Frictional Properties	
Reference slip rate	V_*	1 μm/s
Reference friction coefficient	f_*	0.6
Characteristic slip distance	L	20 mm in VW region 1 m in VS area
Direct effect parameter	a	0.01
Evolution effect parameter	b	0.018 in VW region 0 in VS area
	Other model parameters	
Effective normal stress	σ	50 MPa
Plate loading rate	V_{pl}	21 mm/yr

3. Modeling results

The simulation produces a sequence of full and partial ruptures of the VW region, with 17 events (defined as slip with $V > 0.1$ m/s) occurring in 2000 years, their magnitudes ranging from 6.7 to 8.3 (Figure 3.1c). We observe that earthquakes nucleate at the edges of the VW patch where stress builds up more rapidly. The largest events (Mw > 7.9) generally rupture nearly entirely the VW area. We observe that partial ruptures are systematically confined along the edge of the VW region (Supp.) where pre-seismic stresses are higher due to interseismic stress buildup.

We present details of such a partial rupture, event 12 (Figure 3.1b and c), in Figures 3.2 and 3.3 (a video is available in Supp.). This earthquake reaches a moment magnitude Mw7 and produces an average stress drop of 6.15 MPa (calculated using the spatial average of stress drop distribution approach of *Noda et al.* [2013]). This partial rupture unzips the edge of the VW area over an along-strike length of about 80 km, producing a peak slip of 2.4 m (Figure 3.2a). The earthquake nucleates in a particularly wide zone of higher pre-stress. The rupture is initially crack-like for about 8-10 s and then turns into a unilateral pulse-like rupture until the end of the rupture, for another 20 s (Figure 3.2b). The source time function (e.g., the time evolution of the moment rate released by the entire rupture) peaks at ~11 s after the onset of seismic velocities (Figure 3.3a). The peak moment rate occurs approximately when the rupture area stops expanding along dip. This arrest is at the origin of the healing front that leads to a pulse-like behavior. From there on, the moment rate decreases gradually.

The comparison of the source-time function (Figure 3.3a) with the slip-time functions at points A and B (Figure 3.3b and c) shows that the slip-pulse duration at these points, equal to ~5 s, is small compared to the ~30 s source duration. Most (> 95%) of the final slip is reached much before the end of the rupture. The evolution of slip thus attests to a pulse-like behavior. Seven seconds after the start of the event, the rupture propagates along strike at a mean rupture speed of 2.700±0.002 km/s (the uncertainty is the standard deviation), which is about 90% of the Rayleigh wave speed.

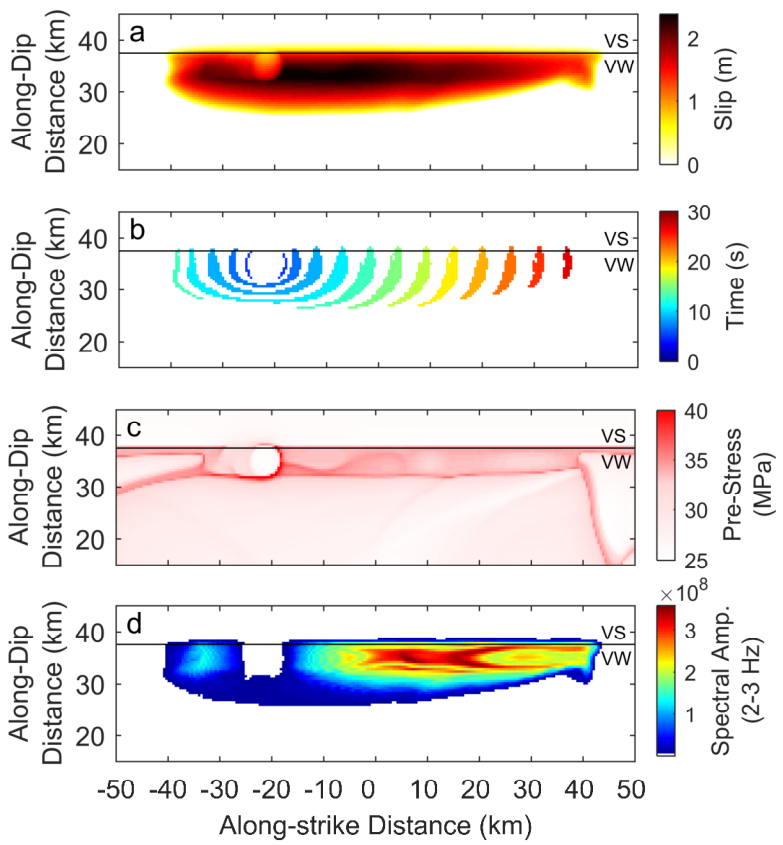

Figure 3.2. *Cumulative slip, rupture front propagation, shear pre-stress, and high-frequency radiation spatial maps of a partial rupture (event 12). (a) Cumulative slip and (b) rupture front propagation of the event. In (b), the lines show, at 2 s time intervals, location where slip rate exceeds 0.5 m/s, with their color indicating the timing during the rupture. (c) Shear stress at the onset of seismic event, defined as the slip rate exceeding 0.1 m/s somewhere on the fault. The stress has already dropped where nucleation has been occurring. The color scale is saturated to better visualize the stress distribution. The maximum and minimum shear stress on the fault are 47 MPa and 24 MPa, respectively. (d) Map of high frequency sources during the rupture. Color shading shows the amplitude of the spectrum of the slip-time function between 2 and 3 Hz. The solid black horizontal line is the boundary between the VS and VW areas.*

Comparison of the slip accumulation (Figure 3.2a) with the distribution of shear stress on the fault prior to the rupture (Figure 3.2c) suggests that the width of the rupture is determined by the extent of the higher shear prestress at the edge of the VW regionand its decrease towards lower stress values in the middle of the fault. Along strike, the rupture arrests at zones of lower stress that have been ruptured by recent prior earthquakes.

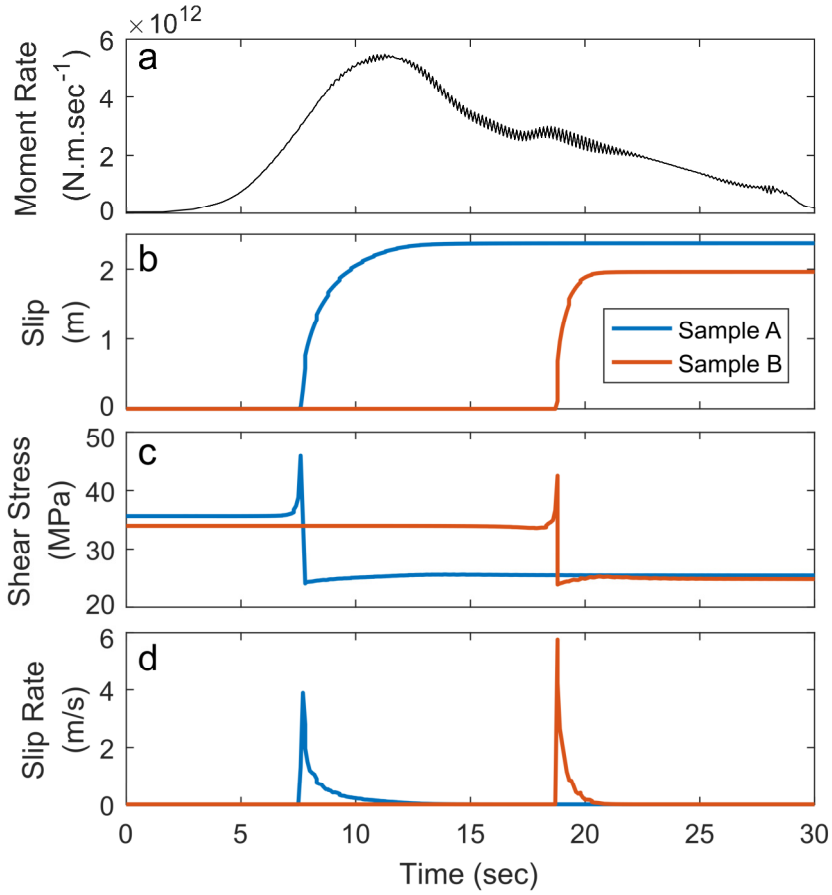

Figure 3.3. *(a) Source-time function (moment rate as a function of time) of the partial rupture (event 12). (b) Cumulative slip, (c) shear pre-stress, and (d) slip rate at the locations of points A and B from Figure 3.1b.*

We observe that the evolution of slip rate is sharper at points near the edge of the VW area, probably due to the higher shear stress there (Figure 3.2c). This effect results in relatively more energetic high-frequency seismic waves radiated from near the edge of the VW area (Supp.). To quantify this effect, we compute the Fourier transform of the moment-rate time function and assess spatial variations of the amplitude of the spectrum at frequencies between 2 and 3 Hz (Figure 3.3d).

Note that the sequence of partial and full ruptures is only possible if the nucleation size is small enough compared to the width of the VW region (Supp.). By changing the width of the seismogenic zone, we find that only full ruptures occur if the ratio between the nucleation size and the width of the VW region is above 1/12. This particular value may be linked to the frictional parameters and geometry chosen in this study and its dependence on these factors requires further study, although we expect that, in any fault model, this value needs to be small enough for the partial ruptures to appear.

4. Discussion and Conclusion

A simple model based on standard rate-and-state friction with a single homogeneous VW patch surrounded by a VS region and loaded with dip-slip motion can produce partial ruptures that unzip the edge of the VW zone. This kind of rupture was observed in the continental context of the Himalayan megathrust during the M7.8 Gorkha earthquake, and in the context of oceanic subduction zones [*Pritchard et al.*, 2007; *Béjar-Pizarro et al.*, 2010]. Such ruptures could also result from a structural control by the fault geometry or from spatial variations of friction properties. In the case of the Gorkha earthquake, the hypothesis that the upper edge of the rupture was controlled by a transition to VS friction can be excluded based on postseismic observations, which show that the area up-dip of the seismic rupture remains locked [*Gualandi et al.*, 2016]. By contrast, there is a possibility that the upper edge of the Gorkha earthquake was controlled by a ramp [*Hubbard et al.*, 2016; *Qiu et al.*, 2016]. This ramp would run beneath the Kathmandu basin. There is, however, no topographic signature of the zone of more rapid uplift that should have resulted.

We therefore prefer the alternative scenario, suggested by the partial ruptures observed in our numerical simulations, that the rupture was confined to the area of interseismic stress buildup at the lower edge of the locked area. This hypothesis could also explain similar ruptures in the context of oceanic subductions.

The pulse-like behavior in our simulated partial ruptures is controlled by the width of the zone within which seismic slip can be sustained due to the stress distribution. Pulse-like ruptures, often observed in various tectonic settings [*Heaton*, 1990], can hence form as a result of the stress concentration at the boundary between VW and VS zone, or at any other band of concentrated stress. Hence they do not necessarily require a narrow or heterogeneous seismogenic zones [*Johnson*, 1992; *Beroza and Mikumo*, 1996; *Olsen et al.*, 1997], intense frictional velocity weakening [*Heaton*, 1990; *Lu et al.*, 2007], or elastic contrast across the fault [*Ampuero and Ben-Zion*, 2008] although such features may be present and indeed required for slip in certain settings, e.g., on low-stressed faults of high static strength [*Zheng and Rice*, 1998; *Noda et al.*, 2009].

In our model, the sources of dominant high-frequency radiation are at the locations of high pre-seismic shear stress, whether it is a partial or full rupture (an example of full rupture is

given in the supplement). The high-frequency radiation sources of the Gorkha earthquake are located down-dip, close to the transition between the VS and VW region, as in our model. While our model succeeds at explaining the location of the high-frequency sources, the effect might actually be stronger in nature than what our model predicts. Indeed, for computational reasons, the nucleation size of our modeled earthquakes is relatively large, leading only to Mw > 6 events. In nature, seismic ruptures can be much smaller. In our model, earthquakes tend to nucleate at the edges of the VW patch where stress is building up more rapidly. This result is similar to the observations that most earthquakes in the Himalaya cluster along the lower edge of the locked fault zone [*Cattin and Avouac*, 2000; *Bollinger et al.*, 2004; *Stevens and Avouac*, 2015]. It is likely that, due to these smaller earthquakes, the stress distribution along the lower edge of the VW zone is much more heterogeneous than in our model [*Lapusta and Rice*, 2003; *Jiang and Lapusta*, 2016]. If the simulated earthquakes could span smaller magnitudes, it would enhance further the high frequency seismic waves radiated from the edge of the VW area [*Avouac et al.*, 2015]. Our explanation for the locations of the HF sources does not exclude the alternative possibility that they coincide with the upper edge of the midcrustal ramp along the Himalayan megathrust [*Elliott et al.*, 2016], which coincides with the steep topography and the zone of higher exhumation rate at the front of the Higher Himalaya [*Lavé and Avouac*, 2001; *Herman et al.*, 2010]. It is indeed well known that high frequency waves are radiated at fault kinks [*e.g.*, *Adda-Bedia and Madariaga*, 2008]. In the case of the Gorkha earthquake, no high frequency radiation was observed at its up-dip extent, a feature that should have been detected if the rupture had reached an up-dip additional ramp.

Our model does not imply that dominant high-frequency waves would only radiate from the edges of VW areas. The rupture of a zone of higher stress left at the edges of a previous partial rupture may dominate the HF radiation, which could then originate from well within the VW area. It is therefore not assured that seismic slip within the locked portion of megathrust would be depleted in high frequencies as a result of the mechanism described in this study. Further investigations are needed to elucidate the factors controlling the source location and amplitudes of high-frequency seismic waves.

Acknowledgments

The data used are listed in the supplements. We thank Yen-Yu Lin for his help with the numerical code. We thank Adriano Gualandi, James Jackson, and Alex Copley for discussions.

Bibliography

Adda-Bedia, M., and R. Madariaga (2008), Seismic Radiation from a Kink on an Antiplane Fault, *Bull. Seismol. Soc. Am.*, *98*(5), 2291–2302, doi:10.1785/0120080003.

Ampuero, J., and A. M. Rubin (2008), Earthquake nucleation on rate and state faults – Aging and slip laws, *J. Geophys. Res.*, *113*(B01302), doi:10.1029/2007JB005082.

Ampuero, J.-P., and Y. Ben-Zion (2008), Cracks , pulses and macroscopic asymmetry of dynamic rupture on a bimaterial interface with velocity-weakening friction, *Geophys. J. Int.*, *173*, 674–692, doi:10.1111/j.1365-246X.2008.03736.x.

Avouac, J., L. Meng, S. Wei, T. Wang, and J. Ampuero (2015), Lower edge of locked Main Himalayan Thrust unzipped by the 2015 Gorkha earthquake, *Nat. Geosci.*, *8*(August), 708–711, doi:10.1038/NGEO2518.

Barbot, S., N. Lapusta, and J. Avouac (2012), Under the Hood of the Earthquake, *Science*, *336*(6082), 707–710, doi:10.1126/science.1218796.

Béjar-Pizarro, M. et al. (2010), Geophysical Journal International, *Geophys. J. Int.*, *183*, 390–406, doi:10.1111/j.1365-246X.2010.04748.x.

Beroza, G. C., and T. Mikumo (1996), Short slip duration in dynamic rupture in the presence of heterogeneous fault properties, *J. Geogr. Geol.*, *101*, 22,449-22,460.

Bollinger, L., J. P. Avouac, R. Cattin, and M. R. Pandey (2004), Stress buildup in the Himalaya, *J. Geophys. Res.*, *109*(B11405), 1–8, doi:10.1029/2003JB002911.

Cattin, R., and J. P. Avouac (2000), Modeling mountain building and the seismic cycle in the Himalaya of Nepal, *J. Geophys. Res.*, *105*(B6), 13,989-13,407.

Chen, T., and N. Lapusta (2009), Scaling of small repeating earthquakes explained by interaction of seismic and aseismic slip in a rate and state fault model, *J. Geophys. Res.*, *114*(B01311), doi:10.1029/2008JB005749.

Cubas, N., N. Lapusta, J. Avouac, and H. Perfettini (2015), Numerical modeling of long-term earthquake sequences on the NE Japan megathrust : Comparison with observations

and implications for fault friction, *Earth Planet. Sci. Lett.*, *419*, 187–198, doi:10.1016/j.epsl.2015.03.002.

Dieterich, J. H. (1972), Time-Dependent Friction in Rocks, *J. Geophys. Res.*, *77*(20), 3690–3697.

Dieterich, J. H. (1979), Modeling of Rock Friction Experimental Results and Constitutive Equations, *J. Geophys. Res.*, *84*(B5), 2161–2168.

Elliott, J. R., R. Jolivet, P. J. González, J. Avouac, J. Hollingsworth, and M. P. Searle (2016), Himalayan megathrust geometry and relation to topography revealed by the Gorkha earthquake, *Nat. Geosci.*, *9*, 174–180, doi:10.1038/NGEO2623.

Galetzka, J. et al. (2015), Slip pulse and resonance of the Kathmandu basin during the 2015 Gorkha earthquake, Nepal, *Science*, *349*(6252), 1091–1095.

Gualandi, A., J. Avouac, J. Galetzka, J. F. Genrich, G. Blewitt, and L. B. Adhikari (2016), Pre- and post-seismic deformation related to the 2015, Mw7.8 Gorkha earthquake, Nepal, *Tectonophysics*, doi:10.1016/j.tecto.2016.06.014.

Heaton, T. H. (1990), Evidence for and implications of self-healing pulses of slip in earthquake rupture, *Phys. Earth Planet. Inter.*, *64*, 1–20.

Herman, F. et al. (2010), Exhumation , crustal deformation , and thermal structure of the Nepal Himalaya derived from the inversion of thermochronological and thermobarometric data and modeling of the topography, *J. Geophys. Res.*, *115*(B06407), doi:10.1029/2008JB006126.

Hubbard, J., R. Almeida, A. Foster, S. N. Sapkota, P. Bürgi, and P. Tapponnier (2016), Structural segmentation controlled the 2015 M w 7 . 8 Gorkha earthquake rupture in Nepal, *Geology*, *44*(8), 639–642, doi:10.1130/G38077.1.

Jiang, J., and N. Lapusta (2016), Deeper penetration of large earthquakes on seismically quiescent faults, *Science*, *352*(6291), 1293–1298.

Johnson, E. (1992), The influence of the lithospheric thickness, *Geophys. J. Int.*, *108*, 151–160.

Konca, A. O. et al. (2008), Partial rupture of a locked patch of the Sumatra megathrust

during the 2007 earthquake sequence, *Nature*, *456*, 631–635, doi:10.1038/nature07572.

Lapusta, N., and Y. Liu (2009), Three-dimensional boundary integral modeling of spontaneous earthquake sequences and aseismic slip, *J. Geophys. Res.*, *114*(B09303), doi:10.1029/2008JB005934.

Lapusta, N., and J. R. Rice (2003), Nucleation and early seismic propagation of small and large events in a crustal earthquake model, *J. Geophys. Res.*, *108*(B4), 2205, doi:10.1029/2001JB000793.

Lavé, J., and J. P. Avouac (2001), Fluvial incision and tectonic uplift across the Himalayas of central Nepal erosion, *J. Geophys. Res.*, *106*(B11), 26,561-26,591.

Loveless, J. P., and B. J. Meade (2011), Spatial correlation of interseismic coupling and coseismic rupture extent of the 2011 Mw=9.0 Tohoku-oki earthquake, *Geophys. Res. Lett.*, *38*(L17306), 2–6, doi:10.1029/2011GL048561.

Lu, X., N. Lapusta, and A. J. Rosakis (2007), Pulse-like and crack-like ruptures in experiments mimicking crustal earthquakes, *PNAS*, *104*(48), 18931–18936.

Meng, L., A. Zhang, and Y. Yagi (2016), Improving back projection imaging with a novel physics-based aftershock calibration approach: A case study of the 2015 Gorkha earthquake, *Geophys. Res. Lett.*, *43*, 628–636, doi:10.1002/2015GL067034.

Moreno, M., M. Rosenau, and O. Oncken (2010), 2010 Maule earthquake slip correlates with pre-seismic locking of Andean subduction zone, *Nature*, *467*, 198–202, doi:10.1038/nature09349.

Noda, H., E. M. Dunham, and J. R. Rice (2009), Earthquake ruptures with thermal weakening and the operation of major faults at low overall stress levels, *J. Geophys. Res.*, *114*(B07302), doi:10.1029/2008JB006143.

Noda, H., N. Lapusta, and H. Kanamori (2013), Comparison of average stress dropmeasures for ruptures with heterogeneous stress change and implications for earthquake physics, *Geophys. J. Int.*, (193), 1691–1712, doi:10.1093/gji/ggt074.

Olsen, K. B., R. Madariaga, and R. J. Archuleta (1997), Three-Dimensional Dynamic

Simulation of the 1992 Landers Earthquake, *Science*, *278*(5339), 834–838, doi:10.1126/science.278.5339.834.

Pritchard, M. E., E. O. Norabuena, C. Ji, R. Boroschek, D. Comte, M. Simons, T. H. Dixon, and P. A. Rosen (2007), Geodetic , teleseismic , and strong motion constraints on slip from recent southern Peru subduction zone earthquakes, *J. Geophys. Res.*, *112*(B03307), doi:10.1029/2006JB004294.

Protti, M., V. González, A. V Newman, T. H. Dixon, S. Y. Schwartz, J. S. Marshall, L. Feng, J. I. Walter, R. Malservisi, and S. E. Owen (2013), Nicoya earthquake rupture anticipated by geodetic measurement of the locked plate interface, *Nat. Geosci.*, *7*, 117–121, doi:10.1038/ngeo2038.

Qiu, Q., E. M. Hill, S. Barbot, J. Hubbard, W. Feng, E. O. Lindsey, L. Feng, K. Dai, S. V Samsonov, and P. Tapponnier (2016), The mechanism of partial rupture of a locked megathrust : The role of fault morphology, *Geol. Soc. Am.*, *44*(10), 875–878, doi:10.1130/G38178.1.

Ruina, A. (1983), Slip Instability and State Variable Friction Laws, *J. Geophys. Res.*, *88*(B12), 10,359-10,370, doi:10.1029/JB088iB12p10359.

Stevens, V. L., and J. P. Avouac (2015), Interseismic coupling on the main Himalayan thrust, *Geophys. Res. Lett.*, *42*, 5828–5837, doi:10.1002/2015GL064845.

Thomas, M. Y., J. Avouac, and N. Lapusta (2017), Rate-and-state friction properties of the Longitudinal Valley Fault from kinematic and dynamic modeling of seismic and aseismic slip, *J. Geophys. Res. Solid Earth*, *122*, doi:10.1002/2016JB013615.

Zheng, G., and J. R. Rice (1998), Conditions under which Velocity-Weakening Friction Allows a Self-healing versus a Cracklike Mode of Rupture, *Bull. Seism. Soc. Am*, *88*(6), 1466–1483.

SUPPLEMENT

S.1. conditions required to produce partial ruptures in our simulations

Figure 3.S1 illustrates the change of earthquake rupture extent in our model when the nucleation size changes with respect to the width of the velocity-weakening (VW) patch. We find that if the ratio of the nucleation size and the VW patch width is smaller than ~0.08, partial ruptures are produced in our simulation. On the contrary, above this threshold, only full ruptures are produced. The value of this threshold is dependent on the frictional parameters that we have chosen in our model. The geometry of the VW patch also influences the behavior of seismic events. For instance, some full ruptures actually begin as partial ruptures but are then revitalized as they meet a neighboring border of the VW patch. Increasing the length of the VW patch would then increase the threshold, for example. Further investigations need to be done to better understand the impact of the geometry of the VW patch and its frictional parameters on the ratio h^*/W required for partial ruptures in a frictionally homogeneous VW area.

S.2. High frequency radiation and slip spatial distribution comparison

Figure 3.S2 compares slip, stress and high frequency radiation from a section of event 12. The high frequency amplitude is slightly asymmetric, skewed towards the border of the VW region. Its maximum is offset from the maximum slip location. This observation is clearer while looking at event 13, which is a full rupture (Figure 3.S3). The high frequency radiation sources are located in zones of higher stress. The zones with large slip are, however, not correlated with the location of the high-frequency sources.

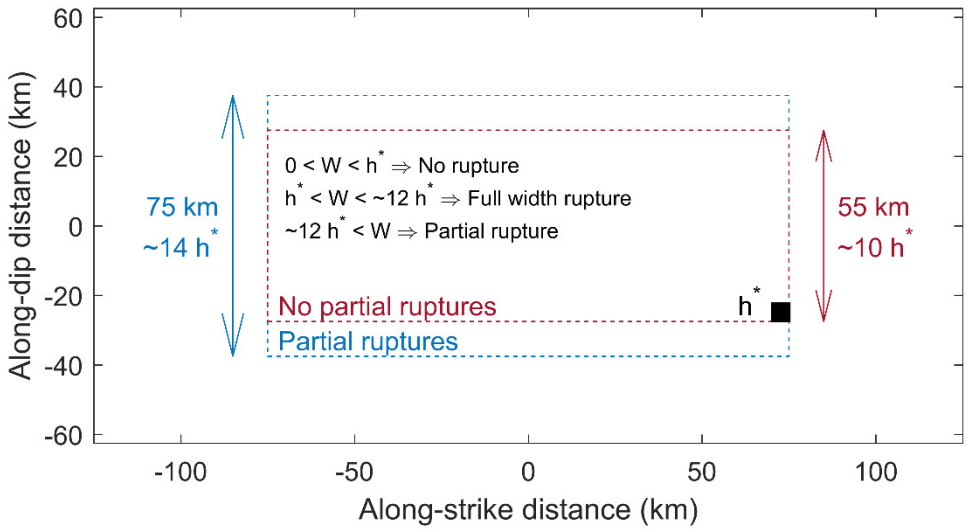

Figure 3.S4. *Illustration of how the width of the VW patch, W, and nucleation size, h*, control the occurrence of partial ruptures in our model. With the parameters considered, the nucleation size,* $\boldsymbol{h^*}$*, needs to be smaller than approximately 1/12 of the width of the VW patch (*$\boldsymbol{h^*/W} < \sim 0.08$*) for the partial ruptures to occur. Otherwise, only full ruptures of the VW patch are produced. The threshold on* $\boldsymbol{h^*/W}$ *may depend on the choice of frictional parameters and geometry of the VW patch.*

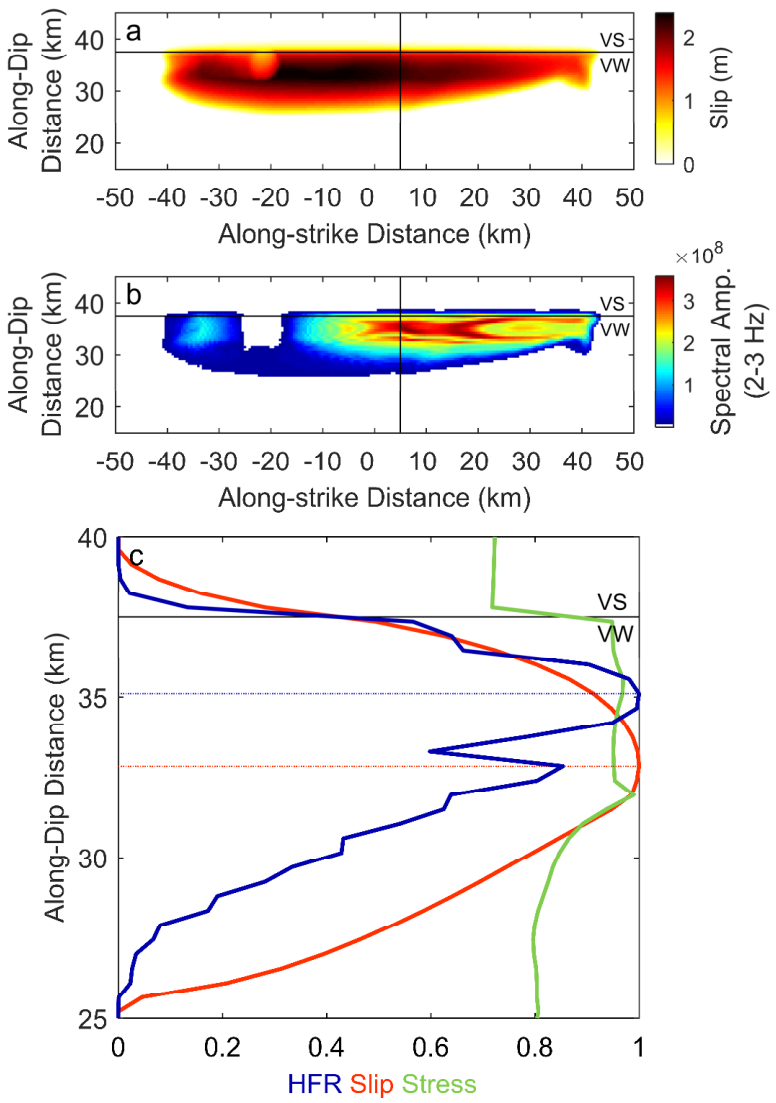

Figure 3.S2. *High-frequency radiation, slip and pre-event shear stress comparison from a vertical section. (a) Slip distribution of event 12 with the vertical section marked. (b) Map of high-frequency sources during the rupture. Color shading shows the spatial variations of the amplitude of the spectrum of the slip-time function between 2 and 3 Hz. The solid black horizontal line is the limit between the VS and VW areas. The solid vertical black line indicates the location of the section shown in (c). (c) Normalized spectral amplitude between 2-3 Hz (blue), slip (red) and pre-stress (green) along the section indicated in (a) and (b). HFR stand for High Frequency Radiation. The horizontal blue and red lines locate the maximum slip and spectral amplitude, respectively. Note that the maximum high-frequency radiation is offset with respect to the maximum slip and located closer to the VW/VS transition.*

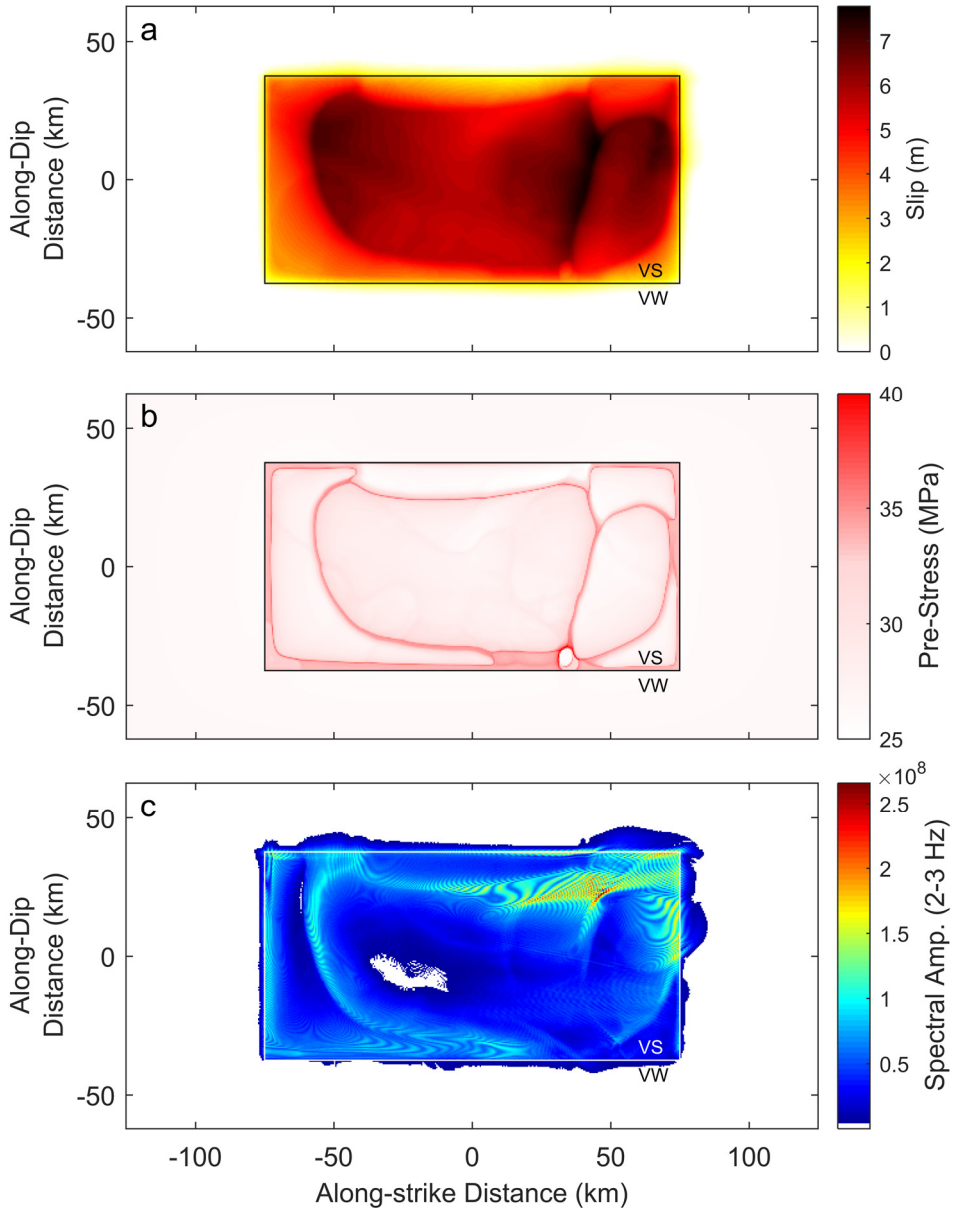

Figure 3.S3. *Cumulative slip, pre-stress and high-frequency radiation source maps of a full rupture (event13). (a) Cumulative slip of the event. (b) Shear stress at the onset of seismic event, when the slip rate exceeds 0.1 m/s somewhere on the fault. The stress has already dropped where nucleation has been occurring. The color scale is saturated to better visualize the stress distribution. The maximum and minimum shear stress on the fault are 45.1 MPa and 24.7 MPa, respectively. (d) Map of high frequency sources during the rupture. Color shading shows the amplitude of the spectrum of the slip-time-function between 2 and 3 Hz. The solid black or white rectangle is the limit between the VS and VW areas.*

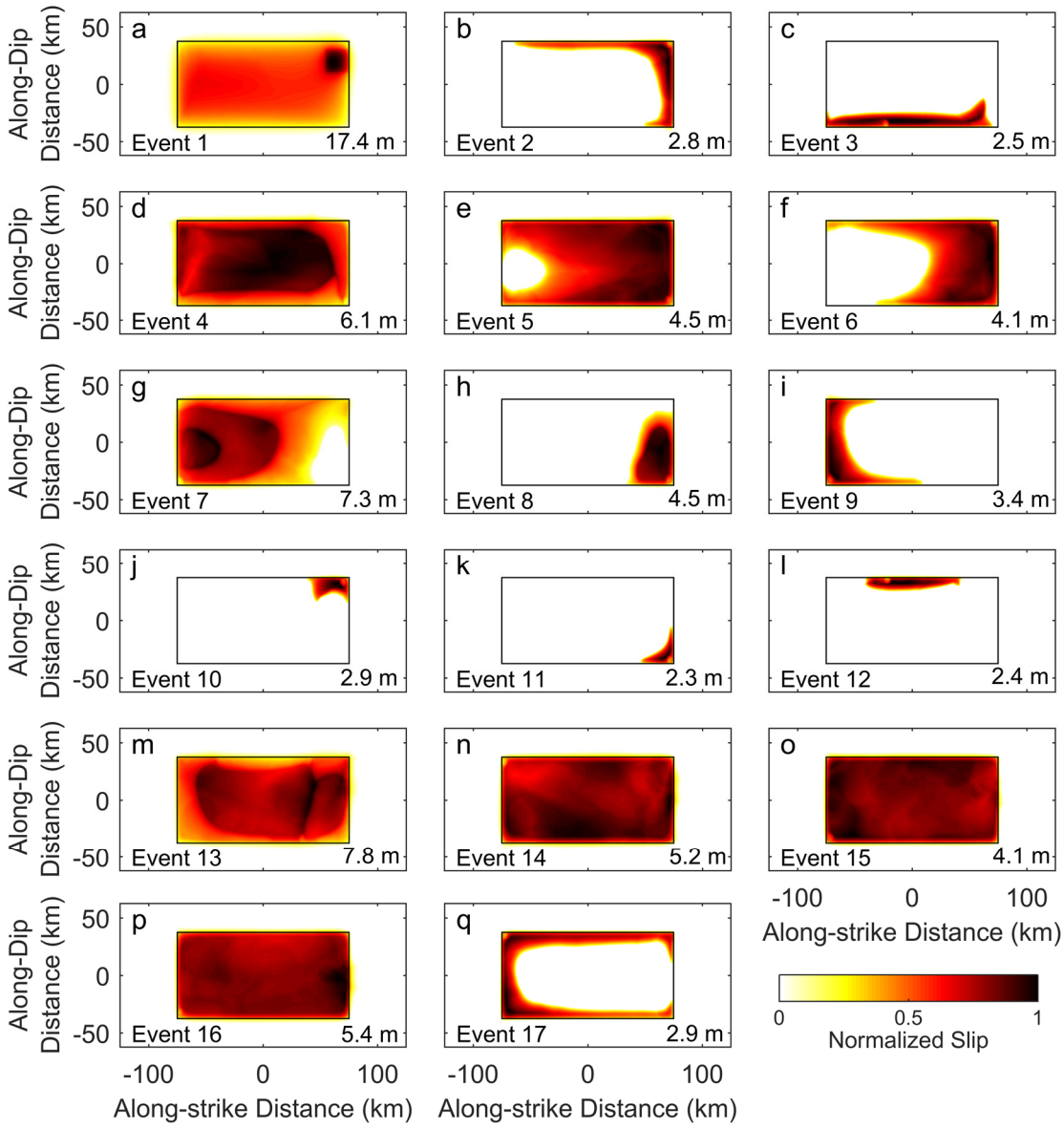

Figure 3.S4*. Normalized slip distribution of all the events of our simulation. The bottom right number indicates the maximum slip of each event.*

***Movie 3.S1**. Event 12 slip rate history. The slip rates are indicated in log scale. Available on (ftp://ftp.gps.caltech.edu/pub/smichel/)*

Conclusion

Throughout the three chapters, we estimated and documented the seismic behaviour of the San Andreas strike-slip fault, the Cascadia subduction zone and the Himalayan megathrust. All three of them are zones of potentially high but still largely uncertain seismic hazard. From historical records, we know that in Nepal, tens of thousands of people were killed by successive events during the last millennium, swiping kings and common people alike. The regions of Cascadia and southern California, at the time of their last large event (M_w>7.5) in 1700 and 1857, where not so populated and thus did not have such impact locally. However, the tsunami provoked by Cascadia's 1700 $M\sim9$ event devastated Japan's coast. Since then, the region of Cascadia and the south portion of the San Andreas Fault have remained relatively silent but still represent a huge threat to the population.

The first Chapter of this thesis evaluated the seismic potential of the northern segment of the locked region of the San Andreas Fault, Parkfield. $M\sim6$ earthquakes rupture relatively regularly this segment every 24 years but are insufficient to release all the moment deficit stocked during the interseismic period between successive events. This hints for less frequent M_w>6.7 earthquakes in the region which would likely be in combination with the expected "big one" $M\sim7.8$ earthquake. Indeed, the last $M\sim7.8$ like earthquake ("Fort Tejon") occurred in 1857 161 years ago, according to paleo-seismology studies [*Sieh,* 1978; *Zielke et al.,* 2010]. We estimate the recurrence time of such events to be 130-200 years.

The same type of analysis applied to Cascadia's subduction zone indicates that $M\sim9$ are indeed expected to balance the moment budget of the region. The shallow part of the subduction is at least partially locked, accumulating moment deficit during the interseismic period, but releases potential $M\sim9$ earthquakes occasionally, as has been inferred from paleoseismological studies [*Goldfinger et al.,* 2012]. Loading of the locked portion of the Cascadia megathrust is unsteady due to recurring SSEs along the deeper portions of the megathrust. The triggering of a Megathrust seismic rupture by SSEs seems however unlikely. The locked and SSE/tremor band portion of the fault seems dissociated along-dip by a transition zone that creeps continuously, a buffer zone that limit the risk of a SSE triggering a large seismic event. Our study shows that the SSEs have their own specific dynamics (associated with tremors) but have similar properties to regular earthquakes. They result from slip on single or multiple deep fault segments highlighting complex interactions between those segments. The lateral delimitation of the segments could be controlled by

the rheological variations, probably related to the geology of the forearc [*Brudzinski and Allen,* 2007]. The factors that allow the smaller rupture, whether a SSE or a regular earthquake, to grow into larger, eventually spanning multiple segments, ruptures remain to be clarified and quantified. This process could result in some sort of super cycle [Sieh et al, 2008]. For example the Gorkha earthquake might have possibly raised the level of stress at its up-dip extent. This would facilitate the next large event of the segment to propagate towards the surface and thus increase furthermore the seismic hazard. It may take a few Gorkha-like earthquakes until the state of stress of the updip portion of the fault allows a larger rupture. The understanding of such dynamics is crucial to estimate future threats.

Despite our preliminary work, estimating the seismic moment to be released in future large earthquakes in the northwest Pacific region of the US is hampered by the lack of resolution on the processes occurring offshore. Further possible work might be aimed in merging all existing available data, including InSAR and GPS data, and use a specifically developed Independent Component Analysis to explore fault processes in this region. The study in Chapter 2 of the Cascadia megathrust was based only on daily GPS measurements. These key instruments are installed on-land and provide good resolution of fault processes occurring under the continent. However, coupling along the fault (i.e. the localisation of locked regions) is poorly constrained offshore and raises multiple questions, especially on the transition zone between locked and unlocked regions of the megathrust. What is the fault behaviour at this transition zone? Why does it lack seismicity? What is the influence of SSEs on the stress build-up along locked portions of the fault? Those questions have strong implications in terms of seismic hazard and we can address those only if we are able to properly detect/measure/separate the tectonic signals of interest. The spatial and temporal evolution of the SSEs and their relation to the transition and locked zones of the megathrust would benefit from spatially denser measurements along the coast and the solution is then to combine all the different data types available. The imaging of SSEs, the transition zone, and the fault's long term coupling would improve tremendously using Interferometric Synthetic Aperture Radar (InSAR) data. Newly launched satellite constellations such as SENTINEL-1A/B acquire SAR (Synthetic Aperture Radar) images with a repeat time of the order of days and additional constellations would be launched in the future (e.g., 2020 NASA-ISRO SAR Mission). The main advantage of InSAR is the extended spatial coverage of

this imaging technique that provides maps of ground deformation at every acquisitions. Now that SAR acquisitions are frequent, systematic, and freely available, we will be able to detect signals that could not be detected before. Merging all these geodetic datasets together will be a significant improvement in resolution for the spatial and temporal evolution of active fault slip in Cascadia, and will generate a tool applicable in other regions with similar instrumentation (e.g., Near Fault Observatories under the European Plate Observing System).

Bibliography

Brudzinski, M. R., & Allen, R. M. (2007), Segmentation in episodic tremor and slip all along Cascadia. *Geology*, *35*(10), 907-910.

Goldfinger, C., Nelson, C. H., Morey, A. E., Johnson, J. E., Patton, J. R., Karabanov, E., ... & Enkin, R. J. (2012). Turbidite event history: Methods and implications for Holocene paleoseismicity of the Cascadia subduction zone. *US Geological Survey Professional Paper*, *1661*, 170.

Sieh, K. E. (1978), Slip along the San Andreas fault associated with the great 1857 earthquake, *Bull. Seismol. Soc. Am.*, *68*(5), 1421–1448.

Sieh, K., D. H. Natawidjaja, A. J. Meltzner, C. C. Shen, H. Cheng, K. S. Li, B. W. Suwargadi, J. Galetzka, B. Philibosian, and R. L. Edwards (2008), Earthquake Supercycles Inferred from Sea-Level Changes Recorded in the Corals of West Sumatra, *Science*, *322*(5908), 1674-1678.

Zielke, O., J. R. Arrowsmith, L. G. Ludwig, and S. O. Akçiz (2010), Slip in the 1857 and Earlier Large Earthquakes Along the Carrizo Plain, San Andreas Fault, *Science*, *327*, 1119–1122, doi:10.1126/science.1182781

Jamais la nature ne nous trompe ; c'est toujours nous qui nous trompons.

Jean-Jacques Rousseau